UNIVERSITY OF SOUTHAMPTON

Superhydrophobic surfaces and their potential application to hydrodynamic drag reduction

by

Brian Gruncell

A thesis submitted in partial fulfillment for the degree of Doctor of Philosophy

in the
Faculty of Engineering and the Environment
Aerodynamics and Flight Mechanics Research Group

January 2014

UNIVERSITY OF SOUTHAMPTON

ABSTRACT

AERODYNAMICS AND FLIGHT MECHANICS RESEARCH GROUP

Doctor of Philosophy

by Brian Gruncell

Superhydrophobic surfaces appear frequently in the natural world, for example allowing insects to respire underwater and plants, such as the lotus leaf, to have self-cleaning properties. Attempts to mimic these superhydrophobic surfaces have been successful on nano- and micro-scales, with increased efficiency of water flowing through micro-channels when the walls are superhydrophobic. This thesis is focused on the proposed use of superhydrophobic surfaces to reduce drag on a much larger scale, applicable to small water craft such as canoes and yachts. The potential for drag reduction using superhydrophobic surfaces arises from the ability of such surfaces to retain an air-layer or plastron on the surface. The presence of a plastron results in slip and reduced shear at the surface, producing a drag reduction. This potential drag reduction is explored through numerical simulations and experimental testing. Computational Fluid Dynamics is used to explore the effect of slip on flow separation and viscous drag, allowing the potential drag reduction mechanisms to be explored. A range of superhydrophobic surfaces have been developed and characterised based on their roughness, contact angle and ability to retain a plastron. Confocal microscopy is used to generate the first high resolution 3D images of the air-water interface on a superhydrophobic surface over a large area. These images confirm the presence of a plastron on the surfaces and help contribute to the understanding of optimal design of superhydrophobic surfaces. These surfaces are explored experimentally in a towing tank with a repeatability of better than 1%. Refinement of the surface design leads to the presence of a plastron producing a relative drag reduction of up to 3% for hydrophobic sand, up to 10% for hydrophobic ridges and up to 15% for a hydrophobic mesh. Overall, superhydrophobic surfaces are shown to be capable of producing a relative drag reduction when a plastron is retained on the surface, although with the penalty of increased roughness-induced drag component. The drag reduction is shown to be linked to both the structure of the surface, and the quality and thickness of the plastron. It is demonstrated that it is difficult to retain a plastron over long immersion periods and manufacturing constraints currently limit applicability.

Contents

List of Figures

List of Tables

Academic Thesis: Declaration Of Authorship

I, Brian Robert Kirk Gruncell, declare that this thesis and the work presented in it are my own and has been generated by me as the result of my own original research.

Superhydrophobic surfaces and their potential application to hydrodynamic drag reduction

I confirm that:

1. This work was done wholly or mainly while in candidature for a research degree at this University;
2. Where any part of this thesis has previously been submitted for a degree or any other qualification at this University or any other institution, this has been clearly stated;
3. Where I have consulted the published work of others, this is always clearly attributed;
4. Where I have quoted from the work of others, the source is always given. With the exception of such quotations, this thesis is entirely my own work;
5. I have acknowledged all main sources of help;
6. Where the thesis is based on work done by myself jointly with others, I have made clear exactly what was done by others and what I have contributed myself;
7. Either none of this work has been published before submission, or parts of this work have been published as:
   (a) Gruncell et al. (2013a)
   (b) Gruncell et al. (2013b) (in the final stages of printing)

Signed: .

Date: .

Acknowledgements

The author would like to thank Neil Sandham, Martyn Prince, Ian Campbell & Angela Busse for their kind support, guidance and welcoming nature througout the PhD.

A special thank you to my family and my beloved Amanda Lee for your love and patience. I would not have made it without you all.

This Thesis forms part of a group project exploring superhydrophobic surfaces between the University of Southampton (Brian Gruncell, Neil Sandham & Angela Busse), Wolfson Unit MTIA (Martyn Prince & Ian Campbell) and Nottingham Trent University (Glen McHale, Michael Newton, Simon Stanley & Joseph Brennan). The funding provided by the Engineering and Physical Sciences Research Council under grant number EP/G058318/1 and EP/G069581/1 is gratefully acknowledged.

For my eternal companions, Vladimir and Estragon, as we wait together in the cold for the elusive Godot ...

Nomenclature

Roman symbols

a	Radius of compound sphere
A	Area or constant
b	Slip length or sphere radius
B	Constant
c	Chord
C	Constant
C_i	Coefficient relating to i
d	Diameter
D	Drag
E	Voltage
F	Fraction of surface area
g	Gravitational constant
G	Mesh growth rates away from the wall
h	Channel half height or plastron thickness or heat transfer coefficient
H	Ratio of roughness to characteristic length scale
I	Turbulence intensity or immersion length or current
k	Roughness height
K	Kurtosis
l	Characteristic length scale
L	Channel length or ratio of roughness periodicity to radius
m	Mass
n	Wall normal coordinate or nano (10^{-9}) or number of
N	Number of cells
p	Pressure
$P_{\%}$	Relative drag increase
q	Heat transfer rate
Q	Volume flow rate

r	Roughness parameter
R	Relaxation factor or reflectance or Resistance
s	Spacing between wire mesh elements
S	Source term or skewness or simulated value or best estimate of error
$S_{\%}$	Overall drag increase
t	Time
T	True value
u	Streamwise velocity component
$\boldsymbol{u}$	Velocity vector
v	Wall-normal velocity component
V	Volume
w	Spanwise velocity component or width of droplet
x, y, z	Cartesian coordinates
z	Fluid depth or roughness height
Z	Cavity aspect ratio

Greek symbols

α	Angle of attack
γ	Surface tension
δ	Boundary layer thickness or lubricating layer thickness
Δ	Change in variable
ϵ	Percentage error in simulation or surface emissivity
η	Non-dimensional grid spacing or refractive index
θ	Contact angle
κ	Capillary length or log-law constant
λ	Non-dimensional slip length
Λ	Perimeter of contact line
μ	Dynamic viscosity or micro (10^{-6})
ξ	Drag modification factor
Π	Wake parameter
ρ	Density
σ	Standard deviation
τ	Shear stress
ϕ	Separation angle or transported scalar
χ	Difference in drag for repeatable cases
ψ	Tilt angle

ε	Ratio of external and internal radii of encapsulated sphere

Subscripts

a	Average amplitude
A	Air or Advancing contact angle
b	Baffles
B	Buoyant material
c	Critical or cavity or based on chord length or conductive
C	Cassie-Baxter state or cell centre value
D	Drag
f	Surrounding fluid
F	Face centre value or premultiplying factor
HS	Hydrophobic samples
k	Supports and leads
l	Turbulent length
L	Laminar
LS	Liquid-solid interaction
LG	Liquid-gas interaction
i	Interfacial or distance from virtual origin
i, j, k	Relating to cartesian directions x,y and z
M	Modelling error
N	At a location above point P or numerical error
p	Perspex plates
P	Projected surface area or at point P
r	Radiative
R	Rib or Receding contact angle
s	Struts or streamwise or substrate
S	Solid fraction or at a location below point P
SB	Stefan-Boltzmann
SG	Solid gas interaction
SS	Stainless steel
t	Transition
T	Turbulent
w	Wall or water
W	Wenzel state or wetted area or heated wire
0	Stagnation or base or cold value
1	First grid point location or at location 1

2	At location 2
τ	Turbulent quantity
%	Percentage difference to baseline

Superscripts

$^+$	denotes a variable expressed in wall-units
$'$	denotes a fluctuating component
$*$	denotes a non-dimensional value

Operators

$\overline{a}$	time-average or bulk quantity of a
∇a	Gradient of a
Δa	Small change in a

Acronyms

ADC	Analogue-digital converter
AR	Aligned ridges
C	Corrected
CFD	Computational fluid dynamics
CFL	Courant-Friedrichs-Lewy
CIM	Coupled interface model
CuC	Coarse copper mesh composite structure
CuF	Fine copper mesh composite structure
DNS	Direct numerical simulation
FVM	Finite volume method
FS	Full slip
G1	Coarse grain sieved sand
G2	Fine grain sieved sand
H	Hydrophobic
ITTC	International Towing Tank Conference
LDA	Laser doppler anemometry
LHS	Left hand side

LVDT	Linear variable differential transducer
MS	Magic Sand
NC	Not corrected
NS	No slip
NVS	Navier-slip
PIV	Particle image velocimetry
RANS	Reynolds-averaged Navier Stokes
RHS	Right hand side
RS	Reduced shear
SIMPLE	Semi-implicit method for pressure-linked equations
SFM	Shear free model
SNR	Signal-to-noise ratio
TR	Transverse ridges
UDF	User-Defined Function
UDM	User-Defined Memory
W	Wetted

Chapter 1

Introduction

This thesis is concerned with the use of superhydrophobic surfaces to reduce hydrodynamic drag. The effect of a superhydrophobic surface is simulated numerically to explore the optimisation of the surface features for drag reduction. Experiments are then conducted to explore the effect of superhydrophobic surfaces on the drag of a flat plate.

This chapter introduces the concept of hydrophobicity and the ability of an immersed hydrophobic surface to retain an air layer or plastron. The potential for using this air layer to reduce hydrodynamic drag is examined. The final section details the aims and objectives of this thesis.

1.1 Literature review & theoretical background

1.1.1 Introduction to hydrophobicity

A hydrophobe is a person that is afraid of water; the meaning can easily be derived from its Greek roots: *hydro-* for water and *phobos* for fear. In terms of surface engineering a hydrophobic surface is one that repels water. In general terms this means that water will tend to roll off the surface easily and a surface that has been immersed in water will be removed dry.

The most common hydrophobic surfaces appear in nature. The lotus leaf (*Nelumbo nucifera*) is the best known and is considered sacred in some cultures (Barthlott and Neinhuis, 1997). The hydrophobic properties of its surface mean that drops

slide easily off the leaf, taking with them any surface containments or dirt. Another example is the Floating Leaf (*Salvinia biloba*) which is shown in Figure 1.1. This type of leaf is typically found floating on ponds and through its complex surface features and waxy coating, creates a hydrophobic surface, allowing it to maintain an air layer on its underside for the gaseous exchanges required in photosynthesis (Koch et al., 2009). In a similar fashion, Fisher spiders are able to respire underwater by maintaining a layer of air, or plastron, on their bodies when submerged (Shirtcliffe et al., 2006; Flynn and Bush, 2008). These fascinating properties and associated benefits have led to interest in the development of biomimetric hydrophobic surfaces for a range of applications.

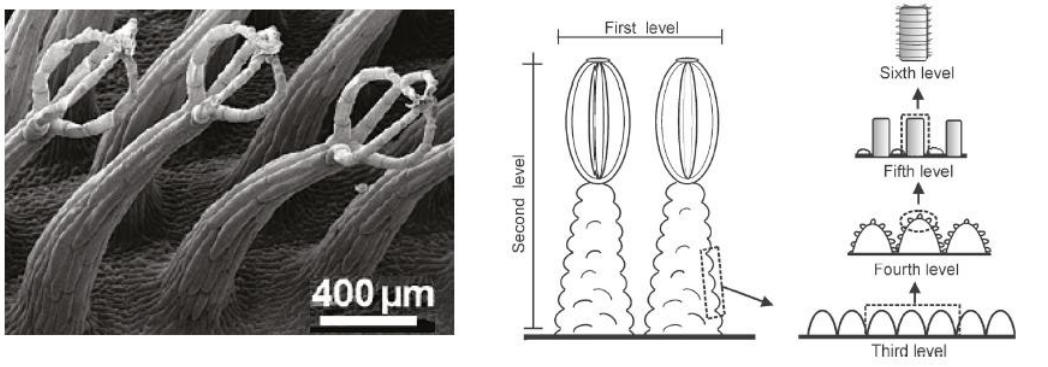

Figure 1.1: Successive scales of roughness on the *Salvinia biloba* leaf, adapted from Koch et al. (2009)

1.1.2 Drop dynamics

A hydrophobic material is defined as one on which a drop of water has a contact angle, θ, of above 90° as shown in Figure 1.2. The contact angle is measured from the surface to the tangent of the drop at the interface and can thus range from 0° to 180°.

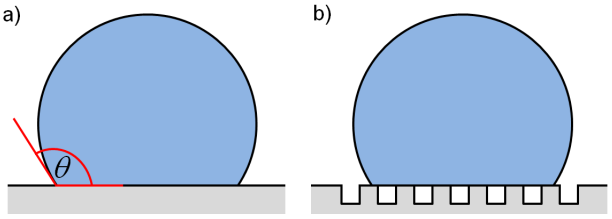

Figure 1.2: A droplet on a a) smooth and b) rough, structured hydrophobic surface

The antonym of hydrophobic is hydrophilic and this is defined by a contact angle of less than 90°. A surface that is extremely hydrophobic can be characterised as superhydrophobic if the contact angle exceeds 150°.

The contact angle can be predicted on a smooth surface, based on the interfacial tensions (γ) between each of the three phases: solid (S), liquid (L) and gas (G) (Rothstein, 2010) as

$$\cos\theta = \frac{(\gamma_{\mathrm{SG}} - \gamma_{\mathrm{LS}})}{\gamma_{\mathrm{LG}}}. \tag{1.1}$$

This equation shows that for a surface to have a high contact angle the interfacial tension between the solid and the liquid needs to be larger than between the solid and the gas. In general the contact angle is calculated for a static drop of a defined size, but the contact angle will vary as the drop moves or changes in size. This is known as contact angle hysteresis and is defined as the difference between the advancing and receding contact angles ($\Delta\theta = \theta_A - \theta_R$). The contact angle hysteresis is closely related to the mobility of a drop on the surface as it determines the critical tilt angle (ψ) at which the drop will start to roll, given by

$$mg\sin\psi = w\gamma_{LG}\Delta\theta. \tag{1.2}$$

The most well known hydrophobic surface is Teflon (PTFE) , which has a contact angle with water of 116° (Zawodzinski et al., 1991). In comparison glass has a contact angle of approximately zero (Cottin-Bizonne et al., 2005). The Lotus leaf has a contact angle of 160° with a contact angle hysteresis of 0.7° (Barthlott and Neinhuis, 1997), hence its self cleaning properties.

As mentioned briefly in Section 1.1.1, many biological surfaces have a degree of roughness that help to induce hydrophobicity. This effect of roughness on contact angle was initially reported by Wenzel in 1936 (Wenzel, 1936). He proposed a roughness parameter (r) based on the actual wetted area (A_W) and the projected area (A_P) which is used as a pre-multiplier of the chemical contact angle. This multiplier is included to account for the effective change in surface area through the addition of surface roughness; interfacial tension has units of energy per unit area and hence for a given projected surface area, a rough surface will have a higher energy level (or effective interfacial tension) than a corresponding smooth surface with the same surface chemistry.

$$\cos\theta_W = r\cos\theta = \frac{A_W}{A_P}\cos\theta \tag{1.3}$$

This equation allows the contact angle to be calculated for a surface that is rough and has been completely wetted by the fluid. It is commonly known as the Wenzel state and demonstrates that a rough surface ($A_W > A_P$) acts to amplify the hydrophobicity or hydrophilicity of the surface.

A similar law was reported by Cassie & Baxter in 1944, but to calculate the contact angle on a composite surface (Cassie and Baxter, 1944). This law is simply an average of the contact angles of the components of a composite surface based on their relative area coverage. It was originally used to demonstrate that the hydrophobic properties of ducks were due to the composite interface formed by air trapped between feathers. The contact angle is given as a function of the contact angle on each of the separate materials (θ_i) and the fraction of the surface covered by each (F_i).

$$\cos\theta_C = F_1\cos\theta_1 + F_2\cos\theta_2 \tag{1.4}$$

For the special case of one of the parts of the composite surface being air, the contact angle between air and water is 180° and equation (1.4) reduces to:

$$\cos\theta_C = F_1(\cos\theta_1 + 1) - 1 \tag{1.5}$$

This shows that the contact angle can be increased by having a larger surface fraction covered by air. The limiting case is when there is no solid interface which results in a contact angle of 180° and the water drop will not touch the surface.

1.1.3 Surface tension & interface stability

Section 1.1.2 described two different wetting modes for a given surface, but gave no indication of whether such a surface is physically possible. For example, considering a regular rough surface of square posts, if the posts were of the order of metres then it would be expected that the surface would be completely wetted by water (in a Wenzel state). However, if the posts were of the order of nanometres then it is likely the water would not penetrate the posts and the surface would be

able to support a composite interface, resulting in a Cassie-Baxter state. A difference in roughness scale cannot be distinguished by Equations 1.3 & 1.5 as they are dimensionless and involve only ratios of length scales. Careful consideration of the scale is required before either equation is employed.

A surface with nano-scale roughness is able to support a composite interface because of surface tension effects. Surface tension arises due to the intermolecular forces within a fluid, these forces attract molecules at the edge of the fluid towards the bulk of the fluid and act to minimise the overall surface area. At large length scales gravitational forces become important as they scale with mass (proportional to length cubed), compared to surface tension effects which scale as force per unit perimeter (proportional to length). To quantify the balance between these two effects a capillary length (κ) is defined as (Batchelor, 1967)

$$\kappa^{-1} = \sqrt{\frac{\gamma}{\rho g}}. \tag{1.6}$$

For the case of an air-water system $\kappa^{-1} \approx 2.73$mm and below this length scale surface tension effects dominate, allowing the Cassie-Baxter state to be supported. However, the effect of surface tension on the wetting state can be more readily understood by considering that surface tension and energy density have the same units and are effectively interchangeable.

A thermodynamic quantity known as the Gibbs free energy (G), describes the amount of energy available within the system to do work based on intermolecular forces, temperature and pressure (Wong and Ho, 2009). Any system in equilibrium will seek out the local energy minimum. In this case an infinitesimal change in the position of the interface may either result in energy being released or used. If it is the former, then displacement of the interface is energetically favourable and it will move to a new position. If it is the latter, then energy needs to be supplied to the system for the interface to move and the position is stable; thus there is an energy barrier between the two states.

The Gibbs energy approach has been used to prove that the Cassie-Baxter state is only possible if the contact angle is above 90°(Carbone and Mangialardi, 2005)[1]. Thus a surface has to be hydrophobic for a composite interface to be energetically

[1]This is not strictly true if a surface has more than one scale of roughness, but this is discussed in later sections

favourable[2]. Given that a surface is hydrophobic it is theoretically possible for a droplet to be in either the Wenzel or Cassie-Baxter state, with both the Wenzel and Cassie-Baxter states being local energy minima. Transition from the Cassie-Baxter state to the Wenzel state can occur quickly (in timescales of the order of 1ms) whilst transition hardly ever occurs in the opposite direction (Reyssat et al., 2008). Indeed, it is hard to picture a transition from the Wenzel to the Cassie-Baxter state when there is no obvious source of vapour. For the remainder of this report it is assumed that a transition from the Cassie-Baxter state to the Wenzel state is irreversible and results in a decrease in the contact angle[3].

It is clearly important to understand the conditions that could lead to the irreversible transition to a Wenzel state. Energy has to be added to the system to overcome the energy barrier between the two states, with the main potential source of energy being the pressure applied to the system (assuming the temperature remains approximately constant). The pressure of the fluid depends on the stagnation pressure (p_0), dynamic pressure and pressure head. Assuming that the fluid properties are constant means that the pressure can be affected by two main parameters, the fluid velocity (u) and the height of fluid (z) according to

$$p = p_0 + \frac{1}{2}\rho u^2 + \rho g z. \tag{1.7}$$

A critical pressure (p_c), above which transition will occur, can be calculated using the Gibbs free energy approach for a given surface geometry. In the case of pillars the critical pressure depends on the solid fraction (F_s), projected area and perimeter of the contact line (Λ) as

$$p_c = -\frac{\gamma \Lambda F_s \cos\theta}{(1 - F_s) A_P}. \tag{1.8}$$

To demonstrate how restrictive the critical pressure may be, consider a regular array of square posts that are 50μm wide and make up 10% of the total surface area. Assuming that the two fluids are air and water and taking the maximum possible contact angle of 180°, gives a maximum pressure difference of 640Pa or 0.0063atm. This can be compared to the pressure generated by a raindrop falling

[2]A composite interface can be sustained on a hydrophilic surface if energy is constantly provided to the system

[3]An electrically tunable surface has been created which switches between the two states (Krupenkin et al., 2005). In this case the air is replaced by water vapour which has evaporated due to a high energy electric pulse.

on the surface, which can be in the range 10^4 - 10^5 Pa (Afferrante and Carbone, 2009). Equation 1.8 also highlights the impact of surfactants, which would act to reduce the surface tension and hence the ability to maintain the Cassie-Baxter state.

A range of biological examples such as the Salvinia leaf (Figure 1.1) appear to overcome this critical pressure by having hierarchical structures of roughness. Such duality in structure scales acts as a safety mechanism; when the pressure is high enough to wet the largest scale of roughness it is insufficient to wet the smallest scales.

The previous analysis has been conducted for a static droplet on a surface, where surface tension forces dominate due to the small scales and low velocities. At larger scales the effect of the surface tension forces becomes less dominant and this can be characterised through the Weber number (We) or the Capillary number (Ca) as

$$\mathrm{We} = \mathrm{Ca.Re} = \frac{\rho u^2 l}{\gamma_{LG}}, \tag{1.9}$$

where u and l are characteristic velocity and length scales respectively and γLG is the surface tension between the two phases. As the surface tension forces become less dominant it is possible for the air-water interface to deform and possibly become unsteady (Spelt, 2006), which could result in potential for wetting.

1.1.4 Drag reduction potential

The previous sections have centred on a single drop on a superhydrophobic surface but now the focus is shifted to flow of water over an immersed superhydrophobic surface. It is assumed that the Cassie-Baxter state can be retained and that a plastron (air layer) will be present at the surface. This will clearly modify the effective boundary condition at the surface. The standard boundary condition for flow over a solid surface is the no-slip condition, where the velocity of the fluid at the wall is equal to the velocity of the wall. This boundary condition is expected to apply for all macroscopic flows except for rarefied gases where the mean free path becomes relatively large. In this case fluid slip occurs at the wall and the no-slip condition is no longer valid. Instead, Navier (1823) proposed a different condition (now known as the Navier-slip condition) which relates the velocity at the wall (u_w) to the wall normal velocity gradient at the wall ($\partial u/\partial n$) by a length

scale (b), known as the slip length. The slip length is the wall displacement at which the velocity profile would linearly extrapolate to zero.

$$u_w = b\frac{\partial u}{\partial n}\bigg|_w \tag{1.10}$$

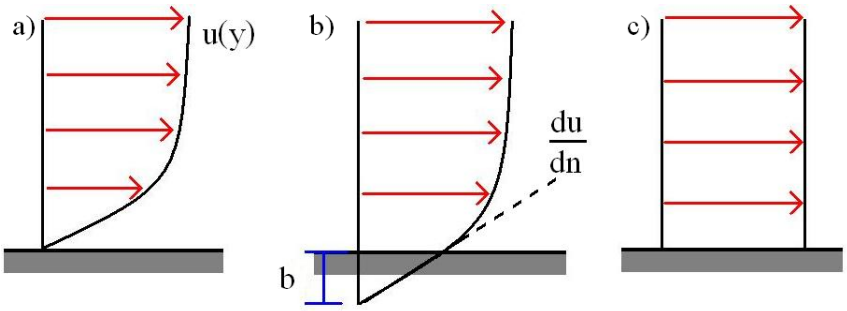

Figure 1.3: Three possible hydrodynamic boundary conditions a) no-slip, b) Navier-slip & c) full-slip

Figure 1.3 demonstrates that as the slip length is increased the wall normal velocity gradient of the stream velocity reduces, the velocity profile qualitatively becomes fuller and the full-slip case is approached. The Navier-slip condition has a lower shear stress at the wall than the no-slip condition, due to the reduced velocity gradient. This highlights that a drag reduction is possible if slip is generated at the surface. This can be confirmed by applying the Navier-slip condition to canonical flows such as Poiseuille flow for which an analytic solution is possible in 2D flow. The flow rate (Q) for a given pressure gradient ($\Delta p/L$) depends on the dynamic viscosity, channel half height (h) and the slip length

$$Q = \frac{\Delta p}{12L\mu}h^3\left(1 + \frac{6b}{h}\right). \tag{1.11}$$

The effect of including a slip length in the analysis is characterised by the term in brackets in Equation 1.11, which serves to increase the flow rate for a given pressure gradient, effectively a drag reduction. Equation 1.11 also demonstrates the importance of matching the slip length to the scales of the flow (e.g. boundary layer thickness or channel height). This can be characterised by a non-dimensional slip length ($\lambda = b/h$). A slip length of a few micro-metres will have a large effect in micro-channels, but if the same slip length were applied to a channel even just 1mm in height then there will be no measurable effect.

The idea of Navier-slip was introduced with regards to its original application of rarefied gases where molecules are physically slipping past each other (intrinsic slip). However, the Navier-slip condition can also be applied to the study of superhydrophobic surfaces, where although no intrinsic slip occurs, the surface produces a similar effect on the flow field, which can be characterised by an effective slip. One possible way of generating effective slip[4] at the surface is by lubricating the flow using a thin layer of less viscous fluid at the wall. Lubrication theory (Vinogradova, 1995) states that the slip length depends on the lubricating layer thickness (δ) and the ratio of the dynamic viscosity of the bulk flow (μ_w) and the lubricating layer (μ_a) as

$$b = \delta \left(\frac{\mu_w}{\mu_a} - 1 \right). \tag{1.12}$$

It is the presence of the less viscous liquid at the wall that acts to reduce the shear stress (τ) at the surface and hence the drag. In the case of an air-water system, the ratio between the two viscosities is approximately 100, reducing the local shear by approximately two orders of magnitude. Lubrication theory pertains to the idealised Cassie-Baxter state, where the solid fraction is reduced to zero and the surface is covered in a complete plastron. In reality, the perfect Cassie-Baxter state cannot be achieved[5] and surface roughness is required to support the air-water interface. This results in a composite interface, with regions of no-slip at the top of the roughness elements and regions of reduced shear at the air-water interface. This introduces complexity as the boundary condition is varying over the surface (typically on a small scale). To overcome this issue the surface can be explored at two scales. Firstly, the surface can be examined locally, where each of the surface elements is included, and the effect of the varying boundary condition can be explored. Secondly, the surface can be examined on a larger scale, where the local surface effects are averaged. In this way the overall effect of the composite interface can be modelled using the Navier-slip condition, once the surface-averaged slip length of the surface is known.

A wide range of techniques are available to directly measure the slip length on a particular surface, including Surface Force Apparatus, Atomic Force Microscopy and a Cone and Plate Rheometer. Each technique has advantages and disadvantages which are not discussed here as the primary point of interest is the magnitude of the slip length in each case. The range of slip lengths presented in Table 1.1 covers at least four orders of magnitude, with three orders of magnitude between

[4]Henceforth, the term slip is used to signify effective slip and the "effective" is dropped for simplicity

[5]See Section 2.2.3 for a discussion of the Leidenfrost effect

Surface	Roughness	θ	b
Mica (Bhushan et al., 2009)	0.2nm RMS	0	0nm
Gold (Baudry et al., 2001)	None	94	38nm
Epoxy+Lotus Wax (Bhushan et al., 2009)	178nm RMS	167	236nm
Silicon wafer (Choi and Kim, 2006)	1-2μm needles	175	20μm
Silicon wafer+nanofeatures (Lee and Kim, 2009)	450μm posts	150	300-400μm

Table 1.1: Slip lengths on a variety of surfaces measured using surface techniques

two surfaces that are both superhydrophobic. This clearly demonstrates that a high contact angle does not necessarily result in a high slip length. The results of Lee and Kim (2009) are encouraging, in that they provide evidence of "giant slip", which, when considered with Equation 1.11, demonstrates that a drag reduction is plausible with a superhydrophobic surface in channels or boundary layers which have a scale of the order of centimetres.

1.1.5 Experimental evidence of drag reduction

The application of superhydrophobic surfaces to drag reduction in micro-channels has been well documented with slip lengths determined from changes in the bulk flow and from measurements of the local slip length using interrogation techniques such as Particle Image Velocimetry.

The largest slip length - up to 120μm - was reported by Daniello et al. (2009) with a reduction in the pressure drop across a channel of up to 50%. Jung and Bhushan (2010) reported a slip length of 100μm and produced the largest non-dimensional slip length ($\lambda = b/l$ where l is the characteristic length scale) of $\lambda = 0.147$. However, there is a large scatter in the non-dimensional slip length reported in various sources as shown in Table 1.2, confirming that the ability of the surface to generate slip is intrinsically linked to the surface features. Micro-Particle Image Velocimetry ($\mu-$PIV) has been used to confirm slip at the surface of such hydrophobic channels with a drag reducing effect seen in both laminar and turbulent flows (Ou and Rothstein, 2005).

Channel Height	Surface Features	Re	b	λ
$2-12\mu m$ (Choi and Kim, 2006)	Transverse Ribs 500nm deep, 230nm pitch	-	$61 \pm 44nm$	0.0051
$2-12\mu m$ (Choi and Kim, 2006)	Parallel Ribs $500nm$ deep, $230nm$ pitch	-	$143 \pm 35nm$	0.0119
$76-254\mu m$ (Ou et al., 2004)	$30\mu m$ Square Posts $15-150\mu m$ pitch	<1000	$6-30\mu m$	0.1180
$76-254\mu m$ (Ou et al., 2004)	Parallel Ribs $30\mu m$ pitch & width	<1000	$7-8.5\mu m$	0.0355
$500\mu m$ (Hasegawa et al., 2009)	Circular Pillars $100\mu m$ pitch, 50-$100\mu m$ diam.	250-400	$0-40\mu m$	0.0800
$640\mu m$ (Govardhan et al., 2009)	Random $\sim 50\mu m$	<150	$0-70\mu m$	0.0011
$700\mu m$ (Jung and Bhushan, 2010)	Nano - roughness	0-5000	$91\mu m$	0.1300
$700\mu m$ (Jung and Bhushan, 2010)	Hierarchical	0-5000	$103\mu m$	0.1471
$5.5mm$ (Daniello et al., 2009)	Parallel Ribs $30\mu m$ deep, $30\mu m$	2000-9500	$70\mu m$	0.0127
$5.5mm$ (Daniello et al., 2009)	Parallel Ribs $60\mu m$ deep, $60\mu m$ wide	2000-9500	$120\mu m$	0.0218

Table 1.2: Slip lengths on a variety of surfaces measured using surface techniques

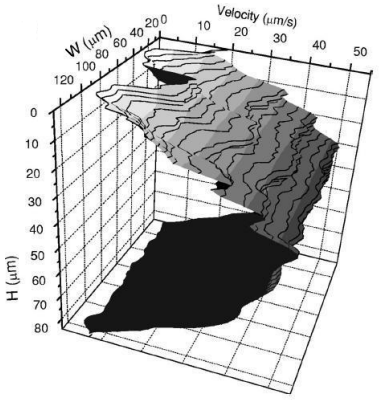

Figure 1.4: 3D μ-PIV profile in laminar flow, with a ridged hydrophobic upper surface (from (Ou and Rothstein, 2005)).

The μ-PIV velocity profile in Figure 1.4 is for laminar Poiseuille flow where the upper wall is patterned with superhydrophobic ridges. The sinusoidal periodicity in the profile at the upper edge corresponds to the ridge-cavity periodicity and hence provides direct evidence of slip and a non-zero velocity at the wall.

The applications presented thus far have been limited to small scales, such as micro-channels. This limitation in scales is understandable as it has been demonstrated that the ability of a surface to retain a plastron (i.e. maintain a Cassie-Baxter state) is intrinsically linked to the capillary length scale of the system. Increasing the overall scale of the problem means that the ability of a surface to retain a plastron is reduced.

However, through careful design and optimisation of the superhydrophobic surface it may be possible to achieve significant drag reductions on a much larger physical scale. The potential for using a lubricating layer of air to decrease drag on watercraft is well documented, for example Elbing et al. (2008) obtained an 80% drag reduction and Fukuda et al. (2000) demonstrated up to a 95% reduction of the drag of model ships. Unfortunately, these impressive drag reductions come with the associated cost of having to continuously supply energy to pump air over the surface, typically negating the improved efficiency. On the other hand they do provide a useful insight into the possibilities of achieving large drag reductions if a stable Cassie-Baxter state can be formed over a large area.

In recent decades a few experimental studies have been conducted on superhydrophobic surfaces and their potential for drag reduction at a larger scale. However, they have produced an incomplete understanding, with some issues clouded

by differences in experimental setup and the surfaces explored. The first macro-scale experiment on superhydrophobic surfaces was conducted in 1997 (Tian and Xue, 1997) where a drag reduction of 18-30% was recorded. These experiments were conducted on a flat plate in a cavitation tunnel with flow speeds from 6-14ms^{-1}. The surface was coated in a low surface energy coating and increased the contact angle from 104° to 147°, with a roughness to boundary layer height ratio of $H \approx 0.002$. However, it appears from their C_D vs. Re curves and the relatively low Reynolds number range that the drag reduction was due to a delay in the transition location and that there was a minimal effect on the viscous drag of the surface above this effect.

The next experimental research was conducted in 2004, where PIV was used to study flow over a flat plate covered with a replica of the lotus leaf (Balasubramanian et al., 2004) showed a slip velocity equivalent to 30% of the freestream value. These profiles were integrated to show a relative reduction in the momentum loss due to the surface but the Reynolds number (based on the chord) of the flow was just $\mathrm{Re_c} \approx 55,000$. The same surface was also used to coat a 3ft ellipsoidal model which achieved a 14% drag reduction at a Reynolds number of the order 10^6 (based on the total length of the model), however as a contoured body is used and the entire body is coated, it is unclear whether the drag reduction is due to a delay of transition, change in the separation location or a viscous drag reduction.

The effect of coating a surface with sand to act as roughness and then adding a superhydrophobic coating has also been explored. Such a coating was applied to a 4.3cm Joukowsky aerofoil (Gogte et al., 2005) and resulted in an 18% drag reduction at a Reynolds number of 1,500 and a drastic reduction to 7% at $\mathrm{Re_c} = 11,000$. Similarly, 1-2" spheres have been coated and dropped in a tank of water to measure their terminal velocities giving a 5-15% drag reduction (McHale et al., 2009) with a Reynolds number (based on the diameter) in the range 10-30,000. In these experiments it was found that both the roughness and superhydrophobic coating was required to achieve the effect, with ethanol used to wet-out the surface and prevent a plastron (air-layer) from forming. However, it is likely that in both of these cases the drag has been affected by a change in the separation location and the resultant wake.

A rotary viscometer has been used to explore a surface with nano-features, with a fluoro-coating to induce hydrophobicity by Zhao et al. (2010). In the laminar flow regime ($\mathrm{Re} \approx 10^4$) a drag reduction of 8.76% was achieved, but increasing the Reynolds number to the turbulent regime ($\mathrm{Re} \approx 10^6$) resulted in an increase

in drag. The same surface was also tested on a flat plate in the turbulent regime and produced a drag increase. This clearly demonstrates that a surface can have a different effect in a laminar or turbulent flow.

The drag on a flat plate with a superhydrophobic surface covered in a roughness of the order of 0.1-0.3mm ($H \approx 0.1$) has been explored and shown a drag reduction of up to 11% (Yu and Wei, 2006). The drag reduction rapidly deteriorated from 11% to 5% as the Reynolds number increased from $\mathrm{Re_c} = 28,000$ to $120,000$ but the drag reduction was confirmed by integration of velocity profiles from PIV. Furthermore, experimental testing of two different surfaces resulted in a drag increase across the Reynolds number range explored, suggesting that it is not sufficient for a surface to be superhydrophobic for it to achieve a drag reduction. A highly structured surface on a flat plate has also been shown to decrease the drag of a surface by up to 50% (Henoch et al., 2006). A silicon nanograss, with pillars just 400nm in diameter, but $1.5\mu m$ high was tested over Reynolds numbers of up to $\mathrm{Re_c} = 500,000$. The 50% drag reduction was recorded in the laminar regime, with a lower (but still substantial) drag reduction of 10-20% in the turbulent regime.

Research has also been conducted on 12mm square channels, with structured side walls. In laminar flow drag reductions of up to 3.7% have been seen with $H \approx 0.003$ (Ogata and Shimizu, 2011) and 8.8-12.6% with $H \approx 0.001$ (Watanabe et al., 2007). However, these two contributions disagree on whether micro-cavities or micro-ridges produce the largest drag reduction. A smaller channel (0.8-1.2mm) with similar scale roughness results in a closer match between the different scales ($H \approx 0.01$) and results in a reduction of the friction factor by 36% (Lu et al., 2010). All of these contributions were conducted with laminar flow and hence, although the surfaces are relatively large, cannot show whether such drag reductions can be extrapolated to higher flow speeds and Reynolds numbers.

The largest experimental slip length is reported from a PIV experiment conducted on a channel 1" high (Ahmad and Parthasarathy, 2007). The surfaces were coated in either a paint mimicking the properties of the Lotus leaf or sand and then a hydrophobic coating (giving a roughness of the order of 12μm, $H \approx 0.0005$). These surfaces produced slip lengths of b = 0.58mm ($\lambda = 0.29$) and b = 1.50mm ($\lambda = 0.59$) respectively, with the larger being nearly four times greater than the largest slip length previously reported. However, the experiments were conducted for turbulent flow at a constant Reynolds number of just 5,500 (based on the channel half height) and the accuracy of determining the slip velocity from PIV over a rough surface is unclear.

Finally, recent experiments by Aljallis et al. (2013) on a flat plate aligned with the flow have demonstrated that a drag reduction of 30% is possible at a Reynolds number of up to $\mathrm{Re_c} = 3 \times 10^6$. However, there results showed that above this Reynolds number range the same surface showed a drag increase, whilst another hydrophobic surface produced an increase in drag in the range of 30%. Furthermore, their experimental setup introduces uncertainty regarding the transition location and the wave making drag component; the shape of their C_D vs. Re curve also suggests that transition is being delayed by the hydrophobic surface.

In conclusion, the application of superhydrophobic surfaces for drag reduction has been explored in various experiments, across a wide range of Reynolds numbers. The majority of experiments suggest that the possibility of producing a drag reduction decreases as the Reynolds number is increased and that the dependence of the drag reduction on the properties of the hydrophobic surface is unclear. It is apparent that an understanding of the drag reduction mechanisms is lacking, with a range of possible causes of drag reduction from a changing separation location to a delay of transition or a reduction in viscous drag. Clearly, any of these mechanisms could be beneficial to certain applications; however the change in separation or transition location would typically be more application specific than a reduction in viscous drag as their use would be limited to a certain Reynolds number range. The majority of evidence reported demonstrates that it is likely to be possible to affect these locations, but there is limited evidence to support a reduction in viscous drag especially at high Reynolds numbers. Furthermore, little is known about the quality or presence of a plastron in any of the experimental work, preventing any conclusions to be drawn about the drag reduction mechanisms.

1.2 Aims & objectives

The preceding section has detailed the potential for superhydrophobic surfaces to produce a hydrodynamic drag reduction, whilst also demonstrating that the understanding of the physical drag reduction mechanism is lacking. The primary objectives of this study are:

1. To improve the understanding of how to design superhydrophobic surfaces to retain an air layer or plastron.
2. To improve the understanding of the properties of the plastron and surface features for the optimisation of drag reduction.

3. To simulate the effect of superhydrophobicity on a range of problems to determine which flow features can be affected by the presence of a plastron (e.g. laminar or turbulent flows, transitional flows or regions of separation).

4. To produce and further develop superhydrophobic surfaces based on the improved understanding.

5. To experimentally determine the effect of superhydrophobic surfaces on hydrodynamic drag in comparison to a wetted state and a smooth surface.

6. To explore the air-water interface through visualisation of the surface and determine whether current models of superhydrophobic surfaces are accurate.

The following chapters seek to address these aims and objectives. Chapters 2 & 3 explores the potential for drag reduction using superhydrophobic surfaces by presenting simulations of various models for the effect of a plastron and composite surface on the hydrodynamic drag. Chapter 4 discusses the design requirements for a superhydrophobic surface to produce a consistent plastron and optimise the drag reduction potential. The superhydrophobic surfaces developed for this study are presented along with visualisations of the surface and air-water interface. Chapter 5 details the experimental setup and data analysis that is used to measure the effect of superhydrophobicity on drag. Chapter 6 presents the results from this experimental testing and discusses the drag reductions achieved. Finally Chapter 7 reports the overall findings of this report, along with potential future work.

Chapter 2

Simulation of flow past hydrophobic spheres

This Chapter[1] explores the potential for superhydrophobic surfaces to be used to reduce the hydrodynamic drag of spheres using Computation Fluid Dynamics. Simulations are conducted on the case of a superhydrophobic sphere encapsulated in a layer of air to explore the effect of hydrophobicity on separation and bridge the gap between previous analytical and experimental work.

2.1 Computational fluid dynamics

In the following sections Computational Fluid Dynamics (CFD) is used to explore the effect of superhydrophobic surfaces on the drag of a variety of configurations. It is therefore pertinent to introduce the basic concepts used in the simulation of fluid flows.

The approach used in this report is the Finite Volume Method (FVM) where the computational domain is split into small cells. Within these cells the fluid is simulated by solving the relevant equations. If the cells are sufficiently small and the relevant equations are modelled accurately this approach can provide an accurate representation of the flow.

The typical approach for steady, incompressible and isothermal fluid flow is to apply conservation of mass and conservation of momentum to each cell or control

[1]Part of this work (Section 2.2) has been published in Physics of Fluids as Gruncell et al. (2013a)

volume and integrate over the domain. This can be explored by considering a 2D case where a fluid (with a density of ρ and dynamic viscosity μ) flows through a square domain subject to a pressure gradient ($\partial P/\partial x_i$) and shear forces (τ_{ij}).

Conservation of mass ensures that the mass of the entire system remains constant, such that the rate of change in mass within the control volume is equal to the net flow of mass into the control volume. A similar concept applies to conservation of momentum, which balances the pressure and shear forces with the rate of change of momentum within the control volume. Application of these principles to a full 3D case produces the Navier-Stokes equations (Anderson, 1995), given by

$$\rho\frac{\partial \boldsymbol{u}}{\partial t} + \rho\left(\boldsymbol{u}\cdot\nabla\boldsymbol{u}\right) = -\nabla P + \mu\nabla^2\boldsymbol{u}, \tag{2.1}$$

for incompressible flow, with

$$\nabla\cdot\boldsymbol{u} = 0. \tag{2.2}$$

In turbulent flows the velocity and pressure are decomposed into a time-averaged (over-bar) and a fluctuating component (prime notation)

$$u_i = \overline{u}_i + u_i' \tag{2.3}$$

$$p_i = \overline{p}_i + p_i' \tag{2.4}$$

This results in a time-averaged equation set known as the Reynolds-averaged Navier-Stokes (RANS) equations:

$$\frac{\partial}{\partial t}\left(\rho\overline{u}_i\right) + \frac{\partial}{\partial x_j}\left(\rho\overline{u}_i\overline{u}_j\right) = -\frac{\partial P}{\partial x_i} + \frac{\partial}{\partial x_j}\left[\mu\left(\frac{\partial\overline{u}_i}{\partial x_j} + \frac{\partial\overline{u}_j}{\partial x_i} - \frac{2}{3}\delta_{ij}\frac{\partial\overline{u}_l}{\partial x_l}\right)\right] + \frac{\partial}{\partial x_j}\left(-\rho\overline{u_i'u_j'}\right) \tag{2.5}$$

$$\frac{\partial\rho}{\partial t} + \frac{\partial}{\partial x_i}\left(\rho u_i\right) = 0 \tag{2.6}$$

These equations are the basis for the analysis conducted in Section 3.1 and 5.3.3, along with a turbulence model to close the system of equations, whereas Sections 2.2 and 3.2 are for laminar flow. It is important to remember that CFD is a modelling tool, and that the results are therefore inherently dependent on the accuracy of the models used. Inaccuracies or errors may be introduced through

the models of the flow (for example the turbulence model used) and through the numerical schemes used (producing artificial numerical diffusion and dispersion).

Simulations using CFD have been conducted in the following sections to explore the effect of hydrophobic surfaces on the drag of a range of test problems. At each stage attempts are made to quantify the errors involved to ascertain the accuracy of the simulations.

2.2 Flow past a superhydrophobic sphere

2.2.1 Introduction

This section is inspired by the work on superhydrophobic spheres by McHale et al. (2009) and McHale et al. (2011). Drop tank experiments demonstrated that a superhydrophobic sphere can fall through a tank of water faster than a smooth sphere (McHale et al., 2009), suggesting a drag reduction. It has also been shown analytically that a sphere encapsulated in a layer of less viscous fluid will experience a reduced drag in Stokes flow (McHale et al., 2011). The analytical approach showed a reduction in the viscous drag, whilst the experiments were conducted at higher Reynolds numbers where inertial effects are important and the drag reduction is likely to be related to a change in separation location. The following numerical simulations are primarily aimed at bridging the gap between the Stokes flow analysis and higher Reynolds number experimental results. The drag reduction mechanism is explored to further understand the performance of superhydrophobic surfaces as an approach for reducing drag.

2.2.2 Flow past a solid sphere

Flow past a solid sphere appears to be a relatively simple test case, however it exhibits a complex range of flow patterns as the Reynolds number is increased. The Reynolds number (Re) is a non-dimensional parameter which characterises the relative importance of viscous and inertial forces. It is defined based on the freestream velocity (U_∞), fluid density (ρ) and viscosity (μ) along with a representative length scale, which is typically taken as the diameter of the sphere ($2b$) so that

Re range	Flow Regime
<1	Stokes flow
∼40	Axi-symmetrical recirculating wake
100-200	Alternate vortex formation
400-300,000	Laminar separation
300,000-3,000,000	Laminar separation, turbulent reattachment & turbulent separation
>3,000,000	Turbulent separation

Table 2.1: Flow regime variation for a solid sphere at various Reynolds numbers

$$\mathrm{Re} = \frac{\rho U_\infty (2b)}{\mu}. \tag{2.7}$$

The flow patterns around the sphere range from a fully symmetric flow at low Reynolds numbers to a vortex shedding regime at moderate Reynolds numbers and steady turbulent separation at high Reynolds numbers (Houghton and Carpenter, 2006), as shown in Table 2.1.

In the various flow regimes the sphere experiences different levels of drag. This is typically characterised by a non-dimensional drag coefficient (C_D), whereby the drag (D) is non-dimensionalised by the density, velocity and frontal surface area.

$$C_D = \frac{D}{1/2\rho U_\infty^2 \pi b^2} \tag{2.8}$$

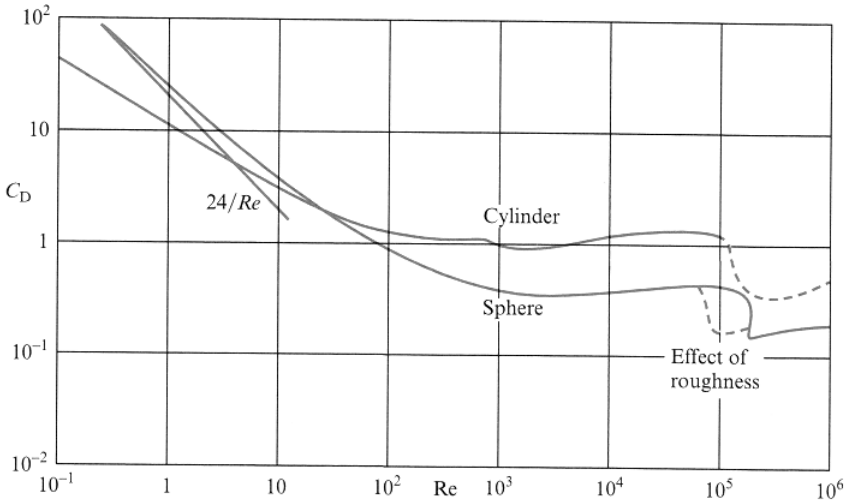

Figure 2.1: Variation of drag coefficient of a sphere with Reynolds number [Reproduced from Douglas et al. (2005)]

The variation of the drag coefficient with Reynolds number is demonstrated in Figure 2.1. The curve can be split into approximately four regions:

1. Very low Reynolds numbers, where the drag coefficient can be calculated based on an analytic expression in Stokes flow

$$C_D = \frac{24}{\mathrm{Re}}. \tag{2.9}$$

2. Low Reynolds numbers, where the viscous forces are also important and the drag coefficient can be calculated based on an experimental correlation

$$C_D = \frac{24}{\mathrm{Re}}\left(1 + 0.15Re^{0.687}\right). \tag{2.10}$$

3. Intermediate Reynolds number, where the drag coefficient is approximately constant at around $C_D \approx 0.4$.

4. High Reynolds number, where the drag coefficient rapidly changes due to the changing separation angle.

In the fourth region the separation angle changes due to a modification in the state of the boundary layer. The laminar boundary layer separates from the sphere relatively early (before the point of maximum thickness) resulting in a wide wake. The wake is a region of reduced pressure and results in a large addition to pressure drag. As the Reynolds number is increased, transition from laminar to turbulent flow occurs. A turbulent boundary layer is less prone to separation and thus remains attached for longer, resulting in a narrower wake and less drag as shown in Figure 2.2.

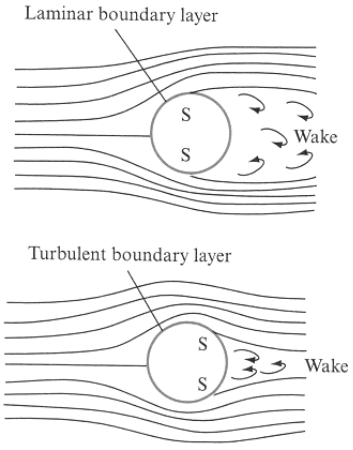

Figure 2.2: Typical flow regimes for a sphere a) laminar separation & b) turbulent separation [Reproduced from Douglas et al. (2005)]

As the Reynolds number is increased further, the turbulent boundary layer becomes less stable and the separation points move further forward, producing a larger wake and more drag. Hence, there is a drag crisis, or a minimum point in the C_D curve (Figure 2.1), where the separation points have moved as far aft as possible.

The drag coefficent of the sphere also depends on the relative surface roughness (k^*) and the turbulence intensity (I). The relative surface roughness is the ratio of the average roughness height (k) and the diameter of the sphere, so that

$$k^* = \frac{k}{2b}. \tag{2.11}$$

The turbulence intensity is quantified through the fluctuations away from the free stream value (denoted with a prime notation), such that

$$I = \frac{\overline{u'^2 + v'^2 + w'^2}}{U_\infty} \tag{2.12}$$

Achenbach (1974) demonstrated that the introduction of disturbances into the flow - either through increased turbulence intensity upstream of the sphere or through surface roughness - results in a lower transition Reynolds number and also causes the drag crisis to shift to a lower Reynolds number. This suggests the drag coefficient is sensitive to the combined effect of Reynolds number, surface roughness and upstream disturbance levels, and careful analaysis of potential changes in the separation location is required when considering flow past a sphere in the Reynolds number range $10^4 < \mathrm{Re} < 10^6$.

2.2.3 Effect of hydrophobicity

McHale et al. (2011) showed analytically that the Stokes drag of a solid sphere can be reduced according to a drag modification factor (ξ) if it is encapsulated in a sphere of a less viscous fluid as shown in Figure 2.3. The drag modification factor (ξ) is calculated based on the ratio of the drag between a solid sphere (radius b) and the same solid sphere encapsulated in a plastron (thickness h, such that the composite sphere has a larger radius $b + h$).

$$\xi = \frac{(\text{Drag of sphere with plastron})}{\text{Drag of sphere}} \tag{2.13}$$

A value of $\xi < 1$ signifies an overall reduction in drag of the encapsulated sphere. The drag modification factor depends on the relative radius of the encapsulated sphere ($\varepsilon = b/a$) and the ratio of dynamic viscosity between the two fluids ($\mu_{aw} = \mu_a/\mu_w$) and for Stokes flow can be calculated using

$$\xi = \frac{2}{3\varepsilon}\left[\frac{1 + 3\mu_{aw}F(\varepsilon)}{1 + 2\mu_{aw}F(\varepsilon)}\right], \tag{2.14}$$

where

$$F(\varepsilon) = \frac{(1+\varepsilon)(2\varepsilon^2 + \varepsilon + 2)}{(1-\varepsilon)(4\varepsilon^2 + 7\varepsilon + 4)}. \tag{2.15}$$

The encapsulated sphere is a model of perfect hydrophobicity, where the water is no longer in contact with the solid body. Such a perfect state may also be achieved using the Leidenfrost effect (Leidenfrost, 1756), where the surface is heated beyond the Leidenfrost temperature which is significantly above the boiling temperature of the fluid, creating an insulating vapour layer between the surface and the fluid.

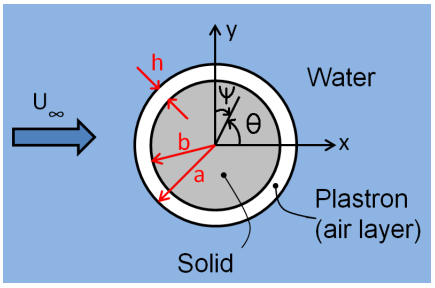

Figure 2.3: Schematic of an encapsulated sphere

The presence of an encapsulating layer on the terminal velocity of a sphere has been explored experimentally by McHale et al. (2009) and Vakarelski et al. (2011) at high Reynolds number ($10^4 < \mathrm{Re} < 10^5$) showing drag reductions of up to 15% and 85% respectively. In each case the drag mechanism is postulated to be a reduced shear at the sphere surface resulting in a delay in separation. The primary difference between the two studies is the mechanism for retaining a plastron on the surface, with the former using randomly structured superhydrophobic surfaces and the latter using the Leidenfrost effect. The random roughness supporting the plastron in the superhydrophobic case ensures that the plastron is energetically stable over time, whilst continuous heating is required to maintain the Leidenfrost plastron for more than a minute. However, the roughness contributes to a composite interface, rather than a perfectly encapsulated sphere, resulting in a lower drag reduction. A combination of the Leidenfrost effect (to generate the vapour layer)

and a rough superhydrophobic surface (to retain it) has recently been suggested (Vakarelski et al., 2012).

Previous numerical simulations have been conducted on a plastron-encapsulated sphere at low Reynolds numbers, with attempts to model a composite interface with slip at the surface (Atefi et al., 2007) and Feng (2010) using a reduced viscosity through a simple application of the VOF (Volume of Fluid) model . These results demonstrate the possibility of drag reduction and delay of separation at finite Reynolds numbers. However, the models are based on assuming it is possible to retain an air layer at the surface and they do not facilitate the design of superhydrophobic surfaces capable of achieving such an effect.

2.2.4 Numerical model

To simulate the flow past a superhydrophobic sphere the Navier-Stokes equations have been solved using a finite volume approach in two coupled domains. The simulations have been conducted to match an air-water system with fluid properties $\rho_w/\rho_a = 815.00$ and $\mu_w/\mu_a = 56.05$. For Reynolds numbers below approximately 130 the flow past a sphere is steady and axisymmetric (Taneda, 1956), furthermore slip at the surface delays the typical flow regimes for a sphere to a higher Reynolds number (Atefi et al., 2007; Feng, 2010). It is possible that the slip/no-slip composite interface may promote a 3D instability but it is considered to be beyond the scope of this work. Hence, the simulation is simplified in the present work by assuming that the flow is axisymmetric with an axis of rotation along the x-axis. For convenience, the problem was solved using the commercial CFD package Fluent™(Fluent, Inc., New Hampshire). The flow is entirely laminar so no turbulence model is required and the major source of inaccuracy in a CFD package is removed. The code is used to solve the Reynolds-averaged Navier-Stokes equations.

The boundary conditions used are a no-slip condition at the solid sphere surface ($\boldsymbol{u} = 0$), constant axial velocity at the inlet ($\boldsymbol{u} = [u_i, 0, 0]$) and a pressure outlet where the gauge pressure is set to zero. The boundary condition at the air-water interface is discussed in detail in the following pages. The SIMPLEC pressure-correction algorithm is used to aid convergence and second order spatial discretisation is used to improve accuracy. Each simulation is run in steady state mode until convergence has been achieved. Convergence is achieved when reducing the average residual ($|R|$) within the domain by an order of magnitude does

not influence the drag by more than 1%. The required residual level was checked across the range of Reynolds numbers and plastrons explored in this study and was found to be in the range of $|R| = 10^{-6}$ to $|R| = 10^{-7}$, with thinner plastrons and higher Reynolds numbers being more sensitive to the convergence level.

The plastron is initially modelled as a layer of air (with fluid properties ρ_a and μ_a) with a constant thickness ($h = a - b$). The two phases (air and water) are considered as two distinct fluids in two separate domains. The air-water interface is treated as being fixed in space and does not deform due to the applied viscous or pressure forces. The coupling between the two phases is conducted through the boundary condition at the air-water interface. To ensure the correct physical behaviour at the interface three conditions have to be imposed. First, the tangential velocity components at the interface have to be matched. Second, the shear stress components tangential to the interface also have to match. Finally, there has to be zero mass transfer across the interface. To impose these three conditions a new boundary condition has been developed through the use of User-Defined Functions (UDF) and User-Defined Memory (UDM). The approach involves a two-way coupling where information from the air domain is used to impose a boundary condition in the water domain and vice-versa. This results in a continuous velocity profile across the interface, but (by virtue of the different dynamic viscosities of the two fluids) a discontinuous velocity gradient profile. The model is implemented in FLUENT by coupling the domains in both directions. That is, during every iteration, solution data from the water domain is used to generate a boundary condition for the air domain and vice-versa.

FLUENT only allows the prescription of either the velocity or shear stress components at the boundary, otherwise the former will be over written. To overcome this issue the velocity condition is applied at the boundary of the water zone and shear stress condition is applied at the boundary of the air zone. It is worth stressing here that this coupled interface boundary condition does not appear to be stable if the two conditions are applied to the opposite zones, although the reason for this is unclear.

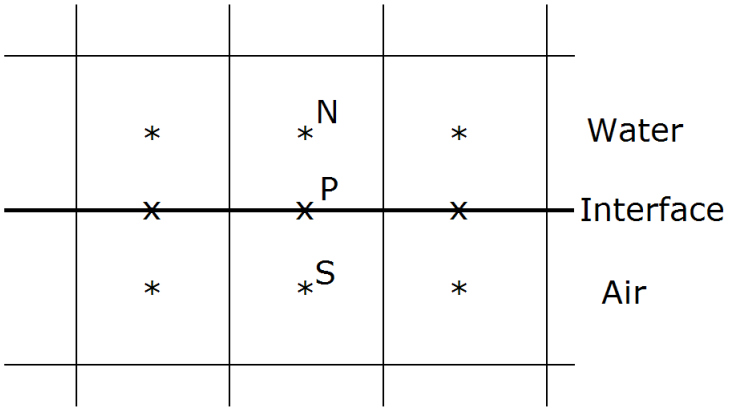

Figure 2.4: Details of application of interface boundary condition

Figure 2.4 shows the setup that is used to calculate the boundary condition. FLUENT stores the flow variables at both the cell centre (stars) and the face centre (crosses). Boundary conditions are applied at the face centre of each cell on the boundary. In this case there are two boundaries at the interface as it is the boundary between two zones. Thus there are two points collocated at P, one for either zone, and it is at these positions that the two conditions are applied.

To satisfy the velocity continuity condition the velocity at point P (attached to the air zone) is simply set to the same value as the cell-centred value at the point N.

$$U_{P,S}^{i+1} = U_N^i \tag{2.16}$$

The previous iteration is denoted as iteration level i, such that the current iteration is $i+1$. The shear stress at point P (attached to the water zone) is then calculated based on the cell-centred value of the interface-normal velocity gradient at the point S and the dynamic viscosity of the fluid, using

$$\tau_{P,N}^{i+1} = \mu_{\text{air}} \left(\frac{\partial U}{\partial n} \right)_S^i . \tag{2.17}$$

Each of the two conditions are implemented as a separate function within a single UDF. This UDF is interpreted within FLUENT and the functions are used to set the velocity or shear components as necessary at the interface. Details of the

calculation of the shear stress components and the source code for the UDF can be found in Appendix B.

This is an idealised model of the air-water interface in that it is assumed that the interface will not deform. This assumption is valid when the contact line is pinned at the top of the roughness elements (which is likely to be the case due to a local energy barrier at the discontinuity in curvature (He et al., 2005)) and the Capillary number (ratio of viscous to surface tension effects) is low. The interface would deform under pressure to produce a balance between the pressure in the external flow, pressure in the cavity and the surface tension. However, by assuming the interface does not deform any pressure difference between the two domains is not alleviated and produces a discontinuous pressure across the interface. The pressure difference was found to be orientated such that if the interface deformation were modelled it would deform towards the substrate, but at low Reynolds numbers and small scales it is assumed that such deformations will be minimal. Higher Reynolds number flows would also likely decrease the stability of the interface due to the increase in the Capillary number, and furthermore other possible instabilities such as something like the Kelvin-Helmholtz instability (due to the discontinuous velocity gradient) or resonant shedding from an open cavity may be excited. This is discussed further in Section 4.1.2 & 3.2.4 where higher Reynolds numbers are explored and the likelihood of wetting occuring is increased. This further demonstrates that the interface model is idealised as it is inherent in this assumption that the Cassie-Baxter state is maintained, and that the surface tension and roughness is capable of preventing capillary penetration causing the wetting out of the cavities (i.e. a transition to the Wenzel state).

The interface is assumed to match the curvature of the solid sphere such that the composite interface is itself spherical in shape. Vakarelski et al. (2011) demonstrated that at a Reynolds number in the range $10^4 - 10^5$ the Leidenfrost effect can be used to produce a nearly completely smooth spherical encapsulating air layer. It is postulated that, at the significantly lower Reynolds numbers explored in this study, an idealised spherical shape is an accurate approximation. However, the results presented in this report should be considered as an optimal case; any interface deformation will likely result in decreased performance of the plastron.

To ensure that the solution is fully resolved, mesh dependency studies have been conducted. Firstly, considering Stokes flow, it was found that the drag only matched the analytic theory (Happel and Brenner, 1986) of a sphere in a freestream when the far-field was at $500b$. This is in contrast to the higher Reynolds number

range where the domain size could be set to $50b$ to achieve domain size independent results. Furthermore, the regions requiring high grid resolution differ between Stokes flow and higher Reynolds numbers, with the former only requiring high resolution close to the sphere and the latter also requiring high resolution in the wake. A sketch of the domains used for the low ($\mathrm{Re} < 1$) and high ($1 < \mathrm{Re} < 100$) Reynolds number cases are shown in Figure 2.5.

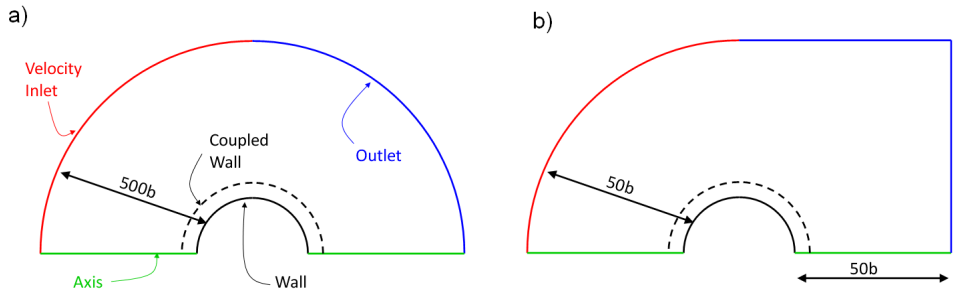

Figure 2.5: Schematic of domain shape and size used for a) low Reynolds number range and b) high Reynolds number range (not to scale)

A structured Cartesian grid has been used for the low Reynolds number mesh, with a semi-circular domain. For the high Reynolds number mesh a multi-block approach with an unstructured mesh has been used, allowing a higher resolution close to the sphere and in the wake, whilst maintaining a lower resolution in the far-field and ensuring a high mesh quality. Initial studies were conducted to explore the overall mesh resolution, with the mesh resolution being successively doubled until a grid independent solution (to within 1%) was obtained for a solid sphere across the full Reynolds number range explored. A typical mesh for the data presented included approximately 1,200 grid points along the semi-circular edge of the sphere and 40 grid points across the plastron. Figure 2.6 demonstrates the successive doubling of mesh resolution and convergence of the results toward a grid independent solution (the percentage change in drag shown is based on the finest grid in each case). The solution converged to the empirical relation (Eqn. 2.10) for a solid sphere, matching to better than 1% across the entire Reynolds number range explored.

As the Reynolds number increases the solution becomes more dependent on the mesh used, as shown in Figure 2.6. For simulations with a plastron the mesh resolution was held approximately constant for radial positions further than $2b$ from the sphere surface, whilst an unstructured quadrilateral mesh was applied in the region close to the plastron. The mesh within and close to the plastron was again successively refined until the drag and velocity profiles within the wake and plastron were grid independent. For simulations with baffles (see Section 2.2.6)

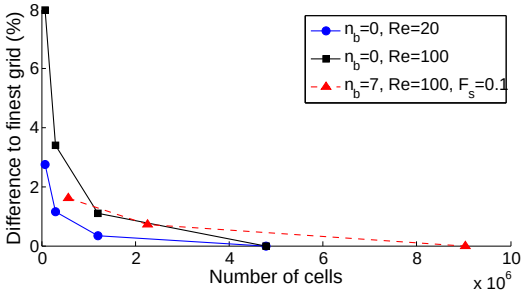

Figure 2.6: Grid refinement study for a solid and plastron-encapsulated spheres (see Section 2.2.6for definitions of F_s and n_b)

the grid was further refined so that the grid points were highly focused around the tips of the baffles. Doubling the resolution demonstrated mesh independence in both the viscous and pressure drag components.

A range of studies has been conducted to ensure that the approach described in Section 2.2.4 is capable of capturing firstly the drag on a solid sphere and secondly the drag of a solid sphere encapsulated in a plastron. Firstly, the flow past a solid sphere has been simulated over the Reynolds number range $0.0001 < \mathrm{Re} < 100$. The low Reynolds number meshes were used up to $\mathrm{Re} < 1$, whilst the high Reynolds number meshes were used above $\mathrm{Re} = 1$. The two meshes produced the same drag to within 1% at $\mathrm{Re} > 1$. Grid convergence and residual independence allows each of the drag values to be cited to an accuracy within $\pm 1\%$ unless otherwise stated. Figure 2.7 demonstrates that the simulations accurately capture the drag coefficient of a solid sphere over a wide Reynolds number range, including the departure from Stokes theory at high Reynolds number. A separation angle, θ_s, (using the convention for θ in Figure 2.3) is defined using the change in sign in the tangential velocity at the first cell centre off the wall. It was verified, as shown in Figure 2.8 that the simulations accurately match the onset of separation at $\mathrm{Re} \approx 24$ and the variation of separation angle with Reynolds number (Taneda, 1956).

Secondly, simulations have been conducted to explore whether the coupled interface model can be used to simulate superhydrophobic spheres. A range of plastron thicknesses ($0.001h/b < 0.2$) has been explored in Stokes flow to allow a comparison to the analytic theory(McHale et al., 2011). Figure 2.9 shows that the theoretical drag reduction due to the presence of the plastron around the sphere is matched well by the coupled interface simulations. Furthermore, Figure 2.10 shows that the velocity profiles in both the air layer and external water flow field match theoretical results deduced from the streamfunctions given in McHale *et*

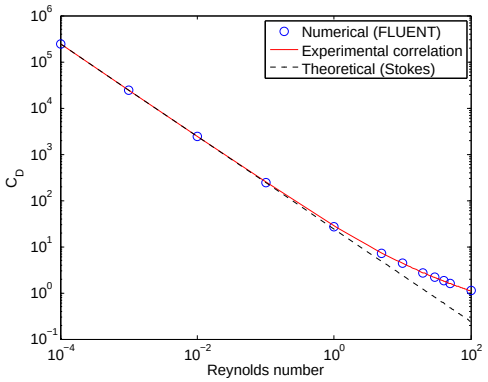

Figure 2.7: Drag coefficient of solid sphere across a wide Reynolds number range

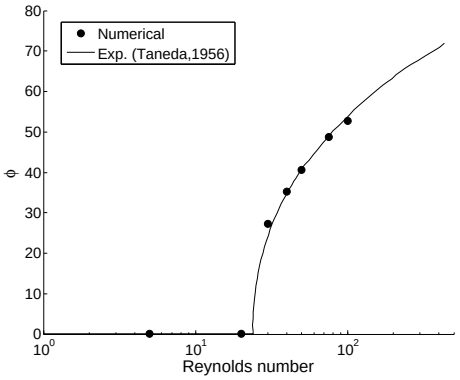

Figure 2.8: Dependence of separation angle on Reynolds number for a solid sphere

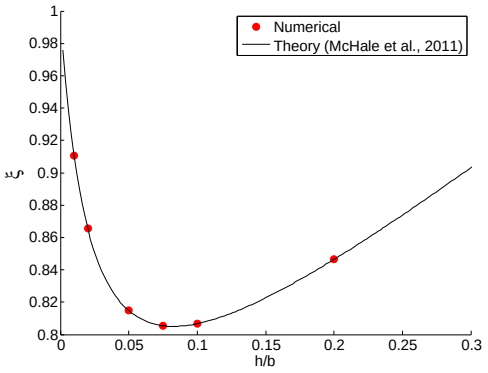

Figure 2.9: Drag reduction due to plastron in Stokes flow

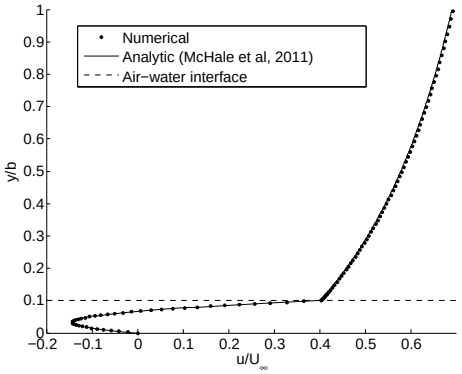

Figure 2.10: Axial velocity at the top of the sphere (Re $= 0.001, h/b = 0.1$)

al.(McHale et al., 2011). The velocity profile demonstrates the generation of slip at the air-water interface ($\sim 0.4U_\infty$) and the discontinuous velocity gradient due to the matched shear stress but difference in dynamic viscosities of the two fluids. This suggests that the coupled interface model accurately captures the physics associated with the presence of a plastron.

2.2.5 Idealised model results

For Stokes flow, in agreement with the analytic theory, a maximum drag reduction of 19% is obtained from Figure 2.9. The drag reduction depends on the thickness of the air layer, with the optimal air layer thickness being approximately $0.1b$. Below this optimum value, the drag reduction decreases with decreasing air layer thickness; the thicker air layer supports a larger circulation and produces less

viscous drag at the interface. Above this value, the thickness of the plastron increases the effective frontal area of the sphere and the increase in pressure drag begins to dominate over the reduction in viscous drag.

Figure 2.11 shows the effect of increasing the Reynolds number of the external flow. The value of ξ slowly decreases as the Reynolds number increases from $\mathrm{Re} = 0.01$. As the Reynolds number is increased above 10 a larger drag reduction is evident, up to 50% for $h/b = 0.1$ at $\mathrm{Re} = 100$. This increased drag reduction was found to be associated with the suppression of the attached vortex regime in the Reynolds number range $30 < \mathrm{Re} < 100$ as demonstrated in Figure 2.12. The reduced shear stress and finite slip velocity at the air-water interface mean that separation from the downstream surface of the sphere is completely suppressed, resulting in a narrower wake. The optimal plastron thickness remains approximately constant throughout the Reynolds number range explored, with the estimated error in the results being close to the size of the symbols in Figure 2.11. It is important to note that a drag reduction of around 10% is achieved for the thinnest plastron tested ($0.01b$), and that the vortex is still suppressed in this case. This suggests that a large drag reduction can be achieved with a small modification to a surface coating.

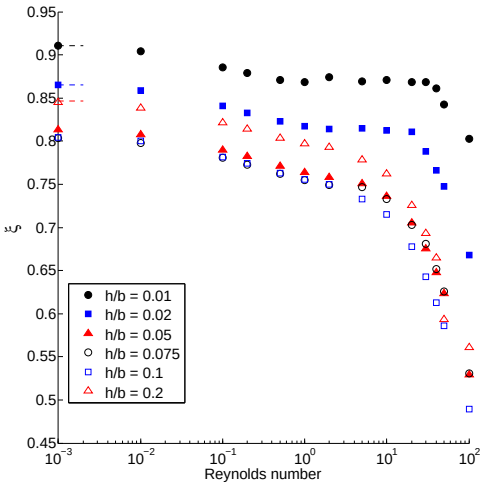

Figure 2.11: Effect of the plastron on drag reduction factor (ξ) for a range of plastron thicknesses

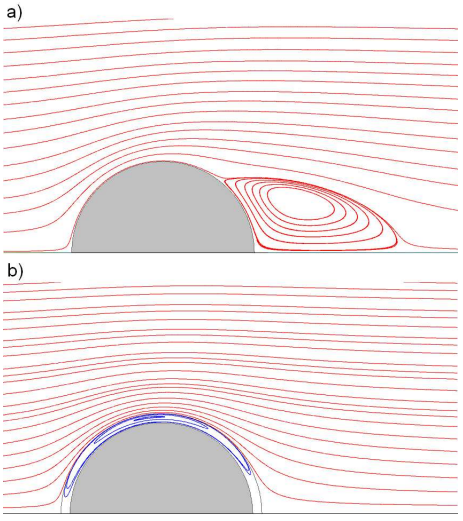

Figure 2.12: Streamlines past a) a solid sphere and b) plastron-encapsulated sphere ($h/b = 0.1$) at Re=100 showing separation suppression

The results described in this section are for a solid sphere which is encapsulated in a sphere of air. This is an idealised (perfectly hydrophobic) case where the water does not touch the solid surface. For a superhydrophobic surface, the fraction of

the surface covered in solid, could not be exactly 0%, as the plastron needs to be supported by roughness elements. Furthermore, it has been assumed that the air-water interface is fixed in position, which is unlikely unless there is some structure beneath the plastron, to which the contact line could be pinned. This structure within the plastron would act to split the single circulation cell that is evident in Figure 2.12b). To explore these issues and the effect of solid fraction on the drag reduction a series of baffles are introduced.

2.2.6 Effect of baffles

In most previous studies, the Navier-slip condition (Min and Kim, 2004; Niavarani and Priezjev, 2009) or alternating regions of no-slip and full-slip (Phillip, 1972a; Cheng et al., 2009) have been used to model the effect of the hydrophobic surface. The first approach provides an averaged effect of the hydrophobicity, assuming a homogeneous surface. In the second approach, the effect of solid fraction is explored by making the solid area smaller until the solid fraction approaches zero. In the previous section an idealised hydrophobic sphere provided a theoretical maximum drag reduction. With the introduction of baffles we now aim to explore the departure away from this idealised case, whilst maintaining a more realistic model of an inhomogeneous hydrophobic surface. The baffles introduced in this

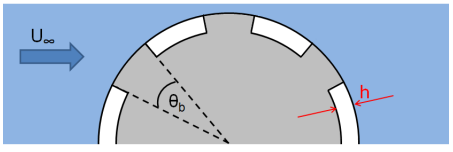

Figure 2.13: Schematic of baffle configuration

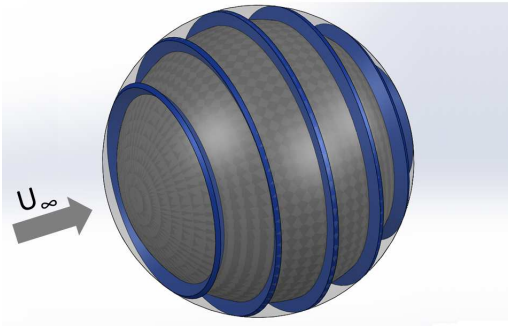

Figure 2.14: Model of solid sphere with axisymmetric baffles and plastron

study are ribs that extend from the solid sphere to the air-water interface. They are aligned perpendicular to the surface and are axisymmetric about an axis parallel to the freestream as shown in Figure 2.14. The baffles can be characterised by two parameters: the number of baffles (n_b) and the area solid fraction of the total sphere surface ($F_S = A_{\text{interface}}/A_{\text{total}}$). The baffles are placed such that they are equally spaced and the angle subtended by each baffle is constant. In the special

case of $F_S = 0$ and $n_b \neq 0$ the baffles are present but have zero thickness; these baffles are treated as double-sided walls with the no-slip condition applied on either side and zero mass or momentum transfer across the wall.

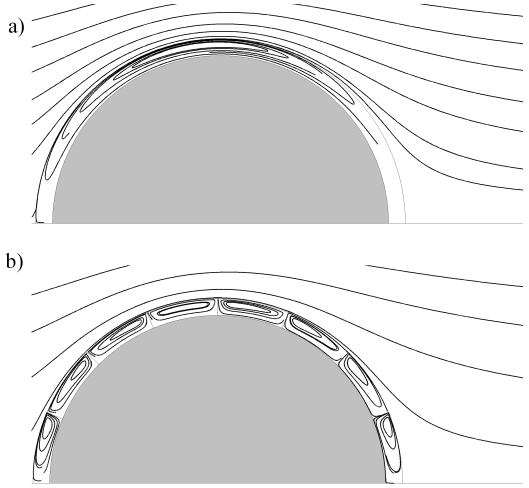

Figure 2.15: Pathlines past an encapsulated sphere a) without baffles and b) with baffles (Re = 100)

The effect of infinitely thin baffles on the circulation within the plastron is demonstrated in Figure 2.15. The presence of 7 baffles breaks the original single circulation cell into 8 smaller circulation cells. The zero thickness of the baffles means that the external fluid flows over only the air-water interface; there is still no contact between the external fluid and the sphere. However, the drag reduction effect is abated due to reduced interfacial velocity around the edges of the baffles as shown in Figure 2.16.

The deficit in interfacial velocity at the edges of the baffles results in a reduction in the local slip and hence an increase in the local shear stress. Clearly, increasing the number of baffles increases the percentage of the surface area where the interfacial velocity is lower than the idealised case and therefore decreases the effect of the plastron. The overall impact of increasing the number of baffles is to decrease slightly the drag reduction as shown in Figure 2.18. However, the attached vortex regime remains suppressed with the presence of zero thickness baffles.

The error bars shown in Figure 2.18 demonstrate that it is difficult to achieve grid independence with zero thickness baffles for a large number of baffles, especially at high Reynolds numbers. This is because of the singular point at the tip of each baffle. To overcome this issue and explore a more realistic situation, the effect of finite baffle thickness has been explored. The baffles are each assumed to subtend the same angle (θ_b), which is calculated for each case to achieve a certain area

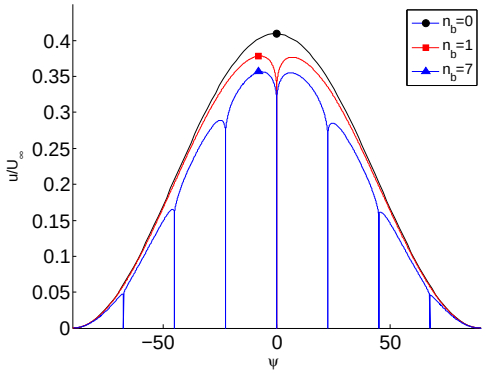

Figure 2.16: Interfacial axial velocity component with zero thickness baffles (Re $= 0.1, h/b = 0.1$)

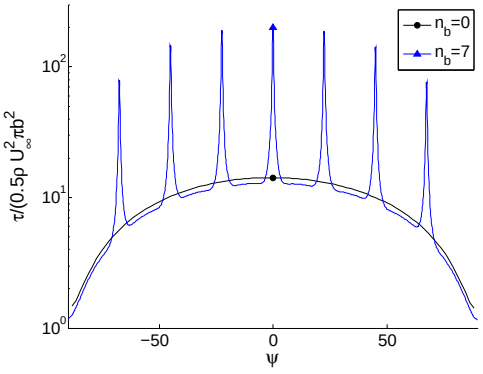

Figure 2.17: Interfacial shear stress profiles with zero thickness baffles (Re $= 0.1, h/b = 0.1$)

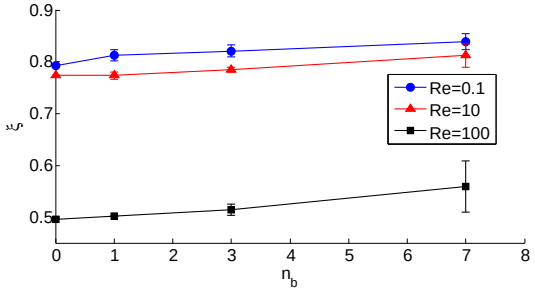

Figure 2.18: Effect of addition of zero thickness baffles on drag reduction ($h/b = 0.1$)

solid fraction (F_S) of the total surface area of the sphere. This means that the external flow will experience patches of no-slip (at the solid baffles) and partial slip (at the air-water interface).

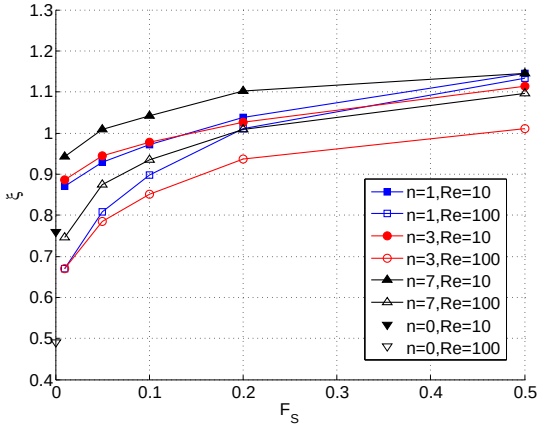

Figure 2.19: Drag reduction for different baffle configurations at Re $= 10$ and Re $= 100$ ($h/b = 0.1$)

The presence of finite-thickness baffles results in the attached vortex regime no longer being suppressed in the majority of cases, and hence the decrease in drag is lower as shown in Figure 2.19. In fact at higher Reynolds numbers and high cavity fractions the drag reduction disappears completely and the presence of the plastron, combined with the baffles, produces an overall drag increase.

There are three related effects which contribute to the overall drag. First, the slip at the air-water interface acts to reduce the shear stress and hence the viscous drag. Second, the combination of no-slip and slip patches affects the separation location, which in turn affects the pressure drag. Third, increasing F_S results in an increase in the relative blockage of the sphere. The increase in blockage becomes the dominant parameter as F_S tends to 1 where the plastron acts to produce an overall drag increase, approaching the drag of a solid sphere of radius $(b + h)$.

Figure 2.20 demonstrates that the drag reduction collapses with the separation angle, suggesting that separation is the key physical process controlling the drag. The increase in the relative blockage ratio and associated pressure drag is important because for the same separation angle as for the original solid sphere of radius b there is an increase in drag. The overall breakdown of the pressure (C_{DP}), viscous (C_{DV}) and total (C_{DT}) drag coefficients is given in Table 2.2 along with the change in drag coefficients ($\%C_{DP}$, $\%C_{DV}$ and $\%C_{DT}$ respectively, where $\%C_{DT} = 100\,(\xi - 1)$) in comparison to a solid sphere. It is clear that the overall effect of the plastron is to increase the pressure drag but decrease the viscous drag. The increase in pressure drag can be attributed to an increase in the overall frontal area, whilst the decrease in viscous drag is due to the reduced shear at the air-water interface. The viscous drag is the main contributor and results in an overall drag reduction. At higher Reynolds numbers the delay in separation results in a narrower wake and a smaller increase in pressure drag. The primary influence of the baffles, whether through increasing n_b or F_s, is a diminished viscous drag reduction. This is due to an increase in the total surface area subject to the no-slip condition and a decrease in the length of the fetch for each cavity, resulting in a lower induced velocity within the cavity. Figure 2.20 also demonstrates that although the drag is primarily affected by the separation angle the solid fraction is also important. For example, for $n_b = 1$ and $F_s = 0.05/0.1$ the same separation angle produces a different drag value.

In the case with finite thickness baffles, the magnitude of the recirculation velocities within each cavity and the associated interfacial velocities are significantly reduced, as shown in Figure 2.21. The velocity is forced to zero at the tops of the

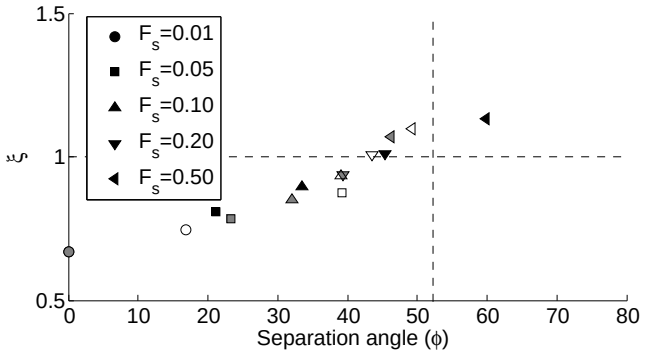

Figure 2.20: Relation between separation angle and overall drag value (Re $= 100, h/b = 0.1$). White symbols: $n_b = 1$, grey: $n_b = 3$, black: $n_b = 7$ The dashed line is for a no-slip sphere(Taneda, 1956).

Re	n_b	F_s	C_{DP}	C_{DV}	C_{DT}	$\%C_{DP}$	$\%C_{DV}$	$\%C_{DT}$
10	-	-	1.53	2.81	4.34	-	-	-
10	1	0.01	3.13	0.48	3.62	+105.1	-82.8	-16.6
10	1	0.20	2.59	1.72	4.31	+69.5	-38.9	-0.7
10	7	0.01	2.90	1.01	3.91	+90.0	-64.1	-9.9
10	7	0.20	2.22	2.28	4.51	+45.6	-18.8	+3.8
100	-	-	0.52	0.59	1.12	-	-	-
100	1	0.01	0.61	0.13	0.74	+17.4	-78.5	-33.5
100	1	0.20	0.72	0.39	1.12	+38.2	-33.6	+0.1
100	7	0.01	0.63	0.20	0.82	+19.5	-66.6	-26.2
100	7	0.20	0.64	0.47	1.11	+22.7	-20.1	-0.1

Table 2.2: Comparison between the pressure and viscous drag contributions for a solid sphere and a plastron-encapsulated sphere with baffles (C_{DP}=pressure drag coefficient, C_{DV}=viscous drag coefficient, C_{DT}=total drag coefficient)

baffles due to the no-slip condition, resulting in a new boundary layer forming and hence a lower interfacial velocity. The shear stress on the baffles is approximately two orders of magnitude higher than at the air-water interface, resulting in a reduced effect. This lower interfacial velocity and increased shear stress will clearly influence the location of the separation point.

Finally, it is interesting to note that the separation point does not move in discrete steps from the edge of each of the baffles. Instead, the separation location moves continuously along the rear of the sphere. In some cases the separation location is mid-way along a section of air-water interface, creating two separate and opposite recirculation cells within a cavity. In this case, the air-water interface is actually acting to promote separation slightly, due to the upstream component of velocity

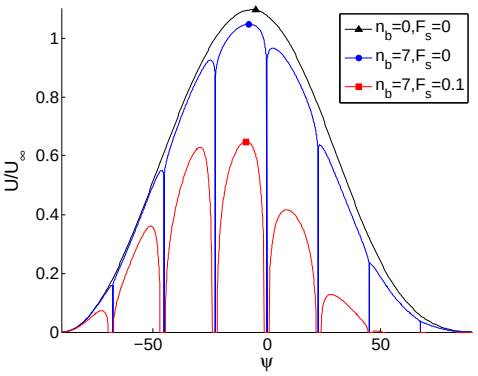

Figure 2.21: Interfacial velocity profiles for a range of baffle configurations ($\mathrm{Re} = 100, h/b = 0.1$)

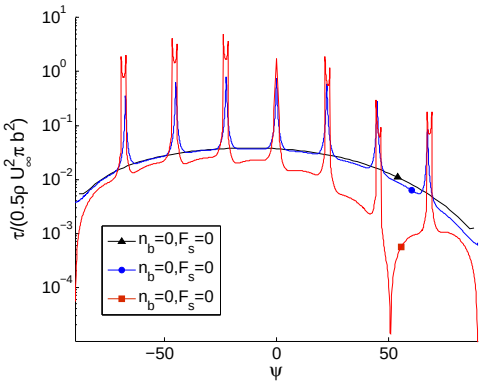

Figure 2.22: Interfacial shear profiles for a range of baffle configurations ($\mathrm{Re} = 100, h/b = 0.1$)

at the air-water interface as a result of slip within the recirculation region as shown in Figure 2.23.

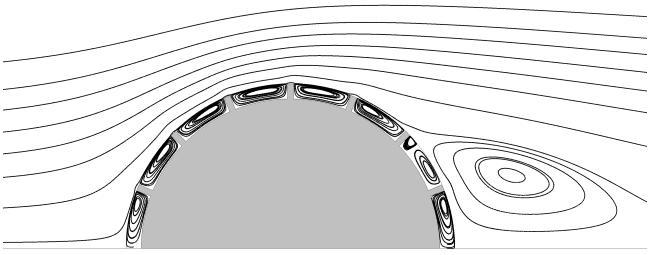

Figure 2.23: Pathlines showing separation from the middle of a cavity section ($F_S = 0.1, \mathrm{Re} = 100, h/b = 0.1$)

2.2.7 Conclusions from sphere calculations

Numerical simulations of a sphere encapsulated in a plastron, or layer of air, from Stokes flow up to a laminar Reynolds number of 100 have been reported. The presence of the plastron produces a drag reduction that matches the analytic solution in Stokes flow and increases to a maximum of 50% at the higher Reynolds numbers. A finite slip velocity and reduced shear stress at the air-water interface result in the complete suppression of the usual attached vortex regime, where the flow is separated but still steady, typically for spheres seen in the range $24 < \mathrm{Re} < 130$.

Baffles are included in the simulations to match a realistic situation where the plastron is supported by roughness elements, producing a composite interface. The

baffles produce a degradation of the drag reduction as they reduce the circulation within each section of the plastron. As the solid fraction increases, separation is no longer completely suppressed, although it is delayed and a drag reduction is still possible. However, if the solid fraction is increased above approximately 10% then the presence of a plastron produces an overall drag increase even though separation is delayed.

Overall it is clear that a surface retaining a plastron composed of a complete air layer, or one which is a composite of several cells, can produce a reduction in the viscous drag. Furthermore, the presence of a plastron can reduce the local shear and hence completely suppress or delay separation. However, the salient part is that it is the detailed surface geometry rather than an averaged effect that is important in determining the overall potential for drag reduction.

Chapter 3

Simulation of flow past flat hydrophobic surfaces

This Chapter explores the effect of the superhydrophobic surfaces on the viscous drag of flat surfaces. The first section is focused on the modification of the effective boundary condition at a hydrophobic surface and whether a significant viscous drag reduction is plausible if a realistic amount of slip is generated on a flat surface. The second section explores the interaction between the air, water and surface at the complex composite interface. The design of the supporting roughness elements is varied to determine how to improve the drag reduction produced by a superhydrophobic surface.

3.1 Application of the Navier-slip condition

3.1.1 Introduction

The expected effect of a superhydrophobic surface is to reduce the wall-normal velocity gradient at the fluid-solid boundary and hence reduce the shear stress or viscous drag. This section explores the possibility of simulating the effect of superhydrophobic surfaces using the Navier-slip condition. The Navier-slip condition models the surface-averaged effect of a modified surface coating and allows analysis of a flow problem without the computational expense of simulating the detailed features of the surface. The Navier-slip condition is shown to produce a drag reduction in both laminar and turbulent channel flows, with the laminar

results agreeing with analytic theory and the turbulent results producing a good correlation with the results from Direct Numerical Simulations.

3.1.2 Poiseuille flow

To determine whether a viscous drag reduction is possible due to the application of the Navier-slip condition the canonical case of 2D Poiseuille flow between two infinite plates is considered (Figure 3.1).

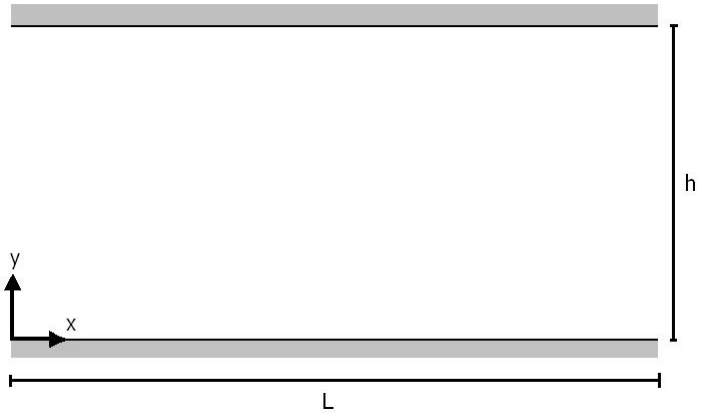

Figure 3.1: Domain for channel flow simulations in FLUENT

In 2D laminar Poiseuille flow the Navier-Stokes equations can be simplified to

$$\frac{\partial P}{\partial x} = \mu \frac{\partial^2 u}{\partial y^2}. \tag{3.1}$$

With the application of no-slip boundary conditions to the two walls the equation can be solved directly to give the developed velocity profile across the channel.

$$u\left(y\right) = \frac{\Delta P}{2\mu L}\left(hy - y^2\right) \tag{3.2}$$

However, if the Navier-slip condition is applied at both the walls, the velocity profile is augmented by a bulk velocity (as shown in Figure 3.2) to give

$$u\left(y\right) = \frac{\Delta P}{2\mu L}\left(hy - y^2 + hb\right). \tag{3.3}$$

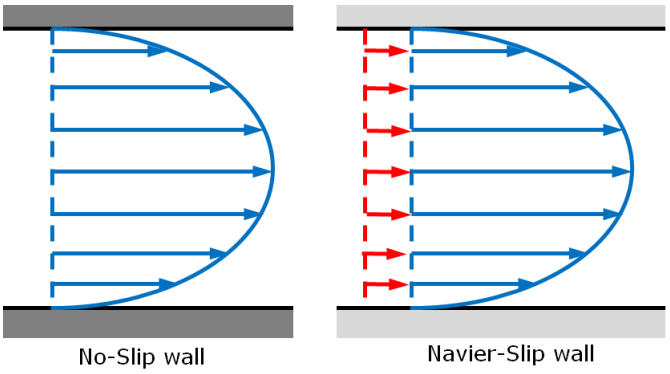

Figure 3.2: Schematic demonstrating augmented velocity profile due to Navier-slip condition

This additional bulk velocity modifies the volume flow rate through a 2D channel by a factor of $(1 + 6\lambda)$, where $\lambda = b/h$ as discussed in Section 1.1.4. This demonstrates that for a given mass flow rate through the channel, a lower pressure gradient or pumping power is required if slip is achieved at the surface.

3.1.3 Numerical model

To verify this analytic result and extend the analysis to turbulent flows a range of simulations have been conducted with the Navier-slip boundary condition. The computational domain used is shown in Figure 3.1. with flow from left to right. It is assumed that the flow is fully developed and thus the inlet and outlet are coupled to create a periodic domain[1]. The mesh at the inlet and outlet are conformal, so no interpolation is required. The domain size is kept constant with $h = 2$m and $L = 4$m for both the laminar and turbulent simulations. The channel Reynolds number is defined based on the mean velocity and channel half height and is set to an arbitrarily low value to ensure laminar flow as given by

$$\mathrm{Re} = \frac{\rho \bar{u} h}{2\mu} = 0.6125. \tag{3.4}$$

Assuming that the fluid has the following properties the Reynolds number definition can be inverted to determine the maximum centreline velocity of $\bar{u} = 5 \times 10^{-4}\mathrm{ms}^{-1}$.

[1]Although a streamwise extent is not typically required as the flow is 1D, FLUENT requires a minimum of two dimensions

$$\rho = 1.225\text{kgm}^{-3} \quad \mu = 10^{-3}\text{Pa.s} \tag{3.5}$$

Within FLUENT, periodic flow can be driven by either the pressure gradient or setting a constant mass flow rate. To ensure similarity between these simulations and the reference DNS results of Min and Kim (2004) & Busse and Sandham (2012a) the pressure gradient is specified. A relationship between the pressure gradient and the maximum velocity is easily derived from Equation (3.1) and this calculated value is used for all simulations at this Reynolds number.

$$\frac{\Delta P}{m} = -10^{-6}\text{Pa.m}^{-1} \tag{3.6}$$

The negative sign is required to ensure that there is a pressure drop in the x-direction and therefore flow in the positive x-direction. Fixing the pressure gradient (regardless of boundary conditions) allows the effect of the slip length on the volume flow rate to be quantified.

The Navier-slip boundary condition is added to FLUENT through a User-Defined Function (UDF). The UDF is written in C as a text file and then interpreted by FLUENT. The UDF defines a profile for the wall velocity based on the wall-normal velocity gradient at the adjacent cell. The wall normal velocity is zero. The UDF is given in pseudo code below and in full in Appendix A.

```
extract face \& thread of boundary
  loop over all faces on boundary
  extract details of cell adjacent to face
  extract velocity gradient at centre of adjacent cell
  calculate velocity based on Navier-Slip length
  smooth velocity
  apply boundary condition
end loop
```

It was found that the boundary condition was unstable unless some smoothing via a relaxation factor (R) is introduced. This is achieved by applying a slip velocity based on the following equation, where a subscript F refers to a face value, C refers to a cell centre value, and n represents the iteration number.

$$u_F^{n+1} = \frac{Ru_F^n + b\,(\partial u/\partial n)_C^n}{1+R} \tag{3.7}$$

The value of R was initially set equal to one, but the solution diverged. Increasing the value of R makes the solution stable and convergence is possible. However, as the slip length is increased the value of R is also required to increase otherwise the boundary condition becomes divergent. A value of $R \sim 50$ is needed for the solution to converge when the $b = 0.02$ (the largest slip length used in this study). The solution was found to be independent of the value of R (once stability has been achieved) and had little effect on the convergence rate, so $R = 50$ was used for all simulations.

The Reynolds-averaged Navier-Stokes equation are iterated to a steady state, in each computational cell using the SIMPLE algorithm for the pressure-velocity coupling and 2^{nd} order spatial discretisation for the pressure and momentum terms. Convergence is assessed using the built-in residual feature of FLUENT. For each case the simulations are run until the average residual in continuity, x-velocity and y-velocity has reduced to below 10^{-8}.

The computational domain is discretised using a structured mesh and a variety of meshes were created to conduct a grid refinement study. All meshes for the laminar cases were conducted with homogeneous meshes in both directions and physically square cells, and thus can be characterised with one length scale. The length scale that is used is the size of one cell normalised by the channel height.

$$\eta = \frac{\Delta x}{h} \tag{3.8}$$

An initial mesh was used to study the effect of the residual on the solution. Within FLUENT, the solution will continue iterating until the residuals of continuity, x-velocity and y-velocity are below a specified value known as the residual (ε). The residual is the sum of the difference between the solution in each cell in comparison to the previous iteration. The effect of the residual is studied over four orders of magnitude. Accuracy of the result is assessed against the percentage difference to the analytic solution of maximum velocity, wall shear rate and volume flow rate, for example for the volume flow rate:

$$Q_{\%} = \frac{Q - Q_0}{Q_0} \times 100\% \tag{3.9}$$

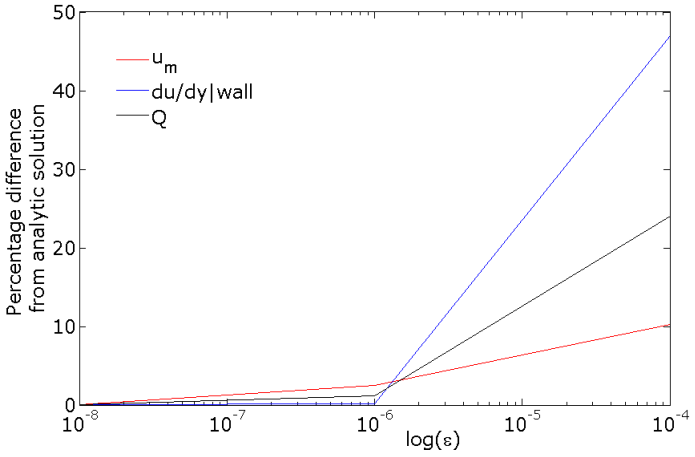

Figure 3.3: Dependence of solution on residual

Figure 3.3. clearly shows that if the default residual (10^{-3}) were to be used, the solution would be entirely unsatisfactory. Indeed, even a value three orders of magnitude lower still results in an error of 2.5% in the maximum velocity, which is the slowest to converge. A value of 10^{-8} gives a satisfactory result (less than 0.5% difference) and was selected for further simulations. A further check was also conducted on an optimised grid, and the same limit was found.

As well as a dependence on residual, the solution will also show a dependence on the mesh size. Four different meshes were generated and then solved with a residual of 10^{-8}. The effect on the same parameters as above is given in Table 3.1. with the total number of cells (N) given to demonstrate the computational cost.

η_x	N	$u_{m\%}$	$(\partial u/\partial n)_{\%}$	$Q_{\%}$
0.040	5,000	0.0015	0.9987	0.0814
0.020	20,000	0.0060	0.4952	0.0258
0.010	80,000	0.0240	0.0231	0.0281
0.005	320,000	0.0970	0.0487	0.0943

Table 3.1: Grid refinement study

The data in Table 3.1 highlights that the maximum velocity and volume flow rate are captured accurately, to within 0.1% of the analytic solution even at relatively low grid resolution. However, the wall normal velocity gradient is only sufficiently captured at a resolution of $\eta_x = 0.01$ and below. As this parameter features in the Navier-slip boundary condition it is deemed necessary for it to be reported

accurately if this condition is to be applied successfully. As there is little difference in the results below a value of $\eta_x = 0.01$ this mesh will be used for a study on the effect of the slip length.

To simulate the effect of the Navier-slip length on turbulent flow it is necessary to make some modifications to the setup. Firstly, the Reynolds number is increased to 5,500 by increasing the pressure gradient to -1Pa.m^{-1}, to match the $Re_\tau \approx 180$ of the DNS simulations of Min and Kim (2004) and Busse and Sandham (2012a). Secondly, a turbulence model is required to close the RANS equations for turbulent flow; the Spalart-Allmaras model is chosen because of the simple nature of the setup, with the flow remaining attached.

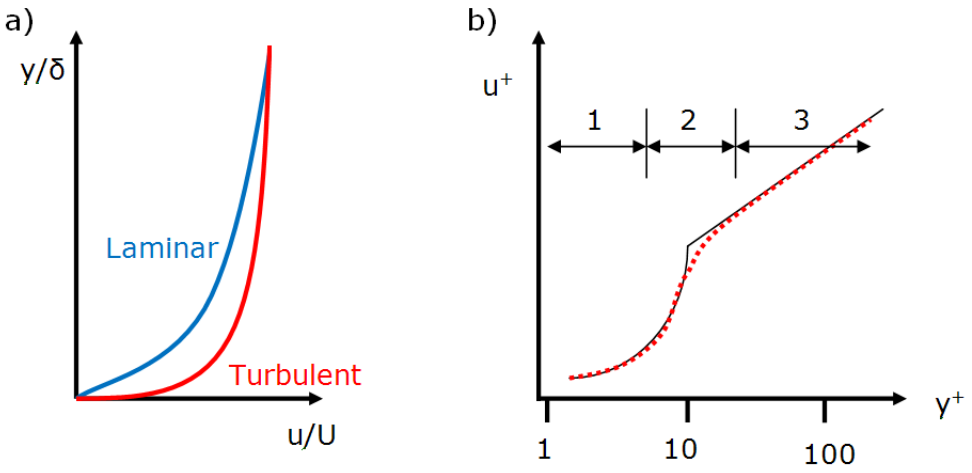

Figure 3.4: Schematic of a) laminar and turbulent boundary layer profiles and b) turbulent boundary layer profile in wall units

Thirdly, the mesh has to be changed to capture the modified boundary layer shape in a turbulent boundary layer. Due to the 'fuller' velocity profile (Figure 3.4a), with higher velocity gradients, the mesh has to be refined in a region close to the wall. The relative wall proximity varies depending on the Reynolds number of the flow past it and is typically signified with wall units, designated by a superscript plus symbol (+). This is a non-dimensional distance defined on the kinematic viscosity (ν) and friction velocity (u_τ). The non-dimensional velocity can also be defined based on the friction velocity.

$$y^+ = \frac{yu_\tau}{\nu} \qquad u^+ = \frac{u}{u_\tau} \tag{3.10}$$

where:

$$u_\tau = \sqrt{\frac{\tau_w}{\rho}} \tag{3.11}$$

The turbulent boundary layer can typically be characterised by three regions as shown in Figure 3.4b):

1. Viscous sublayer - Region close to the wall ($y^+ < 5$) where the velocity profile is linear and can be calculated using $u^+ = y^+$
2. Buffer layer - Crossover region between viscous sublayer and log law region
3. Log-law region - Outside the buffer layer ($y^+ > 30$) where the direct viscous effects are negligible and can be calculated using $u^+ = \frac{1}{\kappa} \ln y^+ + C$

To capture the turbulent boundary layer accurately with the Spalart-Allmaras turbulence model the first grid point needs to be placed within the viscous sublayer. It was initially placed at $y_1^+ = 1$ and meshes were then also produced with at $y_1^+ = 0.5$ & 2, to explore the effect of grid resolution. The coarsest mesh produced a weaker solution, whilst the finer mesh produced the same solution as the initial mesh to within 0.5%. It is therefore taken that the initial estimate of $y_1^+ = 1$ is sufficient to capture the flow accurately in the near wall region.

3.1.4 Application to channel flow

For laminar flow the results match closely to the analytic solution and are presented here to demonstrate the effect that the Navier-slip condition has on the flow. The results are presented in terms of the non-dimensional slip length $\lambda = b/h$.

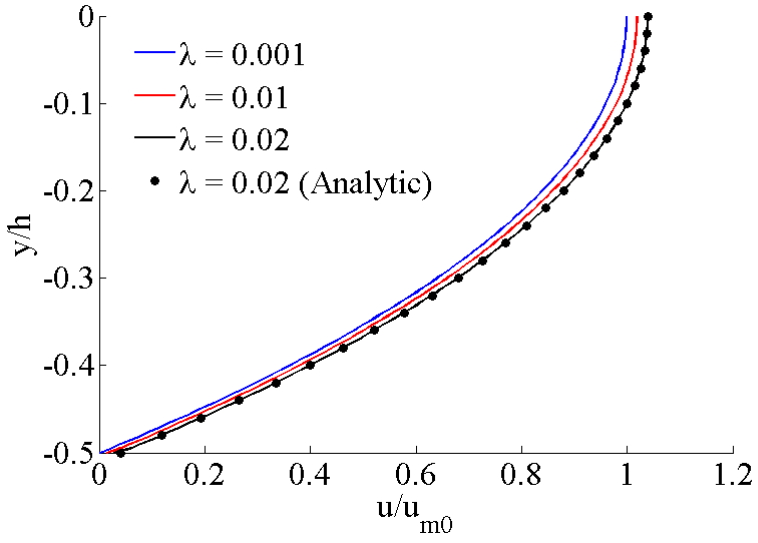

Figure 3.5: Effect of Navier-slip on laminar velocity profile

The profile for $\lambda = 0$ (no-slip) is indistinguishable from the profile for $\lambda = 0.001$. But for a larger slip length the velocity profile is augmented by a bulk flow equal to the slip velocity, which clearly results in an increase in the volume flow rate. The necessity of matching the scales of the channel and slip length is highlighted in Figure 3.5 since if $\lambda < 0.001$ then the effect on the velocity profile, volume flow rate and drag reduction is negligible.

3.1.4.1 Turbulent Results & Validation

In turbulent flow the case of $\lambda = 0.0005$ is very close to the no-slip case and can be used as a reference. Overall, the effect of a given slip length is larger in turbulent flow than in laminar flow, with an increase in the centreline velocity of about 40% for $\lambda = 0.01$. This results in an increase in the volume flow rate.

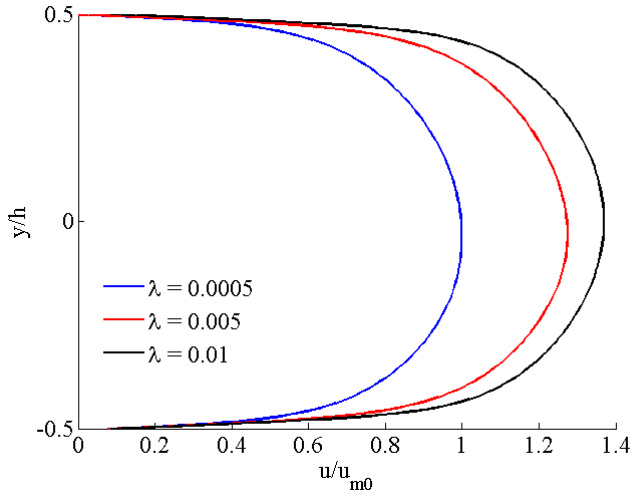

Figure 3.6: Turbulent velocity profiles with Navier-slip boundary condition on both walls

The effect of slip on channel flow can be explored by investigating the mean momentum equation. As discussed in Appendix D the pressure gradient that drives the flow is balanced by the shear stress at the wall. For a given pressure gradient the total shear stress must therefore remain constant. However, Equation D.9 demonstrates that the introduction of a slip length results in a bulk offset in the velocity profile and hence increases the mass flow through the system. Therefore, for a given pressure gradient the shear stress at the wall (or the drag) remains constant regardless of the slip length, but the mass flow increases and gives an increase in efficieny through a reduction in the skin friction coefficient (τ_w remaining constant and $\overline{u}$ increasing). It is perhaps easier to appreciate in the opposite

sense, if the mass flow remains constant then the shear stress at the wall decreases, decreasing the drag and resulting in a reduction in the pressure gradient required to drive the flow.

Plotting the results in terms of wall units allows them to be compared to the classic turbulent boundary layer profile in wall units where the profile can be split into the viscous sublayer, buffer layer and log-law region as discussed in Section 3.1.3. A comparison is also drawn to the initial results of Busse and Sandham (2012a), with Direct Numerical Simulations of channel flow at $\mathrm{Re}_\tau \approx 180$ and a streamwise slip length.

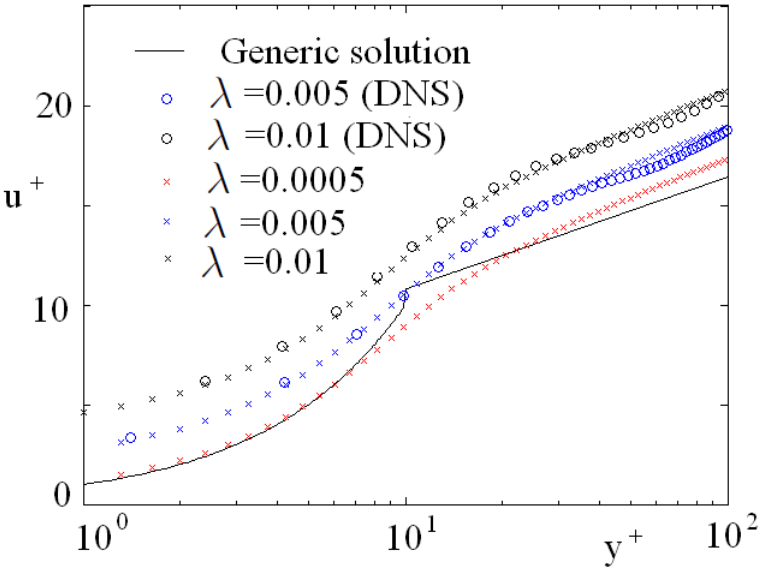

Figure 3.7: Turbulent velocity profiles & comparison with DNS results

Firstly, Figure 3.7 provides clear validation of the results with the (nearly) no-slip profile closely matching the generic solution and the other results matching up well with the Direct Numerical Simulation (DNS) results[2]. The effect of the Navier-slip boundary condition is to shift the entire profile upward in these coordinates, resulting in a shift of the boundary layer closer to the wall. This is the direct opposite of what would happen for a rough surface and agrees with the simulations in Min and Kim (2004) and Fukagata and Kasagi (2006).

The results presented in Figures 3.5 and 3.6 show that the effect is much larger in turbulent flow than in laminar flow. As a comparison the effect on the volume

[2]The DNS results presented here are for early DNS simulations which were later found to require increased resolution, however this only had a small impact on the results, with differences being largest closest to the wall

flow rate is plotted in Figure 3.8, with $Q_{\%}$ being the percentage increase in the volume flow rate compared to a no-slip case.

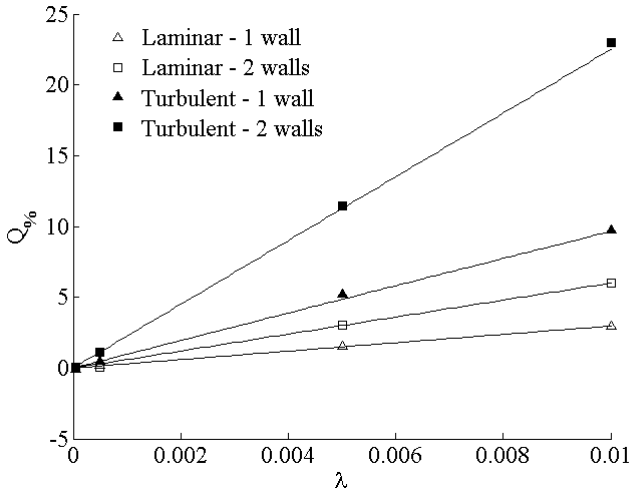

Figure 3.8: Effect on flow rate of having one or both walls with a Navier-slip condition in laminar and turbulent flows

In the case of laminar flow the two straight lines are the analytic solution, showing again that the numerical simulations (symbols) match well. For turbulent flow the straight lines are approximate fits to the data. For the case of one wall with a Navier-slip and one wall with no-slip the effect of a given λ is 3.25 times as large in turbulent flow than laminar flow, whilst if both walls of the channel have the Navier-slip condition applied then the effect is 3.75 times as large. This can then be used to create a semi-analytic solution for the effect of slip on turbulent flow. For the case of two Navier-slip walls the change in volume flow rate is simply:

$$Q_{\%} = 3.75 Q_{\%LAM} = 22.5\lambda \tag{3.12}$$

The only issue with this analysis is that only one turbulent Reynolds number has been explored. However, DNS data (Busse and Sandham, 2012a) suggests that increasing the Reynolds number results in an increased effect of the slip. It is therefore clear that a given slip length has a larger impact on the drag in turbulent flows than laminar flows. The main caveat here is that it is inherently assumed that slip can be generated at the surface. However, the simulations do provide a useful approximation tool. For example, taking the largest slip length reported in literature ($400\mu m$) and a boundary layer thickness of 1cm (similar to that expected in the experimental work reported later), gives a value of $\lambda = 0.04$ and a drag reduction of 90%.

3.1.5 Conclusions from the Navier-slip study

The previous Sections have detailed the exploration of the effect of the Navier-slip boundary condition on both laminar and turbulent channel flow. The laminar results have been validated against the analytic solution and the turbulent results validated against DNS results. The turbulent results are achieved relatively rapidly, and although they do not provide a similar level of detail as a DNS simulation they do provide scope for a quick exploration of the Navier-slip condition.

The conclusions that can be drawn from the assessment of the Navier-slip condition applied to 2D channel flow are that firstly, slip at the surface can produce a viscous drag reduction in a channel flow. Secondly, an increase in the slip length results in an approximately linear increase in the drag reduction for feasible slip lengths. Finally, it has been demonstrated that a given slip length will produce a larger drag reduction in a turbulent flow than a laminar one.

The main issue with the analytic solutions, DNS, and the current simulations is that the slip length needs to be known *a priori*. It is inherently assumed that the surface is capable of achieving such a degree of slip and so the simulations do not provide a clear insight into how a superhydrophobic surface may reduce drag. A different approach is adopted in the next Section in an attempt to better understand the effect on the flow close to the superhydrophobic surface and how slip is generated.

3.2 Superhydrophobic surface parametric study

3.2.1 Introduction

This section extends the analysis in Section 3.1 by simulating the detailed structure of the surface and the interaction between the external water flow and the air trapped inside the surface cavities. By simulating the details of an idealised superhydrophobic surface it will be possible to analyse the effectiveness of a given surface in generating slip and hence in producing a drag reduction. This will facilitate the design of optimal superhydrophobic surfaces.

3.2.2 Analytical understanding

In the Cassie-Baxter state the surface is not homogeneous, which suggests that applying a constant slip length, through the Navier-slip condition (shown in Figure 3.9a), over the entire surface may be erroneous. To model the heterogeneity of the surface two approaches may be taken as shown in Figure 3.9b) and c).

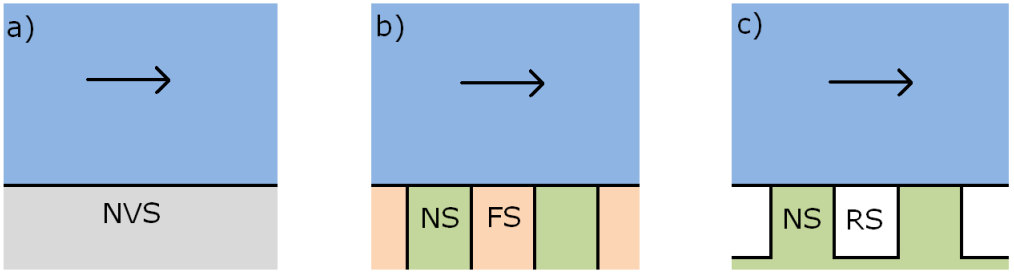

Figure 3.9: Three options for modelling a superhydrophobic surface (NVS = Navier-slip, NS = no-slip, FS = full slip and RS = reduced shear

Figure 3.9 shows the possibility of modelling a composite Cassie-Baxter state using two boundary conditions patterned across the surface. The no-slip (NS) boundary condition is applied at a solid boundary, whilst a full-slip (FS) or shear-free boundary condition is applied to simulate the air-water interface. The use of a full-slip condition is possible due to the difference in kinematic viscosity between the two fluids, resulting in the shear at an air-water interface being at least six times ($\nu_{\text{air}}/\nu_{\text{water}} > 6$) smaller than at a water-solid boundary. The reduction in shear is due to the finite velocity at the air-water interface, which reduces the local wall normal (stream) velocity gradient and the difference in kinematic viscosity, which makes it easier for the external flow to accelerate the flow within the cavity and achieve higher slip velocities. This approach is a typical approach used for superhydrophobic surfaces (for example Phillip (1972a) & Martell et al. (2010)) and is designated as a shear-free model (SFM).

The SFM has been previously used to demonstrate the dependence of the slip length on the pattern of no-slip and full-slip regions by analysing Stokes flow. Phillip (1972a,b) showed that if a pipe is patterned with stripes of no-slip and full-slip, the alignment of the stripes with respect to the flow direction is important.

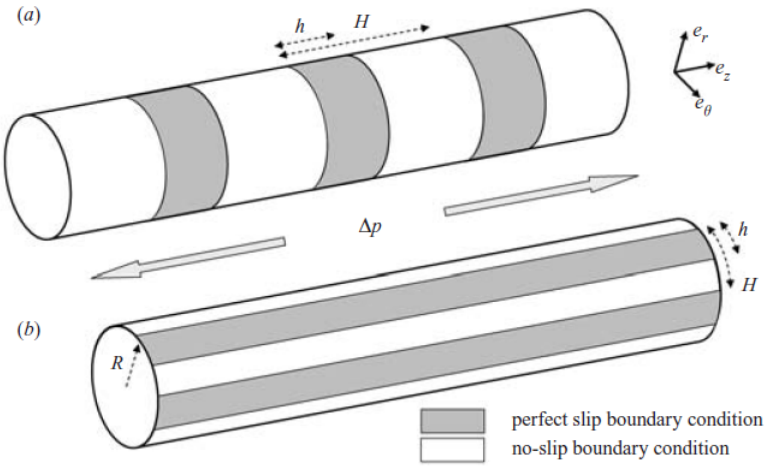

Figure 3.10: Schematic model of regions of full-slip and no-slip in a) transverse configuration and b) streamwise-aligned configuration reproduced from (Lauga et al., 2005)

The effect of the surface patterning was shown to produce the following equations for the surface-averaged slip length, where $L = H/R$ and $F_S = h/H$ as defined in Figure 3.10. In the case of parallel streamwise stripes there is an exact analytical solution (Phillip, 1972a,b)

$$\frac{b}{R} = \frac{L}{\pi} \ln\left(\sec\left(\frac{F_S \pi}{2}\right)\right), \tag{3.13}$$

whilst in the case of transverse stripes an infinite series of Fourier modes has been used to show that for small L (Lauga et al., 2005):

$$\frac{b}{R} = \frac{L}{2\pi} \ln\left(\sec\left(\frac{F_S \pi}{2}\right)\right). \tag{3.14}$$

Two main conclusions can be drawn from this analysis. First, the slip length generated depends linearly on L, such that to maximise the effect the periodicity of the changing boundary condition needs to be the same order of magnitude as the pipe radius. In other words, this means that there must be a matching of scales between the roughness elements, which form part of the Cassie-Baxter state, and the typical length scale of the flow problem being considered. Second, it is evident that the alternative way of increasing the slip on the surface is to increase the percentage of the surface area covered by the air-water interface. A variety of different surface patterns have been explored using the SFM, they are not discussed further

here, but their implications for the optimisation of superhydrophobic surfaces are discussed further in Section 4.1.1.

Returning to Figure 3.9c), an alternative for modelling the Cassie-Baxter state is to model both the air and water phases. This could be achieved with a Volume of Fluid (VOF) method, or similar however it was found that the interface diffused unphysically. Therefore in the present method the air-water interface is assumed to be fixed in space, and the air and water are treated in two separate domains which are coupled by a two-way boundary condition. This allows for the effect of the air flow in the cavities to be included in the analysis.

3.2.3 Numerical model

The channel flow model in Section 3.1 is applied to provide an idealised model of the Cassie-Baxter state. The 2D walls are patterned with ribs aligned perpendicular to the flow direction. The cavities between the ridges or ribs are taken to be filled with air and the interface between the air and water is modelled as flat, in the same plane as the top of the ribs. The air-water interface is modelled in the same way as in Section 2.2 using a coupled interface model. Assuming that the flow is fully developed the flow is then periodic in the streamwise direction and the domain can be reduced to a single rib-cavity module. Furthermore, a plane of symmetry is utilised at the channel centreline to reduce the computational cost. A single cavity-module was used for all simulations after testing demonstrated that the results were insensitive (in terms of velocity profiles and drag reduction) to the number of cavity-modules used.

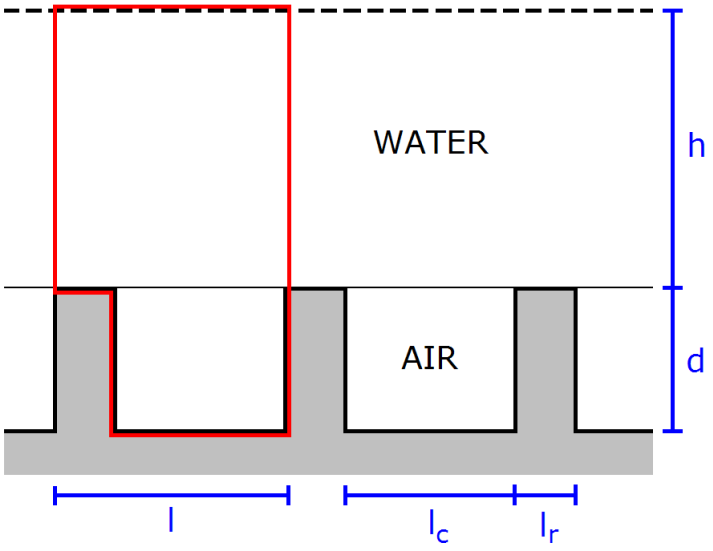

Figure 3.11: Domain for channel flow simulations with composite interface in FLUENT

The air-water interface is assumed to be flat and in line with the top of the roughness elements, producing a flat composite interface. The air-water interface splits two separate domains, one of water and one of air as shown in Figure 3.11. A User-Defined Function is used to match the tangential velocity and tangential shear stress at the interface (full details in Appendix C). This model may be seen as an idealised case, where it is assumed that the Cassie-Baxter state is maintained, and the surface tension effects are sufficiently strong to maintain a flat interface. It is understood that the interface has the potential to deform at higher Reynolds numbers and large spacing between roughness elements, and that this would detract from the performance of the surface in terms of producing a drag reduction. This analysis can therefore only demonstrate the maximum drag reduction for each configuration. The setup is geometrically similar to that of a lid-driven cavity; however in a lid-driven cavity the velocity is constant across the lid, whilst in the current setup the velocity will vary along the interface and depend on the external flow field.

Assuming that the fluid properties remain constant there are four dimensionless parameters which will affect the solution. These are the Reynolds number,

$$\mathrm{Re} = \frac{\rho \bar{u} h}{2\mu} \tag{3.15}$$

cavity fraction

$$F_C = \frac{l_c}{l}, \tag{3.16}$$

cavity aspect ratio

$$Z_C = \frac{d}{l_c}, \tag{3.17}$$

and the channel-module ratio

$$H = \frac{l}{h}. \tag{3.18}$$

The three length ratios can clearly be combined together to create other parameters, such as the ratio of cavity depth to channel half height. However, it is felt that the parameters listed above have the most physical significance in terms of helping to design superhydrophobic surfaces; the cavity fraction represents the fraction in the Cassie-Baxter eqation, the cavity aspect ratio quantifies the effect of the depth of the surface features and the channel-module ratio will demonstrate the importance of matching scales between the roughness and boundary layer.

The Navier-Stokes equations have to be discretised to allow the use of finite volume methods. The pressure and momentum equations were discretised using second order schemes. Pressure-velocity coupling is achieved using the standard SIMPLE method and as small physical scales are used throughout these simulations double precision settings are used within the solver. Convergence was achieved in all cases with the Under-Relaxation Factors set to default values.

As in previous sections each mesh was created in Gambit using a journal file. Meshes were produced which had a certain number of cells in the x- and y-directions (N_x and N_y) each of which had growth rates away from the wall (G_x and G_y). Mesh independency was then assessed based on the maximum centreline velocity (u_C^*), maximum interface velocity u_i^*) and pressure gradient.

Label	N_x	N_y	G_x	G_y	u_C^*	u_i^*	$\Delta P/L$
K	40	160	1	1.015	0.657800	7.3964	1,427,904
L	80	160	1	1.015	0.646206	7.4002	1,430,680
M	160	160	1	1.015	0.652440	7.3932	1,431,674
N	200	160	1	1.015	0.652229	7.3904	1,432,937
O	240	160	1	1.015	0.652666	7.3837	1,435,695

Table 3.2: Grid refinement study for composite interface

As an example of the grid study, Table 3.2 shows the effect of changing one of the four mesh parameters on the final solution. Mesh M was chosen as it is the first to lie within 0.5% of the results of the finest mesh. A similar method was

also taken to optimise N_y, G_x and G_y to ensure the results were independent of the mesh. The final mesh used for each case is actually mesh M; this mesh was then adapted for each geometrical parameter. For example, if F_S is 0.5 then the number of cells in the x-direction is split evenly between the rib and the cavity, but if F_S is increased to 0.9 then 90% of the number of cells in the x-direction are on the interface.

Independency was also assured from the residuals by running the simulation to different levels of convergence. This was conducted for two Reynolds numbers which bracket the range of Reynolds numbers explored in this report.

Label	Re	Residual	Iterations	$\Delta P_{\%}$
A4	0.4	10^{-3}	470	1.477
	0.4	10^{-4}	3,290	-2.876
	0.4	10^{-5}	19,250	0.226
	0.4	10^{-6}	42,080	0.020
	0.4	10^{-7}	65,060	0.018
	0.4	10^{-8}	88,000	-
A16	1000	10^{-3}	570	117.40
	1000	10^{-4}	2,340	86.48
	1000	10^{-5}	13,810	27.44
	1000	10^{-6}	42,580	4.590
	1000	10^{-7}	78,500	0.434
	1000	10^{-8}	114,900	-

Table 3.3: Effect of residual on solution for CIM model

These results highlight that it is important to use the smallest residual tested (10^{-8}) to ensure residual independency (less than 0.5% difference). The effect of residuals is larger for a higher Reynolds number but a convergence level of 10^{-8} is used for all simulations for simplicity.

To verify that the interface boundary condition works as desired, plots of the tangential interface velocity (u_i) and shear stress (τ_x) were generated for each side of the double-sided wall. The interface velocity and shear stress are normalised by the mean channel velocity (u_m) and shear stress at the wall (τ_0) in classic Poiseuille flow respectively.

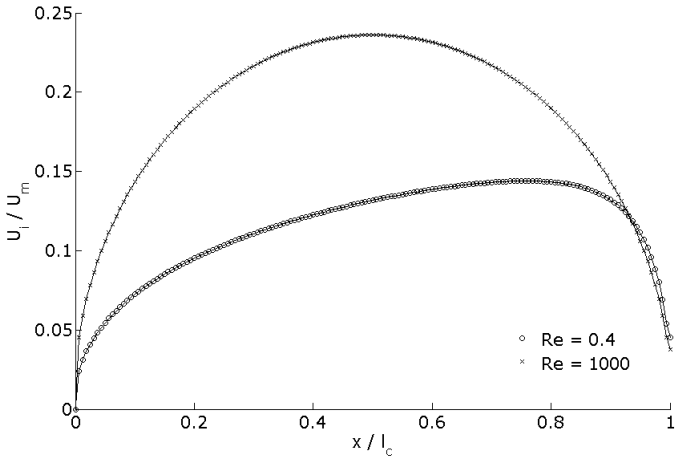

Figure 3.12: Normalised interface velocity along the length of the cavity (line = data from water domain, symbols=data from air domain)

Verification of the matching of the interface velocity across the interface is clear when it is known that Figure 3.12 actually shows four profiles. For each Reynolds number a solid line is plotted for data on one side of the interface and crosses / diamonds are plotted for the other side. The velocity profiles shown in Figure 3.12 show how the velocity increases from zero at the trailing edge of the rib to a peak near the middle of the cavity and falls back to zero at the start of the next rib. The fact that neither profile actually reaches zero at the start of the next rib is an artifact of the use of a periodic boundary condition and the definition of the line on which the data is exported. The result is that the line includes the last point of the preceding rib but not the first point of the subsequent rib. Reversing the flow direction, so that the domain includes a cavity-rib module rather than a rib-cavity module gives the same result as Figure 3.12 except that the profile does not go to zero at the start of the cavity but does go to zero at the end of the cavity. The profiles are otherwise the same and so it is understood that this is not an error in the application of the boundary condition but just an issue related to exporting the data.

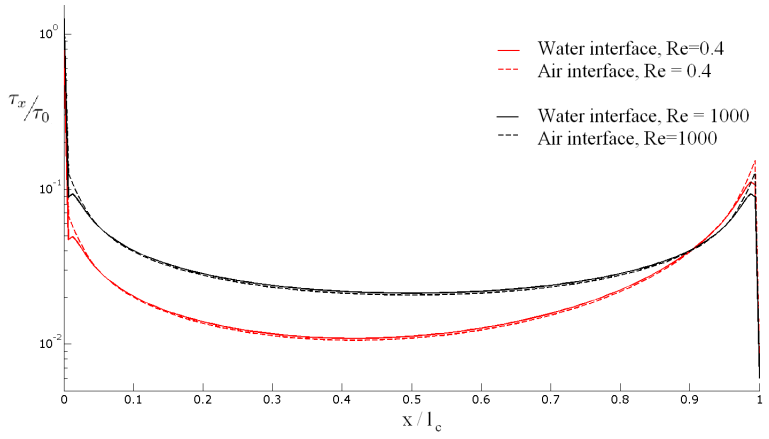

Figure 3.13: Normalised shear stress across the interface

The shear stress profiles in Figure 3.13 match up well and the same trend is achieved on either side of the interface. However, they do not match up as closely as the interface velocity profiles, especially at the edge of the cavity. To quantify the difference across the interface for each condition a percentage error is calculated as given below.

$$\varepsilon_u = \frac{u_i^A - u_i^W}{u_i^W} \times 100\% \tag{3.19}$$

$$\varepsilon_\tau = \frac{\tau_i^A - \tau_i^W}{\tau_i^W} \times 100\% \tag{3.20}$$

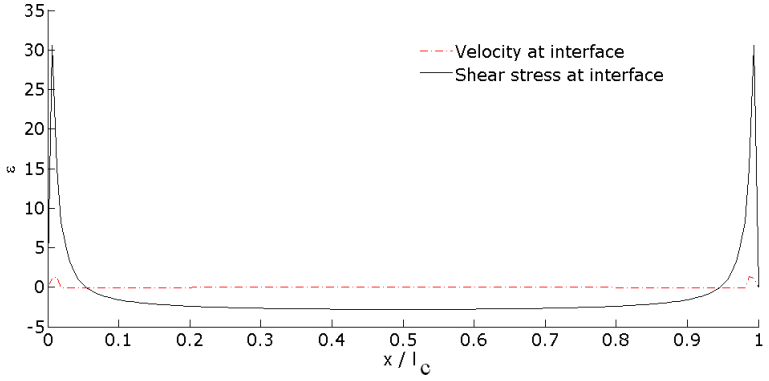

Figure 3.14: Percentage error in the interfacial velocity and shear stress

This highlights quite clearly that the largest errors are in matching the shear stress across the interface. Taking an average across the length of the interface gives an error of 0.06% for the velocity and 2.9% for the shear stress. The largest errors in the shear stress are at the edges of the profile. However, as there is jump in

the boundary condition at the rib-cavity junction it is expected that there will be issues in resolving the flow accurately in this region as was previously experienced for the sphere case with baffles (see for example Figure 2.17). A mesh refinement study was conducted to check whether this error can be reduced by increasing the number of cells along the interface or by clustering more points near the transition location. Although a finer grid resulted in a reduction in the error as defined in Equation (3.20) it had an entirely negligible effect on the extracted slip length. This suggests that the previous level of accuracy in the shear stress boundary condition is acceptable.

To validate the the results they are compared to that of Davies et al. (2006), where a similar approach was used, also within FLUENT. They used both a shear free model (SFM) and coupled interface model. Comparisons are made for the normalised interface velocity for both models and two Reynolds numbers. It was found that the data matched extremely well if the data from Davies et al. (2006) is reversed, i.e. the flow is in the opposite direction.

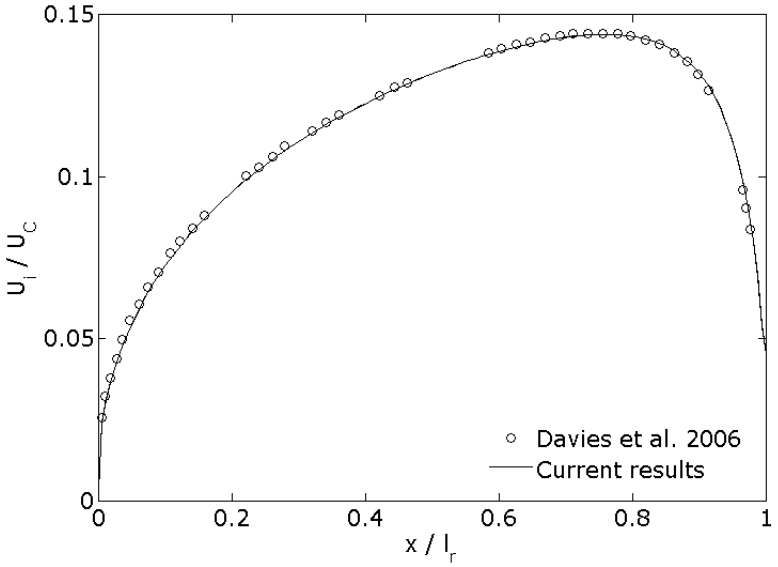

Figure 3.15: Validation of interface velocity with Davies et al. (2006) for reversed x-axis

The current data has been checked thoroughly to ensure that no minus sign has been missed. The data was extrapolated from Davies et al. (2006) by graphically digitising the figure from the article. The current data makes more physical sense, since increasing the Reynolds number results in a shift in the peak interface velocity downstream; this is consistent with the increase of inertial effects. Overall this suggests that in Davies et al. (2006) the data was plotted in the wrong direction.

Assuming that this is the case, Figure 3.15 is clear validation that the method described above can achieve accurate results.

3.2.4 Results

In general, the flow patterns closely match the classic Poiseuille profile. The streamwise velocity decreases from the peak velocity near the centreline to roughly zero at the wall with a parabolic shape. The main deviations from the Poiseuille profile are in the near wall region. At the interface there is a non-zero streamwise velocity component which decreases the friction at the walls, resulting in a decrease in the pressure gradient required to drive the flow (for a fixed volume flow rate). The coupled boundary at the interface results in a recirculation region inside the cavity.

The effect of the Reynolds number and three geometrical parameters (F_C, Z_c and H) are explored systematically in the following discussion to determine the important design factors for a superhydrophobic surface in terms of generating slip.

The overall effects of Reynolds number and F_C are depicted in Figure 3.16. At low Reynolds number the effect of the coupled interface extends quite far into the channel, with a wavy profile. At higher Re inertial effects begin to dominate, the streamlines become straighter and the effects of the coupled interface extend less into the channel.

Increasing the cavity fraction results in a higher interface velocity and lower channel centreline velocity. The lower velocity at the centreline appears to suggest that the flow rate is reduced, however this is an artifact of the specification of a constant volume flow rate. The coupled interface results in a higher average velocity close to the wall, thus to keep the volume flow rate constant the centreline velocity must decrease, resulting in a flatter velocity profile.

The increase in cavity fraction results in an increase in the circulation in the cavity. This results in an increase in the effective slip length and is visualised in Figure 3.17 for a range of Reynolds numbers.

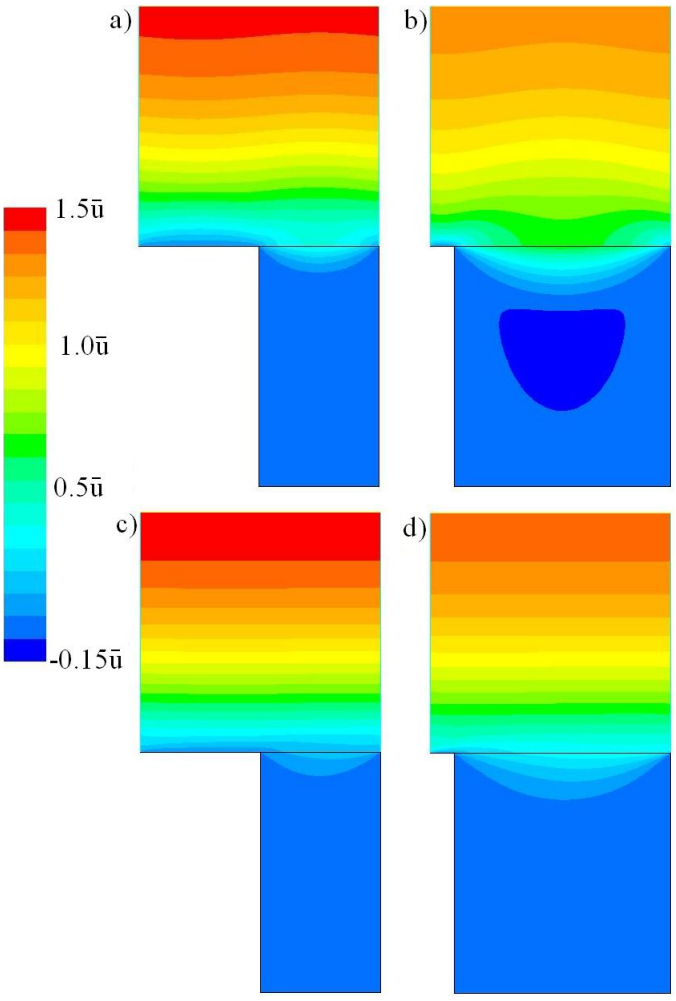

Figure 3.16: Streamwise velocity contours for a) $F_C = 0.5, \mathrm{Re} = 0.1$, b) $F_C = 0.9, \mathrm{Re} = 0.1$, c) $F_C = 0.5, \mathrm{Re} = 1000$, d) $F_C = 0.9, \mathrm{Re} = 1000$

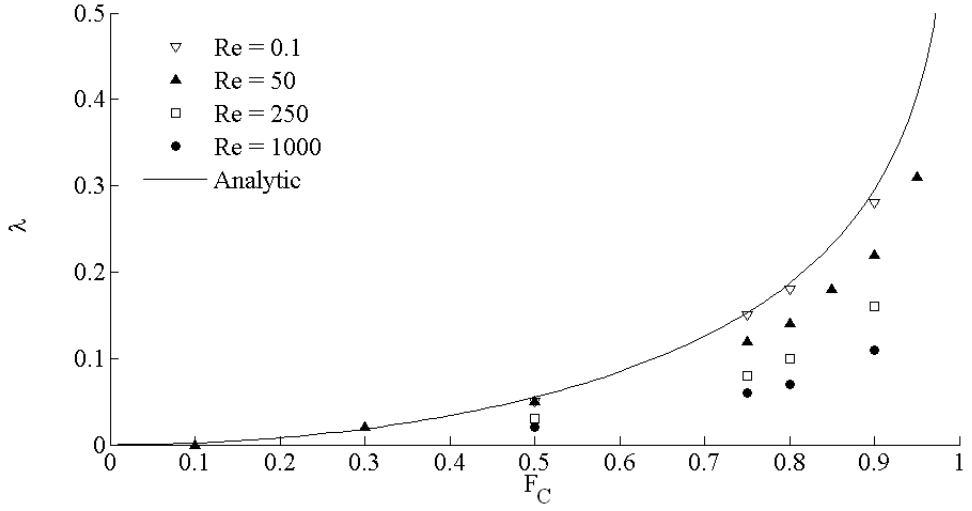

Figure 3.17: Effect of Reynolds number and Cavity Fraction on the effective slip length (λ)

The results all exhibit a similar upward trend in slip length with shear-free fraction. The trend matches the analytic expression of Equation 3.14 at the limit of small Reynolds number. As the Reynolds number is increased the effective slip length is reduced, suggesting that slip would be negated (even at high cavity fraction) at high Reynolds number. However, this analysis is for laminar flow and no conclusions can be drawn about turbulent flows.

At very low cavity fractions the effective slip reduces to zero and the no-slip condition is retained. Increasing the cavity fraction has a greater effect at higher values of F_S. However, reducing the contact area is problematic as it acts to increase the distance between the roughness elements and hence harder for an air-water interface to be supported. This highlights the balance between increasing the effective slip and preventing wetting of the surface. Furthermore, considering the similarities to shear- and lid-driven cavity flows it is clear that increasing the cavity fraction will increase the cavity-Reynolds number (with an increased cavity size and an increased peak velocity across the interface). Increasing the Reynolds number will not only make the air-water interface deform to a greater extent it has also been shown to increase the instabilities within both open (Rowley and Williams, 2006) and closed cavities (Shankar and Deshpande, 2000).

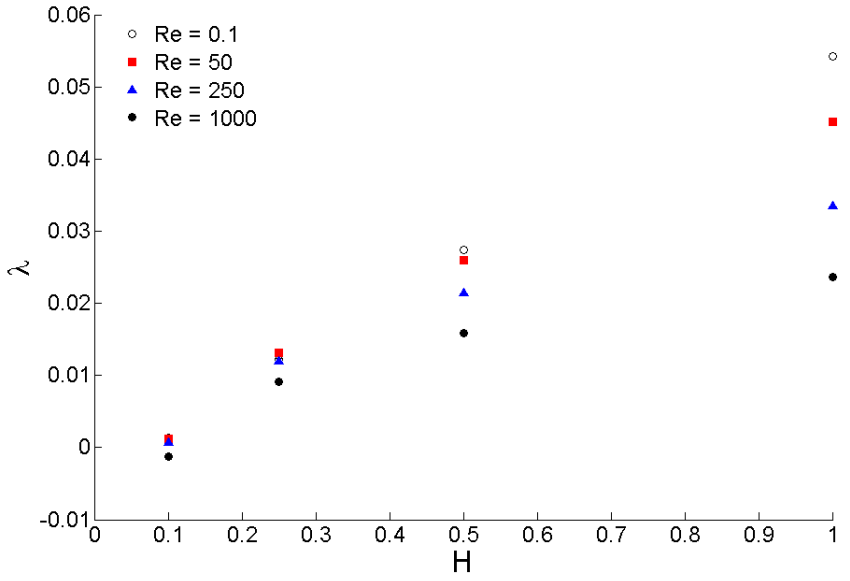

Figure 3.18: Effect of channel-to-module ratio (l/h) on effective slip length (λ)

The effect of the channel-to-module ratio or the streamwise periodicity of the surface features can be quantified through the parameter $H = l/h$. At high values

of H the surface features are a similar scale as the channel and as H reduces to zero the channel becomes much larger compared to the streamwise scale of surface features. The largest effective slip is seen at high values of H as the effect of the coupled interface penetrates further across the channel. Equation (3.14) predicts that the slip length will reduce to zero as H approaches zero. Figure 3.18 shows that the slip becomes negative at a finite value of H for high Re. This means that the coupled interface can produce a drag increase rather than a drag reduction. No separation was evident, so it appears that the drag increase is due to having to periodically accelerate and decelerate the flow.

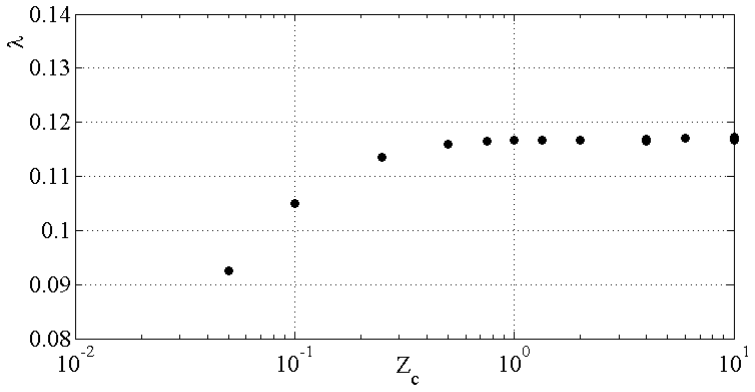

Figure 3.19: Effect of cavity aspect-ratio on the effective slip length

The shape of the cavity was also explored through the cavity aspect-ratio ($Z_C = d/l_c$). In the limit of $Z_C = 0$ circulation is reduced and the no-slip condition should be retained. As Z_C is increased the slip length, approaches a limiting value of about $\lambda = 0.117$ at $Z_C \approx 1$. This corresponds to the maximum circulation within the cavity. At higher values of Z_C multiple recirculation regions appear, but there is no change in the magnitude of the circulation of the first recirculation cell or the interface velocity. For all other simulations (including the previous analysis of F_C and Re) a value of $Z_C \geq 1$ is used to ensure that the results are independent of the cavity shape.

Overall an increase in slip was found to correlate directly with the maximum interface velocity, while the reduction in drag is a direct result of the slip velocity at the interface. Figure 3.20 shows that the reduction in drag is due to a reduction in the contribution from the viscous drag. For a flat, no-slip surface the viscous drag contribution is 100%, and this reduces to less than 50% at $F_C = 0.9$ due to the reduction in shear at the air-water interface. The pressure drag is found to increase due to the pressure difference in the streamwise direction across the

rib within the cavity, but this is outweighed by the reduction in the viscous drag component.

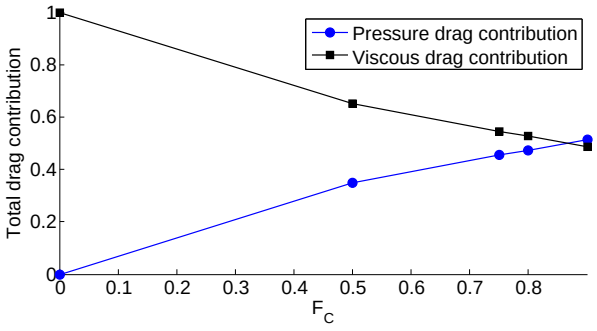

Figure 3.20: Effect of cavity fraction on the drag breakdown between viscous and pressure drag

It is possible to create a semi-empirical relationship for the effective slip length based on the cavity fraction and Reynolds number. The effect of F_C is already included in Equation (3.14) which can be pre-multiplied by a factor based on the Reynolds number

$$\lambda = F(\mathrm{Re}) \log\left(\sec\left(F_S \pi/2\right)\right)/2\pi. \tag{3.21}$$

The function of Reynolds number was calculated using a least squares fit to the data

$$F(Re) = \frac{-0.00016\mathrm{Re}^2 + 0.4108\mathrm{Re} + 85.79}{\mathrm{Re} + 87.51}. \tag{3.22}$$

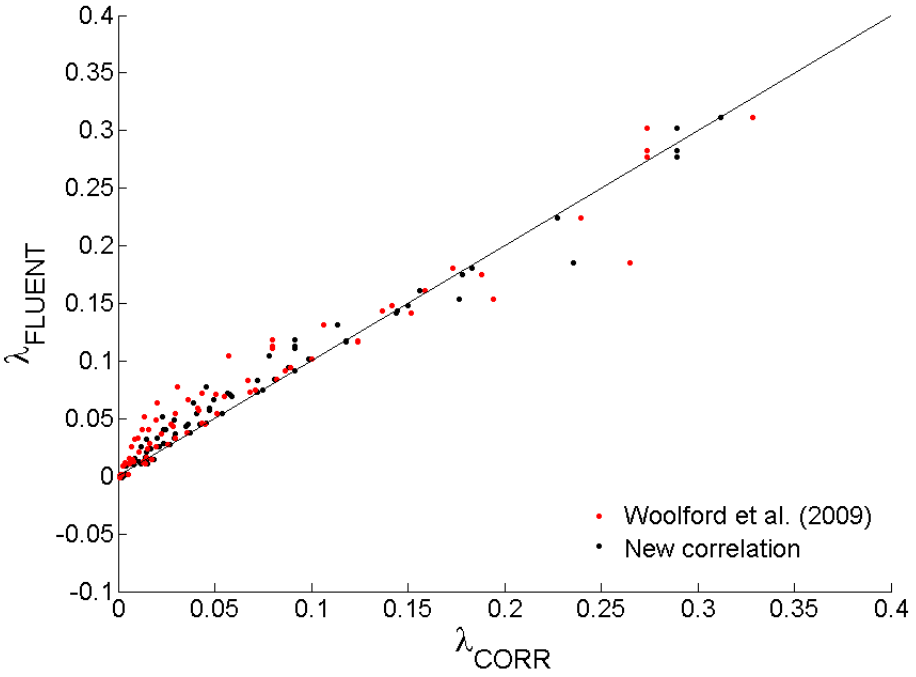

Figure 3.21: Plots of predictions of effective slip length

Equations (3.21) & (3.22) thus allow the prediction of slip length based on a the shear free fraction and Reynolds number, assuming that the cavity is sufficiently deep. At a similar time a similar study was published which produced a similar relationship (Woolford et al., 2009).

$$F(Re) = 0.172 + \frac{2.36 \times 10^5}{(\mathrm{Re} + 540)^2 + 2.14 \times 10^4} \tag{3.23}$$

As shown in Figure 3.21 the two correlations produce similar results, although the new correlation results in a slightly higher R^2 value (0.97 compared to 0.94).

The main limitation of the method resulting in Equations 3.22 or 3.23 is that the interface is fixed. The effect of interface curvature or movement up or down the cavity is not simulated. However, the simulations can be used to gain a qualitative insight into the movement of the interface. By extracting the pressure difference across the interface (zero thickness) it is possible to explore the effect that geometrical parameters and Reynolds number have on the pressure difference as shown in Figure 3.22.

In the majority of cases the pressure of the water is higher than the pressure of the air. This suggests that if the interface were free to move it would likely deflect

inward and result in a decrease in effective slip as suggested by Teo and Khoo (2010) and Salamon et al. (2005). Furthermore, increasing the Reynolds number results in an increase in the pressure difference across the interface, suggesting that the cavities are more likely to become wetted.

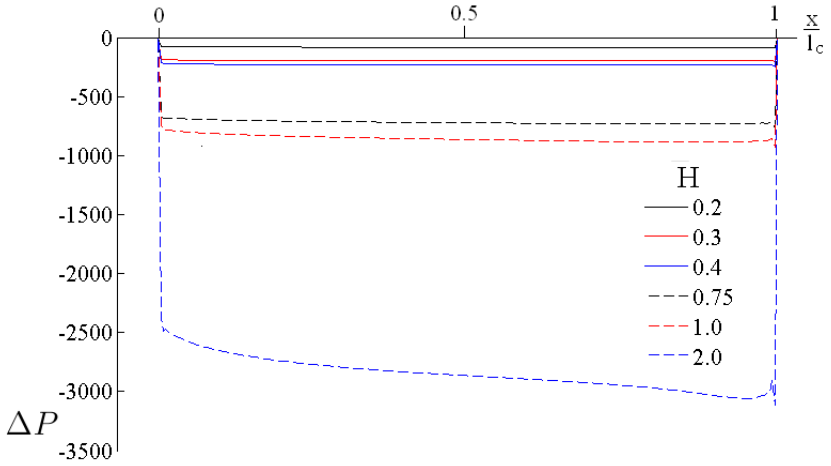

Figure 3.22: Effect of H on the pressure difference across the interface

Increasing the height of the channel relative to the streamwise length of the surface features (decreasing H) results in an decrease in the pressure difference across the interface. This demonstrates that the cavities would be more stable and highlights a requirement for an optimal value of H, sufficiently small for small interface deflections, and sufficiently large to produce a large slip. These observations are based on an assumption that a deflection away from a flat interface would result in a stable surrounding pressure-field. For example, if the interface deflects toward the surface then it is assumed that the change in flow does not reinforce the pressure field leading to an instability. Finally, the pressure jump across the interface reiterates the idealised nature of the model, in that it is assumed that the surface remains in a Cassie-Baxter state throughout and hence the results presented are for the maximum slip length for a given geometry and Reynolds number.

3.2.5 Conclusions from the parametric study

Numerical simulations of the Cassie-Baxter state, through modelling both the air and water phases, have been conducted. The approach has demonstrated that drag reductions in a channel flow are possible through the use of superhydrophobic surfaces. The presence of the air-water interface produces a reduction in the shear stress at the wall, which is directly dependent on the interfacial velocity that

is generated. This results in a reduction in the viscous drag component and - although a small increase in pressure drag is seen - produces a reduction in the total drag of the surface.

The simulations in this section have demonstrated that the drag reduction is highly sensitive to the exact details of the superhydrophobic surface. It is important to minimise the percentage of the surface that has a solid boundary, and ensure that the cavities are sufficiently deep to allow a circulation cell to develop. It is also important to match the scale of the roughness to the scale of the channel; if the scales are too disparate it is possible to get an increase in the drag of the surface. However, increasing the disparity between the scales of the surface roughness and the channel results in an decreased pressure difference across the air-water interface, which makes sustaining an air-water interface more likely. This suggests a trade-off between maximizing the slip generated by an idealised surface and producing a surface which is physically capable of retaining a plastron. The effect of Reynolds number has also been explored, and it has been demonstrated that increasing the Reynolds number results in a decrease in the efficiency of a given surface in producing a drag reduction.

3.3 Chapter Review

This Chapter has used CFD to demonstrate the potential for using superhydrophobic surfaces to reduce the viscous drag on a flat surface. The main conclusion that can be formed from this chapter is that the potential for drag reduction depends on the ability of the surface to generate slip at the wall and hence varies from surface to surface, depending on the exact surface geometry.

The key findings can be summarised as:

- A viscous drag reduction can be achieved in a channel flow by patterning a surface with regions of no-slip and air-water interface / free-shear.
- Increasing the slip length results in an approximately linear increase in the viscous drag reduction.
- A given slip length will have a greater effect and produce a larger drag reduction in turbulent than laminar flow.

- At higher Reynolds numbers, although a slip length will have a greater effect it is harder to achieve such a slip length.
- The same surface will therefore not produce the same drag reduction in a different flow field.
- Modelling the flow using the coupled interface model demonstrated that it is possible to reduce the drag of a smooth surface by adding roughness (which would typically increase the drag), but retaining an air layer or plastron within the roughness cavities.
- The drag reduction can be increased by increasing the cavity fraction of the surface.
- The scale of the roughness elements supporting the plastron needs to be matched to the scale of the flow problem considered for an optimal drag reduction.
- Circulation cells within air layer help to generate interfacial velocity and hence reduce the shear stress.
- The roughness elements need to be sufficiently deep to ensure a circulation cell can develop to allow a significant slip velocity at the air-water interface.

The simulations conducted in this Chapter have proven useful in understanding the drag reduction mechanisms involved in a range of flow problems. It is important to note that the simulations have been conducted on idealised models, and as such likely represent the maximum drag reduction possible. However, the results presented above can be used to help design an optimal superhydrophobic surface in Chapter 4.

Chapter 4

Superhydrophobic surface creation and visualisation

This chapter considers the improvement of the design of superhydrophobic surfaces. A variety of design trade-offs are explored and an improved surface design for hydrodynamic drag reduction is discussed. The chapter then presents the superhydrophobic surfaces studied experimentally later in this thesis and the manufacturing process for each. The surfaces are also characterised in terms of roughness and their ability to retain a plastron.

This chapter first provides all of the information that the author has collected about the optimisation of a superhydrophic surface to produce a drag reduction and then proceeds to discuss the various hydrophobic surfaces that have been created as part of this project. The research and creation of the surfaces were carried out in parallel and hence not all of the ideas presented in Section 4.1 were fully developed during the manufacture of the surfaces. The initial surfaces were therefore created using sand to provide a relatively easy and simple method for roughening the surface, this was then developed towards the idealised roughness presented in Chapters 2 & 3 and the optimised design presented at the end of Section 4.1.

4.1 Superhydrophobic surface design & optimisation

This section explores the design optimisation of superhydrophobic surfaces. It has been alluded to in the preceding sections, that the design of superhydrophobic surfaces is not simple, as there are a range of conflicting aspects. Therefore it is important to define a clear goal for the application of such a surface. In this section, the primary goal of the use of superhydrophobic surfaces is to produce a viscous drag reduction on a flat surface.

4.1.1 Optimisation for slip

One of the main approaches that could be used to increase the slip of a surface is to increase the percentage of the surface which is covered by the air-water interface. This was clearly demonstrated in Section 3.2 and also by the majority of literature: for example analysis of Stokes flow (Phillip, 1972a), molecular dynamics simulations (Cao and Guo, 2006), laminar simulations (Maynes et al., 2007; Cheng et al., 2009) and turbulent simulations (Jeffs et al., 2009; Martell et al., 2009). By increasing the cavity fraction F_C the interfacial velocity increases and departs further from the no-slip condition, resulting in a larger effective slip length. The interfacial velocity is linked to the circulation within the cells of air in between the roughness elements, as increasing the circulation strength will result in an increase in the interfacial velocity. This suggests that the cavity can be designed to optimise the circulation. The analysis conducted in Section 3.2 and Davies et al. (2006) demonstrated that the cavity needs to be at least as deep as it is wide to maximise the slip. It may be possible to design the cavity in a circular shape or similar, but it is likely that any gains will be minimal once the cavity is sufficiently deep. Overall, this suggests that to maximise slip the structures need to have a high-aspect ratio, for example tall, thin ridges or pillars spaced far apart, as this will maximise both F_C and the aspect ratio.

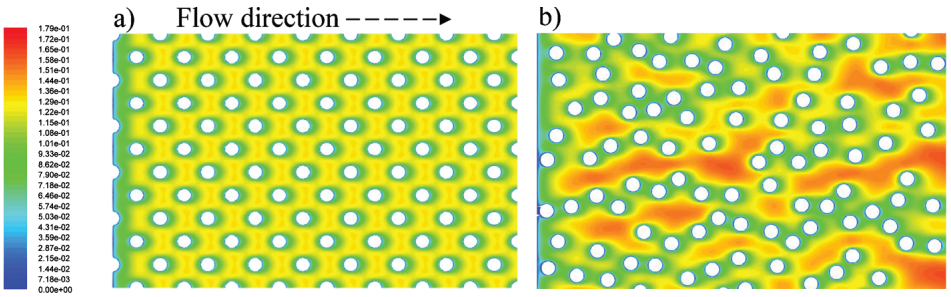

Figure 4.1: Interfacial slip velocities past circular pillars in a) structured arrangement and b) random arrangement [reproduced from (Samaha et al., 2011)]

Another important point to consider is the layout of the structures. Figure 4.1 demonstrates the difference between using a structured arrangement and a random arrangement of regular pillars. The regularly spaced pillars produce an even distribution of interfacial velocity, whilst the random structures produce a more streaky distribution. This is because with a random arrangement there is opportunity for an increased fetch (streamwise length over a solid surface), resulting in an increase in the maximum slip velocity and the average effect of the surface (Samaha et al., 2011; Benzi et al., 2006). It remains to be seen as to how a random arrangement of random surface structures would impact the slip produced.

A variety of surface structures have been suggested to improve slip, with the most studied being configurations of ridges, posts and cavities. Analytical studies of Stokes flow have demonstrated that ridges aligned with the flow direction can produce a slip length twice that of ridges aligned transverse to the flow direction (Phillip, 1972a,b; Lauga et al., 2005). This has been corroborated by experiments (Choi et al., 2006) and numerical simulations (Cheng et al., 2009) and it has been shown that the increase in efficacy of the aligned ridges in comparison to transverse ridges increases with increasing Reynolds number (Maynes et al., 2007). Configurations of posts have been found to produce a larger effect than aligned ridges in the case of high F_C in both laminar (Cheng et al., 2009) and turbulent flows (Martell et al., 2009, 2010), whilst cavities produced the smallest effect of these four configurations (Cheng et al., 2009). This effect is related to the flow being periodically accelerated over cavities and transverse ridges resulting in a reduced fetch. Figures 2.21 & 3.15 demonstrate that the interfacial velocity peaks between the two roughness elements, but returns to zero at the edge of the roughness elements. With a reduced fetch the flow encounters more roughness elements in a streamwise direction and prevents the production of high speed streak (as seen in Figure 4.1. This acts to reduce the surface-averaged interfacial velocity and hence

the average slip length of the surface. This is supported by the DNS studies of Min and Kim (2004); Busse and Sandham (2012a) which demonstrate that it is primarily important to generate slip in a streamwise direction and that if slip is generated in just the spanwise direction it can result in an increase in the drag of the surface.

One conclusion that is drawn by the majority of previous studies (e.g. Davies et al. (2006); Martell et al. (2009); Daniello et al. (2009)), including the analysis in Section 3.2 is that the hydrophobic structures need to be matched in scale to the features of the flow considered, for example the channel half height or the boundary layer thickness. Equation 1.11 and Figure 3.18 both clearly demonstrate that the larger the surface features the larger the drag reduction effect. This highlights an important issue with the use of superhydrophobic surfaces to reduce drag, namely that the ability of a surface to produce slip is intrinsicially linked to the scale of the surface roughness, whilst the surface roughness itself will act to increase the drag of the surface.

Another way of tuning the slip produced by a given surface is to change the contact angle of the surface. It is clear that increasing the contact angle will make a surface more hydrophobic (by definition), but Ybert et al. (2007) demonstrated that increasing the contact angle also results in an increased slip length

$$b \propto \frac{1}{180 - \theta}. \tag{4.1}$$

Equation 4.1 shows that as the contact angle approaches 180° the slip length will increase rapidly. This suggests that small gains in contact angle produce large gains in the surface's ability to generate slip.

For a surface to produce slip efficiently the overall composite surface should be as flat as possible. This includes the air-water interface which has the possibility to deform and this deformation can have a detrimental effect on the drag especially for transverse grooves (Enright et al., 2006; Teo and Khoo, 2010; Busse and Sandham, 2012c). If the air-water interface deflects into the cavity then the velocity close to the air-water interface will be reduced as it is effectively sheltered by the tips of the roughness elements, resulting in reduced interfacial velocity and reduced slip. This effect is powerful as Biben and Joly (2008) demonstrated that a deflection of the interface down into the cavity by just 10% of the cavity width could completely remove the drag reducing effect, leaving flow past a rough surface

and hence resulting in a drag increase. This also highlights the importance of minmising the physical obstruction to the flow by the combination of the roughness elements and air-water interface (Cao and Guo, 2006).

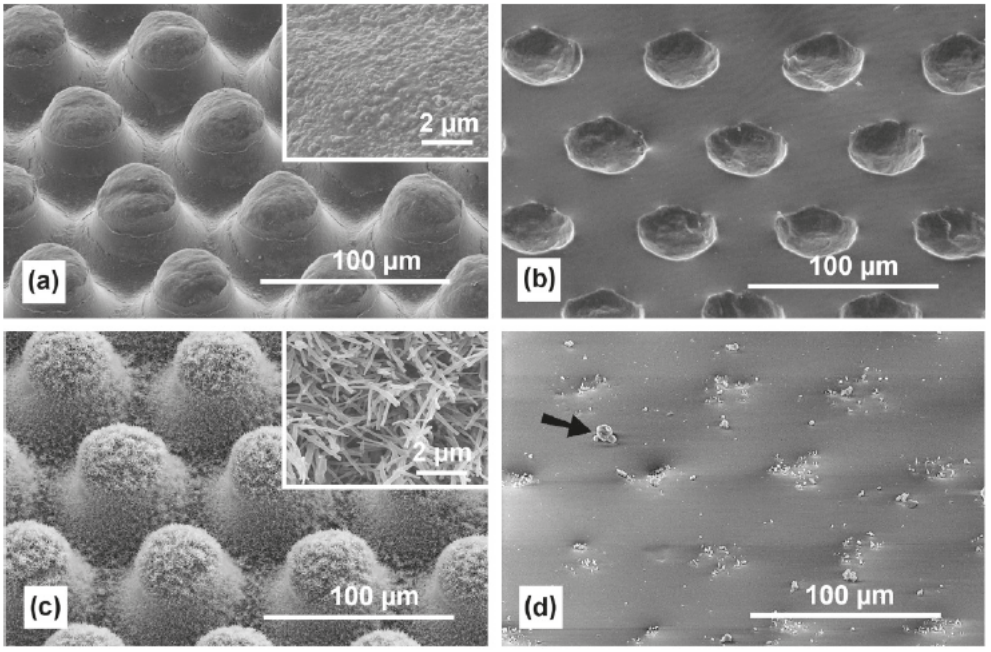

Figure 4.2: SEM images of a) surface with micro-roughness and c) heirachical roughness and b) & d) their respective contact areas visualised with a cryogenically frozen drop [reproduced from (Ensikat et al., 2009)]

One way to improve the overall slip is to use dual scale roughness as shown in Figure 4.2. The two scales of roughness each serve a purpose, the smallest scales prevent the water from wetting the tips of the roughness elements and the larger scales then provide a larger area beneath the tips within which an air layer can be retained. The combination provides a much smoother air-water interface and an increase in the F_C.

Overall, it is concluded that the ideal surface for producing slip is one with high aspect-ratio roughness which allow for the maximum F_C. These roughness elements should be arranged in a random fashion to maximise the ability for high speed, interfacial streaks and have a second scale of roughness to help support a flat interface.

4.1.2 Optimisation for plastron retention

The potential for drag reduction is related to the ability of a surface to generate slip, but this ability itself is linked to the ability of the surface to retain a plastron. If the surface cannot retain a plastron for a relatively long period of time then any drag reduction will be transient. Thus, it is important to consider the optimisation of a surface so that it is less susceptible to pressure and dissolution of the gases within the plastron over time.

As discussed in Section 1.1.3 the ability of a surface to retain a plastron, or stay in the Cassie-Baxter state, is determined by an energy balance. The Cassie-Baxter and Wenzel states are both local energy minima, but transition typically only occurs from the Cassie-Baxter state to the Wenzel state (Reyssat et al., 2008). Therefore, it is important to ensure that the surface does not become wetted out in any condition, as this is in practice an irreversible process.

It is clear at this stage that to enable a plastron to be present on a surface a combination of surface chemistry and surface roughness is required. The surface chemistry is needed to ensure a high contact angle, whilst the roughness provides a structure within which the plastron can be maintained. The importance of the scale of the roughness can be explored by returning to Equation 1.8 which shows that the critical pressure scales with A_P/Λ. The critical pressure therefore scales with $length/length^2$ and hence a reduction in the size of the surface features results in an increased ability to withstand pressure. Jung and Bhushan (2008) also demonstrated that increasing the scale of the roughness reduces the critical pressure, but the interface is more susceptible to dynamic instabilities such as surface waves, meaning that wetting could occur below the critical pressure. The presence of the parameter $F_s/(1-F_s)$ (where F_s is the solid fraction and $F_s = 1-F_C$) also demonstrates that to increase the critical pressure a higher value of solid fraction F_s is required. These two criteria - of high F_s and small scales - clearly create a conflict with the requirements for high slip presented in Section 4.1.1, and this is discussed further in Section 4.1.4. Furthermore, any trade-off will be affected by increasing Reynolds numbers, as higher scales and speeds will result in higher shear stresses at the interface and produce larger deformations. In nature it is seen that insects capable of retaining a plastron are typically found in regions of reduced flow velocity for exactly this reason (Flynn and Bush, 2008).

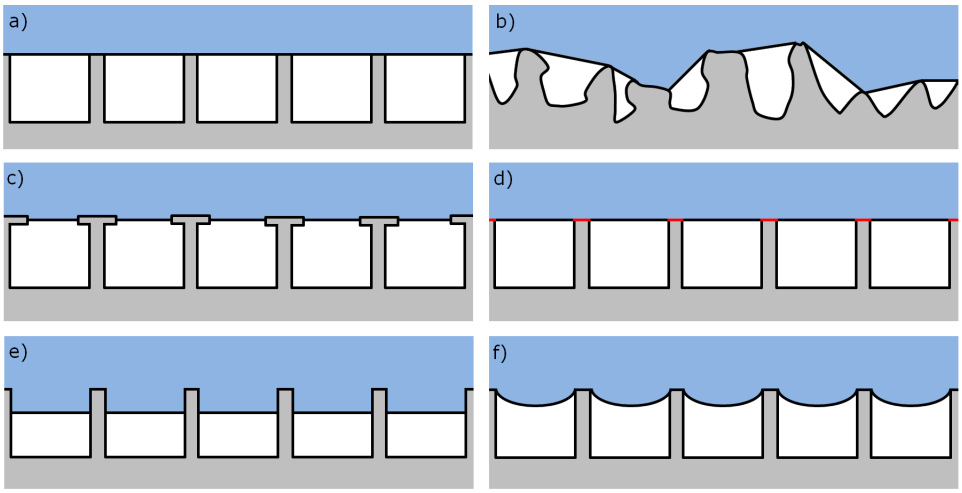

Figure 4.3: Schematic of alternative superhydrophobic surface designs a) high aspect ratio structured surface b) random rough surface c) recurved structure d) hydrophilic tips (red) e) partially wetted and f) curved interface

Figures 4.3a) & b) depict schematically the difference between a structured and a random superhydrophobic surface. The random structure will inherently result in some parts of the surface becoming wetted at a lower critical pressure than others, due to the random spacing between the roughness elements (Samaha et al., 2011). This is perhaps the optimal design in nature, as it allows for a fail safe mechanism where the surface has a gradual response to pressure. However, in this case the randomness of the spacing will act to reduce the operating range of the surface, which may already by highly limited by the critical pressure. This is an important consideration as Moulinet and Bartolo (2007) demonstrated that even a single defect in the surface can cause a relatively large area of wetting.

Attempts have been made to increase the energy barrier between the Cassie-Baxter and Wenzel states and hence make transition harder. One approach is to use a recurved or overcut structure (Spori et al., 2008) as shown in Figure 4.3 c). This ensures that for the interface to travel downwards into the cavity it has to increase the total interface surface area, which increases the energy requirements (Lobaton and Salamon, 2007). A similar approach is to treat the tips of the roughness elements with a hydrophilic coating (see Figure 4.3 d). The hydrophilic tips will act to pin the air-water interface at the top of the roughness and hence reduce the likelihood of wetting (Barthlott et al., 2010). In nature the critical pressure is increased by using multiple scales of roughness to ensure that the air water interface is smooth (see Figure 4.2d) and by using the flexible properties of insect

hairs to deform and align under load to ensure that the plastron is retained (Crisp and Thorpe, 1948).

The sharp tips of the roughness elements provide a natural energy barrier, and hence the air-water interface will typically become pinned at this point. For wetting to occur the interface needs to deform downwards into the cavity as shown in Figure 4.3 f). This highlights a reason for the cavity to be deep as it will allow the interface to deform downwards but not touch the bottom of the cavity. It also highlights that a good surface for plastron retention may usefully have a high contact hysteresis, such that when pressure is applied the contact angle may change before the contact line moves; one way to achieve this would be to have contoured tips to increase the length of the contact line (Oner and McCarthy, 2000). A similar result may also be achieved by utilising a dual scale of roughness (Enright et al., 2006). If the side walls of the cavity in Figure 4.3 e) were themselves patterned with a smaller roughness scale they would provide local energy minima, and allow the air-water interface to move partway down the cavity. In each of the three cases dicussed in this paragraph, the modifications would allow for partial wetting in a high pressure scenario, which could then be recovered to a full Cassie-Baxter state if the pressure were removed.

One of the main issues with retaining a plastron is that the plastron will be likely to diminish over time due to gaseous diffusion over the air water interface. In plants and animals the gaseous diffusion serves to balance the use and production of gases in photosynthesis and respiration (Shirtcliffe et al., 2006) allowing a plastorn to be retained indefinitely (Flynn and Bush, 2008). But with a biomimetric superhydrophobic surface there is no way to replenish the gases within the plastron and the gases will diffuse into the water, reducing the total volume of the air and making the plastron smaller. The timescale over which an artificial plastron may remain stable is unclear, although it typically follows an exponential decay (Govardhan et al., 2009), suggesting that gaseous diffusion is the primary process. Bobji et al. (2009) demonstrated that air bubbles within cylindrical pores disappeared after just 40 minutes, whilst other literature suggests the plastron can last up to 300 minutes (Govardhan et al., 2009), 400 hours (Poetes et al., 2010) or 130 days (Ditsch-Kuru et al., 2011). This discrepancy between the dissolution time may be explained by differences in the surface area of the air-water interface or differences in the immersion depth. The gaseous diffusion rate increases exponentially with the linear increase in hydrostatic pressure due to immersion depth in water (Poetes et al., 2010).

Overall, it is clear that designing a surface capable of retaining a plastron is possible, but it is harder for a plastron to be retained as the scale of the surface roughness is increased. To aid the surface in maintaining a plastron and minimising the risk of wetting a variety of approaches are possible, however, all increase the complexity of the surface and may produce difficulties in how to physically manufacture the surface.

4.1.3 Optimisation for manufacturing

The surfaces discussed in the previous sections have all been idealised; the roughness elements were all regular in size and shape and can be patterned easily to cover a large area. However, in reality it can be difficult to manufacture such regular and complex surfaces on a small scale but over a large area. This section explores the potential difficulties in the manufacturing process.

The three main requirements for the manufacture of superhydrophobic surfaces are that the process provides a hydrophobic surface chemistry, whilst ensuring that control can be maintained over the scale and structure of the surface roughness, and that the process can be applied over a relatively large surface area (for example areas of the order of $1m^2$) for applications in hydrodynamics.

To achieve the combination of the first two requirements two approaches can be undertaken; the roughness can added first and then coated in a hydrophobic chemical, or a hydrophobic substrate can be made rough. A substrate is hydrophobic if it has a low surface free energy such that it interacts weakly with fluids through van der Waals forces (Zettlemoyer, 1969); examples of chemical groups which tend to produce hydrophobic surfaces are hydrocarbons, fluorocarbons and Zinc Oxide (Nosonovsky and Bhushan, 2008). As the hydrophobicity of the surface is dictated by just the outer edge of the surface it can be applied in a variety of ways, such as sol-gel (Shirtcliffe et al., 2005), dip coating (Cui et al., 2009) self-assembing monolayers (Song et al., 2009), electrochemical deposition (Li et al., 2003) and chemical deposition (Wang et al., 2006). However, as the contact angle is highly altered by the addition of roughness, the flat surface contact angle is not a vitally important critertia, as long as the surface is sufficiently hydrophobic (Nosonovsky and Bhushan, 2008).

A range of approaches are available to make a surface rough:

- SAND - A simple approach to adding random, irregular roughness to a surface (Shirtcliffe et al., 2009).
- MECHANICAL ABRASION - Rubbing a surface with an abrasive material leaves marks and scrapes of a similar scale to the roughness of the abrasive material (Nilsson et al., 2010).
- CHEMICAL DEPOSITION - Submerging a surface in a reactive solution can lead to structures forming on the surface. Control of flow direction can lead to directionality in the structures. (Shirtcliffe et al., 2009)
- ETCHING - By masking certain parts of a surface it is possible to etch a shape such as pillars or ridges into a surface (Choi et al., 2006).
- MACHINING - Surface features can be machined from a surface using milling machines or lasers.
- GROWTH - Carbon nano tubes can be grown on a substrate. Applying a DC current can allow directional growth.

The primary trade-off when considering the manufacture of a superhydrophobic surface is the balance between complexity and cost, and attempting to achieve as close as possible to the idealised surfaces discussed in Sections 4.1.1 & 4.1.2. At the cheap and fast end of the scale is the addition of roughness through sand or similar roughness elements. This will be a relatively quick procedure, involving just one or two steps, but will result in a surface which is random and irregular. On the other hand, using a milling machine or a laser cutter would produce a surface which is highly regular and repeatable, but the time required to machine would scale inversely with the size of the roughness elements to be cut. Furthermore, the availability of machines which are capable of using small cutters $\mathcal{O}(200\mu m)$ to cover a surface 3 orders of magnitude larger is also limited and one quote provided for such a task was over $£2,000$ per A4 sheet. The cost and time taken to manufacture a surface are not only prohibitive in terms of producing the surface in the first place but also begin to offset any potential benefits from reducing the drag such as increased fuel efficiency. Overall, the most attractive approach is to use a technique which can produce a hydrophobic surface over a large area in one step to prevent prohibitive costs due to manufacturing times.

4.1.4 Summary and optimal design

The key balances that have been discussed in the preceding sections are related to the scale of the surface roughness and the complexity of the surface features. A larger surface roughness element will typically result in a larger effect of slip on the flow field and hence a greater drag reduction, it will also make producing the surface easier as it will require less fidelity in the manufacturing process. However, a larger surface roughness may make retaining a plastron harder and potentially also result in an increase in the drag of the surface due to the effect of the roughness. Increasing the complexity of the surface features will clearly make it harder for the surface to be manufactured but also result in an increased ability to retain a plastron and make the plastron more effective in producing a drag reduction.

In an air-water system the capillary length scale is approximately 2.7mm and hence this is the largest surface features that would be capable of retaining a plastron. However, simple testing by the author showed that it is hard to maintain a plastron with a roughness scale larger than roughly 0.5mm regardless of the surface chemistry. In the experimental study conducted in Chapters 5 & 6 the Reynolds numbers explored are up to 3,000,000 which means that a surface roughness of 0.5mm is considered fully rough in a hydrodynamic sense (see Section 5.2.2 for further details), meaning that it has a large impact on the drag.

Overall this suggests that the optimal superhydrophobic surface for this study is a structured surface of ridges or posts which is produced using a simple method to cover a large area. There is still a trade-off between having a larger structure to promote slip but produce more drag due to the roughness, which will depend on how effective the structures are at retaining a plastron with a flat interface shape. There is also a trade-off between the complexity of the surface produced, with the potential for producing a measurable drag reduction and also the cost of producing such a complex surface. In this thesis, the view was taken that there is currently insufficient evidence of drag reduction to warrant the production of highly complex and expensive surfaces and hence surfaces have been created with progressivly greater fidelity and expense. The following section details three separate approaches that have been used to successfully create hydrophobic surfaces over a large area.

4.2 Superhydrophobic surface manufacture

4.2.1 Hydrophobic sand

Sand has been used as a simple starting point in producing a hydrophobic surface as it can easily be attached to a flat perspex backing sheet using a variety of glues. The procedure for attaching the sand was to abrade the perspex surface slightly to provide a better attachment for the glue, the surface was then cleaned using white spirit and then water and allowed to dry. The glue was then applied evenly in a relatively thick coat to the entire surface before being coated in sand. The sand was then tamped down using a flat surface to ensure that the sand was embedded within the glue. Once dry, the excess sand was removed and the edges trimmed with a sharp knife. It was found that the glue layer needed to be relatively thick to ensure that the sand stuck well to the surface. Initial samples were created using a variety of glues including Spray Mount™, super glue and epoxy resin, but all were found to either not produce a consistent layer of glue or were not resistant to ethanol, abrasion or UV. The best approach was found to be to use a relatively viscous metallic paint[1].

To make the sand hydrophobic two approaches were used. The first was to use a commercially available sand (Magic Sand[2]). Details of the chemical coating on the Magic Sand are not provided by the manufacturer but it is rumoured to be Trimethylsilanol. The second was to use typical building sand and then apply a hydrophobic coating. To produce a more regular/controlled random surface the sand was sieved to produce different gradings. The sand was first dried and then sieved using a mechanical sieve. The gradings were chosen to ensure a difference in hydrodynamic roughness class and were taken as $250\mu m < \mathrm{G1} < 400\mu m$ and $150\mu m < \mathrm{G2} < 250\mu m$.

[1]For example Fortress Metal Black Paint - EAN: 0000004024491

[2]The Magic Sand used in this study is actually called Aqua Sand™(Moose Enterprise, 7-13 Ardena Court, East Bentleigh, Melbourne, VIC 3165, AUSTRALIA) but for continuity it is referred to as Magic Sand

Figure 4.4: Droplets of water on piles of hydrophobic sand with coin for scale. (L-R = Magic Sand, G1 with Granger's™solution, G2 with Granger's™solution

The difference in grain size between the three types of sand used can be seen in Figure 4.4. Although the Magic Sand is not sieved it is clear that it has a much larger grain size in general. The Magic Sand also shows the presence of a plastron through the silvery sheen on the surface. The plastron is present on the other two types of sand but is much harder to capture on camera. This is due to the plastron only being visible when it reflects light; with the larger grain size the air water interface is not flat but follows the sand grain roughness, producing a undulating surface and a wider spread of interface-to-observer angles and hence increasing the likelihood that light will be reflected back to the observer. On the G1 and G2 sand the plastron is flatter and requires the observer to view the surface at a highly oblique angle.

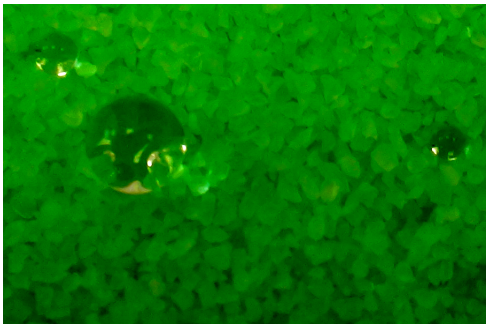

Figure 4.5: Droplets of water on hydrophobic Magic Sand (adjusted contrast & colour balance)

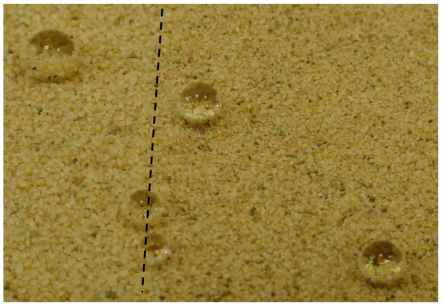

Figure 4.6: Droplets of water on G1 (right half) and G2 (left half) hydrophobic sand

Figures 4.5 & 4.6 demonstrate that the sand grains are hydrophobic and are able to support water droplets of a variety of sizes. The presence of the plastron on Magic Sand when immersed in water is also confirmed in Figure 4.7, where the air-water interface is visualised through the reflected light. The plastron appears to completely cover the surface but it is apparent that the air-water interface itself is not flat, although it does appear to be smooth.

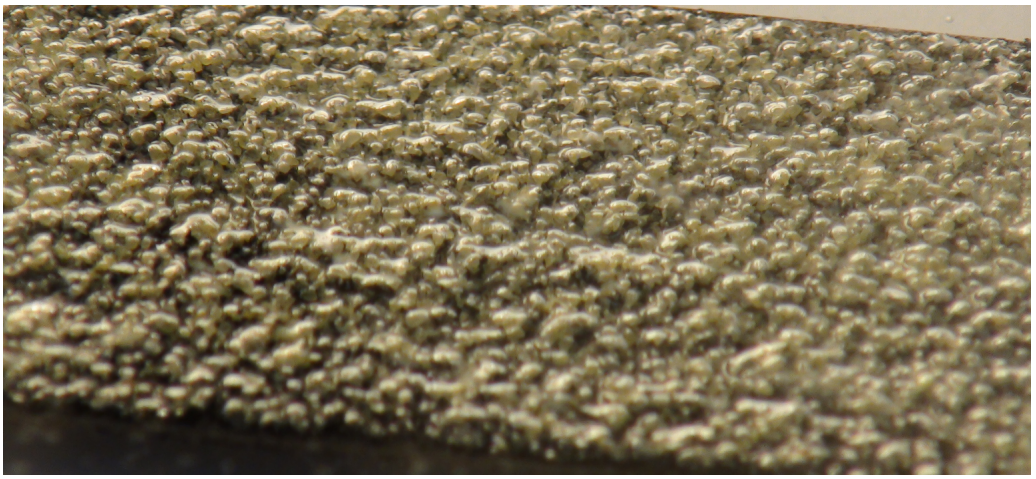

Figure 4.7: Photo of Magic Sand immersed in water demonstrating refelctivity of the plastron

A range of coatings were applied to the graded sand to impart hydrophobicity but the best performing was found to be a commercially available product - Granger's™solution[3]. This solution was diluted 20:1 with water and the sand was immersed in it for 10 minutes. The sand was then baked in an oven for a few hours at 80° to dry it and the process was repeated a few times. This hydrophobic sand was then attached to the perspex in the same way as the Magic Sand. Examples of water droplets on the sand are shown in Figure 4.5 & 4.6 and this also demonstrates the difference in scale of the sand grains.

4.2.2 Hydrophobic ridges

A variety of approaches to creating a hydrophobic surface with structured roughness were explored, including polymer gel-coats, micro machining, 3D printing and laser cutters. The polymer gel-coats proved to be an effective idea if the right chemical composition could be achieved, but in this case a compound could not

[3]Grangers International Ltd, Grange Close, Clover Nook Industrial Park, Alfreton, Derbyshire, UK, DE55 4QT

be created that would set satisfactorily[4]. Both the micro-machining and 3D printing turned out to be incapable of producing the required degree of accuracy and the laser cutters proved too expensive. A process involving chemical etching of a high contrast, epoxy based photoresist (SU8-50) was eventually used to create the structured surfaces detailed in this Section.

The surface designed to have a regular surface structure that would produce a relatively flat air-water interface and maintain a relatively thick plastron, whilst being as smooth as possible. An additional design criteria that was considered was the ability to create a directional surface. This led to the design of a regular arrangement of grooves, similar to riblets. The grooves were designed to be as close a match as possible to those used in experiments on cylinders by Muralidhar et al. (2011). Although the design is similar they are applied in a different hydrodynamic environment in this study, where the grooves produce a transitional roughness on a smooth surface rather than being applied to the effect on separation on a sphere. The design also incorporates breaker ridges, to help support the plastron in a direction aligned with the ridges, with the breaker ridges spaced 5mm apart, giving an aspect-ratio of 50:1. The structured surface can either be considered as ridges with breaker ridges, or as stretched cavities; the first description is used in this study.

SU8-50 is an epoxy which solidifies when it exposed to ultra-violet light. This occurs as the molecular chains cross-link and allows for certain regions of a certian to be masked, ensuring that they do not solidify and can be cleaned away afterwards. The process used to develop the surfaces is demonstrated in Figure 4.8 and given in detail below[5].

[4]This work was carried out by Simon Stanley from Nottingham Trent University as part of the larger group project that this work contributes to

[5]These surfaces were created by Joe Brennan under the supervision of Micheal Newton at Nottingham Trent University, based on the surface specification was proposed by the author

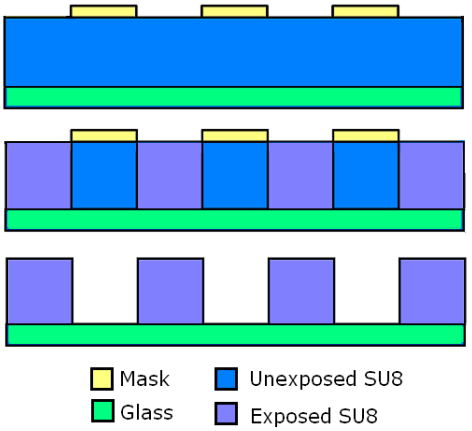

Figure 4.8: Key stages of creation process for hydrophobic ridges

1. Clean glass slides in a solution of 20% Decon 90 and 80% Filtered and deionised water using an ultrasonic cleaner for 10 mins.
2. Rinse with water and isopropanol before drying on a hotplate at 90°C to remove any moisture.
3. Once cool place the samples in a solution of 2% 3-Aminoproyltriethoxysilane and 98% acetone for 1 min.
4. Rinse with acetone and allow to dry.
5. Spin coat SU8-50 on to the glass slides (Spin coater speeds are 500rpm for 5s, 2000rpm for 30s with accelerations of 200rpm/s for 0-500 and 300rpm/s for 500-2000)
6. Place on a hotplate at 65°C for 30 mins then 95°C for 30 mins.
7. Once cool, expose on a mask aligner for 15s using a soft contact method.
8. Place on a hotplate at 65°C to cross link the SU8-50.
9. Develop in MicroDev EC solvent for about 20 min.
10. Rinse in isopropanol and blow dry with nitrogen.
11. Apply Granger's™ in 20:1 solution with warm water. Dry in oven at 80°C for 3 hours.

This approach includes spin-coating the SU8 onto the glass tiles. This process is limited to a relatively small scale and hence the SU8 is used to coat 5cm square

glass sheets, which are then tiled together on to a backing sheet of perspex measuring 280×200mm. The glass tiles are glued to the backing sheet using araldite glue and then placed between two granite blocks; this ensures the top of the ridges on each tile are aligned and that the total thickness of the composite surface is 3mm.

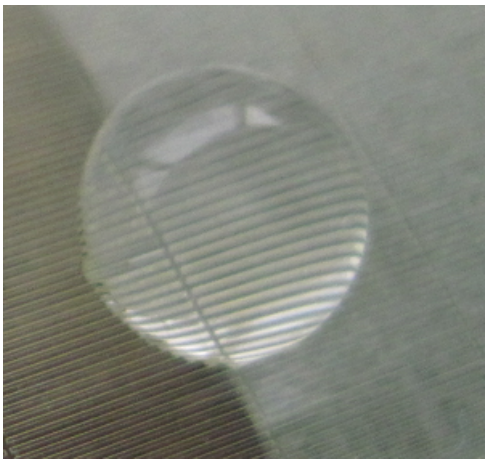

Figure 4.9: Droplet of water on ridged $100\mu m$ hydrophobic surface

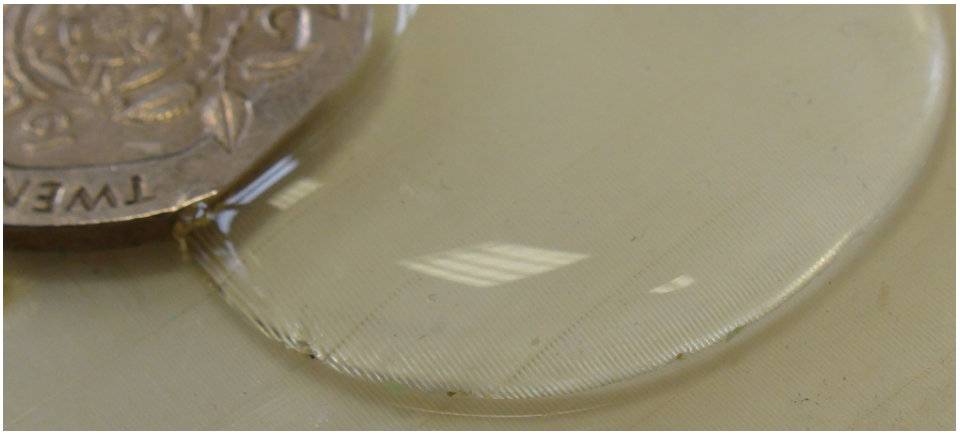

Figure 4.10: Photo of plastron on ridged hydrophobic surface with coin for scale and effect of directionality on contact angle

The approach to producing regular ridges has been successful as shown in Figures 4.9 & 4.10. The ridges that have been produced are regular and have sharp edges. The surface is also capable of producing a stable plastron (visualised by increased reflectivity), although this is difficult to visualise and capture on camera due to the transparent glass, water and SU8. The directionality of the surface produces a asymmetry of the contact angle on the surface, as can be seen by the ripples in the contact line in Figure 4.10.

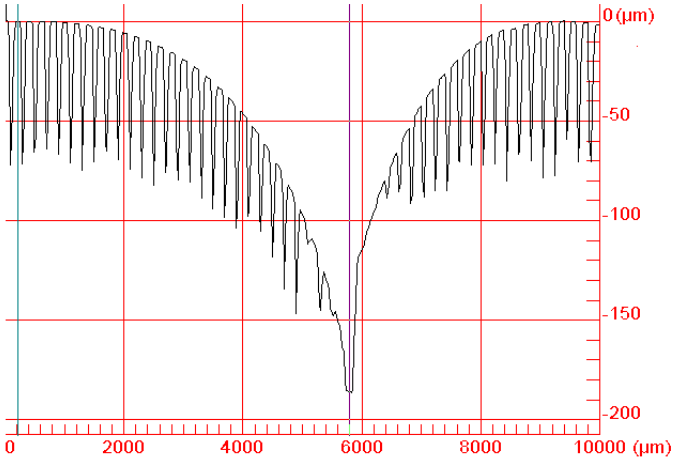

Figure 4.11: Stylus profilometry of ridged surfaces with unequal axis scales (image provided by Joe Brennan, Nottingham Trent University)

However, two limitations of the manufacturing technique were observed and although considered small, need to be carefully considered when analysing the results. The first issue is that the spin coating process results in a meniscus forming on the glass tiles, as shown by the curvatuve in Figure 4.11, where a contact based profilometer has been used to measure the profile across the intersection between two tiles. Therefore, near the edge of the tiles the depth of the SU8 is reduced, resulting in shallower ridges and the elimination of the ridges completely at the extremities. This effect covers approximately 1mm around the edge of each 5cm tile and hence accounts for 4% of the surface area. Note that the stylus was too large to fit between the ridges and hence the depth of the ridges could not be measured accurately with this method (further surface profiling is discussed in Section 4.3). An important point to note from Figure 4.11 is that the top of the ridges align neatly as expected due to the use of granite blocks to level the surfaces.

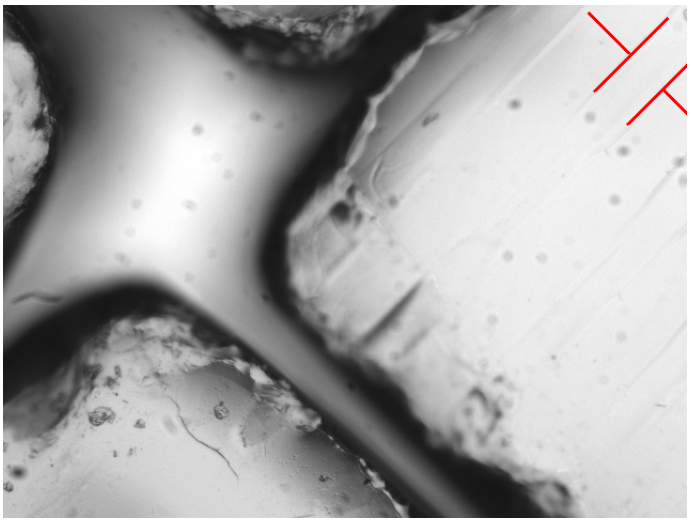

Figure 4.12: Microscope image of junction of four glass tiles (red lines spaced approximately 100μm apart)

The second issue is that it is relatively difficult to align the edges of the tiles accurately. In Figure 4.12 the red lines mark the scale of the ridges ($100\mu m$) and can be used to estimate that in this case the tiles are each offset by 100-200μm. This is not significant in itself, but becomes a difficulty when the glass samples are tiled together, possibly producing discrepancies of up to nearly 1mm. Furthermore, the gaps between the tiles produce much deeper roughness elements than the $100\mu m$ deep ridges. Although these issues present difficulties it is still considered that the tiled, ridged surfaces are satisfactory for the purpose of testing the drag difference between a hydrophobic and a wetted state.

4.2.3 Hydrophobic mesh

The final approach to producing a hydrophobic surface in this study is through a copper mesh. The mesh provides a regular roughness which is then made hydrophobic through a simple chemical treatment. The choice of copper as a material was linked to the simple (one-step, involving no complex methodology) chemical treatment which could be applied [6]. Two different scale copper meshes have been used, a coarse (#18) and a fine mesh (#60). The characterisation of a mesh is given in terms of the number of openings per inch ($\#n_o$) with the mesh woven from a wire of diameter d and spaced a distance s apart. The cavity fraction of

[6]The resultant turquoise colour was produced by the chemical treatment and is not the typical verdigris (copper carbonate) but instead copper carboxylate.

the surface can be calculated as $F_C = (s-d)^2/s^2$. Details of the mesh spacing and size can be seen in Figure 4.13 and Table 4.1.

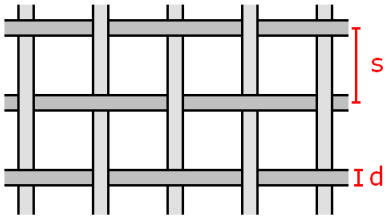

Figure 4.13: Schematic of mesh

$\#n_o$	s(mm)	d(mm)	F_C
#18	1.41	0.36	0.55
#60	0.42	0.16	0.39

Table 4.1: Details of fine and coarse copper meshes

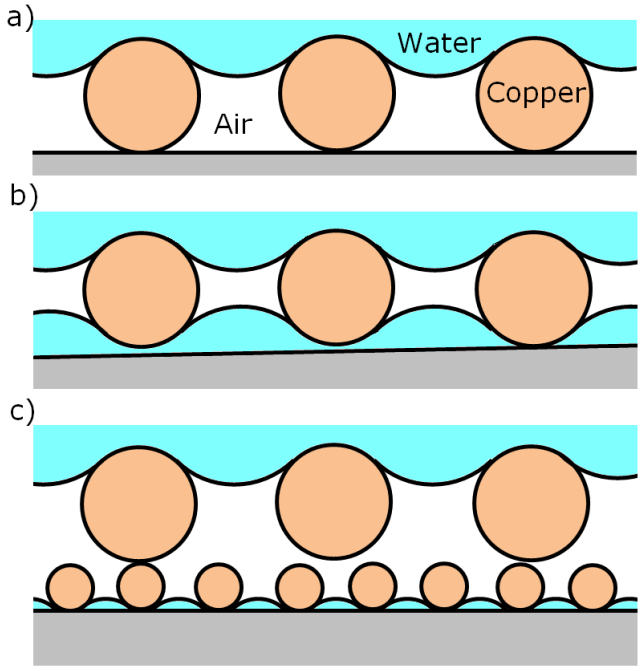

Figure 4.14: Schematic side view of a) idealised flat copper mesh b) wetted underside due to gaps & c) dual scale mesh to ensure high quality plastron regardless of gaps

Figure 4.14 demonstrates the plain weave used in the mesh, and hence the orthogonal symmetry and independence of the shape on weave direction. To ensure that the final copper mesh remains flat it was stretched flat and attached to a perspex backing sheet at 20mm intervals using copper wire stitches. Copper wire is used to ensure that when the surface is chemically treated the attachment points do not become weak points in the hydrophobicity. Initial tests showed that in practice due to the relative stiffness of the copper fibres, it buckled slightly in places. In an idealised case, the copper mesh would be perfectly flat on the backing sheet

of perspex and a thick plastron would be present (Figure 4.14a). However, due to the buckling of the surface it meant that in some places water was able to get between the copper mesh and the perspex sheet as shown in Figure 4.14b. This would reduce the plastron thickness and the volume of air supported within the copper mesh. To overcome this issue a second smaller mesh was placed between the larger mesh and the perspex sheet (Figure 4.14c). The smaller mesh is more resistant to wetting due to the smaller scales and helps prevent water penetrating from the back of the larger copper mesh. In this way a large plastron could be supported stably, even though there were slight gaps between the two sheets of copper mesh.

The process used to impart hydrophobicity to the copper mesh structure was relatively simple and was applied once the mesh had been attached to the sheet of perspex. The approach used was suggested by Wang et al. (2006) but was modified slightly to ensure that the copper mesh was clean at the start.

1. Rinse the sample in 0.3M hydrochloric acid to remove any copper oxide.
2. Rinse in deionised water.
3. Rinse in ethanol.
4. Place in 0.01 molar solution of *n*-tetradecanoic (myrisitic acid) and ethanol at room temperature for 5-7 days.
5. Allow to dry at room temperature for 7 days.

This method produces clusters of $(Cu(CH_3)CH_{12}COO)_2$ or copper carboxylate nano-flowers. After the initial immersion process these clusters grow from the surface, and after 5-7 days they can completely coat the surface (Wang et al., 2006). The successful production of such a hydrophobic coating to the copper was found to be sensitive to the Molar concentration of the solution. In 1L of ethanol a 0.01M solution required only 0.28g of myristic acid, clearly requiring scales with a high precision, as a 0.015M solution was found to not achieve the desired result.

Two different copper meshes were created, the first used a fine mesh as a base layer and then had a coarse mesh on top. The second had a fine mesh as both the base layer and the top mesh in an attempt to reduce the hydrodynamic roughness. The two surfaces are shown side by side in Figure 4.15 along with a coin to show scale. The turquoise colour of the copper mesh is a result of the chemical treatment with myristic acid.

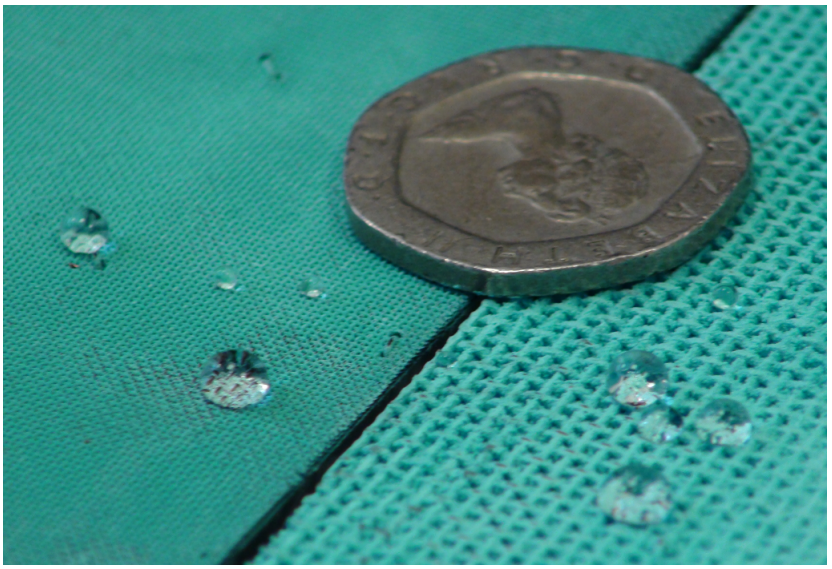

Figure 4.15: Hydrophobic copper mesh with droplets with coin for scale (coarse=right, fine=left)

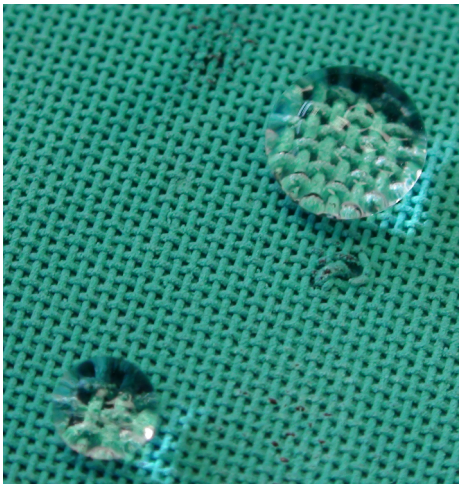

Figure 4.16: Fine hydrophobic copper mesh with droplets and areas of high reflectivity showing the presence of a plastron

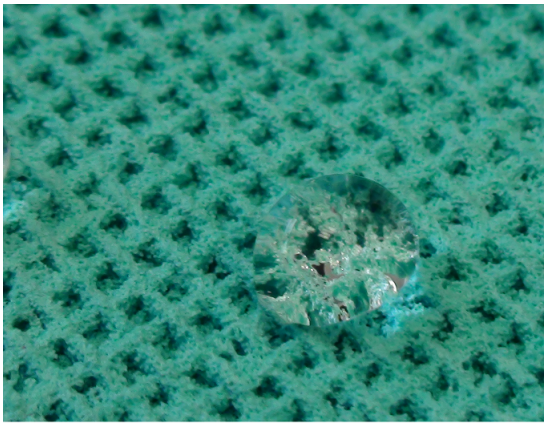

Figure 4.17: Coarse hydrophobic copper mesh with droplet and areas of high reflectivity showing the presence of a plastron

Figure 4.16 & 4.17 show close up of water droplets on the meshed surface. It is possible to see the air-water interface through the reflections within the water droplet and it is clear that the air is present on the surface. In Figure 4.16 one of the stitches used to attach the mesh to the perspex backing sheet is shown. For the fine mesh the stitches act to add an extra roughness as they protrude from the smaller mesh, whilst for the coarser mesh there is minimal distruption to the shape of the mesh. The stitches themselves are hydrophobic and hence no

water is able to penetrate through to the backing sheet. The photograph of the coarse copper mesh in Figure 4.17 also demonstrates the additional small scale of roughness which is generated by growing the copper nano-flowers on the surface. The nano-flowers slightly decreases the overall cavity fraction compared to the base mesh, but there is still sufficient area to allow a plastron to form within the cavities. The hydrophobic copper was found to be stable to UV and water over a period of months, with no further hydrophobic coating growing and no verdigris appearing, and the surface remaining hydrophobic. However, the surfaces were susceptible to abrasion, and were hence touched minimally throughout the testing process.

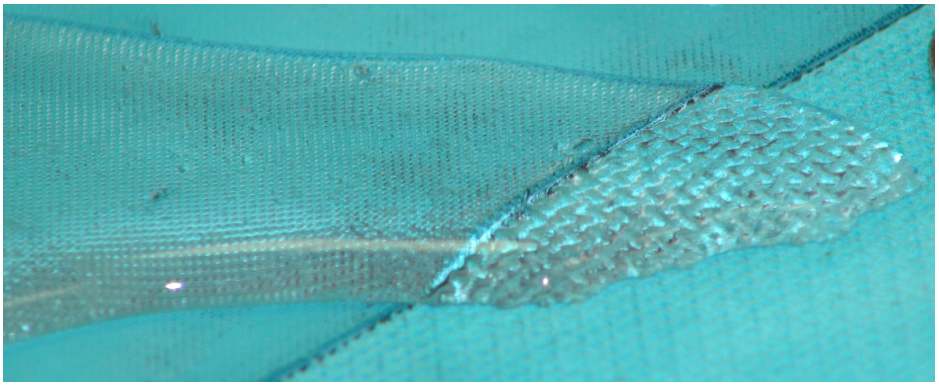

Figure 4.18: Hydrophobic copper mesh with reflective plastron

The presence of a plastron when the surface is covered in water is also demonstrated in Figure 4.18. Similar to the hydrophobic ridges, the regular nature of the roughness means that the contact line follows a relatively discrete shape.

4.3 Surface characterisation & visualisation

This Section details the characterisation of the superhydrophobic surfaces used in the experimental study. First the surface roughness of each surface is explored and then a new technique is used to visualise the air-water interface of the plastron.

4.3.1 Surface roughness measures

At first glance the roughness of a surface is easy to characterise, but it is hard to define mathematical parameters which are able to clearly differentiate between different surface roughnesses. One of the obvious ways to characterise the surface

roughness is through the difference between the lowest valley and the highest peak. Mathematically one can define the mean amplitude (R_a) which in a 2D case can be defined based on the profile $z(x)$ being sampled at N discrete points (Woan, 2009).

$$R_a = \frac{1}{N}\sum_{i=1}^{N} z_i \tag{4.2}$$

However, the mean amplitude highlights an important issue, which is how to define the zero-plane. Figure 4.19a) demonstrates that the mean amplitude allows one to average out the surface features (red-line) and hence give an average height from the surface (z_0), yet it is unclear where to take the zero; should it be the substrate, the lowest valley height, the mean valley depth. Figure 4.19a) demonstrates that the mean amplitude allows one to average out the surface features (red-line) and hence give an average height from the surface (z_0), but again it is unclear where to take the zero; should it be the substrate, the lowest valley height or the mean valley depth?

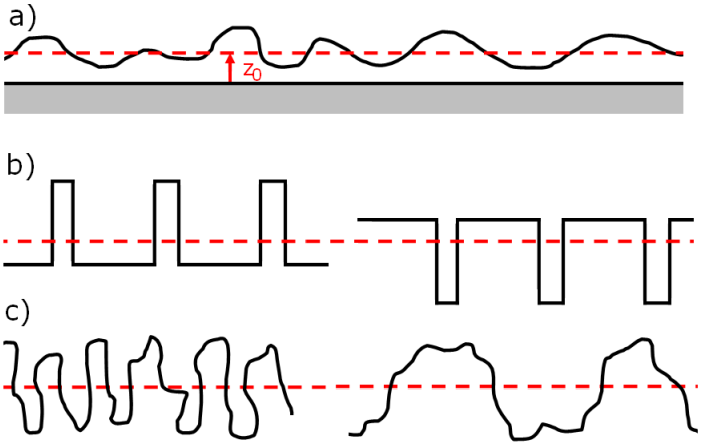

Figure 4.19: Schematic of a) mean roughness height b) effect of skewness (positive skewness on right) and c) effect of kurtosis (high kurtosis on right)

One possible way to overcome this is to use the variance (σ^2) of the profile. The variance gives a measure of the distribution away from the mean amplitude and is therefore independent of the zero-plane (Woan, 2009).

$$\sigma^2 = \frac{1}{N-1}\sum_{i=1}^{N} (z_i - R_a)^2 \tag{4.3}$$

However, the variance of the profile only describes the average distance from the mean, it does not describe the structure of the surface in any way. For example, the two structures shown in Figure 4.19b) would both have the same variance. To further differentiate between surfaces other higher order measures can also be used, such as the skewness (S) and kurtosis (K) (Woan, 2009):

$$S = \frac{N}{(N-1)(N-2)} \sum_{i=1}^{N} \left(\frac{z_i - R_a}{\sigma} \right)^3 \tag{4.4}$$

$$K \approx \left[\frac{1}{N} \sum_{i=1}^{N} \left(\frac{z_i - R_a}{\sigma} \right)^4 \right] - 3 \tag{4.5}$$

The skewness is related to the relative height distribution of the profile, with a positively skewed profile having extreme asperities at the bottom as shown in the right hand side of Figure 4.19b). The kurtosis is a measure of how sharp the peaks of a surface are Woan (2009), with a high kurtosis value producing a more slowly varying surface as shown in the right hand side of Figure 4.19c). Using these measures and the understanding developed in Section 4.1, a superhydrophobic surface should have a negative skewness and a high kurtosis as shown in the left hand surface in Figure 4.19.

These measures are still perhaps unsatisfactory and a wide range of other roughness measures are available, with Gadelmawla et al. (2002) reporting 59 different measures. Other measures are found to exist within the hydrodynamic community, where the roughness itself is not only important, but how it interacts with the flow around it; for a turbulent boundary layer this is typically characterised by a zero-plane displacement (d_0) and a roughness length scale (k) such that the velocity profile (Jackson, 1981) can be defined as:

$$u^+ = \frac{1}{\kappa} \ln \frac{y - d_0}{k} \tag{4.6}$$

The zero-plane displacement height attempts to quantify the height at which the mean shear stress on the surface acts and accounts for the effective blockage effect and the sheltering of parts of roughness elements from the external flow by the higher extremities, this is especially the case for overlapping surfaces such as closely packed spheres (McClain et al., 2006). As different roughness shapes will have different effects on flow past the surface a universal length scale for the effect of

roughness in turbulent flow is difficult to define. A typical measure is the equivalent sand grain roughness (k_s) introduced by Nikaradse (as cited in Schlichting (1960)); this allows various rough surfaces to be defined through their relative effect on a turbulent boundary layer profile in comparison to the *yard-stick* of mono-disperse sand grain roughness. However, Colebrook (1939) demonstrated that different surface structures can have different effects in the transitional roughness regime, regardless of the equivalnt sand grain size. This is discussed further in Section 5.2.2, and it is sufficient here to note that the equivalent sand grain size may be up to a factor of 30 smaller than the physical mean amplitude. The effect of a variety of non-sand grain roughness can be estimated using experimental correlations, but currently cannot be calculated directly from the surface profile. Various attempts have been made to relate the equivalent sand grain roughness to the physical surface features, such as the Sigal-Danberg parameter (Sigal and Danberg, 1990), and to use a minimum number of parameter to simulate the effect of any roughness from smooth to fully rough (Busse and Sandham, 2012b). However, this can still result in errors of up to 40% in k_s (McClain et al., 2006), which suggests that a universal relation of surface roughness to its hydrodynamic effect is still not available.

To characterise the surface it is necessary to take measurements of the surface profile. This can be achieved using contact or optical procedures. As optical procedures provide a complete 3D representation of the surface rather than just a 2D line profile these methods were preferred. In particular, all of the surfaces were scanned with the Alicona InfiniteFocus microscope at the University of Southampton; this microscope allows a 3D (i.e. $z\,(x, y)$) representation of the surface to be constructed by scanning the surface.

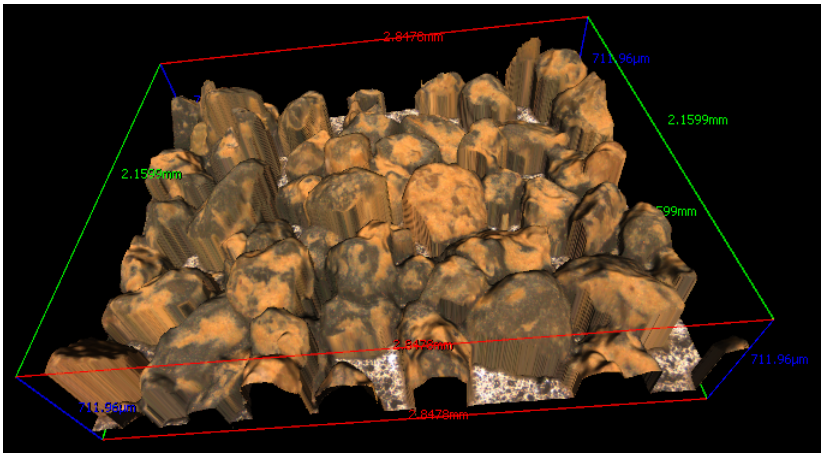

Figure 4.20: Scanned surface of $G1$ sand with realistic colour

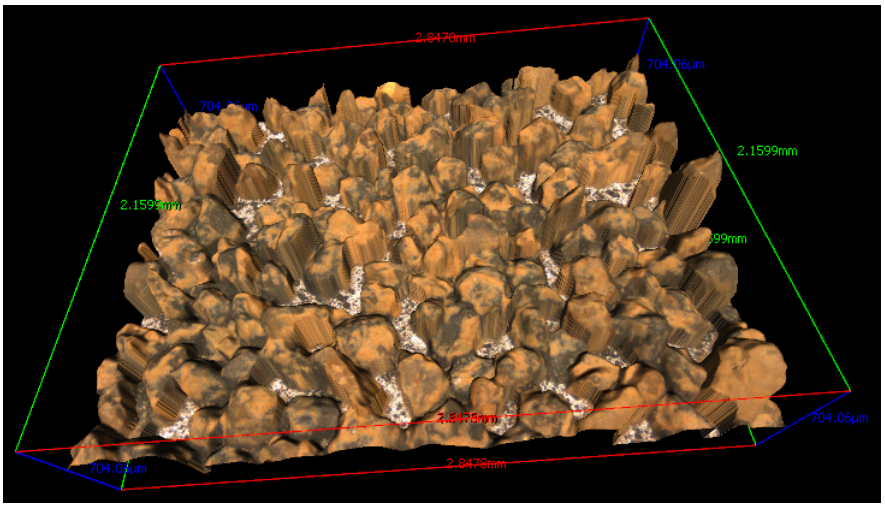

Figure 4.21: Scanned surface of $G2$ sand with realistic colour

Figures 4.20 & 4.21 show 3D representations of G1 and G2 graded sand surfaces. The extent of the sample shown is the same for each Figure and allows a clear comparison of the difference in scales between the surfaces. The variety in both grain size and shape is evident for both samples, with some roughness elements protruding higher than others. Furthermore, both surfaces also demonstrate that it is difficult to achieve a 100% surface coating, with some areas of the surface remaining bare and smooth.

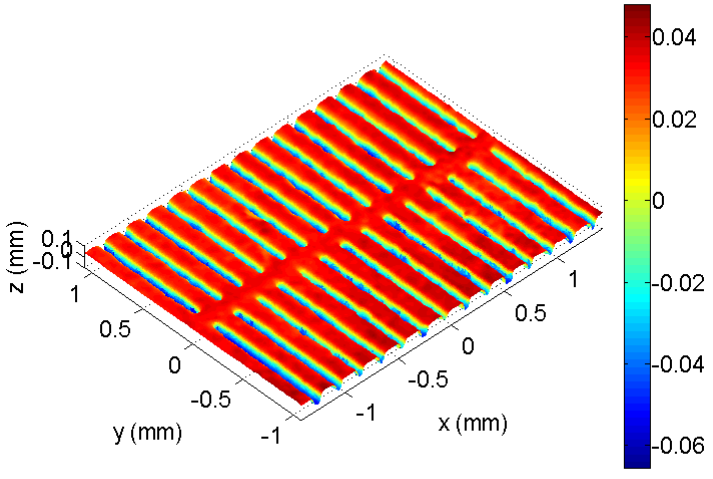

Figure 4.22: Scanned ridges coloured by height

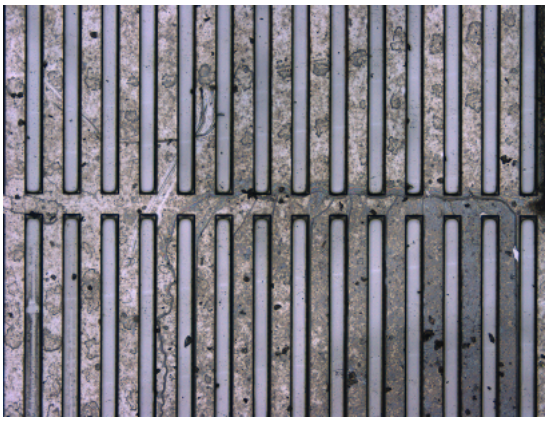

Figure 4.23: Microscope image of $100\mu m$ ridges using $5\times$ optical zoom

The ridged surfaces proved difficult to accurately measure with the microscope due to the transparency of both the glass tiles and SU8 coating. The vertical faces of the ridges also provide another difficulty due to the microscope imaging from directly above the surface. Figure 4.22 shows that the top edge of the ridges are captured accurately, but due to the difficulties mentioned the sides and bottom of the ridges show some variation. However, a photograph taken with the microscope (Figure 4.23) demonstrates that the ridged surfaces are extremely well defined, with regular spacing between the ridges and sharp sides.

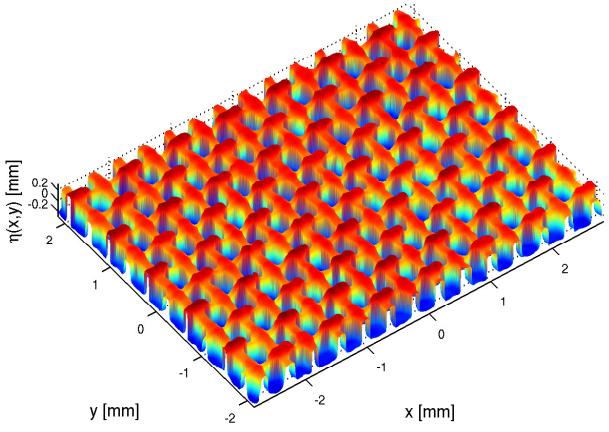

Figure 4.24: Scanned fine copper mesh coloured by height

A similar scan was taken of the fine copper mesh (CuF) with Figure 4.24 showing the 3D representation of the surface. The regularity of the surface is obvious in comparison to the surfaces coated in sand. Furthermore, the scan highlights the

deep holes in the mesh, which will be accentuated in the actual surfaces used as they are constructed from two layers of mesh, whilst the scan was taken on just one.

Surface	$R_a(\mu m)$	σ (mm)	S	K
Sand (MS)	862	0.260	1.51	-0.39
Sand (G1)	219	0.135	1.40	-0.88
Sand (G2)	142	0.085	1.50	-0.37
Transverse ridges (TR)	21	0.031	-1.49	-0.02
Aligned ridges (AR)	12	0.011	0.96	-0.21
Copper (CuF)	317	0.315	1.17	-1.57

Table 4.2: Roughness parameters for the rough surfaces explored

As previously mentioned the roughness parameters help to show the general structure of the roughness as shown in Table 4.2, with the MS and CuC[7] being the roughest surfaces, whilst the ridged surfaces are the smoothest. The largest standard deviation is found to be for the copper surfaces and is accompanied by a low kurtosis showing that these surfaces have larger and relatively more peaks than the other surfaces.

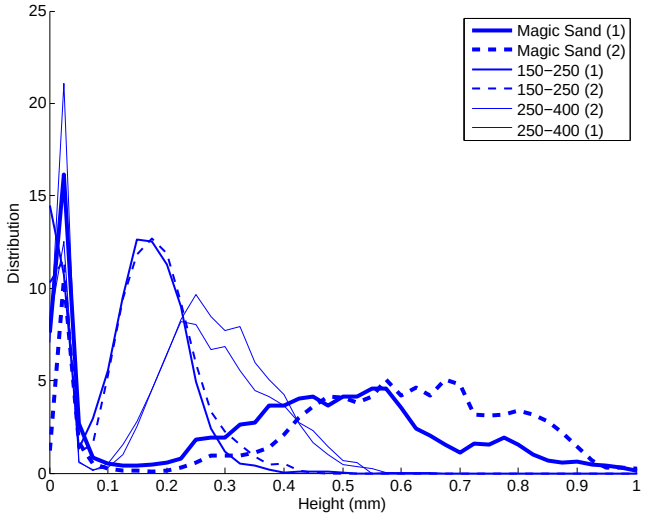

Figure 4.25: Surface height probability distribution of surfaces

[7]Data was not available for the coarse copper mesh, as the microscopes were incapable of measuring sufficient depth in the mesh to provide a meaningful surface profile for analysis

The surface height probability distribution is also a useful visible measure of the effective roughness of the surfaces, assuming that the general structure is known. Figure 4.25 demonstrates the distribution of the height for each surface, with each curve encompassing a total area of 100%. It is clear that there is a narrow distribution for G1 and G2, compared to a relatively wide distribution for the MS which contained a wide range of grain sizes. However, all sets of sand grains cover a much wider distribution range than the monodisperse sand grains of Nikuradse, with the data of Colebrook and White (1937) demonstrating that just a 2.5% area coating of a larger roughness size can result in significant change in the effective hydrodynamic roughness of the surface. The distribution for the ridged surfaces is not shown as it is a regular surface and is not clearly visible on the scale used in the Figure.

4.3.2 Confocal microscopy & image processing

4.3.3 Background Theory

Confocal microscopy is an imaging technique that increases the resolution of a traditional microscope and allows 3D images of a sample to be constructed. A traditional microscope uses a single light source to illuminate the specimen evenly and light is reflected back to the observer, allowing the sample to be seen as a whole. The main feature of a confocal microscope is a pinhole, which ensures that only light from the plane in focus is returned to the observer.

Confocal microscopy is typically used in biomedical applications in conjunction with lasers of a certain wavelength. Using fluorescent dye it is possible to measure the light that is fluoresced by the surface, which will normally be of a different wavelength, allowing the incident wavelengths to be removed from the result. In this case a much simpler option can be used, as the hydrophobic surfaces can be imaged in the reflected light mode. In this mode a laser above the surface is used to illuminate a certain point on the surface known as the voxel. Any surface or interface at this point will reflect light back to the photodetector. By repeatedly moving the voxel, it is possible to build up a 3D image of the surface.

The reflected light mode can also be used to determine the position of the air-water interface because of the difference in refractive indices (η) between the two media. The reflectance (R), depends on the incident angle (θ_i) and the value of η

in the medium the light is coming from (1) and going to (2) according to (Hecht, 1987)

$$R = \left[\frac{\eta_1 \cos\theta_i - \eta_2 \sqrt{1 - \left(\frac{\eta_1}{\eta_2} \sin\theta_i\right)}}{\eta_1 \cos\theta_i + \eta_2 \sqrt{1 - \left(\frac{\eta_1}{\eta_2} \sin\theta_i\right)}} \right]^2 . \tag{4.7}$$

If the value of $R < 1$ then total internal reflection occurs and all of the incident light is reflected. If $R > 1$ then some light is reflected and some passes through the boundary. In the case of an air-water interface on a superhydrophobic surface the values are $\eta_1 = 1.330$ and $\eta_2 = 1.008$ producing a critical angle of $\theta_C = 48.8°$. For confocal microscopy, this means that it is hard to detect steep surfaces. Firstly, the amount of light reflected is reduced if the incident angle is above the critical angle. Secondly as the reflected angle equals the incident angle, the reflected light will not be directed exactly back at the photodetector. This is a limitation of the confocal setup, but should not affect the results presented here, which are aimed at developing a qualitative picture of the surface and the air-water interface.

4.3.4 Image capture & processing

In this study a 20× water-immersion lens is used to focus the laser. This produces a viewing area that is a square of side $750\mu m$. The viewing area is divided into 512×512 pixels, meaning that each pixel covers $\sim 1.5\mu m$. To construct a 3D image of the surface, a series of 2D scans are conducted at a variety of levels separated by a step height change(Δh) of $96 - 10\mu m$. This height is chosen as initial tests showed that step heights of $\sim 10\mu m$ were optimal in terms of accuracy, as surfaces are smeared over a distance of this order. The voxel, or interrogation volume, is approximately 700nm wide and $1\mu m$ deep, meaning it is at most half of the final pixel size in each dimension.

For each individual image, the microscope records each pixel in a series of horizontal sweeps, with the photo-detector remaining fixed but optics changing the focal point of the laser. Once an image is recorded the focal depth of the optics is changed and another 2D image is produced. This is repeated until a stack of 2D images has been created sufficient to cover the total depth of the sample. An automatic tiling procedure within the control software is then used to expand the viewable area by stitching together multiple stacks as shown in Figure 4.26.

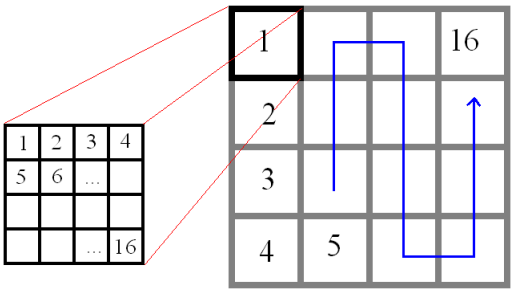

Figure 4.26: Construction of a wider view area by tiling of stacks (inset = 4×4 pixel image, main = tiled images)

Each individual stack of images can be processed in approximately 2-5mins, depending on the height of the sample. This means that each 4×4 3D sample takes roughly 35-80 minutes, with approximately 20 minutes required to ensure that the correct parameters are specified. The tiling procedure involves physically moving the sample beneath the confocal microscope using a motorised stage which is accurate to $< 0.5\mu m$. The tiling is calibrated with a biomedical sample (highly curved and highly detailed) to ensure that the relative location of each stack is correct.

There are two main concerns with the movement of the stage for this preparation. First, the lens is immersed in the water, and concerns arose about whether surface tension effects could move the plastron as well. However, tests showed that when the samples were moved over a large distance the plastron remained in the same position when the sample was returned to the original location. The second concern was the finite time taken between samples and whether the plastron may reduce in thickness over time. To check whether this was occurring, samples were retested after intervals of up to 24 hours and no discernible difference was observed.

The data was exported from the control software in the form of a JPEG for every height level. The control software automatically stitches together the pictures from each stack, with the average value taken if any images overlap (typically 2-5 pixels). These images were then processed in MATLAB in a few stages to create a 3D visualisation of the surface:

1. Saturation adjustment

2. Dithering

3. Noise reduction

4. Surface detection

The processing software is used to determine whether there is a surface present at each pixel location based on the reflected light intensity. This is achieved by converting the original grayscale image into black and white by dithering. To ensure that the surface features are detected using this approach, it is necessary to adjust the intensity of the image so that any surface features are above the intensity threshold of 50%. The saturation level is remapped based on a lower and upper limit, for example with limits of 0 and 0.5, all the saturation values are remapped onto the range 0 to 1, with everything above 0.5 in the original image having a saturation value of 1. This example case could also be seen as reducing the threshold value to 25%. In all cases, the images were slightly too dark, so the lower limit was set to zero, with the upper limit being set independently for each sample.

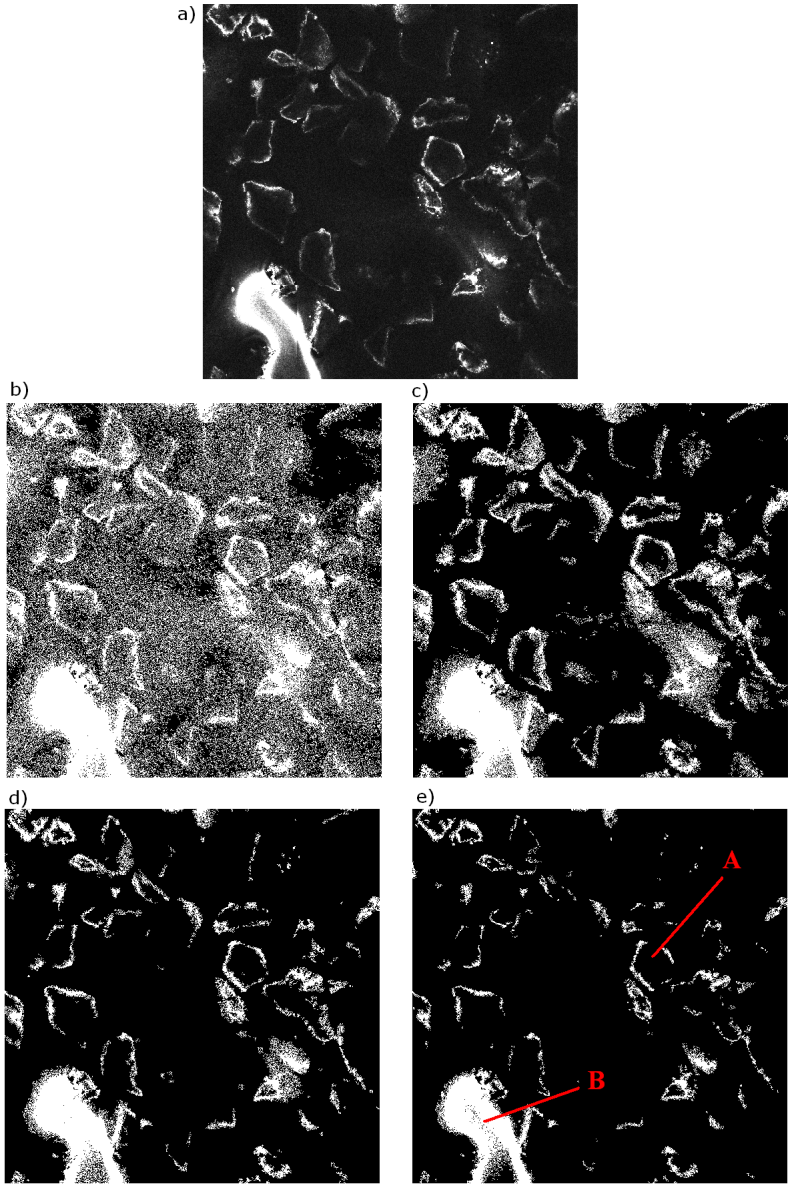

Figure 4.27: Effect of image saturation adjustment on a) original image mapped to b) 0.25, c) 0.35, d) 0.50 and e) 0.75 of the original range

The effect of saturation adjustment on the ability to determine edges is evident in Figure 4.27, with Feature A highlighted as an example. As the saturation range is increased the thickness of the outline of each element reduces, which can lead to some edges disappearing completely. On the other hand, decreasing the saturation range results in more defined outlines of elements, while too small a range results in background noise. Another complication is that due to the high reflectivity of the air-water interface (Feature B) the optimal saturation range is different to that

of the solid substrate. However, as each image may contain both substrate and air-water interface, the same range is kept for each stack of images.

The penultimate stage in image processing is noise reduction. This is achieved by removing groups of inter-connected pixels that contain fewer than a set amount of pixels. This threshold value was set at 50 pixels during testing and the final surface was found not to depend on this value unless saturation adjustment was not completed successfully.

The final stage is identifying the substrate and air-water interface in each image. This is relatively easy by eye, as evident by the broad curve indicating the presence of the air-water interface in Figure 4.27, but is difficult to achieve reliably in software. This is especially true as there are two separate surfaces, which are likely to come into contact at some point.

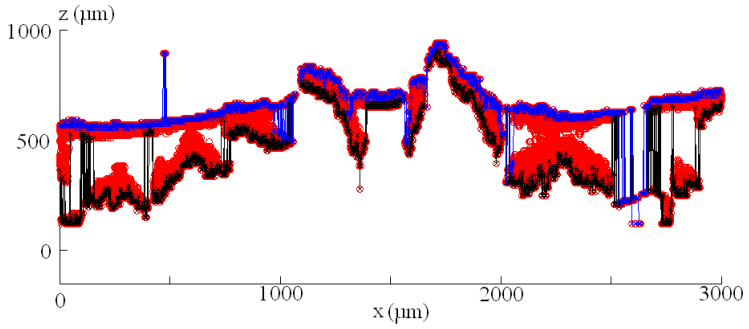

Figure 4.28: 2D slice through 3D profile showing all instances of surface detection (red), identified substrate (black) and identified air-water interface (blue)

Figure 4.28 demonstrates, for one of the worst cases with poor saturation and adjustions, the difficulty in determining each surface. A data point is plotted in red for each case where the algorithm has detected sufficient reflected light for a surface to be present. It is visually clear in most places that the black and blue lines follow the trend of each separate surface. However, it is difficult to determine the details of how the two surfaces interact. A range of approaches were tested in terms of extracting the two seperate surfaces from the raw data, including the development of peak finding algorithms and incorporating ideas from the data processing for PIV, but it was found that the best approach in terms of defining the two surfaces reliably was to use the maximum and minimum height of reflected light at each location. Careful tuning of the saturation adjustment and the noise reduction was carried out on each sample manually to ensure that the algorithm only detected the substrate and air-water interface. It was found that it is easier to

accurately detect the air-water interface, within 1-2 step heights ($\mathcal{O}(10\mu\text{m})$) due to it having a high reflectivity. The confocal microscope images and processing algorithm are capable of accurately determining whether a plastron is present on a surface and providing a clear idea of the location and shape of the air-water interface.

4.3.5 Air-water interface visualisation

Figure 4.29 shows 3D surface plots of the substrate (Magic Sand) and air-water interface for a range of immersion times. The colours of the surface plot are linearly related to the height of the surface. First, it is evident that Magic Sand does support a plastron when immersed in water, with a surface coverage of roughly 80%. The air-water interface typically sits about 400-500μm above the bottom of the substrate, and it appears that the largest elements are what is supporting the interface. These largest elements also appear to protrude above the top of the interface. In each case, it appears that the air-water interface drops rapidly close to each of the larger elements. However, it is postulated that this is due to the prevention of total internal reflection when the air-water interface is too steep and as such, it is just that the interface cannot be visualised, not that it has dropped to the substrate level.

One of the main concerns about the visualisation of the interface and applicability of hydrophobic surfaces to drag reduction was the longevity of the plastron over time. However, Figures 4.29b) and d) show remarkable similarity even though the sample remained immersed and in the same place for an hour. Furthermore, although the sample had to be moved overnight (hence a different viewpoint), the sample remained immersed and Figure 4.29f) clearly shows that the plastron has hardly reduced over a period of 24 hours.

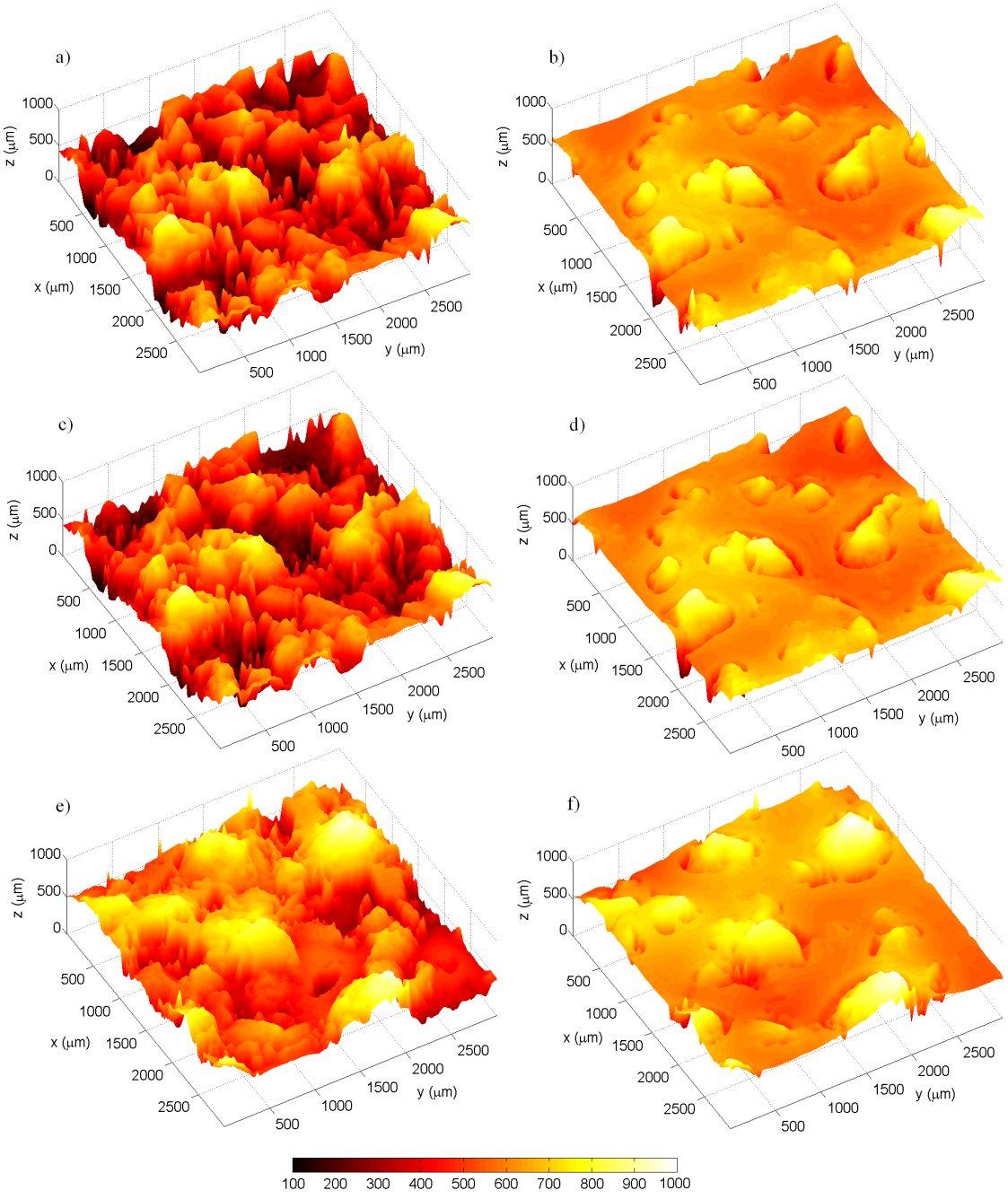

Figure 4.29: Surface plots of solid surface (a,c,e) and air-water interface (b,d,f) after 1 hour (a,b), 2 hours (c,d) and 24 hours (e,f)

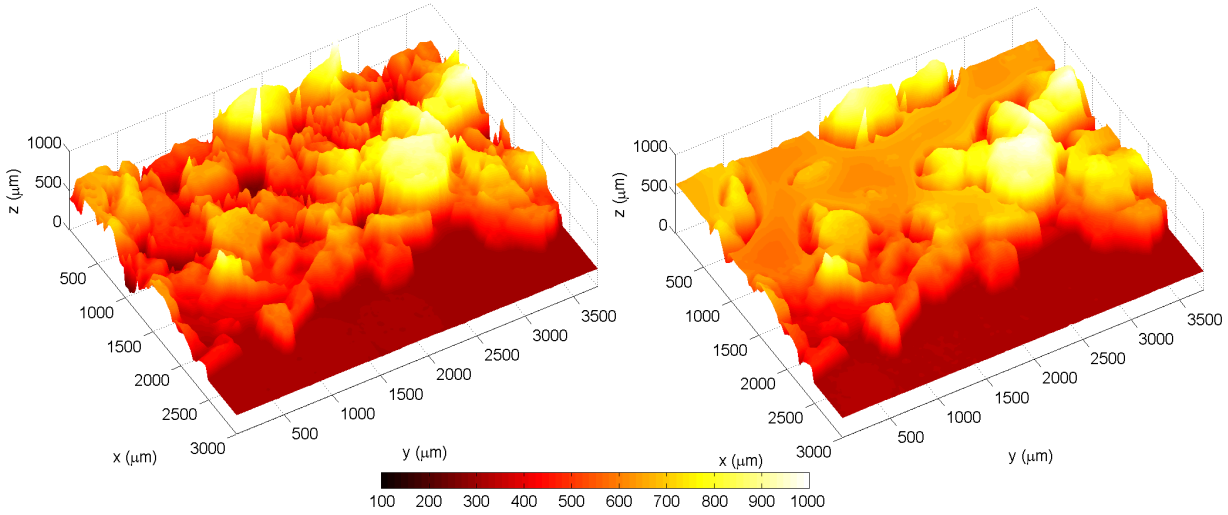

Figure 4.30: Surface plots of solid surface (a) and air-water interface (b) at the edge of the superhydrophobic surface

Figure 4.30 shows the air-water interface and substrate at the edge of a Magic Sand sample. The edge of the sample is clear, about $500\mu m$ from the edge. At this edge the interface appears to follow the roughness elements very closely with nearly vertical edges of the air-water interface at the narrowest points between roughness elements. This suggests that there is a step change at the superhydrophobic boundary and the air-water interface does not extend towards the hydrophilic perspex surface.

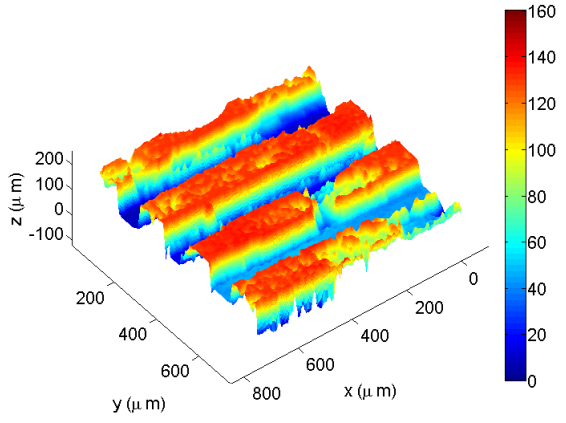

Figure 4.31: Surface plot of solid substrate for ridged surface

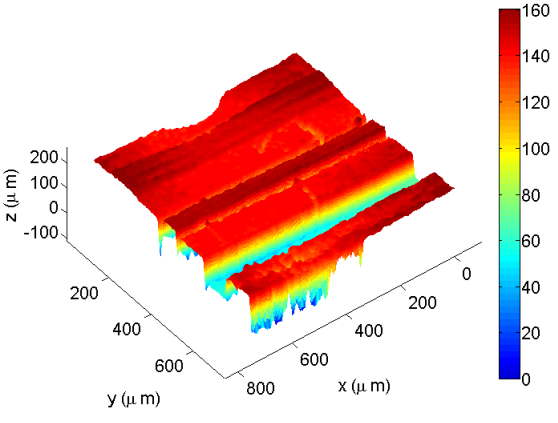

Figure 4.32: Surface plot of air-water interface for ridged surface

The confocal microscope was less successful on the ridged surfaces due to the transparency of the surface and the vertical edges of the ridges, especially attempting to

image the bottom of the ridges through the air-water interface. Figure 4.31 & 4.32 demonstrate that the ridged samples are retaining a plastron, with the air-water interface protruding slightly above the flat tops of the ridges. The irregular shape of the ridges in Figure 4.31 is an artefact of the imaging of these surfaces, as they produce a large amount of out-of plane light when imaging the surface itself. The images also show that one of the three grooves shown is not supporting any air. Insufficient data was available (with 5 areas sampled) to determine whether this wetted groove is an anomaly, or whether similar features appear over the entire surface.

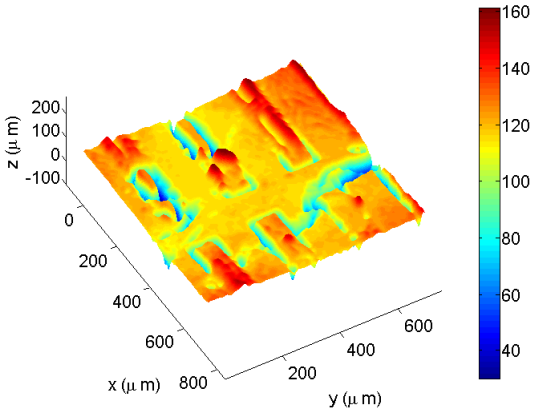

Figure 4.33: Surface plot of air-water interface for ridged surface demonstrating protrusion of bubbles

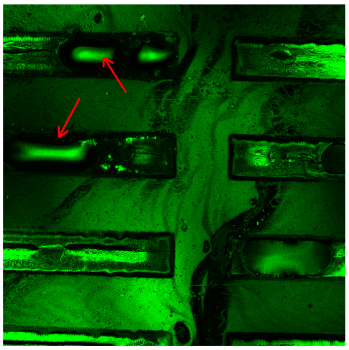

Figure 4.34: Raw confocal image for Figure 4.33 showing interface curvature

The protrusion of the air-water interface above the top of the ridges is clearer in Figure 4.33, which shows the air-water interface over a junction of the primary ridges and a breaker ridge. From inspection of the raw images and observations during the image acquistion it is clear that the plastron is retained within the ridges and although it protrudes $\approx 10 - 30\mu$m past the height of the top of the ridges it does produce an air layer directly above them. Figure 4.34 demonstrates that the protrusions are a real phenomenon and not an artefact of the data processing, with the areas highlighted with arrows having a smooth change in reflectivity casued by the interface curvature. These areas are also visible in Figure 4.33 but their edges, along with the edges of the ridges, are shown as low regions due to the steep interface and substrate respectively being at too oblique an angle to produce a reflection.

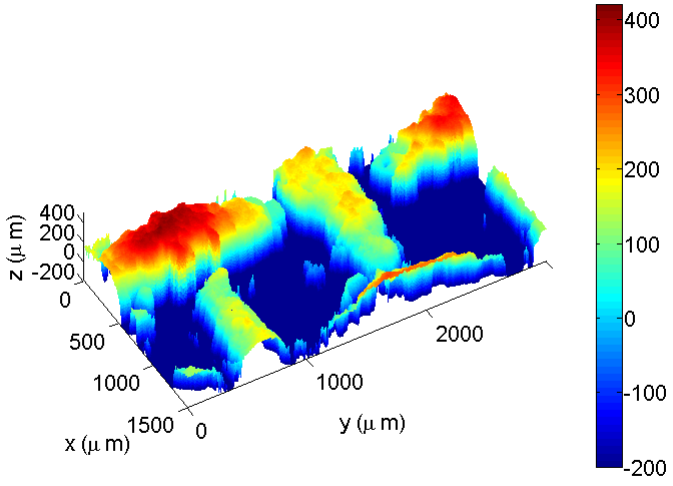

Figure 4.35: Surface plot of solid substrate for CuC

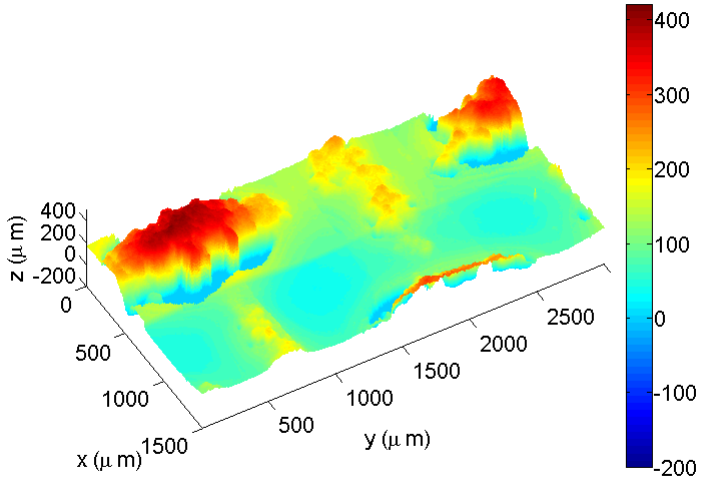

Figure 4.36: Surface plot of air-water interface for CuC

The copper surfaces were successfully imaged, with the regular structure of the coated mesh producing a clear reflection along with the reflection from the air-water interface. The focal length of the lens meant that the second (lower) layer of mesh could not be imaged, but this is insignificant as the images show that the air-water interface follows the surface of the upper mesh. Figure 4.35 & 4.36 show that the air-water interface on the CuC surface is approximately flat and sits approximately 300μm beneath the peaks in the mesh. The plastron appears to curve up sharply towards the highest elements as no reflection was captured in this region. The air-water interface curves slightly towards the mesh in the centre of

the opening, but with the second mesh beneath this layer suggests a plastron with a thickness of $> 300\mu$m. The mesh openings enable large areas of roughly 750μm square with a relatively flat air-water interface, showing that the CuC surface is capable of supporting a high quality plastron.

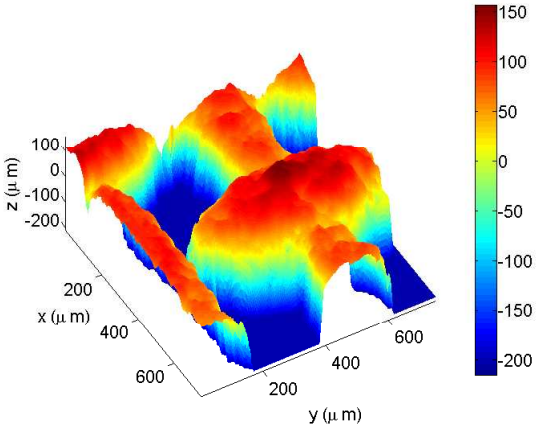

Figure 4.37: Surface plot of solid substrate for CuF

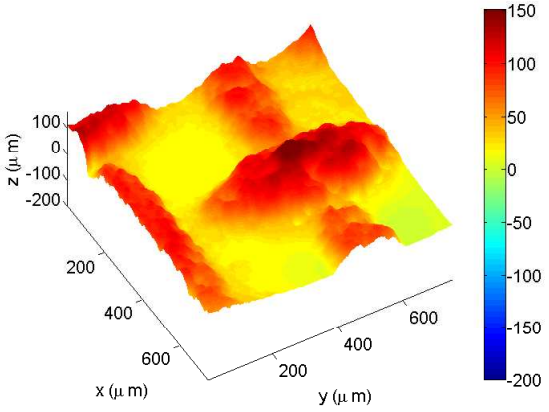

Figure 4.38: Surface plot of air-water interface for CuF

A similar high quality plastron is supported on the CuF surface as shown in Figure 4.37 & 4.38. In comparison to CuC the interface is smoother for the CuF surface, with the edges of the interface showing a shallower connection to the mesh. The interface also shows a curvature towards the substrate, but sits only 150μm below the peaks. The openings in the mesh are smaller than for the CuC surface and hence the discrete areas of air-water interface cover a smaller region. Figure 4.39 demonstrates further the high quality of the plastron, with the interface remaining regular over a large surface area.

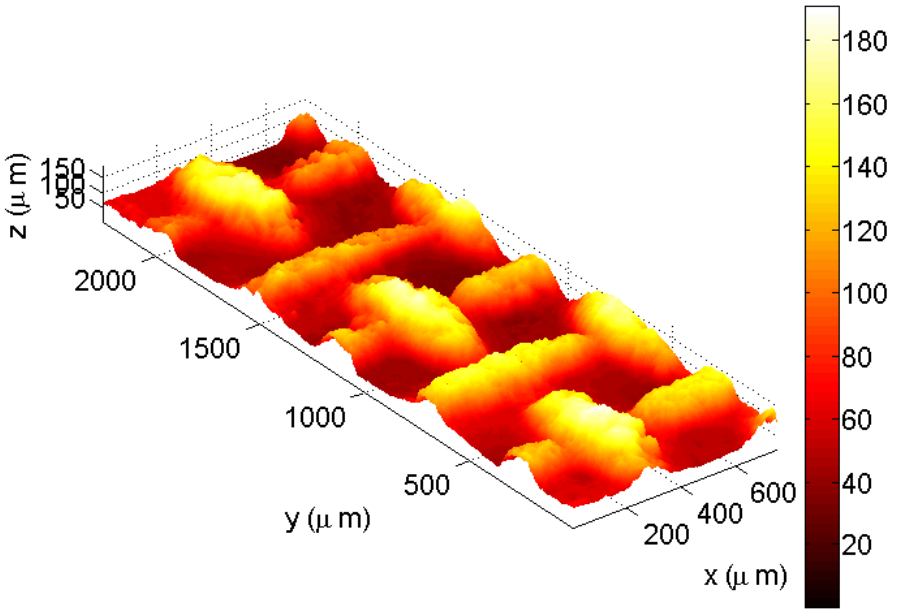

Figure 4.39: Surface plot of air-water interface for CuF over a large surface area

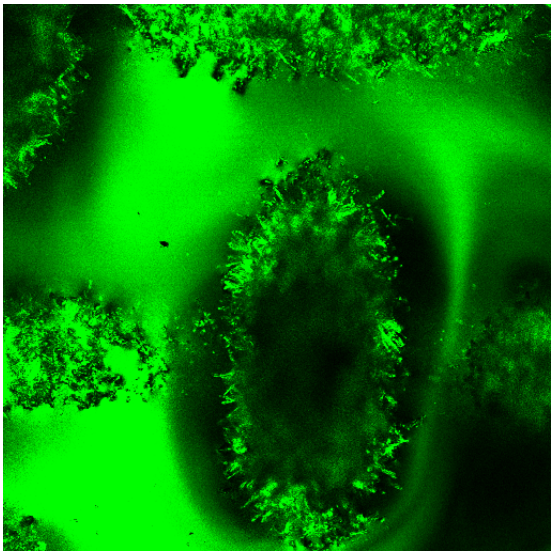

Figure 4.40: Raw confocal image for CuF demonstrating the secondary scale of roughness and interaction with the air-water interface

The secondary scale of roughness apparent on the wetted surface in Figures 4.35 & 4.37 is not a poor surface reconstruction, but is actually the low resolution representation of the nano-flowers caused by the hydrophobic coating. This secondary scale of roughness is clear in Figure 4.40 and helps to support the plastron. At the

upper edge of Figure 4.40 it is clear that the air-water interface is following these smaller scales and that it is intersecting the side of the mesh, rather than passing over the top of the mesh elements.

4.4 Chapter Review

This chapter has explored the current understanding of the design requirements for a superhydrophobic surface in terms of producing a drag reduction. There is a complex trade-off between larger surface features for an increased slip length and ease of manufacturing, and smaller surface features that facilitate the retention of a plastron and ensure a lower hydrodynamic roughness. Three different types of superhydrophobic surfaces have been created with a broad range of surface features and coating techniques. These surfaces were chosen to enable the effect of different parameters of the surface on the potential drag reduction, whilst ensuring that the surfaces were within the available manufacturing limits.

Each of the surfaces were characterised in terms of their roughness, contact angle (see Table 6.1 in Chpater 6) and their ability to retain a plastron. The surface roughness measures allow a quantitative comparison of the relative roughness of each set of surfaces and the measured contact angles demonstrate the relative hydrophobicity of the samples. The ability of a surface to retain a plastron has been examined using a new application of confocal microscopy, providing the first high resolution images of an air layer trapped on a surface, with a quantitative representation of the air-water interface. These images confirm the presence of a plastron on each of the surfaces and also provide information about the position and curvature of the interface. The key conclusions regarding the shape of plastron are that the air-water interface is not flat, but does appear to remain constant over time. The curvature of the interface depended on the geometry of the roughness with for example, random roughness elements protruding above the top of the interface, but structured surfaces showing an air-water interface protruding above the top of the surface. Overall it is clear that the quality of the plastron is a key parameter and that this is a complex interaction between the surface roughness shape, size and the surface chemistry.

Chapter 5

Experimental design & setup

5.1 Introduction

To explore the potential of the surfaces developed in the previous chapter for hydrodynamic drag reduction, an experimental setup is developed for a towing tank where the drag on a flat plate can be directly measured. The primary aims of the experiments are:

- To provide accurate measures of the drag of a variety of superhydrophobic surface coatings.
- To ensure repeatability of the measurements by controlling the test environment.
- To explore the effect of removing the plastron from the surface on the drag.
- To explore other hydrodynamic measures to help develop an understanding of how the flow behaves over the surface coating.

To understand the effect of surface roughness and surface coatings on flow past a surface it is pertinent to first explore the theoretical understanding of flow past a surface, including transition to turbulence in the boundary layer.

5.2 Boundary layer theory

5.2.1 Laminar & turbulent boundary layers

As fluid flows past a surface it is retarded close to the wall due to the no-slip condition and the effects of viscosity. This results in a boundary layer of fluid, within which the velocity starts from zero at the wall and increases to the freestream value at the edge of the boundary layer. The state of the boundary layer can be classified as either laminar or turbulent depending on the Reynolds number of the flow. At higher Reynolds numbers the boundary layer will become turbulent with three-dimensional, unsteady and swirling flow present. A turbulent boundary layer is more resistant to separation and results in a higher skin friction and heat transfer rate than a laminar boundary layer, but the difference in the boundary layer profile also results in a change in the boundary layer growth and increased drag on the surface. Two dimensional analysis of laminar and turbulent boundary layers (Anderson, 2005) can be used to show that the boundary layer thickness (δ) grows in the downstream direction (x) as

$$\delta_L = \frac{5x}{\mathrm{Re}^{0.5}} \tag{5.1}$$

and

$$\delta_T = \frac{0.37x}{\mathrm{Re}^{0.2}}, \tag{5.2}$$

where the subscripts L and T refer to laminar and turbulent flow respectively. A momentum analysis can also be conducted to determine the local skin friction coefficient (C_f), which can then be integrated over the length of a flat plate to calculate the total skin friction coefficient (C_F) (as discussed in for example Anderson (2005)), for both laminar and turbulent flows.

$$C_{FL} = \frac{1.328}{\sqrt{\mathrm{Re}_c}} \tag{5.3}$$

$$C_{FT} = \frac{0.074}{\mathrm{Re}_c^{0.2}} \tag{5.4}$$

The total skin friction coefficient can also be seen as half the drag coefficient (C_D) for a flat plate as there is no pressure drag. The laminar drag coefficient for a flat plate is lower than the turbulent drag coefficient across the entire Reynolds

number range as shown in Figure 5.1, showing that transition from a laminar to a turbulent boundary layer results in an increase in drag (on a flat plate).

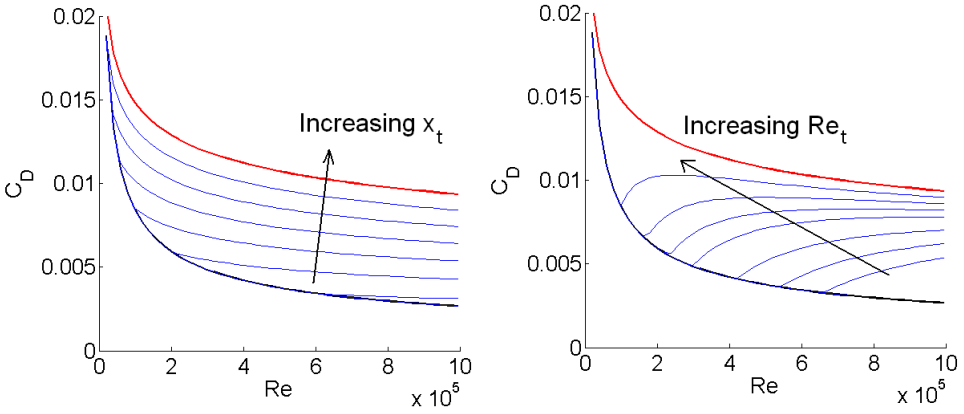

Figure 5.1: Effect of a) constant transition location and b) constant transition Reynolds number on drag coefficient

Transition occurs as disturbances within the flow grow; these disturbances can be caused by roughness, vibrations or high levels of background turbulence. Typically a boundary layer will experience a laminar, transitional and turbulent stage as it develops in the streamwise direction.

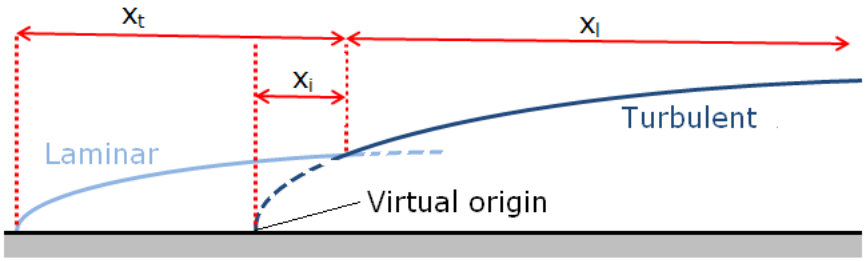

Figure 5.2: Effect of virtual origin on growth of a turbulent boundary layer

The drag can be calculated using equation 5.2, based on the length of the turbulent boundary layer from the virtual origin $(x_i + x_l)$ from which an initially turbulent boundary layer would produce the same momentum thickness as shown in Figure 5.2. The virtual origin location can be calculated relative to the transition location (x_t) (Houghton and Carpenter, 2006) as

$$x_i^{4/5} = \frac{0.037\left(\frac{\nu}{U_\infty}\right)^{0.2}}{0.664\left(\frac{\nu}{U_\infty}\right)^{0.5} x_t^{0.5}}. \tag{5.5}$$

The effect of the transition location can vary across the Reynolds number range explored depending on whether transition occurs at a constant transition location (for example if turbulators are used), or if transition occurs at a constant Reynolds number as shown in Figure 5.1.

5.2.2 Roughness

The size of the roughness elements are typically classified by how far they extend into the non-dimensional turbulent velocity profile (Schlichting, 1960). To achieve this it is necessary to non-dimensionalise the scale of roughness (k) by the friction velocity (u_τ) and kinematic viscosity (ν).

$$k^+ = \frac{ku_\tau}{\nu} \tag{5.6}$$

For standard k-type roughness (Jimenez, 2004) the surface is then classified as hydraulically smooth if $k^+ < 5$ and completely rough for $k^+ > 50$. The effect of roughness on the classic log-law profile was explored experimentally by Nikurasdse in 1933 (as cited in (Schlichting, 1960)), leading to

$$u^+ = \frac{1}{\kappa}\ln\left(\frac{y}{k}\right) + \frac{\Pi}{\kappa}W\left(y/\delta\right) = \frac{1}{\kappa}\ln y^+ + 5.1\frac{\Pi}{\kappa}W\left(y/\delta\right) - \Delta u^+. \tag{5.7}$$

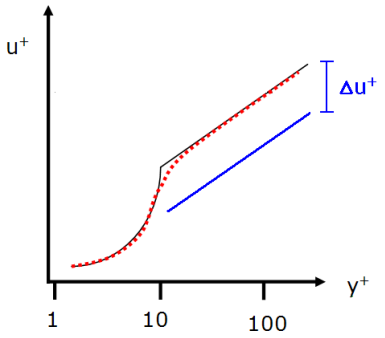

Figure 5.3: Effect of roughness on turbulent boundary layer profile

The effect of roughness is included in the parameter Δu^+ and produces a downward shift of the log-law profile as shown in Figure 5.3. However, the effect of any rough surface will typically depend on the structure and scale of the rough suface, with a universal definition of the roughness length scale (k) difficult to define (see discussion on roughness measures in Section 4.3.1.

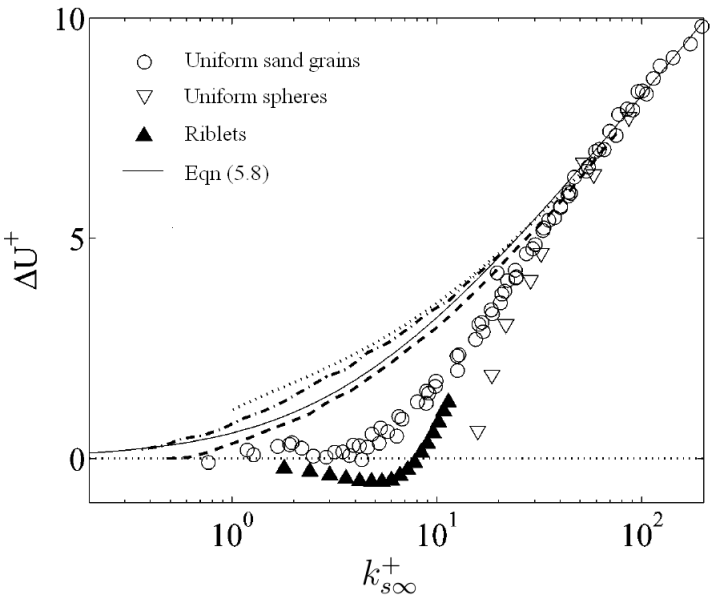

Figure 5.4: Effect of roughness element shape on drag increase, modified from Jimenez (2004), with the dashed lines the industrial surfaces (e.g. wrought iron) of Colebrook (1939)

Figure 5.4 demonstrates that different surface structures produce a variety of transitions between smooth and fully rough surfaces. The data is plotted in terms of $k_{s\infty}^+$ which is the equivalent sand grain roughness in the fully rough regime (such that all the data collapses in this region), with this length scale ($k_{s\infty}$) then being used as a material parameter (Jimenez, 2004). The variations evident in Figure 5.4 are related to the different types of roughness producing varying degrees of sheltering and interaction between roughness elements. Nikuradse's sand grain data and the data for spheres in Figure 5.4 show a much sharper transition than the data for industrial surfaces of Colebrook (1939); this is because the uniform size of the (sieved) sand and spheres ensures that each roughness element reacts in the same way to the other roughness elements as the local Reynolds number is changed (Bradshaw, 2000). The wide range of roughness scales evident on industrial surfaces results in some roughness elements reacting in different ways as the Reynolds number is increased, as effectively any critical roughness height is smeared across the range of roughnesses present on the surface. This was confirmed by Colebrook and White (1937) who demonstrated that the larger roughness elements contribute a disproportionally large effect on the overall drag and can shelter the smaller elements, reducing the local flow velocity and hence their overall contribution. Figure 5.4 also demonstrates the effect of riblets on Δu^+, showing that a drag reduction is possible if the riblets are operated within a certain design window. For *d*-type roughness the outer flow can pass over the tops of the roughness elements due to

circulation within the closely spaced cavities and results in Δu^+ being independent of the size of the roughness in wall units (Cui et al., 2003). For large d-type roughness it is has also been demonstrated that the circulation within the cavity can produce a reduction in the total drag of the surface (Tani et al., 1987; Choi and Fujisawa, 1993).

Overall, Colebrook (1939) suggested that a *universal* interpolation formula could be used to determine the effect of a rough surface in the transition regime, once the equivalent sand grain roughness had been determined in the fully rough regime. This equation forms the basis for the traditional Moody chart for pipe flow.

$$\Delta u^+ = \frac{1}{\kappa} \ln\left(1 + 0.26 k_{s\infty}^+\right) \tag{5.8}$$

This can then be used to calculate the local skin friction coefficient producing the following equation (White, 2006).

$$\mathrm{Re}_x = 1.73 \left(1 + 0.3\mathrm{Re}_x \left(\frac{k_{s\infty}}{x}\right) \left(\frac{C_f}{2}\right)^{0.5}\right) \exp\left(\kappa \left(\frac{2}{C_f}\right)^{0.5}\right) \times \ldots$$
$$\left[\left(\frac{2}{C_f}\right)\kappa^2 - 4\kappa\left(\frac{2}{C_f}\right)^{0.5} + 6 - \frac{0.3\mathrm{Re}_x \left(\frac{k_{s\infty}}{x}\right)\left(\frac{C_f}{2}\right)^{0.5}}{1 + 0.3\mathrm{Re}_x \left(\frac{k_{s\infty}}{x}\right)\left(\frac{C_f}{2}\right)^{0.5}} \left(\kappa\left(\frac{2}{C_f}\right)^{0.5} - 1\right)\right] \tag{5.9}$$

This equation is implicit in terms of C_f, Re_x and k and is solved numerically in this report using the Newton method. Equation 5.9 is used to calculate the local skin friction coefficient for the transitionally rough case. The local skin friction coefficients are then integrated over the surface to calculate the total drag coefficient.

Another important point to consider regarding roughness is that it can have an indirect effect on the drag of a flat plate since it influences the transition location. Surface roughness can influence transition in two ways: generating additional disturbances within the flow field and altering the mean velocity profile so that disturbances are amplified faster (Merkle, 1974). Modifying the transition location results in a change in the effective turbulent boundary layer length and hence the overall drag. This can be detrimental to experiments on surfaces with different

roughness as a change in drag could be attributed to either a change in transition location or a change in k^+.

Surface roughness will clearly increase the level of disturbance in the flow and thus typically produce an earlier transition. In its own right this is not as such a source of error, but it does make comparisons between surfaces difficult. In these experiments surface roughness is required to retain a plastron on a superhydrophobic surface but the roughness will produce an earlier transition if the roughness is upstream of the transition location, and furthermore the transition location will then depend on the size and structure of the roughness. As detailed later it was found to be important to trip the flow to be turbulent well ahead of the test plates, with care taken to ensure that the trips are sized to produce *correctly* stimulated flow (Erm and Joubert, 1991).

A final consideration regarding the effect of roughness is the relaxation of the boundary layer as it passes over a step change in roughness such that the outer flow convects further downstream before being influenced by the change in roughness. Antonia and Wood (1975) demonstrated that this results in an internal boundary layer growing from the change in roughness as shown in Figure 5.5.

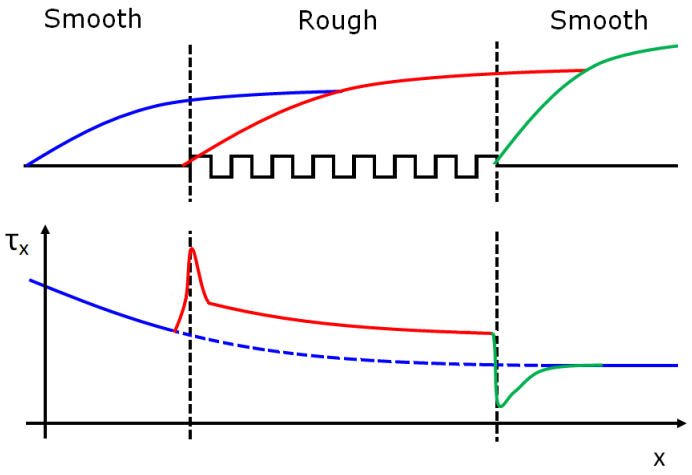

Figure 5.5: Effect of boundary relaxation over smooth-to-rough and rough-to-smooth transitions

The upstream roughness influences the outer layer up to $20 - 100\delta$ downstream of the step change, and has been confirmed experimentally (Antonia and Luxton, 2004; Loureiro et al., 2010) and analytically (Deaves, 1981; Chamorro and Porte-Agel, 2009), with the near wall region relaxing to the new surface roughness much faster (Taylor et al., 1993a). Figure 5.5 also demonstrates the initial overshoot of the wall shear stress at the junction between rough and smooth surfaces (Taylor

et al., 1993a; Efros and Krogstad, 2011), which is due to the sudden retardation (for smooth-to-rough) and acceleration (for rough-to-smooth). This discussion is important for the use of hot film gauges as the gauges themselves are typically hydraulically smooth, such that the sensor is then in the immediate vicinity of a rough-to-smooth junction. A hot film gauge used to measure the effect of roughness should thus produce a (counter-intuitive) reduction in the measured shear stress.

5.3 Experimental design

The experimental facilities that were available for use in this study are:

1. Plint Flume - 30cm square recirculating flume, flowspeed up to 0.5m/s
2. Lamont Towing Tank - 30 x 2.4 x 1m (LxWxD) with a carriage speed of up to 2.5m/s
3. Southampton Solent University Towing Tank - 60 x 3.7 x 1.8m (LxWxD) with a carriage speed up to 4.0m/s

Figure 5.6: Southampton Solent Towing tank with carriage and acquisition equipment

Experiments were initially conducted in both the Plint Flume and Lamont Towing Tank but it was found that due to problems with flow speed control and carriage control respectively, both had issues with repeatability. The majority of the results presented in Chapter 6 were acquired at the Southampton Solent Towing Tank unless otherwise stated. This had advantages of a higher speed range and good speed control, resulting in improved repeatability.

5.3.1 Initial design

The primary aim of the experimental tests is to measure accurately the friction drag of a variety of surface coatings. This introduces a range of design requirements to be able to draw conclusions from the results obtained. The first is to maximise the contribution of the viscous drag to the overall drag so that the effect of the surface coating on the drag measurement is maximised. It was therefore decided early on in the project that the experimental setup would consist of a flat plate at zero incidence to the flow direction. Two different flat plates were designed and manufactured: Plate A and Plate B. Plate A was the first design iteration and is discussed in detail first, followed by the reasons for designing a second plate and finally a detailed discussion of the features of Plate B.

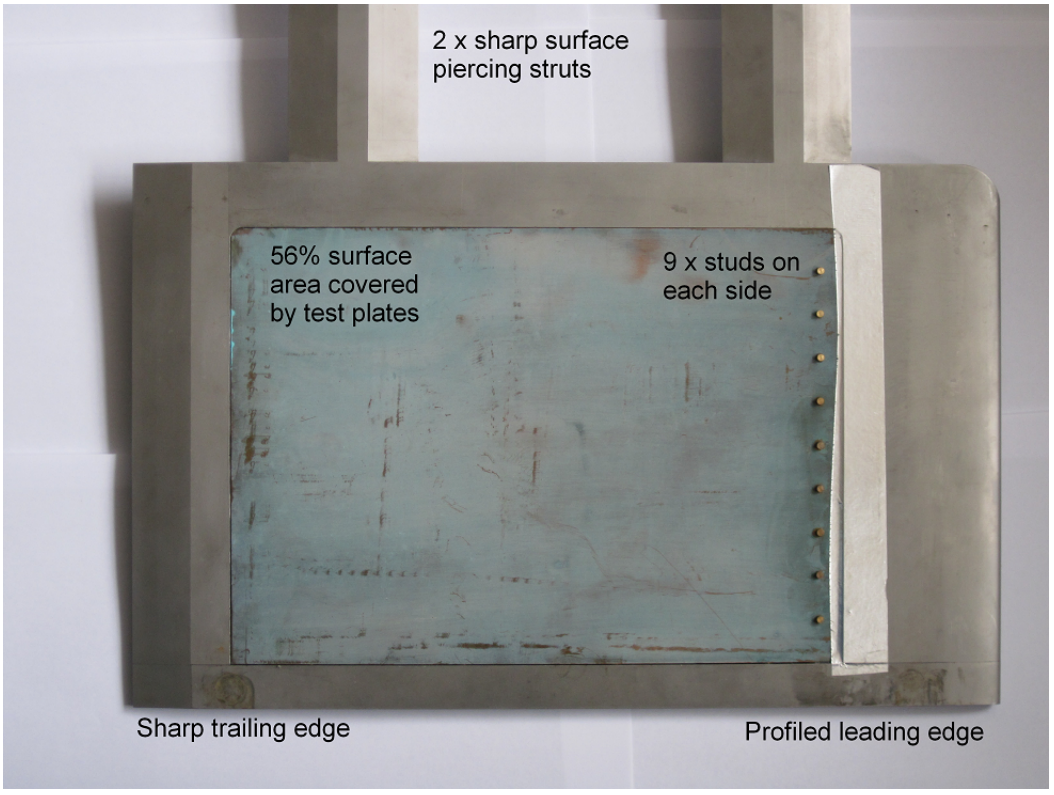

Figure 5.7: Plate A with annotations showing key features

The design of Plate A was focused around providing a consistent platform from which the surface coatings could be explored; from testing one surface to another it is necessary to ensure that the other contributors to drag are constant so that any differences in drag can be attributed solely to the change in surface coating. Therefore it was necessary to ensure that the leading edge and trailing edges,

supporting struts and remaining uncoated body not only provide a minimal contribution to the total drag but also are consistent from run to tun. To achieve this the leading edge was designed to have a super-elliptic leading edge such that the leading edge has continuous curvature, minimising the chance of leading edge separation or transition enhancement (Narasimha and Prasad, 1995). The trailing edge was designed to have a finite thickness to provide a constant separation location from the aft of the body and ease the manufacturing process. The main body of the plate was supported on surface piercing struts. This allows the body to be below the water surface, reducing the wave drag produced and allowing sensors and electronics to be above the water surface. The struts have a sharp leading and trailing edge to minimise the wave and spray drag components. The entire body and supporting struts was machined out of a single piece of stainless steel which had been lapped to a thickness of 10mm. This process ensured that the steel was completely flat and had minimal residual stresses to prevent warping at later stages. The overall size of the plate was dictated by the difficulties in producing hydrophobic samples over a large surface area. A compromise was made at 280 × 200mm to allow relatively small samples whilst producing a measurable drag.

The plate was manufactured from stainless steel to meet the requirements for a high stiffness whilst being inert in the relatively corrosive environment of water. A thickness of 10mm was chosen as a balance between being thinner for low weight and low pressure drag and being thicker to ensure low flexibility and to provide room for replaceable surfaces.

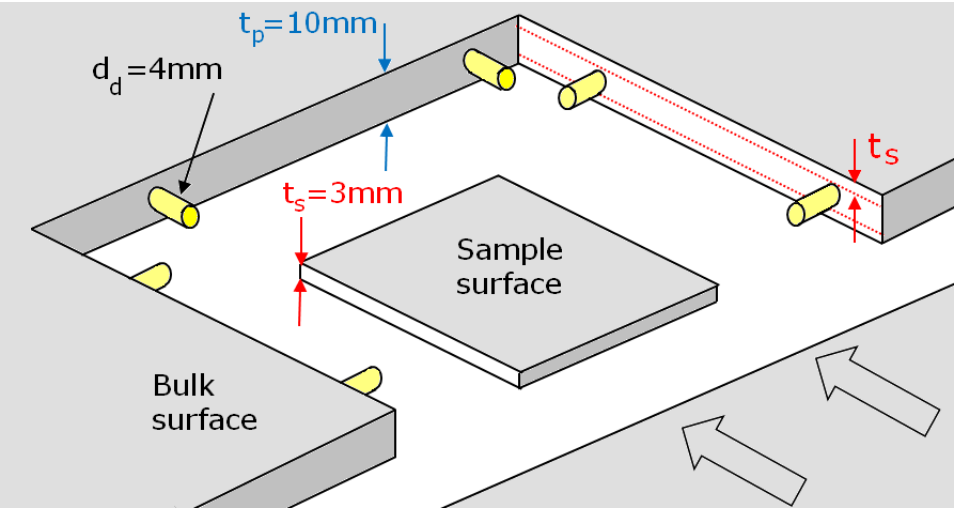

Figure 5.8: Plate A mounting mechanism for different surface samples

The plate holder is designed to allow the interchange of part of the surface on both sides. Figure 5.7 demonstrates that 56% of the surface area on each side is removable, allowing for the surface properties to be modified without affecting any other part of the experimental setup. The plate was designed to hold the sample surfaces in by adjusting the removable bottom edge to act in compression on the edge of the samples (as shown by the arrows in Figure 5.8) while the height of the sample surface in relation to the bulk body of the plate can be adjusted by modifying the diameter of dowels (d_d) depending on the thickness of the sample (t_s).

Plate A was tested in both the Lamont and Solent towing tanks and initially produced results with poor repeatability. Although the repeatability issues were largely overcome (see Section 5.6) there were some issues with the design of Plate A that were considered to be detrimental to the overall testing program. These issues were:

- Plate A is relatively small and produced drag values in the range 0.1-10N. Although sufficient resolution was available to capture the high drag values, the smallest drag values were not measured accurately.
- The transition location was found to vary greatly from run to run and was presumed to be due to background currents in the tank. This effect was reduced by the introduction of turbulators but was still an issue due to the small streamwise length of the plate.
- The sample mounting mechanism did not work as envisaged. To ensure that the samples were held in place they had to be stuck down with mastic. This was found to be inconsistent and time consuming.
- The samples were found to be too flexible and deformed producing a curved surface when they were mounted.

A final point that was noted during this initial testing phase was that the plastron was affected by the buoyancy of the air. As the plate was in a vertical configuration the effect of buoyancy was to push the majority of the plastron up to the top edge of the sample. To overcome these issues a second plate (Plate B) was designed and manufactured.

5.3.2 Design modifications

The key design requirements of Plate B were to produce a larger overall drag value with increased repeatability. One of the main factors that can be modified to produce a larger drag through an increase in viscous drag is the total surface area. It was decided to increase the streamwise length of the plate so that the transition location would have a lower effect on the drag. Furthermore, a blank surface was included upstream of the transition location (determined from hot film measurements on Plate A) to ensure that the sample surfaces also have no effect on the transition location.

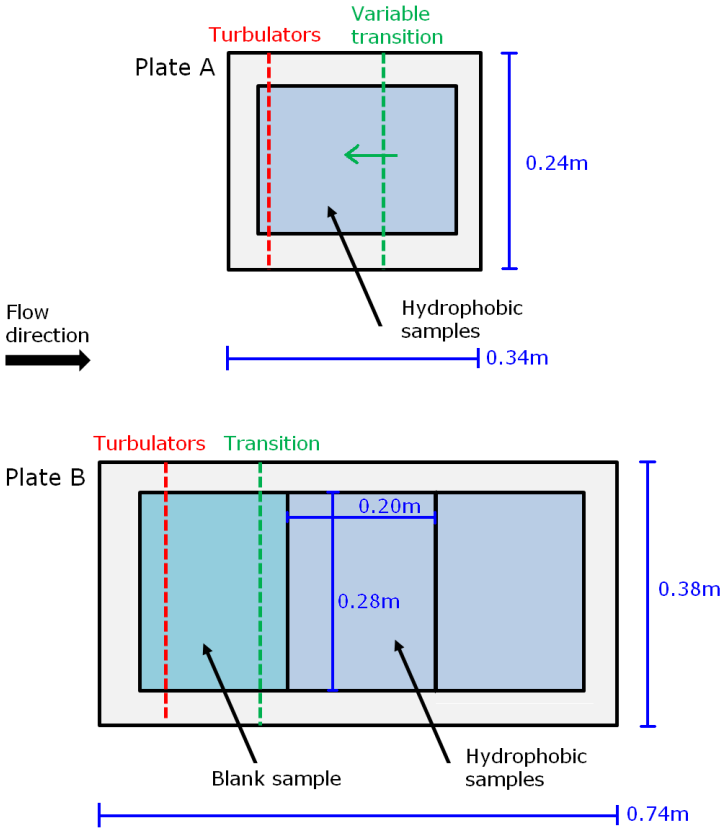

Figure 5.9: General design differences between Plate A and Plate B

Two different configurations were explored in terms of material and structural design. The first was to continue using stainless steel and the second was to use a plastic such as Delrin or PVC. The primary design advantage of the plastics is that they are lighter and easier to machine, which would result in a quicker experimental procedure and cheaper and quicker manufacture of the plate. The disadvantage of the plastics is that they are six times weaker and to achieve a similar level of

stiffness to the stainless steel plate the thickness needs to be increased to 25mm from 10mm. This increased thickness would result in a weight reduction of up to 30% in comparison to a stainless steel plate and facilitate attachment of the struts and sample surfaces due to increased space for screws. However, it would also result in an increased pressure drag component which would be independent of the sample surface coatings. Overall it was considered that a larger stainless steel plate was the optimal design; the issue of mounting a 20kg plate over 1.8m of water was overcome using a flotation device. Using the basic theory that buoyancy is equal to the weight of displaced fluid, it was calculated that the volume of buoyant material (B) required depends on the volume and density (ρ_{SS}=stainless steel, ρ_p=perspex, ρ_w=water) of the perspex plate(p), struts (s) and hydrophobic samples (HS).

$$V_B = \frac{\rho_{SS}\left(V_p + V_s\right) + \rho_P V_{HS} N_{HS} - \rho_w\left(V_p + V_s + V_{HS} N_{HS}\right)}{\rho_w - \rho_B} \tag{5.10}$$

The total amount of water that needs to be displaced to support the plate holder is just under 20L. A safety factor of 1.5 is introduced and a buoyancy aid was built to displace 30L of water, using six 5L bottles.

The plate was designed to be mounted to the underside of the carriage using a similar arrangement of surface piercing struts to Plate A. However, due to the plastron buoyancy effect noticed on Plate A it was decided that the design of Plate B would include removable struts so that the plate could be mounted in both a vertical and horizontal configuration.

A range of potential mechanisms were explored for mounting the hydrophobic samples to the plate. The new mounting procedure needed to be secure, adjustable, repeatable and quick. Furthermore, the mounting mechanism needed to have minimal impact in the hydrophobic surface and not protrude above the flat bulk of the body of the plate. Three candidate mounting systems were explored in detail, but eventually both a magnetic mounting system and velcro were discarded due to being too insecure and too inaccurate respectively. The final design included staggered tapped screw holes in the central body of the plate, ensuring that the samples could be attached securely and accurately. The screws were countersunk to ensure that the top surface of the sample is flat and shims could be included to modify the height of the sample with respect to the main body of the plate.

Plate B was manufactured within the University of Southampton by the Engineering Development and Manufacturing Centre (EDMC) although quotes were also

obtained from external companies. A single piece of stainless steel was machined on a computer-aided mill. The plate was confirmed to be flat within 0.5mm over its entire length and the depth of the recessed pocket accurate to 100μm.

5.3.3 Validation

To validate the design of Plate B numerical simulations were conducted. The simulations explored whether the new design is capable of producing an increase in drag in comparison to Plate A and that a slip length of a feasible magnitude will produce a measurable effect on drag. The simulations were conducted in FLUENT using a 2D representation of the plate, with the geometry accurately representing that of Plate B, with a super-elliptic leading edge and finite trailing edge. The Reynolds numbers of the simulations were chosen to match the higher flow speeds in the towing tank (2-4m/s) where the flow over the plate is known to be fully turbulent. The flow is solved as incompressible, isothermal and steady state using the RANS equations with the addition of the standard $k-\epsilon$ turbulence model. A range of meshes were tested to determine a grid independent solution and a different wall normal spacing was used for each Reynolds number to ensure an optimal value of $y_1^+ \approx 35$ for the use of wall-functions (Fluent Inc., 2005).

The simulations demonstrated that the drag of Plate B was approximately three times larger than that of Plate A, with a range of drags from 5-30N[1], which matches well to the maximum operating range of the sensor ($D_{\max} = 38$N). The results also show that the drag of the flat plate can be split into contributions from 85% viscous drag and 15% pressure drag, showing that the chosen design of a flat plate does well to maximise the viscous drag contribution.

[1]The lowest speeds that were originally explored using Plate A were not tested for Plate B as the measured drag values were found to be too small to measure accurately

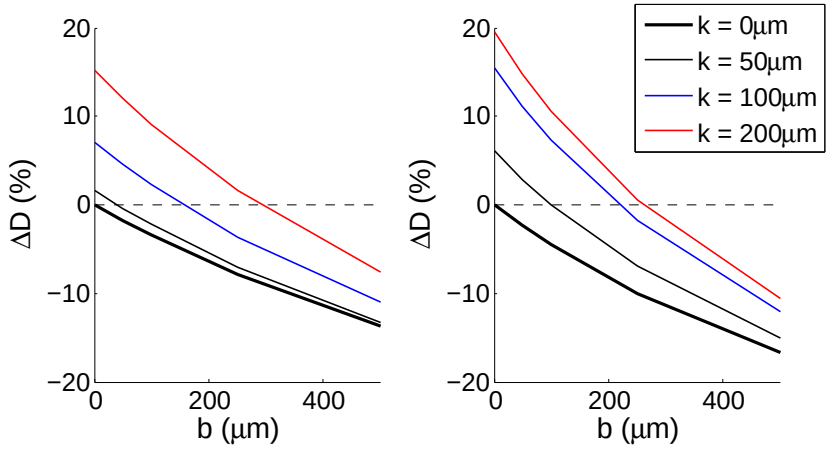

Figure 5.10: Effect of equivalent sand grain roughness (k) and Navier-slip length (b) on the drag of the flat plate simulated using FLUENT a) 2m/s b) 4m/s

Figure 5.10 shows the effect of surface roughness and slip on the drag of the plate. Increasing the effective sand grain roughness results in an increase in the drag whilst increasing the slip length acts to reduce the drag, with a measurable drag difference (ΔD) of up to 20%. A combination of roughness and slip is shown to produce a balance between two opposing effects. This highlights the importance of minimising the hydrodynamic effect of the roughness whilst attempting to maximise the roughness scale to increase the plastron thickness and hence the slip length. The simulations suggest that it is possible to add roughness to a surface, increasing the drag and then add a hydrophobic coating to reduce the drag below the original, smooth level of drag. This also highlights the importance of measuring the drag in both the hydrophobic and wetted state; otherwise a rough hydrophobic surface may be tested and in producing an overall drag increase be discarded completely as ineffective, however the surface may still be producing slip but insufficient to overcome the effect of roughness.

The numerical results are also useful in determining whether an effect would be visible using interrogation techniques such as PIV, LDA and hot films to explore the flow field in detail. A boundary layer profile would help to determine the potential drag reduction mechanism, whilst a wake study would likely corroborate any measured change in drag. Numerical boundary layer studies suggest that the effect of hydrophobicity is confined within the near wall region where the results depend highly on the wall location, which is difficult to accurately determine (especially for rough surfaces). This will also be further complicated by the high reflectivity and unevenness of the plastron which would make using visual techniques close to

the plastron difficult. However, Figure 5.11 demonstrates an investigation of the effect of slip in the wake; the velocity deficit is reduced by slip and shows that a measurable effect of the hydrophobicity is apparent at locations relatively far downstream.

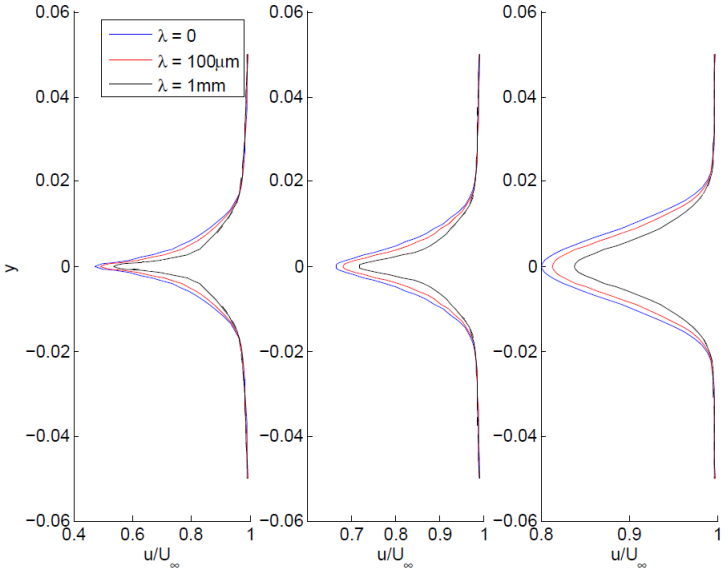

Figure 5.11: Effect of slip length on the wake of Plate B from Navier-slip simulations at streamwise locations of $x/c = 1.01$, $x/c = 1.35$ and $x/c = 2.03$ from the leading edge

Figure 5.12 demonstrates the effect of surface roughness and slip on the shear stress distribution along the streamwise length of the plate. The dashed lines designate the start ($x/c \approx 0.38$) and end ($x/c \approx 0.9$) of the sample area, with the third showing the start of the chamfered trailing edge ($x/c \approx 0.95$). These results agree with the research reported in Section 5.2.2 in that immediately after the sample area the boundary layer is adjusting to the new surface. In each case there is an overshoot of the shear stress, for example the rough surface shows an increased τ_x over the sample area, but at the end of the sample shows a relative decrease in comparison to the smooth surface in the immediate vicinity of the change in roughness. A relaxation in the opposite direction is observed for the first time for a surface with slip, suggesting that a hot film gauge placed downstream of the sample would show a misleading increase in τ_x.

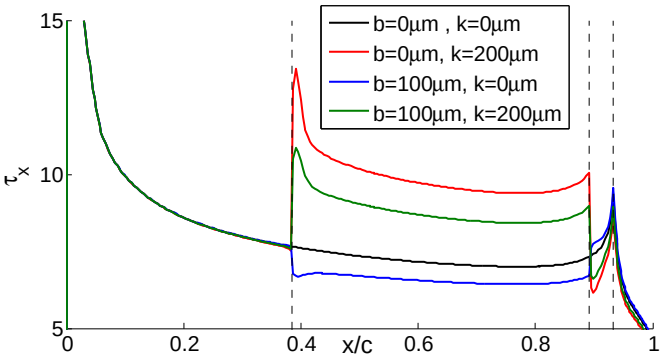

Figure 5.12: Numerical results for the effect of roughness and Navier-slip on the shear stress at the wall on the flat plate

These numerical results have demonstrated that if sufficient slip can be generated at the surface using a superhydrophobic coating, the effect of the coating should be visible in the drag measurements, boundary layer profile (although difficult to measure), wake profile and local shear stress profile. Facilities were unfortunately not available to conduct PIV or LDA in water during this study, so boundary layer and wake profiles could not be explored. However, a combination of drag measurements, shear stress measurements and an appreciation of the boundary layer relaxation process would provide a useful insight into the potential drag reduction process.

5.4 Data processing

5.4.1 Data recording & signal processing

The signal from each of the sensors has to pass through numerous stages of conditioning before it is able to be passed to the computer to be recorded and stored. In the current setup the main stages through which the signal must pass are:

- Sensors
- Amplifier with gain and offset
- Low-pass filter
- Analogue-to-digital converter
- Recording software (Lasso™)

- Post-processing

The force blocks used to measure lift and drag in the experiments work using a Linear Variable Differential Transducer (LVDT). The LVDT produces an analogue signal with an infinite resolution. However, when the signal is passed to the computer it needs to be digitised by the Analogue-to-Digital Converter (ADC). The number of output values is set by the bit level of the ADC used. In these experiments a 16-bit converter is used, resulting in 65,536 (2^{16}) discrete output levels. The resolution error is then determined by dividing the output voltage range by the number of output levels. Figure 5.13 shows the effect of digitising an analogue signal with a large resolution error.

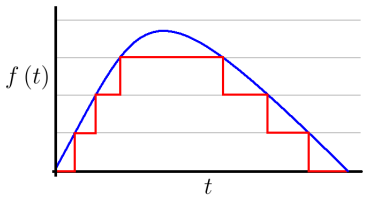

Figure 5.13: Conversion of analogue to digital signal

This clearly shows the importance of minimising the resolution error. Assuming that the bit level of the ADC converter is fixed, the only way of affecting the resolution error is with the settings of the amplifier. The amplifier allows a gain (G) and offset (ϕ) to be applied to the analogue signal before the conversion takes place. To minimise the resolution error the gain and offset should be used to maximise the use of available output voltage range. For example consider an 8-bit/256 level converter with a 10V range which gives a resolution error of 0.039V. If an analogue signal with zero gain has an amplitude of 1V, then the resolution will only allow the signal to be recorded in 4% steps. However if the gain is increased by a factor of 4 then the signal will cover a wider region of the possible output range and reduce the steps to about 1%.

In the flat plate experiments it was found that there were quite large oscillations in the force values during the run. Therefore the gain and offset were adjusted so that at the maximum expected load the signal used approximately 75% of the available range. This ensures the minimum resolution error whilst preventing the signal from going out of range during oscillations or zero shifts. However, the use of a gain can also be detrimental on the signal because it will amplify any background noise as well as the desired signal. The base amplitude must be sufficiently large that it dominates any background noise and gives a large Signal-to-Noise Ratio (SNR). If

the SNR is too small the signal will be obscured by random fluctuations. Therefore, the amplitude of the signal needs to be maximised whilst the background noise needs to be minimised. One detail that affects the base amplitude of the signal is the working range of the LVDT. Initial experiments were conducted with a LVDT with a working range of 3mm, but this was changed for an LVDT with a working range of 1mm. The smaller working range LVDT produces a larger voltage signal for a given displacement, which increases the SNR.

It is also necessary to consider the effect of ground fluctuations and ground loops on the signal. Ground fluctuations can be minimised by the use of dual-ended inputs, that is, measuring a signal and a ground level for each channel. Any fluctuations in the ground should affect both signals and thus disappear when one signal is subtracted from the other to obtain the final signal. Another consideration is the effect of ground loops on the system. This occurs when parts of separate circuit are designed to be at the same potential and are then connected (most commonly ground). In most cases the wire connecting the circuits to ground will have zero potential drop across it, however if a current is induced in it a potential drop will occur, which could have different effects on the two circuits connected at this point. To minimise these effects it is best to carefully consider how each circuit is grounded and ensure that the signal has a high amplitude as discussed above. While testing at the Solent and Lamont tanks, the only issue with ground loops has been related to the triggering of acquisition and was fixed by connecting the AC and DC ground levels.

Ideally, background noise should be minimised to an extent that it is no longer an issue. Unfortunately, background noise will inevitably appear in the system, for example through background vibrations of the carriage. One way of reducing the background noise is to use a relatively low sample rate. However, this can result in an erroneous representation of the signal and it is better to have a high sample rate to increase the number of data points in a run. Increasing the number of data points (N) increases the confidence in the mean of the data set. This is quantified by the standard error of the mean ($\sigma_{\bar{x}}$) (Kirkup, 1994), which clearly decreases as N increases according to

$$\sigma_{\bar{x}} = \frac{\sigma}{\sqrt{N}}. \tag{5.11}$$

The level of uncertainty can be calculated based on the z-score of the confidence limit multiplied by $\sigma_{\bar{x}}$ (Field, 2005). Taking a 95% confidence limit gives an

uncertainty in the mean value of $\pm 1.96\sigma_{\tilde{x}}$. The importance of having a relatively high sample rate is increased when running the carriage at high speed. At the highest speed the time taken to traverse the length of the measured run is about 6 seconds. Therefore a sample rate above 35Hz should be chosen to ensure that the number of data points always remains above 200.

An important consideration to take into account for selection of a sampling frequency is the frequency of the power supply. Power supplies operate at a *constant* frequency and can produce unwanted background noise at these frequencies. Therefore it is important to avoid sampling rates around 50Hz and higher harmonics. The final constraint on the sample rate is that it should ideally be a prime number. A prime number sample rate is ideal as it has no lower frequency harmonics meaning that any key frequencies are easier to identify. The use of a filter and sufficiently high sample rate should negate any issues, but as one is free to choose the sample rate a prime is used wherever possible. In this case, the first prime above 35 is chosen and therefore the sample rate is set as 37Hz.

The Nyquist Sampling Theorem (Smith, 1997) is used to ensure that the sampling rate is sufficiently high to prevent the effects of aliasing. This theorem requires the sample rate to be at least twice that of the highest frequencies in the signal. In the majority of tank tests a 10Hz filter has been used, thus requiring a sample rate of at least 20Hz. In these experiments a Chebychev low-pass filter has been used due to availability. The data collected when using the hot films was sampled at 1kHz, which was set based on the maximum frequency response of the films and the Nyquist Sampling theory

The drag and side-force on the flat plate are measured using two force blocks. To ensure that there is no coupling between the drag and side force the two force blocks are aligned at 90° to each other. The force blocks work on the principle that the deflection of a beam under load will linearly depend on the load applied [2]. Each force block has four struts in parallel which then deflect under load. The struts on the drag block have been machined down so that they are thinner than the side force block. This means that the struts will deform more under a given load, which increases the sensitivity. The deflection of the struts is measured using an Linear Variable Differential Transducer (LVDT). The signal passed to to the recording software is hence a measure of the physical displacement of the beams, modified by the gain in the amplifier. As the LVDT and deflection of a beam follow

[2]Assuming that the deflection is elastic. The force blocks have mechanical stops to prevent the load causing permanent deformations

a linear relationship, the force blocks can be calibrated using a 2-point calibration. Figure 5.14 shows that a calibration procedure of adding a load of 0kg and 1kg and applying a linear fit, can be used to accurately predict any mass in the range 0-2kg.

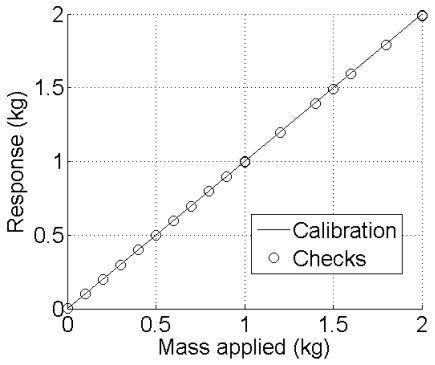

Figure 5.14: Calibration check of force blocks

The error in the calibration check is greatest (0.6%) when the smallest masses are used as they will have the greatest variation in mass. The error in the calibration is within the precision of the scales used to measure the masses initially. The calibration curve can also be extrapolated to twice the initial calibration range.

During the tank tests, weights are used which have been measured as 10N. This 10N weight is specific to the location of the tank and takes into account the variation of the acceleration due to gravity around the world.

5.4.2 Drag component isolation

In the theoretical analysis of the drag on a flat plate it is assumed that the flow is parallel to the plate, or that equivalently the angle of attack (α) is zero. To match the experimental results to theory it is therefore essential to ensure that in the experiment $\alpha = 0$.

The experimental setup allows α to be varied about the quarter-chord position of the flat plate. The force blocks are also located at the quarter-chord position because this is the theoretical Centre of Pressure (CoP). The force blocks remain in the same axis as the flat plate and thus always measure the lift (L) and the drag (D). However, these values need to be corrected if there is any incidence on the plate due to three effects:

1. Misalignment of velocity and drag
2. Lift induced drag
3. Reduction in incident velocity component

If the flat plate is at some angle of attack, the drag measured by the force blocks (D) will actually not be in the same direction as the movement of the carriage down the tank. The drag on the carriage in the axis of motion will be F_X, whilst the lift or sideforce experienced will be (F_Y), with the force vectors rotated about the CoP.

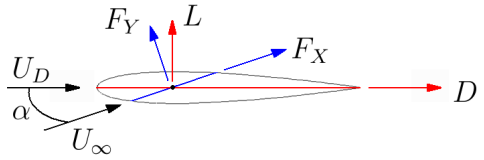

Figure 5.15: Alignment of force vectors

Ultimately, the values required are F_X and F_Y as these are values in the coordinate system aligned with the tank. To convert between the measured axis and this axis the following relationships are used.

$$F_X = D\cos\alpha + L\sin\alpha \tag{5.12}$$

$$F_Y = L\cos\alpha - D\sin\alpha \tag{5.13}$$

Finite wing effects also introduce lift induced drag (D_i) when a flat plate is at an angle of attack. The lift-induced drag coefficient (C_{Di}) can be estimated using the following equation where the aspect ratio is defined as $A_R = (span)^2/S$, where S is the planform area.

$$C_{Di} = \frac{1.1C_L^2}{\pi A_R} \tag{5.14}$$

The overall value of lift induced drag can then be calculated and subtracted from the original value of D before the coordinate transformation occurs. Thus equation 5.12 becomes:

$$F_X = (D - D_i)\cos\alpha + L\sin\alpha = \left(D - \frac{1}{2}\rho U_\infty^2 S C_{Di}\right)\cos\alpha + L\sin\alpha \qquad (5.15)$$

Finally it is necessary to take into account the effect that α has on the magnitude of the incident velocity and use this in calculating the final drag coefficient C_{DF}, where the effect of angle of attack has been corrected.

$$C_{DF} = \frac{\left(D - \frac{1}{2}\rho U_\infty^2 S C_{Di}\right)\cos\alpha + L\sin\alpha}{\frac{1}{2}\rho U_\infty^2 \cos^2\alpha S} - \frac{1.1 C_L^2}{\pi A_R}\cos\alpha \qquad (5.16)$$

Equation 5.16 depends only on measured variables, except for α which needs to be determined for each run. A laser pointer has been used to determine α to within 0.3° by measuring the movement of the laser down the length of the run. However, this was quite time consuming and introduces another value which needs to be recorded manually each run. Thus a correlation has been developed to determine α from the amount of lift produced at each speed. Firstly, a set of drag and lift values were taken for three different values of α. The values of lift were plotted against angle of attack, and a gradient ($\partial L/\partial\alpha$) determined for each speed. A correlation was then determined for $\partial L/\partial\alpha$ as a function of speed (Figure 5.16).

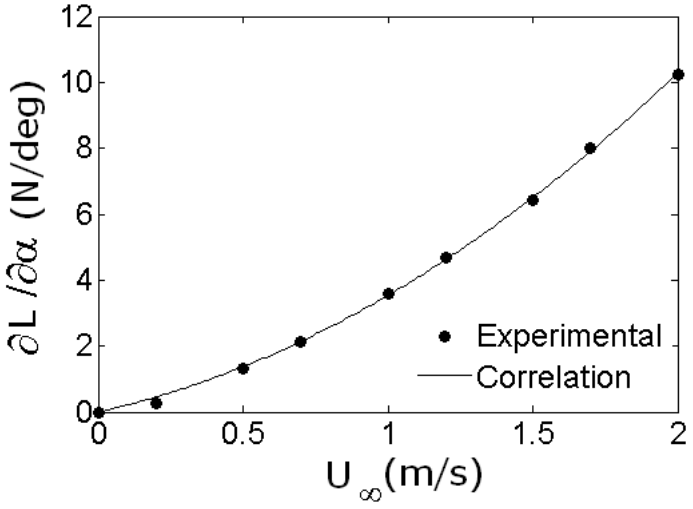

Figure 5.16: Correlation between lift and angle of attack

$$\frac{\partial L}{\partial \alpha} = 1.6015 U_\infty^2 + 1.9344 U_\infty \qquad (5.17)$$

The angle of attack can then be determined (assuming that there is no lift at $\alpha = 0$):

$$\alpha = L\frac{\partial \alpha}{\partial L} = \frac{L}{1.6015U_\infty^2 + 1.9344U_\infty} \tag{5.18}$$

To minimise the error in calculating the angle of attack, a value of α is calculated for each run and averaged for each set of data (between adjustments of the angle of attack, or removal of the plates). It is this averaged value of α that is then inserted into Equation 5.16. A sensitivity analysis shows that a variation of 0.3° results in an error of $< 0.5\%$ at the highest speed and $< 0.1\%$ at the slowest speed.

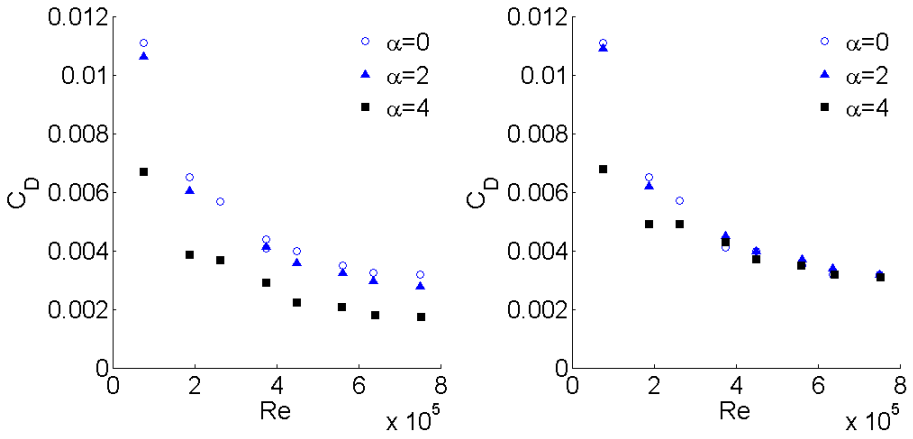

Figure 5.17: Drag coefficient curves for a) raw data & b) data corrected for AoA effects

Figure 5.17 shows the effect of correcting for AoA effects on the final drag coefficient. The corrected values match well for all Reynolds numbers above 40,000 but do not match well for the highest angle of attack at the slowest speeds. This is probably due to the small values of drag at slow speeds being harder to measure, producing a greater error in the correlation. However, it is possible to align the plate holder to within 1° by aligning the plate using a laser pointer to minimise the lift forces. Therefore, the inconsistency in parts of the data in Figure 5.17b) is considered to be inconsequential. To avoid confusion in the rest of the report, no distinction is made between F_X and D. All other references to a drag value are assuming that the corrections for angle of attack effects have already been completed.

The effect of water temperature on the flat plate experiments is primarily to influence the water viscosity. The viscosity of water is known to decrease by about 3%

with a 1°C increase in temperature at typical tank temperatures. This is clearly a relatively large sensitivity and would result in the same magnitude variation in the Reynolds number. The variation of water viscosity with temperature is relatively complex, especially around the boiling and melting points and is further complicated by pressure. Many different correlations have been proposed to describe the overall relationship over a wide range of temperatures and are often quoted with an accuracy of a few percent. However, in these experiments the temperature range $(10 - 25°\mathrm{C})$ is small allowing a model to be used which is specifically designed for this range, namely

$$\mu = 2.414 \times 10^{-5+247.8/(T-140)}. \tag{5.19}$$

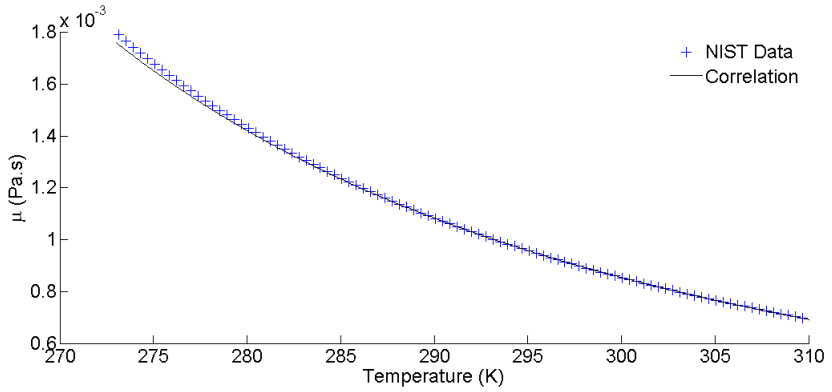

Figure 5.18: Effect of water temperature on dynamic viscosity

The correlation shown in Figure 5.18 matches the data from the National Institute of Standards and Technology (NIST) (Lemmon et al., 2011) within 0.5% and it is therefore assumed that there is a negligible error in determining the water viscosity once the temperature is known. It is worth mentioning here that the towing tanks contain relatively dirty water and may contain contaminants as the water is not often replaced. The effect of particulates and chemicals in the water on the water properties are unknown without conducting experiments on a sample. It is assumed that any effect will be minimal and consistent over the timescale of a typical test campaign (1 week), however between test sessions some discepancies were noted and are discussed later. The temperature of the tanks should remain relatively constant over a few days due to the large volume of water. Therefore the temperature of the water was recorded at the start and end of each day, with a linear interpolation to estimate the temperature for each run. Initial measurements were conducted with a mercury thermometer, but it is only possible to read the

temperature to about ±0.5°C. A digital thermometer was used after the initial tests as it has an accuracy of ±0.05°C allowing the water viscosity to be determined to within 0.5%. Campbell et al. (2002) reports that a thermocline is possible within towing tanks, producing stratification. However, multiple tests confirmed that there is no significant thermocline in the tanks used during these experiments.

To compare the drag of the flat plate to the value calculated from theory it is necessary to account for the drag of the supporting struts. To achieve this the flat plate was tested at different immersion depths. The difference between the drag at difference immersion levels is then attributed to the increase in the area of the struts that is immersed. For example, Figure 5.19 shows an original immersion level (I_1) and an increased immersion level (I_2).

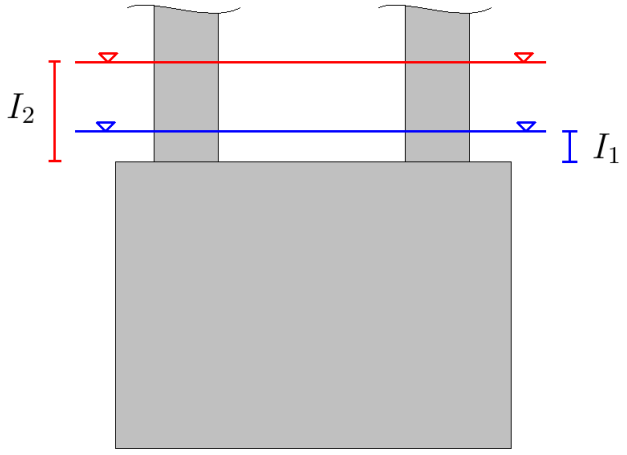

Figure 5.19: Sketch of two different immersion levels demonstrating the approach used to calculate the strut drag

The drag coefficient of the struts (C_{DS}) can then be calculated based on the change in drag between the two immersion levels (ΔD_I) and the change in the area of the strut (ΔS_S).

$$C_{DS} = \frac{\Delta D_I}{\frac{1}{2}\rho U_\infty^2 \Delta S_S} \tag{5.20}$$

The drag coefficient of the strut varies with speed due to the change in change in viscous drag, wave making and how the wake impinges on the second strut. Thus a correlation is developed for the variation of C_{DS} with Reynolds number.

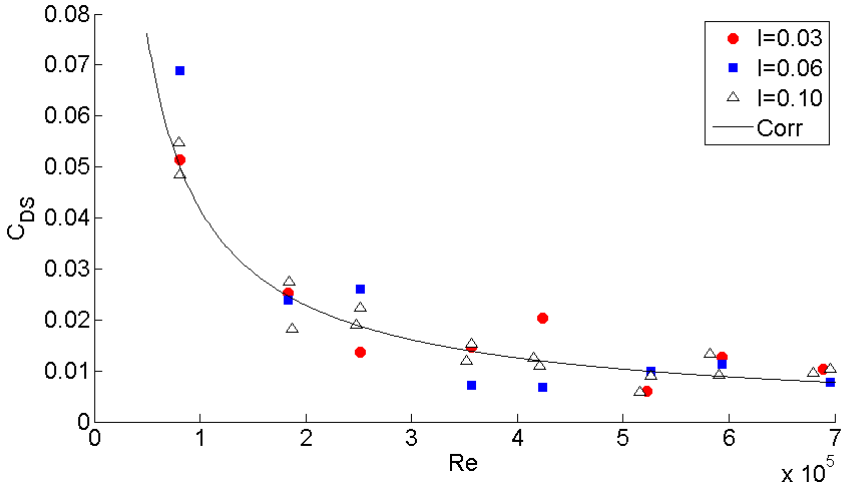

Figure 5.20: Correlation of strut drag coefficient with Reynolds number

$$C_{DS} = 902.49 Re^{-0.867} \tag{5.21}$$

Figure 5.20 shows that there is significant scatter around the correlation line, with an R^2 value of 0.8. Nonetheless, the current relationship can still be used to calculate the drag of the flat plate with the drag of the struts removed based on the immersion depth (I), streamwise length (l_s) and the number (n_s) of struts as

$$D_F = D - 902.49 \rho U_\infty^2 I n_s l_s Re^{-0.867}. \tag{5.22}$$

Turbulators or studs were used in the experiment to provide a consistent transition location. The primary effect of turbulators is to trip the boundary layer flow to be turbulent, however they will also have a finite drag value attached to them. The drag value of the turbulators D_t can be calculated based on the standard drag formula, with a C_D value of 1.2 (that of a cylinder protruding from a wall). The studs used were cylinders 2mm high and had a radius of 1.5mm, in comparison to the boundary layer thickness at this location of approximately 5mm.

$$D = \frac{1}{2} \rho U^2 S C_D \tag{5.23}$$

However, complications arise in that the turbulators are a similar scale to the boundary layer; thus to increase the accuracy of the model of D_t the boundary layer profile needs to be considered. The boundary layer profile depends on the

Reynolds number of the flow at the turbulator location and the boundary layer state (laminar or turbulent).

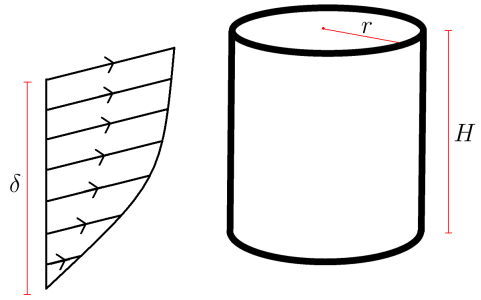

Figure 5.21: Effect of velocity profile on turbulator drag

The velocity profile at the turbulator location is expected to be laminar, however in some cases, natural transition may have occurred upstream and the boundary layer will already be turbulent. The laminar boundary layer is self-similar and can be calculated using the Blasius approach, however it is simpler to use a polynomial approximation to the velocity profile so that the velocity profile can be integrated analytically. The velocity profile is expressed in non dimensional form with $U_\star = u/U_\infty$ and $y_\star = y/\delta$.

$$U_\star = \frac{3}{2}y_\star - \frac{1}{2}y_\star^3 + \frac{\Lambda}{4}\left(y_\star - 2y_\star^2 + y_\star^3\right) \tag{5.24}$$

The Polhausen parameter, Λ, quantifies the effect an external pressure gradient on the flow. In this case it is assumed that there is no external pressure gradient and the last term in Equation 5.24 is ignored. For a turbulent flow the boundary layer profile can be estimated using:

$$U_\star = y_\star^{\frac{1}{7}} \tag{5.25}$$

The turbulator drag can then be estimated by integrating Equation 5.23 over the height of the stud.

$$D_t = \int_0^H \frac{1}{2}\rho U(y)^2\,(2r)\,C_D\,\mathrm{d}y \tag{5.26}$$

Solution of this equation requires the use of Equation 5.24 or 5.25 in a dimensional form and results in the following equations respectively:

$$D_{tL} = \rho r U_\infty^2 C_D \left(\frac{3H^3}{4\delta^2} - \frac{3H^5}{\delta^4} + \frac{H^7}{28\delta^6} \right) \tag{5.27}$$

$$D_{tT} = \frac{7}{9} \rho r U_\infty^2 C_D \frac{H^{9/7}}{\delta^{2/7}} \tag{5.28}$$

These equations define the drag on an individual turbulator and so need to be multiplied by the number of studs to calculate the total drag component. It is assumed that the studs are sufficiently spaced apart that there is no interference effect.

The use of turbulators was refined through the project with an initial design of circular studs, spaced 20mm apart and located just upstream of the sample on plate A ($x = 0.06$m). However, this was a rudimentary design as the studs were insufficiently upstream of the sample to ensure that transition is occurring upstream and independently of the sample surfaces[3]. A modified turbulator design was included on plate B, with conical studs spaced 10mm apart at $x = 0.125$m (details of the turbulators used can be seen in Table 5.1. This updated design reduced the overall drag on the turbulators, and introduced smaller, but more frequent (in a spanwise direction) disturbances to reduce the extent of wedges of laminar flow between the studs. The hydrophobic samples were also placed a further 0.085m downstream to ensure that the breakdown to turbulence has largely occurred before the start of the rough surfaces.

Plate	Shape	H	r	x-location	Distance to sample	Spacing
A	Circular	3mm	1mm	0.06m	0.02m	20mm
B	Conical	1.5mm	1mm	0.125m	0.1m	10mm

Table 5.1: Details of turbulators used in towing tank experiments

Other turbulator designs were considered, as for example, Erm and Joubert (1991) suggest that sand grit is more a more effective turbulator, producing a transition location and turbulent boundary layer profile that are less dependent on the free-stream velocity and turbulator design. However, when immersed in water it was found that sand grit quickly came away from the backing paper or the backing paper itself delaminated and rippled. Trip wires were also experimented with and found difficult to reliably mount to a thin plate. Studs were ultimately retained due

[3]Research has also shown that such large studs could actually act to stabilise Tollmien-Schlichting waves and delay transition (Fransson and Brandt, 2005)

to their robust and reliable nature, such that although they may have had a small influence on the turbulent boundary layer profile, this was consistent throughout the experiment. Ideally a longer plate could have been used to ensure that the boundary layer is independent of the turbulator design; however this was not feasible due to the ability to manufacture only a few of each of the hydrophobic surfaces to be tested.

5.5 Hot film analysis

5.5.1 Hot film theory

Hot wire and hot film anemometry is based on the principle that the resistance of thin wire elements depend on the temperature of the element. The resistance at a certain temperature (R_W) will depend on the heat transfer coefficient (α_0), temperature difference and cold resistance R_0, where the subscripts W and 0 refer to the heated and cold values.

$$R_W = R_0 \left(1 + \alpha_0 \left(T_W - T_0\right)\right) \tag{5.29}$$

These thin wire elements, with a temperature dependent resistance can be used as a thermal sensor by monitoring the resistance of the wire. They can also be used to measure the thermal conduction rate away from the wire by including such an element in a Wheatstone bridge with a feedback loop. The Wheatstone bridge produces an output voltage proportional to the difference between the resistances in the bridge and, by incorporating a feedback loop, the voltage applied to the heated element can be varied to balance the bridge. For example, if the bridge is out of balance, with the heated element having too low a resistance, then the feedback loop increases the voltage through the element, increasing the heating of the element (and hence the resistance) until the bridge is in balance.

The rate of Joulean heat production (q_j) due to electric current through a wire can be calculated (Sandborn, 1972) based on the wire resistivity (σ^{-1}), current through the wire (I) and dimensions of the wire as

$$q_j = \frac{4I^2\sigma^{-1}}{\pi D^2}\left[1 + \alpha\left(T_W - T_0\right)\right] = \frac{I^2 R}{l} \qquad \text{where} \qquad \sigma^{-1} = \frac{R\pi D^2}{4l}. \tag{5.30}$$

Assuming that the heated element is held at a constant temperature by the Wheatstone bridge and feedback loop, the heat production due to the current must be balanced by the heat conducted and radiated into the surroundings. The radiated heat is typically small and hence, for a hot film, the heat production is balanced by heat loss to the substrate (subscript s), supports or leads (k) and surrounding fluid (f):

$$q_j = q_s + q_k + q_f \tag{5.31}$$

Assuming that the gauge has been in operation for a while, the conduction to the supports or leads can be assumed constant, due to the much larger mass of the supports. In the case of hot films in water, the heat loss to the substrate can also be considered as negligible due to the high thermal conductivity of water (Alfredsson et al., 1988) and hence the majority of the heat is conducted into the fluid. However, to ensure minimal heat conduction to the substrate perspex has been used as the substrate material due to its low thermal conductivity.

Therefore, by combining Equations (5.30) and (5.31) it can be shown that the heat conducted into the fluid is related to the output voltage (E) from the Wheatstone bridge:

$$E^2 \propto I^2 R \propto q_f \tag{5.32}$$

Appendix E follows Keith (1990) but highlights the key assumptions in the analysis and shows that the heat conducted into the fluid from the wall can be related to the shear stress:

$$q_f \propto \tau^{1/3} \tag{5.33}$$

The analysis conducted is based on the Reynolds analogy between diffusion and advection of heat and vorticity to create viscous and thermal boundary layers respectively (Sandborn, 1972) and is based on the assumption that the thermal boundary layer is entirely contained within the viscous sublayer (Keith, 1990). The equations are equally valid for both laminar and turbulent flow, but the assumptions break down for separated flow. Finally, by combining Equations (5.32) and (5.33), it is clear that the voltage is related to the shear stress at the wall via

$$E^2 \propto \tau^{1/3} \qquad \text{or} \qquad E^2 = A\tau^{1/3} + B. \tag{5.34}$$

This demonstrates that a hot film sensor is theoretically capable of measuring the shear stress at the wall if calibration can be developed to determine the values of A and B in Equation 5.34. Alfredsson et al. (1988) discusses the variety of techniques which may be used to develop a calibration with Preston and Stanton tubes being the most common, although these techniques themselves are indirect measures of the shear stress.

The approach demonstrated above is for a boundary layer in equilibrium, however, Figure 5.22 highlights the multiple viscsous and thermal boundary layers that are present in the current experimental setup. At a smooth-to-rough interface there is a step change in the shear stress at the wall and a new internal layer develops from this step. At a finite distance downstream of the step this internal layer will have grown to form a new equilibrium boundary layer (Townsend, 1965).

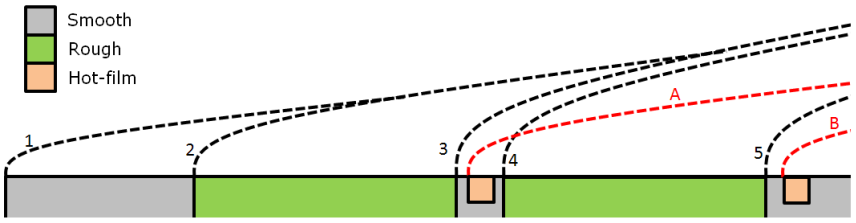

Figure 5.22: Schematic of viscous and thermal boundary layers past step changes in surface roughness

With multiple step changes in roughness and heating it is likely that the internal layers will not reach an equilibrium before the next layer starts (for example the rough-smooth-rough step changes from layers 2,3 and 4 in Figure 5.22). This demonstrates that there is are inherent difficulties in measuring flow over rough surfaces with hot film gauges. The hot film gauge must be placed in a location downstream of a necessary step change in roughness (the gauge itself being smooth) and hence the gauge will be measuring in a non-equilibrium boundary layer; if the gauge were placed further downstream, where equilibrium had again been achieved it would then be measuring a boundary layer that does not depend on the roughness upstream of the step. However, Taylor et al. (1993b) demonstrated that after an abrupt change in surface roughness the thermal boundary layer quickly adapts to the downstream roughness and is close to equilibrium after a short distance, unlike the viscous boundary layer which can take up to 40δ and is slowest

for a rough-to-smooth transition (Antonia and Luxton, 2004). This suggsets that the hot film gauge will be capable of measuring the skin friction after a step change in roughness, regardless of whether the viscous boundary layer has achieved equilibrium.

5.5.2 Hot film sensors & operation

The wall shear stress was measured in this report using a Tao of Systems Integration Inc. (TSI) 1750 constant temperature anemometer. The Senflex® hot films (SF9902) were purchased from TSI and consist of a $100\mu m$ wide, $0.2\mu m$ deep and 1.45mm long nickel sensing element. The elements are deposited onto a 120×20mm Upilex® polymide film substrate, with copper leads ($13\mu m$ deep) allowing the solder contacts to be about $100\mu m$ away from the sensing element itself. The cold resistances of the sensors varied - due to slight differences in manufacturing - in the range 9.2-10.2Ω, with the leads contributing approximately 0.4Ω.

Each sensor was attached to a piece of perspex ($40 \times 280 \times 3$mm) using super glue, with care taken to ensure that the film was flat and the sensor aligned with the flow direction. The attachment of the film to a small spacer of perspex enabled the location of the hot film to be varied in the streamwise direction, due to the modularity of the sample attachment procedure. The connection leads for the hot film were soldered onto the copper connectors on the film and then coated in Araldite® to waterproof the connections. This resulted in a slight bulge but was considered sufficiently far away from the sensor to have a minimal impact.

The resistance required to balance the bridge was chosen depending on the exact resistance of the sensor, so that the Over-Heat Ratio (OHR), and hence the signal-to-noise ratio can be maximised, whilst working within the thermal limitations of the sensor. This led to resistances in the range 52-58Ω to ensure that the OHR was kept close to $R_W/R_0 = 0.5$, with a value of $\alpha = 0.3\Omega/°\text{C}$ taken from the manufacturers specification (as defined in Equation 5.29).

Bench tests conducted with a square-wave generator demonstrated that the maximum frequency response of the hot film sensors is approximately 250Hz (Freymuth, 1981; Khoo et al., 1999). Above this frequency the thermal lag in the probe means that the system does not respond fast enough to accurately measure signals of higher frequencies. To ensure that the signal is accurately sampled a 500Hz low-pass filter was used and a sampling frequency of 1KHz.

The applicability of these sensors to measuring the flow in water can be established by considering whether the thermal layer formed as water flows past the heated element remains within the viscous sublayer. Haritonidis (1989) shows that for this to be the case the following two criteria must be satisfied, where Pr is the Prandtl number.

$$l^+ < 4.1\mathrm{Pr} \tag{5.35}$$

$$3.12\left(\mathrm{Pr}l^{+2}\right)^{-1/3} < 1 \tag{5.36}$$

For the first criterion the LHS is in the range 4-19 whilst the RHS is approximately 30. For the second criterion the LHS is in the range 0.2-0.6 and hence both criteria are satisfied. The effect of roughness is to to increase the skin friction and reduce the thickness of the viscous sublayer making it harder to pass these criteria. It is also necessary to ensure that the rate of heat loss from the sensor is primarily through conduction into the fluid. The ratio of the radiative (r) to conductive (c) heat transfer can be calculated using the heat transfer coefficient ($h = 62\mathrm{W/m^{\circ}C}$) and surface emissivity ($\epsilon = 0.04$) of Nickel and the Stefan-Boltzmann constant (σ_{SB}) (Sandborn, 1972).

$$\frac{q_r}{q_c} = \frac{\epsilon\sigma_{\mathrm{SB}}\left(T_w^4 - T^4\right)}{h\left(T_w - T\right)} \tag{5.37}$$

For the sensors used in this study the ratio $q_r/q_c < 0.01$, showing that the majority of the heat loss from the sensor is through conduction to the fluid. Each hot film was also allowed to stabilise in temperature before each use to ensure that any conduction into the substrate is consistent throughout the experiments. For each experimental setup that involved the use of hot films the temperature of the water was found to be invariant to 0.1°C over each testing window and hence no temperature corrections were required.

The conduction to the substrate will have numerous effects on the hot film response. First, as the hot film heats the substrate it results in a reduction in the overall percentage of the hot film voltage that depends on the shear stress. The heated substrate also then increases the effective sensor width and length, increasing the thermal layer thickness at the probe (Haritonidis, 1989) and making it

harder to satisfy the constraints of Equation 5.35 & 5.36 (ensuring that the thermal boundary layer is within the viscous sublayer). The additional mass of the heated substrate will also act to reduce the frequency response of the hot film as it will produce a thermal lag[4]; the general dynamic response of the probe will also be adversely affected by the increase in sensor width and length, as it will average out any fluctuations over the sensor area (Wietrzak and Lueptow, 1994).

Overall, it has been demsontrated that the hot film is capable of measuring the shear stress of a smooth turbulent boundary layer. The introduction of roughness poses questions about the validity of hot film results downstream of a step change in roughness. However, the hot film gauge should provide a qualitative picture of the effect of the roughness on the shear stress, although it is necessary to remember that any results are likely to be for a non-equilibrium boundary layer, and the hot film measurements taken at a location where the shear stress is relaxing to the new boundary condition.

5.5.3 Hot film signal analysis

The hot film signals were captured simultaneously with the drag measurements, using the same acquisition and triggering system. Figure 5.23 shows an example of the hot film signal acquired without the automatic triggering and demonstrates the acceleration from rest, acquisition phase and deceleration to static again, with the hot film returning to the zero value.

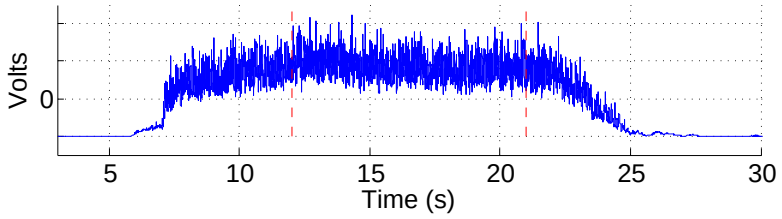

Figure 5.23: Example hot film signal through an entire run from start up to stop, with red lines showing the acquisition window

The raw voltages from the hot film signal are stored and then analysed once each testing session was complete. A zero value was taken at the start of each run to ensure that there was no drift in the calibration occurring, but the original

[4]Perspex was used as the substrate due to its low thermal conductivity, however a better approach may have been to use a ceramic such as Macor which would have a better dynamic response.

zero from the start of each test session was used for all calculations to remove the artificial effect of background currents on the zero. The calibration procedure used in this experimental setup is similar to that used by Madavan et al. (1985), where the voltage is matched to the analytical shear stress for either a laminar (τ_{wL}) or turbulent (τ_{wT}) boundary layer.

$$\tau_{wL} = 0.332 \left(\frac{\rho U_\infty^3 \mu}{x} \right)^{0.5} \tag{5.38}$$

$$\tau_{wT} = 0.02975 \left(\frac{\rho^4 U_\infty^9 \mu}{x} \right)^{0.2} \tag{5.39}$$

These two equations were used to calculate the shear stress at the hot film location, with a manual decision over whether to use a laminar power law, or to use a turbulent power law with a virtual origin. The calibration was found to be insensitive to the use of a virtual origin.

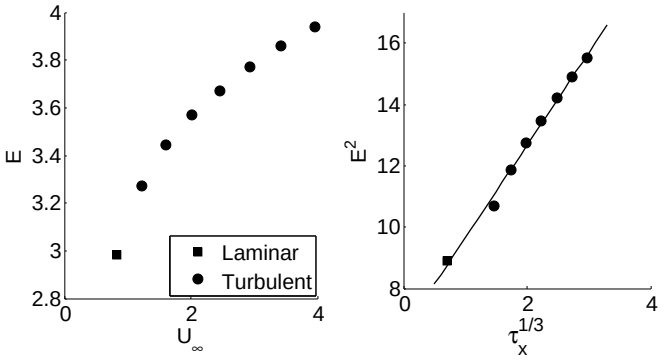

Figure 5.24: Hot film voltage variation with speed (left) and calibration curve (right)

Figure 5.24 demonstrates the increasing voltage required to balance the Wheatstone bridge as the carriage speed and hence the shear stress is increased. Plotting $\tau_x^{1/3}$ vs. E^2 demonstrates a linear correlation as expected from Equation 5.34. This allows the constants A and B to be calculated and hence a calibration between τ_x and E to be developed. (Madavan et al., 1985; Sandborn, 1979) suggest that the calibration is an iterative procedure, but with this experimental apparatus the calibration was accurate after a single attempt. Figure 5.24 suggests that the same calibration can be used in laminar and turbulent flow, corroborating Brown (1967) and disagreeing with Bellhouse and Schultz (1966). However, the data presented henceforth is primarily concerned with turbulent flow.

The calibration is applied to each hot film signal and then passed through a Fast-Fourier Transform (FFT) routine in MatLab to explore the frequency content. Each signal is split into 1 second windows using the Hann window, such that each segment overlaps by 50% as shown in Figure 5.25.

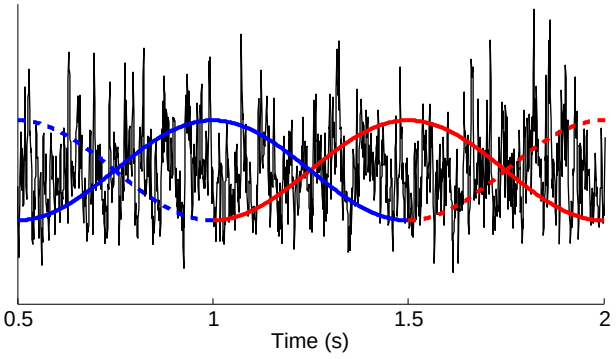

Figure 5.25: Example hot film signal with 50% overlapping Hann windows

The window ensures that the frequency content extracted by the FFT is then an accurate representation of the signal rather than including the edge effects of a square window (Shin and Hammond, 2008). The signal is split into overlapping segments to provide an averaged spectrum, whilst the length of 1 second ensures that there are 1,000 data points within each segment to retain a high discretisation of the frequency.

$$f^+ = \frac{f\nu}{u_\tau^2} = \frac{f\mu}{\tau_w} \tag{5.40}$$

For some plots the frequency is scaled into wall units (f^+) using the mean value of the shear stress taken from the mean of the calibrated hot film signal.

5.6 Error & uncertainty analysis

5.6.1 Accuracy and precision

The accuracy of measured or simulated value (S) is how closely it matches the true value (T). In an ideal situation the two values will match exactly and the measured value will be an accurate representation of the real life situation. However, in the majority of cases there will be finite difference between S and T and this is

known as the error (ϵ) (Barford, 1985; Bevington and Robinson, 2003). Errors can typically be classified as either modelling errors (ϵ_M) or numerical errors (ϵ_N):

- Modelling errors arise due to the incorrect use of assumptions and approximations. They are generally systematic errors.
- Numerical errors appear due to issues with the measurement systems. A numerical error tends to increase the uncertainty in the result as they typically have a random nature.

To ensure that the results are as accurate as possible it is necessary to try and minimise both types of error. The systematic nature of modelling errors means that they can typically be accounted for once the experiments have been completed. However, it is still appropriate to attempt to minimise the modelling error so that the effect of any model on the result is reduced. On the other hand, the random nature of numerical errors mean that they must be considered in detail before the experiments are conducted, or at least analysed after the experiment to provide a measure of uncertainty.

Ideally the results of an experiment will be as accurate as possible, however it is important to distinguish between accuracy and precision. Accuracy is a measure of the difference between the true value and the measured value and is therefore linked to the definition of ϵ. Precision on the other hand is a measure of the repeatability of the results and allows the uncertainty in the result to be quantified (Bevington and Robinson, 2003). Therefore, for an experiment to be *accurate* (in a conventional sense) it has to achieve both high accuracy and high precision by minimising the systematic and random errors respectively.

5.6.2 Sources of error

In tank testing there are a wide range of sources of error that need to be considered as presented in Table 5.2

The effect of systematic errors are accounted for in the data analysis discussed in Section 5.4.2, however the random errors are discussed here along with how they were systematically approached to minimise their effect.

One of the main design points of a towing tank is the requirement to tow the test sample through water at a constant speed. The carriage needs to accelerate and

Source of error	Systematic / Random
Calibration of force blocks	Systematic & Random
Angle of attack	Systematic
Water temperature	Systematic
Strut drag	Systematic
Turbulator drag	Systematic
Carriage Speed	Random
Windowing of data	Random
Background currents	Random
Wave drag	Random
Transition location	Systematic & Random
Ground Fluctuations	Random
Aeroelastic effects	Random
Mounting of plates	Random
Electronic signal conditioning	Random

Table 5.2: Potential sources of error in experimental tank testing

decelerate at the start and end of the run due to the finite length of the tank. These acceleration and deceleration zones are avoided when taking measurements to ensure that the speed is as constant as possible along the measurement length. At the Lamont tank, the speed is determined by calibrating it against both the DC input to the generator and the RPM of the shaft (measured using an encoder). Along the length of the run a feedback loop attempts to keep the speed constant based on these two measured parameters.

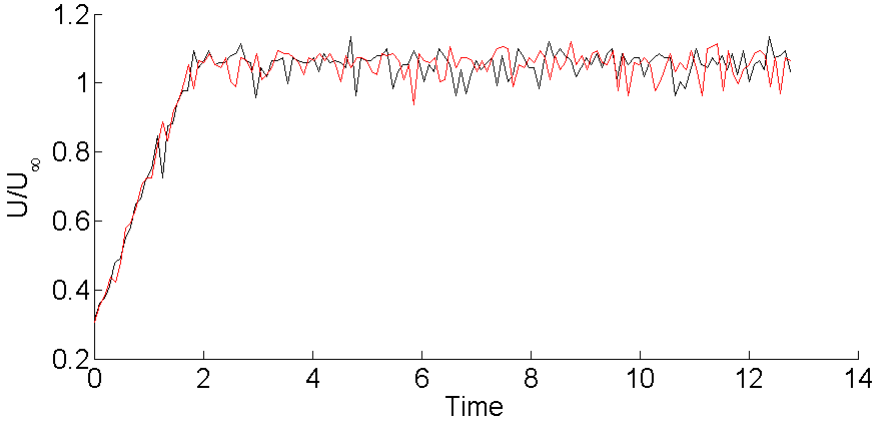

Figure 5.26: Variation in speed at the Lamont tank on two different runs (U=1.4m/s)

Figure 5.26 highlights three important things about the variation of speed along the length of the run. Firstly, the signals have a relatively good agreement between runs, suggesting that the average speed down the run is consistent and in this case

the average speed is actually consistent to 3dp. Secondly, the acceleration zone is clear in the signal, with the ramp increase in speed. Including the acceleration zone results in an average speed slightly lower than the true value. The third point to note is the low sample rate, which is evident from the coarse & spiky nature of Figure 5.26 and this low sample rate reduces the precision of the signal at the Lamont tank. At the Solent tank the speed is measured by the time it takes for the carriage to cover a given distance and resulted in good accuracy and precision of the speed measurement, with repeat measurements typically being consistent to 3dp for the same speed setting. Overall, it is considered that the speed measurement is sufficiently accurate to have a minimal impact on the drag.

Initial tests at the Lamont tank showed that the average drag value for a given run is sensitive to the windowing of the data. To minimise this effect the data logging was triggered by a magnetic reed switch on the carriage, so that for each run the data was collected over exactly the same portion of the tank. This reduces the possibility of human error in including some data from when the carriage was at its set speed. This also enabled the average speed to be measured accurately as the distance covered is accurate to within ± 0.001m and the time to 0.01s.

Another potential source of error is that unlike, a wind tunnel where flow conditioners can be used and the turbulence level set by the design of screens, a towing tank is a nominally stationary body of water. However, as the plate is repeatedly towed through the water it disturbs it and can generate currents and waves within the tank. The background currents can influence the relative flow velocity and with the drag varying with U^2 it could have a large impact on the measured drag value. The waves within the tank could also impact on the drag as the strut drag component with depend on the incident waves. Finally, the background level of turbulence within the tank could impact the transition location. Therefore it is necessary to ensure that these effects are minimised. The tanks are fitted with beaches (wooden planks) at the side which help damp the waves after each run. The background currents can be monitored by dropping a droplet of ink into the tank to see whether it falls vertically through the water. Back to back tests confirmed the standard procedure and demonstrated that the drag measurements were consistent if 5 minutes was left between each run to allow the tank to settle again and the waves within the tank to dissipate. Furthermore, between each set of runs it typically took 30-45 minutes for the sample plates to be changed, allowing further time for the tank to settle. This approach should be sufficient to ensure that the effect of background currents and waves is minimised. But to

ensure that any systematic build up of currents is consistent between data sets each was sample was tested using the same test matrix.

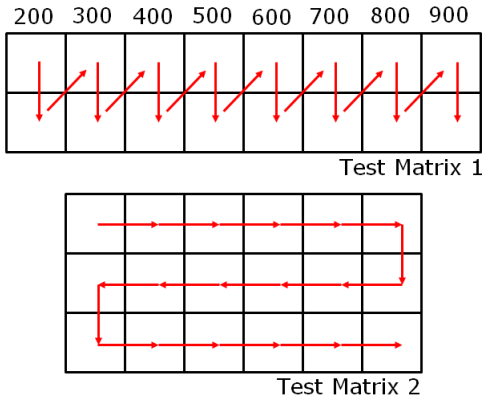

Figure 5.27: Two different test matrices used during tank testing

The test matrices in Figure 5.27 refer to the different speeds set on the controller, with values from 0-999 covering the speed range of 0-4.5m/s approximately linearly. A time limit of 5 minutes was set between each run, defining that each set of samples would take 1.5 hours, not including the time to mount the plate. Test Matrix 1 was used for the majority of the tests, with a duplicate result at each speed taken before proceeding to the next speed. This also allowed the repeatability of the results to be analysed during the testing and facilitates the detection of anomalous results or faults with the data acquisition. Test Matrix 2 was designed to explore the effect of both immersion time and high speed runs on the plastron, as it allows for comparisons between runs after short and long intervals and both before and after the high speed runs.

Another source of random variability of results is the variation of the ground signal. Although the measurements were based around a differential input the ground was found to cause variations in the results. This was especially true for the hot film data as it is especially sensitive. Indeed, the first few tests of the hot film data at the SSU tank were found to be inconclusive and expensive, with many hot film gauges being overheated and destroyed. This was eventually linked to a poor earthing of the carriage, where up to 50 Volts was passing between the metallic components of the carriage and the electronics. This grounding issue was fixed and the hot film anemometer placed in an electrically isolated box. However, some data was still lost when a fire alarm triggered the resetting of power to the building, resulting in a widely fluctuating ground signal for a few hours. To monitor these potential issues the zero values for both the force and hot film measurements were recorded before each run and then analysed before the data was accepted.

The largest source of random error in the experiment was found to be the mounting of the samples. Although the plate was designed with ease of mounting in mind, consistent mounting of the plates proved difficult. In the final design the samples were screwed to the plate with countersunk screws and care was taken to ensure that the thickness of each sample matched the depth of the recessed region in which they are held. However, due to slight variations in size this sometimes left small gaps between the samples and the plate at the edge. This was most apparent for the ridged surfaces as discussed further in Section 6.1.4. Although this could impact the accuracy of the results it should not affect the precision as it would be consistent within a set of data.

5.6.3 Least count

The least count of a measurement is the smallest differentiation that could be made between two measurements using the same apparatus. In this experimental setup the least count is harder to define as the signals are fluctuating. The LVDT used to measure the changes in forces were quoted as being capable of measuring to an infinite resolution[5], however to achieve this would require perfect signal processing equipment. The LVDT used for drag measurements had a working range of 1mm, which through the flexures of the force block was scaled to covering a working range of approximately $\pm$50N, this was then processed by a 16-bit giving a least count of the order of 0.001N.

A more realistic estimation of the least count can be achieved by considering the base fluctuations or electric noise on the signal. For the drag measurements the standard deviation in the zeroes was roughly 0.3N, and with measurements sampled at 1000Hz for at least 3 seconds, this gives an estimate of the the standard deviation of the mean as 0.005N. Taking a 95% confidence limit results in a least count or significant value of 0.01N. The minimum drag values measured for Plate B were approximately 2N which shows that the least count accounts for a maximum of 0.5% of the measured drag. A similar analysis of the electric noise on the hot film signal shows that the least count of the hot film accounts for a maximum of $< 0.1\%$ of the measured signal.

[5]RDP Electronics Ltd, Grove Street, Heath Town, Wolverhampton, West Midlands, WV10 0PY, http://www.rdpe.com/displacement/lvdt/lvdt-principles.htm

5.6.4 Repeatability estimation

At the beginning of the project the repeatability of the results was very poor. However, through addressing the issues discussed in the preceding Sections, the repeatability has been systematically improved from results with a best estimate of the error of 16.8% to 0.8%. The assessment of repeatability is conducted by considering the difference in drag between any two drag measurements that should give the same value, regardless of whether the runs are back to back, or days or weeks apart. This difference in drag ($\chi = C_{D1}/C_{D2}$) is shown in Figure 5.28.

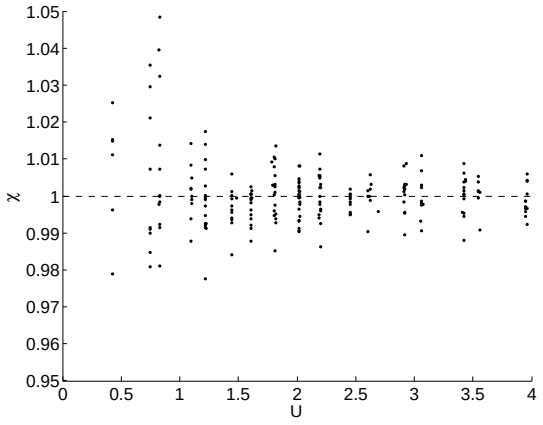

Figure 5.28: Repeatability of drag measurements across speed range

The values of χ are larger at the slowest speed, where the physical drag values are lower and the precision in the drag measurements have a larger effect. Above a speed of around 1m/s the distribution of χ appears approximately constant, suggesting that the repeatability is associated with the random errors rather than the capabilities of the measuring equipment.

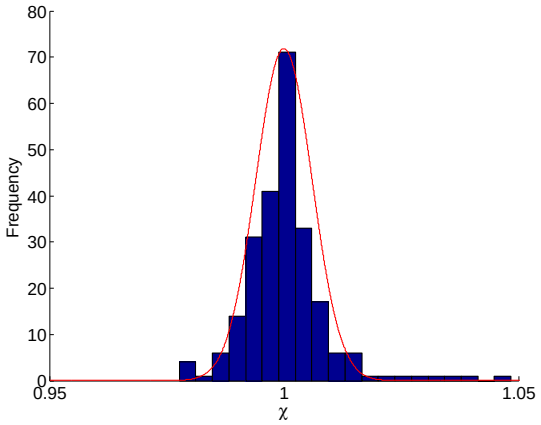

Figure 5.29: Histogram of errors in measurements demonstrating a normal distribution (red line)

The best estimate of error (S_n) can then be calculated from the distribution of χ, as Figure 5.29 shows that it follows an approximately normal distribution. The best estimate of error in X allows the result to be quoted with a certain degree of precision.

$$X = X_n \pm S_n \tag{5.41}$$

The value of S_n can be calculated based on the difference of each value from the mean ($\overline{X}$), the number of original measurements (n) and the number of measurements in a sample (s) (Barford, 1985).

$$S_n = \frac{1.96\sigma}{\sqrt{s}} = \frac{1.96}{\sqrt{s}} \frac{\sqrt{\sum (X - X_i)^2}}{\sqrt{n\,(n-1)}} \tag{5.42}$$

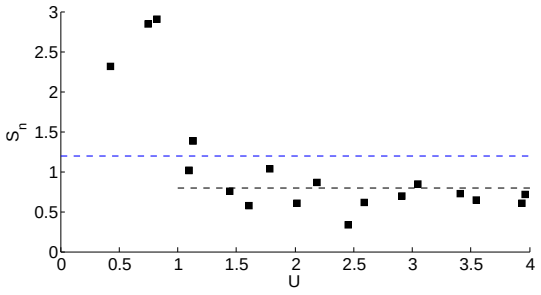

Figure 5.30: Confidence limit (95%) in drag measurements across speed range (blue = total mean, black=mean at higher speeds)

The standard deviation of χ for this data is 0.87% and using a 95% confidence limit (the value of 1.96 in Equation 5.42 and taking two measurements for each data point gives a best estimate of error as 1.2%. However, Figure 5.30 shows that the value of S_n is much lower above a speed of 1m/s. Therefore for speeds above 1m/s the best estimate of error can be refined to 0.8% and the drag coefficient values can be quoted to an accuracy of $\pm 0.8\%$.

A similar approach was also conducted for the hot film signals but is not included for brevity. The repeatability of the hot film results was consistent across the entire speed range and resulted in a best estimate of error of 4%, similar to that reported by Bellhouse and Schultz (1966).

Analysis of the least count for each measurement (0.5% for drag and $< 0.1\%$ for the hot film measurement) has demonstrated that the acquisition equipment is capable of achieving the estimates of error given above. Any future improvements in the repeatability of the experiments should therefore focus on further improving the experimental setup (e.g. reducing errors in mounting the samples and oscillations in the mounting) rather than improcing the precision of the acquisition equipment.

5.7 Chapter Review

This chapter has detailed the development of an experimental setup capable of directly measuring the drag of superhydrophobic surfaces in high Reynolds number ($\mathrm{Re} \approx 10^6$) boundary layer flow. The experiment has been designed to produce a maximum contribution from the viscous drag component and allow for the easy replacement of sample surfaces whilst maintaining a consistent experimental setup. Successive iterations of the experimental design produced a repeatability estimate of 0.8% above speeds of 1m/s, with the most important design consideration being the fixing of the location of transition to a turbulent boundary layer through use of turbulators.

Numerical simulations of the experimental setup demonstrated that a significant drag reduction could be measured if a slip length of approximately 50μm or larger is generated by the surface and that a combination of roughness and slip could also produce an overall drag reduction in comparison to a smooth surface. The simulations also demonstrated that it would be difficult to measure the expected change in the boundary layer profile due to the difficulties of measuring close to a rough and highly reflective surface. However, wake studies and hot film

measurements should demonstrate a measurable effect of slip occurring at the surface.

Chapter 6

Experimental testing of superhydrophobic surfaces

This Chapter details the experimental investigation of the effect of a range of superhydrophobic surfaces on the drag of a flat plate aligned to the flow. Measurements are taken in both a hydrophobic state with a plastron present and a wetted state once the plastron has been removed, so that the direct effect of the plastron can be identified. Results are presented for experiments with Plate A and with the improved design of Plate B as discussed in Chapter 5. Hot film measurements are also presented to explore the effect of a superhydrophobic coating on the structure of a turbulent boundary layer.

6.1 Drag measurements

6.1.1 Introduction

The effect of each superhydrophobic surface is characterised by measuring the total drag coefficient and comparing it to the baseline case at the same Reynolds number. Throughout this Section there are two main effects which need to be distinguished: the effect of roughness and the effect of a plastron. These two effects can be defined as an *overall* drag increase or a *relative* drag increase.

1. Overall drag increase ($S_{\%}$) - The percentage change in drag in comparison to a smooth surface (C_{DS}).

$$S_{\%} = \left(\frac{C_D}{C_{DS}} - 1 \right) \times 100\% \tag{6.1}$$

2. Relative drag increase ($P_{\%}$)- The percentage change in drag in comparison between a hydrophobic, plastron retaining state (C_{DH}) and a rough wetted surface (C_{DW}).

$$P_{\%} = \left(\frac{C_{DH}}{C_{DW}} - 1 \right) \times 100\% \tag{6.2}$$

These two parameters help to delineate between the different effects of superhydrophobic surfaces. It has been emphasised throughout this Thesis that a surface needs to be both rough and hydrophobic to retain a plastron. The effect of the roughness is considered by changing the sample surface and running through the test matrix, with comparisons made to a smooth surface. The effect of the plastron on the drag is determined by running through the test matrix with a plastron present and then immersing the surface in ethanol before immersing it in water a second time. As ethanol has a low surface tension it completely wets the surface and allows water to penetrate the roughness and prevent a plastron being formed. The drag is then measured over the test matrix once more. Therefore, the parameter $P_{\%}$ allows a comparison between the same rough surface with (H - hydrophobic state) and without (W - wetted state) the presence of a plastron.

The combination of $S_{\%}$ and $P_{\%}$ allows for three possible permutations for the hydrophobic state

- $S_{\%} > 1 \cap P_{\%} > 1$ Overall increase in drag with the total drag increase being a combination of an increase in drag due to the plastron and the roughness.
- $S_{\%} > 1 \cap P_{\%} < 1$ Overall drag increase with a relative reduction in drag due to effect of the plastron.
- $S_{\%} < 1 \cap P_{\%} < 1$ Overall drag reduction.

The values of $S_{\%}$ and $P_{\%}$ are calculated for each surface based on the average drag coefficient values at each speed tested. Due to the changing water temperature the smooth surface data has been interpolated to match the Reynolds numbers explored for each surface.

Surface	Designation	R_a	k^+	$\theta(^\circ)$
Smooth	Smooth	-	-	73(°)
Magic (coarse) Sand	MS	400-800μm	66-140	150(°)
Medium Sand	G1	250-400μm	25-53	102-133(°)
Fine Sand	G2	150-250μm	16-35	108-140(°)
Aligned ridges	AR	100μm	4-17	150(°)
Transverse ridges	TR	100μm	4-17	123(°)
Fine copper mesh	CuF	420μm	35-74	115-140(°)
Coarse copper mesh	CuC	1.41mm	116-250	129-132(°)

Table 6.1: Designation, roughness and contact angle of samples

For ease of reference the different surfaces are described along with their designation and estimated k^+ values (based on smooth wall u_τ) in Table 6.1. These surfaces were chosen to cover the entire range of smooth (ridged surfaces at low speeds), transitional (G1, G2, CuF) and fully rough surfaces (MS, CuC) to aid the understanding of what type of roughness is required to support a plastron and may produce a drag reduction.

Each hydrophobic sample was tested in hydrophobic state and then again immediately afterward in a wetted state after removal of the hydrophobicity with ethanol.

6.1.2 Smooth plate and surface roughness

The drag of a flat plate is known to increase with speed at an approximately quadratic rate. This can be seen from the classical formula for drag.

$$D = \frac{1}{2}\rho U_\infty^2 S C_D \tag{6.3}$$

Figure 6.1 demonstrates that the raw drag data for both a smooth and a rough plate do approximately follow a quadratic polynomial. There are some deviations away from a U^2 trend which are related to the drag coefficient varying with speed.

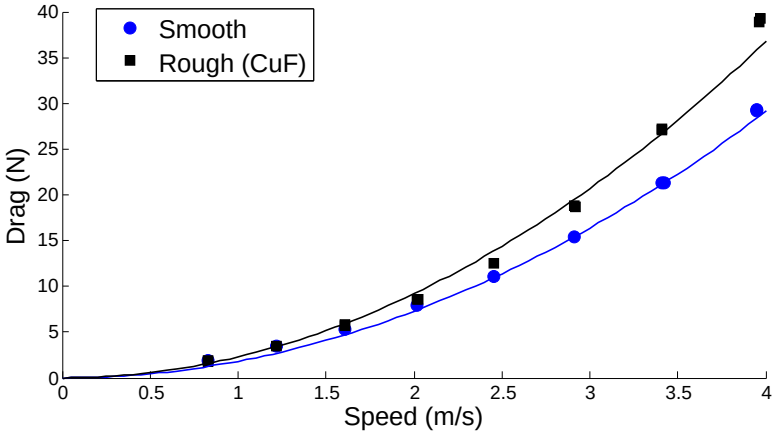

Figure 6.1: Drag variation with speed for raw data for a smooth and rough surface. Lines are quadratic fits

Each collected set of data has been processed to remove as much as possible of the known drag contributions. For example Section 5.4.2 showed that the strut, turbulator and angle of attack contributions can all be calculated separately.

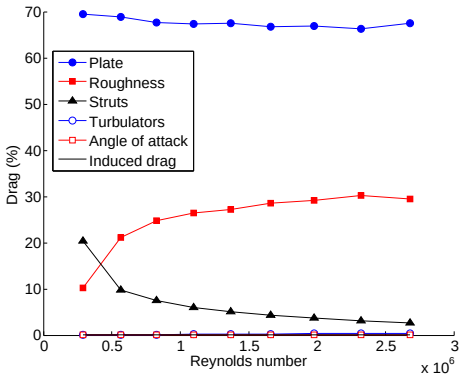

Figure 6.2: Drag component breakdown

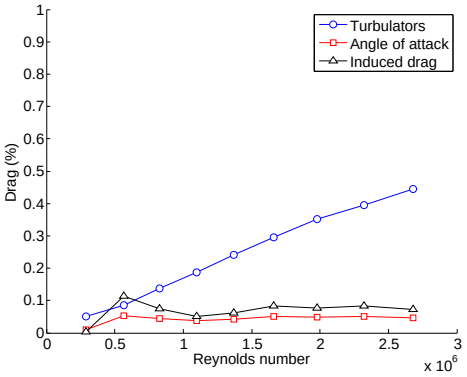

Figure 6.3: Drag component breakdown for smaller components

Figure 6.2 shows that the two largest contributions to the drag apart from the viscous drag of the surface are the strut drag and the effect of the roughness. The effect of the turbulators and angle of attack effects were found to be minimal (Figure 6.3) when the plate was aligned accurately.

The variation of the drag with speed is typically characterised using an $\mathrm{Re} - C_D$ plot, with a laminar boundary layer having a lower drag coefficient than a turbulent one (as discussed in Section 5.2.1).

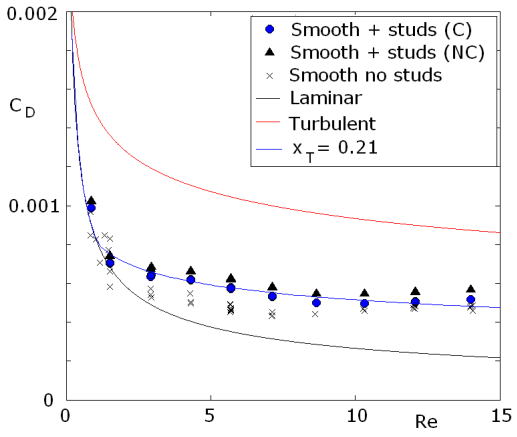

Figure 6.4: Drag coefficient variation for smooth surface with and without turbulators for Plate A (C=corrected for turbulator drag, NC= not corrected for turbulator drag)

Figure 6.4 demonstrates that for Plate A the drag coefficient variation is between the laminar and turbulent solutions, suggesting that the plate is experiencing a partly laminar and a partly turbulent boundary layer, with transition occurring part way along the plate. The data for the smooth surface without studs or turbulators shows a large degree of scatter, especially at low speeds and the upwards trend suggests that the transition location is moving forward as the carriage speed or Reynolds number is increased. The scatter in these results is associated with the background currents and turbulence in the tank influencing the transition location and hence the drag. The use of turbulators (cylindrical for Plate A) removes the influence of the background currents by acting to fix the transition location, which is corroborated by the match between the corrected data with the analytical curve for a constant transition location at $x_T = 0.21$m. The corrections for the cylindrical studs are larger than the conical studs used for Plate B.

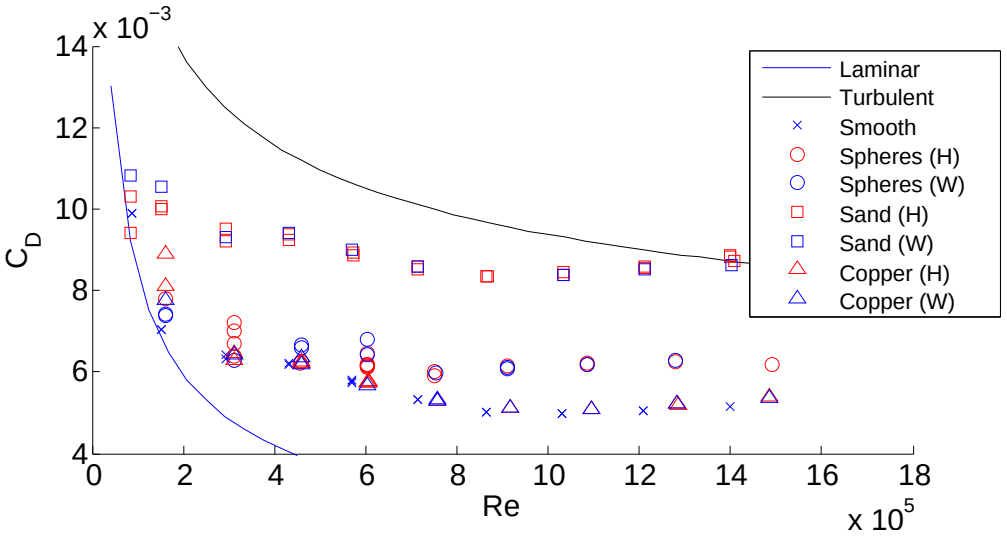

Figure 6.5: Drag coefficient variation for smooth, rough and hydrophobic surfaces for Plate A

A variety of hydrophobic surfaces were tested on Plate A with results shown in Figure 6.5. Some of the surfaces are not presented in Section 4.2 as their performance was negligible[1]. The rough surfaces show an increase in drag coefficient with increased roughness however, the effect of the plastron was found to be within experimental error for all of the surfaces tested. All subsequent tests were conducted with Plate B, which was designed to improve repeatability of results and ensure that transition occurred upstream of the samples.

For Plate B the majority of the flat plate is experiencing a turbulent boundary layer and the data is above the ITTC-57 correlation as shown in Figure 6.6. The ITTC-57 correlation represents previous experimental data from tank testing of various ship designs (ITTC, 2002) and within the Reynolds number range explored produces the same drag coefficient as the analytical turbulent profile in Equation 5.2.

[1]The 180μm hydrophobic glass spheres were created in a process similar to the hydrophobic sand, with the spheres coated in Granger's solution (although the Granger's did not bond well to the glass). Three different smooth copper surfaces were chemically treated with stearic acid, persulfate and amonia respectively. The surfaces were created by Simon Stanley & Neil Shirtcliffe at Nottingham Trent University

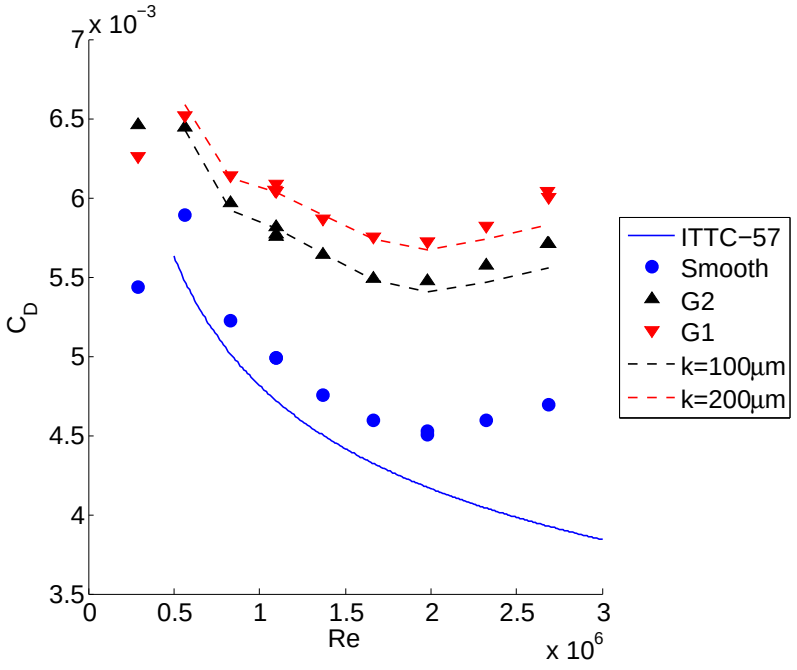

Figure 6.6: Drag coefficient variation for smooth and rough surfaces

The data at the lowest Reynolds number is included to show that the data for each surface dips towards the laminar profile (not shown, but lower than the ITTC-57 line). This suggests that the plate is experiencing a large proportion of laminar flow over the surface at these low speeds. Further data at these low speeds was not collected due to lower accuracies in measuring a much smaller drag value. The smooth data is markedly above the ITTC-57 line and it is thought that this is related to the wave drag and interference drag components generated by the struts. The wave drag component cannot easily be measured, but it is expected that the it would increase rapidly around a Froude number (Fr $= u/\sqrt{gL}$) of 1 (Douglas et al., 2005), which corresponds to Re $\approx 2 \times 10^6$ in this experimental setup. The increasing drag difference between the smooth data and ITTC-57 in Figure 6.6 therefore suggests that the offset wave drag component is important. Although the wave drag component cannot be measured, it will remain consistent throughout the experiments at each speed due to the design of the surface piercing struts and hence will not reduce the precision of the results.

The effect of the roughness is consistent between the two different roughness grades, showing an increase in the drag of the surface over the entire Reynolds number range. The dashed lines in Figure 6.6 are based on the semi-analytic expression for an equivalent sand grain roughness (k_{eq}) in Equation 5.9, but taking the smooth data from Figure 6.6 as a baseline rather than the ITTC-57 (so that

the effect of wave drag is accounted for). The general trend is matched well by both G1 and G2, with both showing a slight increase above the predicted values at higher Reynolds number. This is expected because although the sand grain roughness remains constant, the k^+ value and hence the effect on drag increasing due to higher u_τ values at higher flow speeds. Overall the scales of the surface match relatively well between the actual (G1=250-400μm, G2 = 150-250μm) and predicted equivalent values (G2=200μm, G1=100μm) considering that the ratio between these can be as high as 15 (Chuah et al., 1982). The ratio is typically closer to 1 for sand grain roughness as the solidity and packing is high, but is still expected that the equivalent sand grain roughness will be lower than the sand grain size (McClain et al., 2006). This ambiguity in the definition of k_{eq} is already apparent before taking into account the effect of the sand grains being partly immersed in glue, and considerations such as the mean elevation height and location of the zero plane (Taylor et al., 2006). Overall, the effect of surface roughness appears to be captured accurately with the experimental setup.

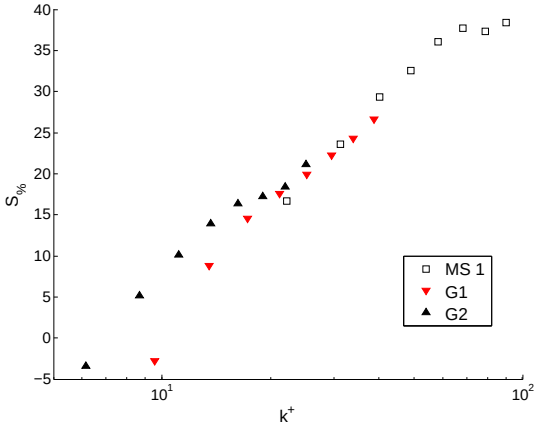

Figure 6.7: Variation of effect of sand grain roughness in wall units

The effect of the sand grain roughness can be scaled into wall units to demonstrate that it produces a consistent hydrodynamic effect as shown in Figure 6.7 and that the experiments are producing the expected effect (Jimenez, 2004). The roughness is scaled using the mean roughness height (calculated from the surface scans in Chapter 4) and a friction velocity (u_τ) based on the analytical expression for a smooth turbulent boundary layer. The typical axes for the plot in Figure 6.7 are ΔU^+ vs. k^+, however in the present case the offset in the velocity profile is not available. This introduces uncertainty as the value of u_τ will naturally be higher for a rougher surface and the availability of a range of roughness measures allows for the scale of the abscissa in Figure 6.7 to potentially vary. However, as all of the

data shown is for sand grain roughness, any effect should be consistent for each set of data. Hence, regardless of the u_τ and therefore the exact k^+ values the data will still collapse successfully.

6.1.3 Effect of hydrophobic sand

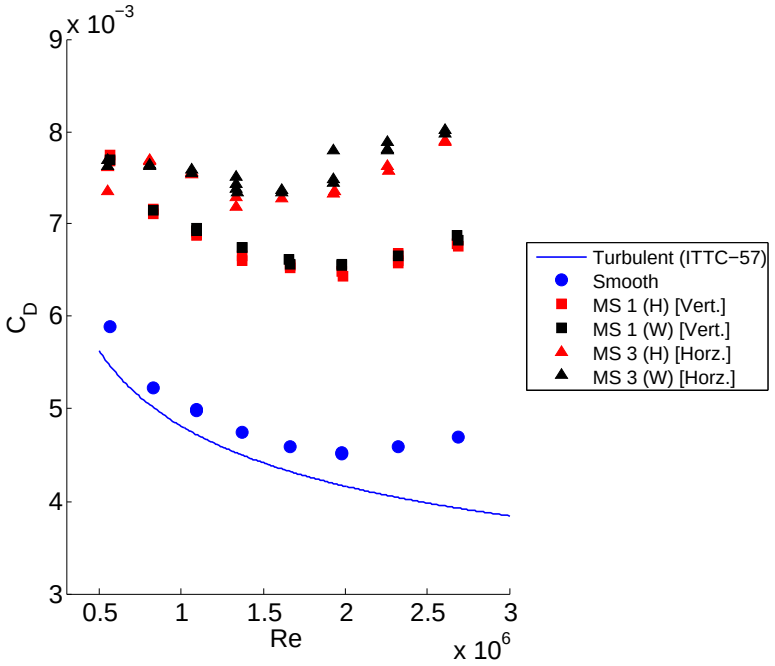

Figure 6.8: Drag coefficient variation for MS in both vertical (Vert.) and horizontal (Horz.) configurations

Figure 6.8 demonstrates the increased drag over the entire Reynolds number range in comparison to both the smooth surface and G1 and G2. This follows the expected trend as the Magic Sand (MS) has a roughness height approximately double that of the G1. Two separate sets of data are shown for MS, with Plate B being in a vertical orientation for one and in a horizontal configuration for the other. The data sets shown in Figure 6.8 have all been corrected for the drag of the supporting struts, with the same correlation used in both vertical and horizontal configurations, but with the appropriate number of struts. The increase in drag for the horizontal configuration over the vertical configuration supports the hypothesis that there is a wave drag component that has not been accounted for and which is increased in the horizontal configuration due to an additional 2 struts.

The main point of interest in Figure 6.8 is that for each set of MS data both a hydrophobic (H - red) and wetted state (W - black) are shown. The hydrophobic

state is slightly lower than the wetted state, suggesting that the effect of the plastron is to produce a relative drag reduction, in comparison to the same rough surface but without a plastron. It is evident that the drag reduction is relatively small and that the overall effect is similar in the two configurations, although perhaps slightly higher in the horizontal case.

The effect of the plastron can be quantified by considering the relative change in the drag coefficient ($P_{\%}$) as introduced in Section 6.1.1. Four sets of hydrophobic sand were tested in the vertical configuration, both G1 and G2 (treated with Granger's) and two different sets of MS.

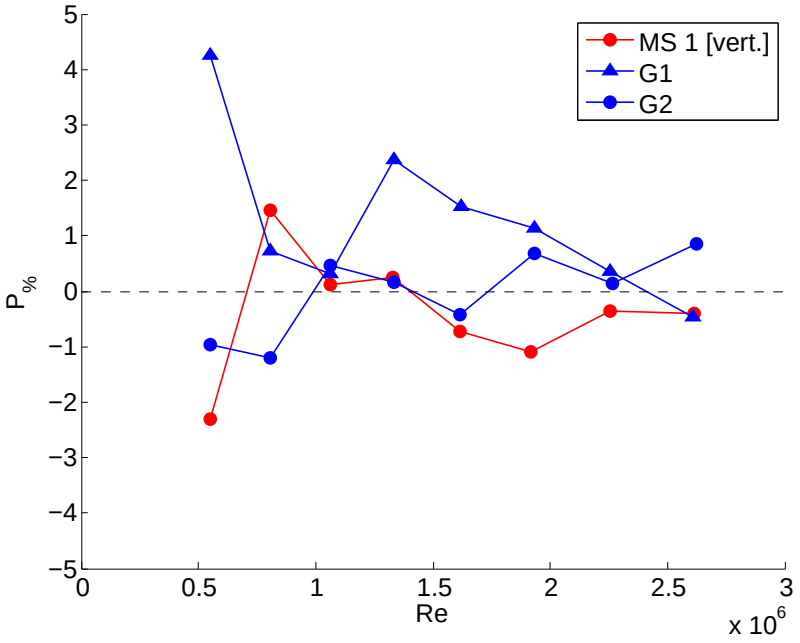

Figure 6.9: Effect of plastron on the relative drag of Plate B in horizontal configuration for hydrophobic sand samples

The two sets of graded sand G1 and G2 produced a plastron that had a negligible effect or produced a relative increase in drag. The drag increase in Figure 6.9 can perhaps be linked to visual observations during the experiments that the plastron sustained by the Granger's coated sand was of poor quality, which itself can be linked to these surfaces having the lowest contact angle of all the hydrophobic surfaces tested. Rather than forming a continuous plastron, any air on the surface appeared to form *large*, discrete bubbles on the surface, that protrude much further into the log-law region than the roughness elements themselves as shown in Figure 6.10 & 6.11. The additional roughness of these bubbles would act to reduce the effect of the plastron and it has been shown that such protrusions can produce

an increase in drag (Teo and Khoo, 2010; Busse and Sandham, 2012c). It is also possible that these additional protrusions will, through acting as roughness, reduce the mean velocity at a given height above the surface and reduce the ability to generate interfacial slip.

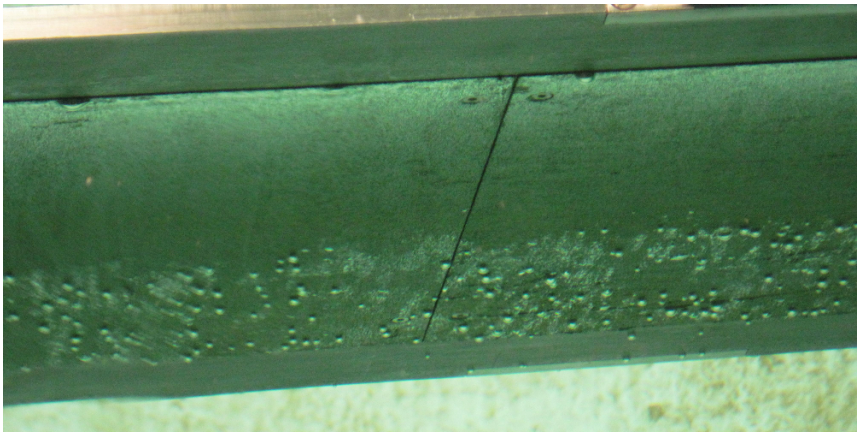

Figure 6.10: Photo of G2 sand soon after immersion with large bubbles present on the surface below a critical depth

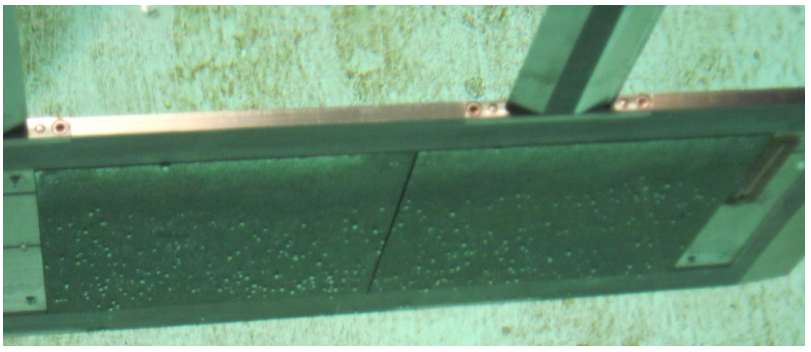

Figure 6.11: Photo of G1 sand soon after immersion with large bubbles present on the surface

There is also a critical hydrostatic pressure above which the bubbles are forming, with a horizontal split between regions of bubbles and no bubbles in both Figure 6.10 & 6.11. The critical depth is deeper for G2 as the grain size is smaller and hence the distance between roughness elements is lower, resulting in the surface being able to withstand a higher pressure. It is plausible that below this depth, the hydrostatic pressure is sufficient to cause the air-water interface to deflect towards the surface and cause wetting; the air comes away from the cavities of the surface but there is insufficient energy provided by buoyancy to cause the air bubble to detach from the surface.

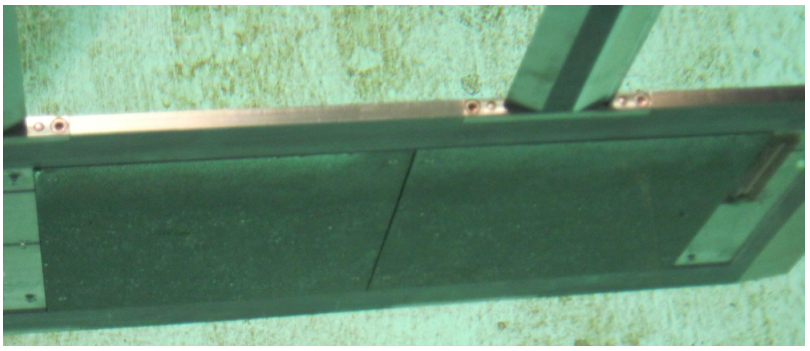

Figure 6.12: Photo of G1 sand after approximately 1.5 hours of experimental testing, with reduced plastron and bubbles present

Observations during testing suggest that the bubbles are deformed under shear and the air within the bubbles smeared over the surface. This is demonstrated in Figure 6.12 where the bubbles have been reduced to a negligible level by the end of the testing program. This is consistent with the trend of G1 in Figure 6.9, as the effect of the bubbles will act to increase the drag as the speed increases but only to a certain speed range, after which the speed deforms the bubbles, reducing the height and hence the additional drag that they produce.

The MS surface appeared to produce a much higher quality plastron, with the entire surface showing signs of reflectivity, which can be linked to the higher contact angle. This was translated to a relative drag reduction of up to 1.5% for MS in a vertical configuration as shown in Figures 6.9 and repeated for a second implementation of the surface in Figure 6.14. This negative $P_{\%}$ confirms the relative drag reduction apparent in Figure 6.8, but it is apparent that the surface still produces a higher drag value than the smooth surface.

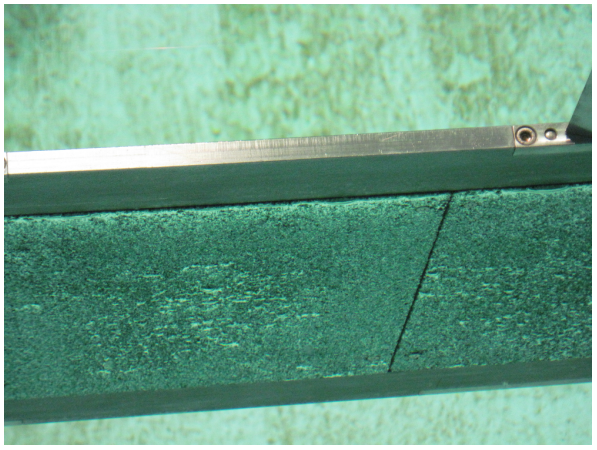

Figure 6.13: Photo of MS soon after immersion with reflective plastron and relatively large bubbles

The overall quality of the plastron on the MS was good but the distribution of the plastron over the surface was uneven as shown in Figure 6.13. The buoyancy of the air on the surface caused it to move towards the edge of the sample closest to the water surface, resulting in a thicker plastron at the top edge and a thinner plastron towards the bottom edge. The random structure of the sand grains presumably allows the air to move relatively freely within the plastron and hence react to the buoyancy force. To overcome this issue MS was also tested in a horizontal configuration on Plate B. The plastron then has a consistent effect of buoyancy over the top and bottom surfaces and produces an even plastron distribution. Experiments were also conducted with injection of air onto the surface before the start of each run, and for the lower surface of MS this resulted in a thick continuous layer of air, with a mirror-like surface. However, this additional air was not stable and was shed when the carriage moved and was found to have no impact on the drag.

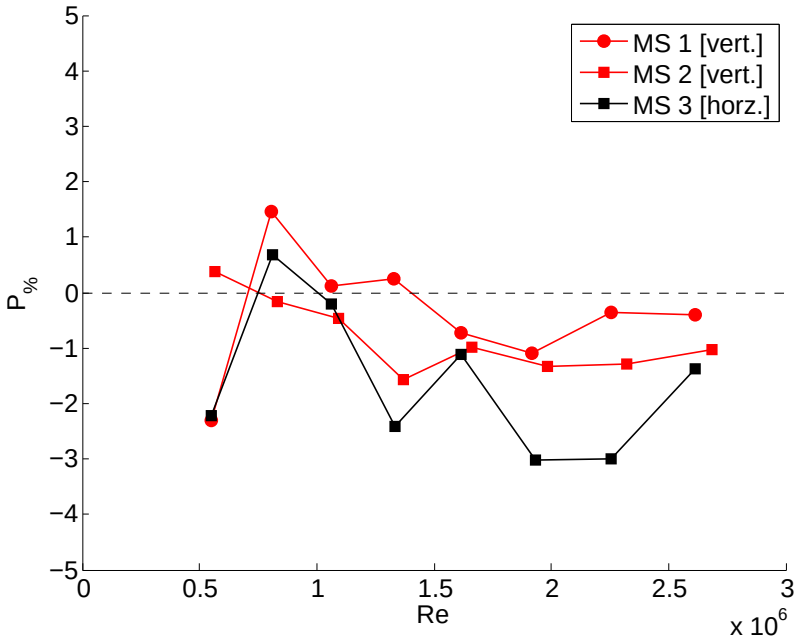

Figure 6.14: Effect of plastron on relative drag of Plate B in both horizontal and vertical configuration for MS

Figure 6.14 demonstrates that the improved quality and distribution of the plastron results in an increased effect, with values of $P_{\%}$ falling as low as -3%. This suggests that a plastron can be used to reduce the drag of an already rough surface if a plastron can be maintained on the surface. For all implementations of the surface the minimum value of $P_{\%}$ occurs at medium to high speeds in the Reynolds number range explored, suggesting that there is an optimal Reynolds

number, or that the plastron is degrading over time (with the tests conducted using Test Matrix A).

6.1.4 Effect of hydrophobic ridges

Two different alignment of hydrophobic ridges were explored, with the ridges either aligned with the streamwise direction (AR) or transverse to the flow direction (TR). Nottingham Trent University constructed these surfaces and provided 3 sets of both AR and TR. The samples had issues with tiles becoming detached, and due to the long lead time in manufacturing the surfaces some data had to be discarded as shown in Table 6.2.

Sample	Date tested	Number of sample sheets	Issues
AR1	Oct 2012	2	-
AR2	Mar 2013	4×0.71	1 tile fell off at high speed
AR3	Mar 2013	4×0.71	6 tiles fell off. No data
TR1	Oct 2012	4	-
TR2	Mar 2013	4×0.71	-
TR3	Mar 2013	4×0.71	-

Table 6.2: Details of the different ridged samples tested and the issues faced

The number of sample sheets used for different set of samples varied due to manufacturing constraints. Initially all the samples were created in a transverse configuration and hence for AR1 the transverse sample was rotated, meaning that the only one sample sheet could fit in on each side. For AR2-3 and TR2-3 the number of tiles on each sample was reduced to facilitate the manufacture of the samples by preventing the requirement for the glass tiles to be cut into smaller squares. Both of these points can be visualised in Appendix F.

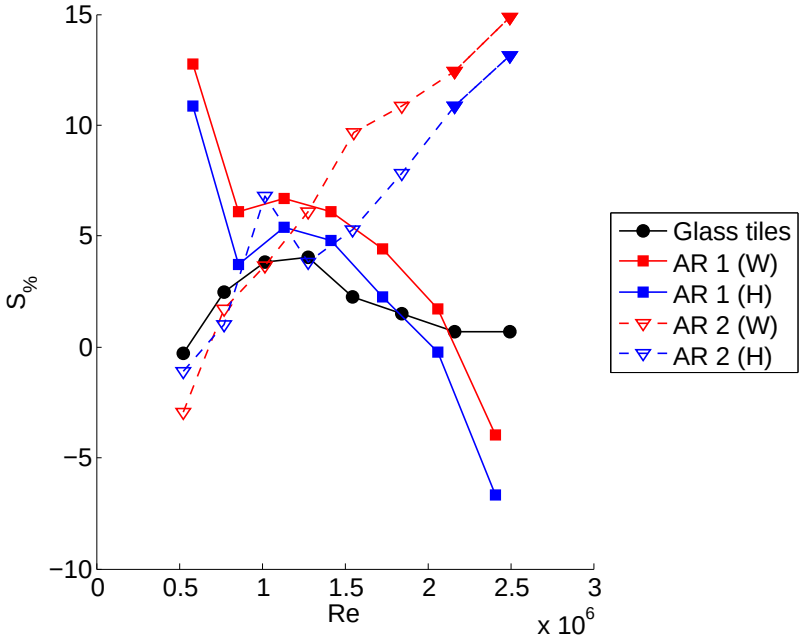

Figure 6.15: Effect of aligned ridges (AR) on drag of Plate B in comparison to a smooth surface. Further details in text

The effect of the aligned ridges (AR) in comparison with the smooth plate is explored in Figure 6.15. The two sets of data for nominally the same surface demonstrate a different trend, with AR1 showing a decrease in drag as Re increases and AR2 showing an increase in drag; this difference in trends is discussed further in Section 6.3. However, the two sets show a relatively consistent effect of the plastron, with the wetted state producing a higher drag than the hydrophobic state. The wetted states for the aligned ridges can also be seen as a riblet structures as they are long roughness elements aligned with the flow direction and span roughness heights of $4 < k^+ < 17$. AR1(W) shows a drag reduction in comparison to a smooth surface but only at the highest Reynolds number, where $k^+ \approx 16$. This is at the upper limit of the known working range ($8 < k^+ < 20$) of riblets (Walsh, 1983; Choi et al., 1993) but the data does not show the expected drag reduction at lower values of k^+. This could be related to the breaker ridges, which may act to modify the optimal riblet size or remove the effect for small k^+ or that the riblets used are not in an optimized form of v- or u-shaped grooves, or thin ridges (Bechert et al., 1997).

The curves shown for AR2 in Figure 6.15 are distorted slightly due to a single tile (1% of the hydrophobic surface area) becoming detached after a high speed run in the hydrophobic state. The data shown for AR2 is then in two states, the first at high speed (full symbols) where a direct comparison can be made between the

hydrophobic and wetted states (with a tile missing in each case) and the second (open symbols) where the hydrophobic state data has a complete surface covering and the wetted state has a tile missing. The expected effect of the missing tile is to increase the drag due to the large step in the surface, and hence the confidence in the drag difference for the open symbols of AR2 is reduced.

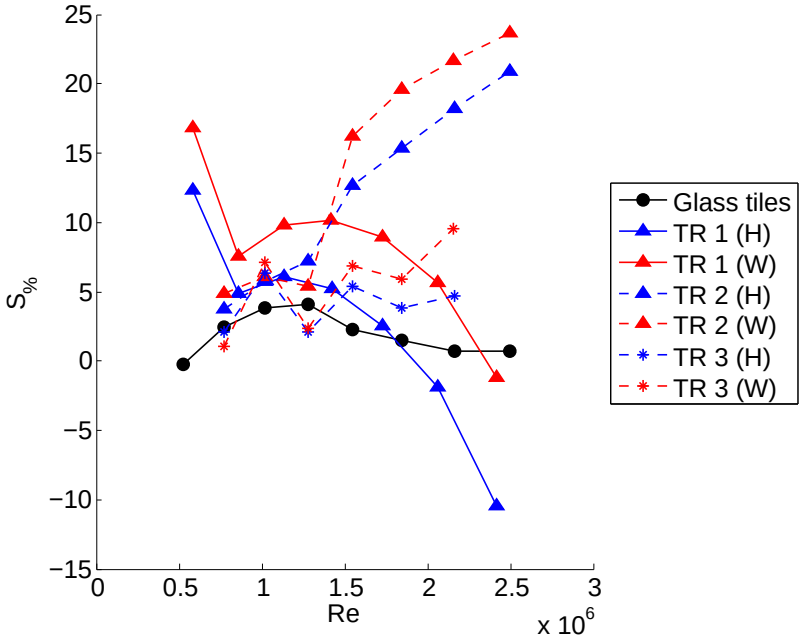

Figure 6.16: Effect of transverse ridges (TR) on drag of Plate B in comparison to a smooth surface.

Three sets of transverse ridges (TR) were tested in both the hydrophobic and wetted states. All three sets show an increase in drag in comparison to a smooth surface for the wetted state, but TR1 demonstrates a decrease in drag in comparison to a smooth surface of up to 11%. In combination with the results for AR it is apparent that there is some systematic shift in the results related to the change of sample. In each of the two TR and three AR cases the surfaces should have produced the same drag, but are different by up to 25%. This is discussed further in Section 6.3.

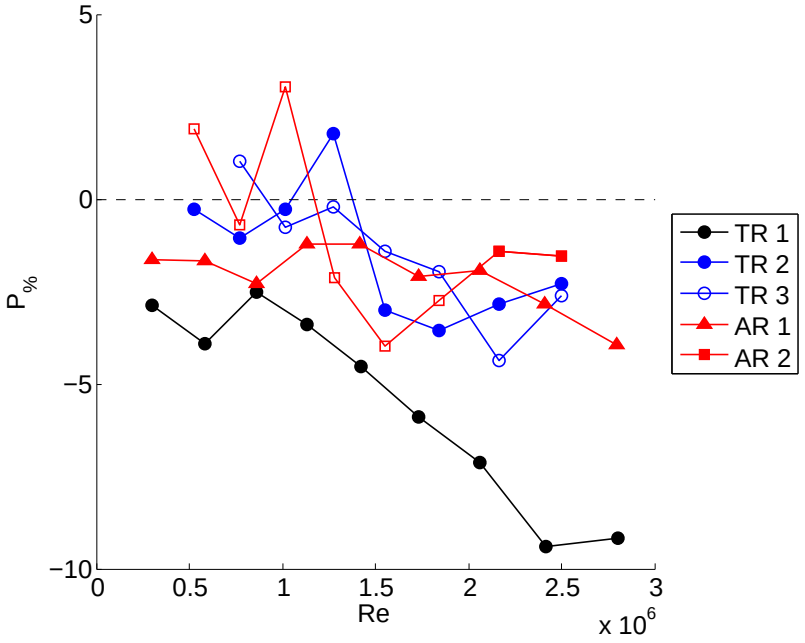

Figure 6.17: Effect of plastron on the relative drag of hydrophobic ridges

The five sets of data from the two different configurations of hydrophobic ridges are shown in Figure 6.17 in terms of the effect of the plastron on the relative drag. It is apparent that the presence of the plastron on each of the surfaces produces a drag reduction of up to 9.5%, though average 2-4%. The effect of the plastron is shown to increase in speed, with the samples showing a similar magnitude of $P_{\%}$ expect for TR1. For TR2 and TR3, the samples have a reduced surface area covered with a hydrophobic sample (see Table 6.2), but this is insufficient to account for the reduced effect between TR1 and TR2-3. One possible explanation for this is the reduced quality of the plastron on samples TR2-3 where, during the experiments, discrete bubbles were observed on the surface as shown in Figure 6.18.

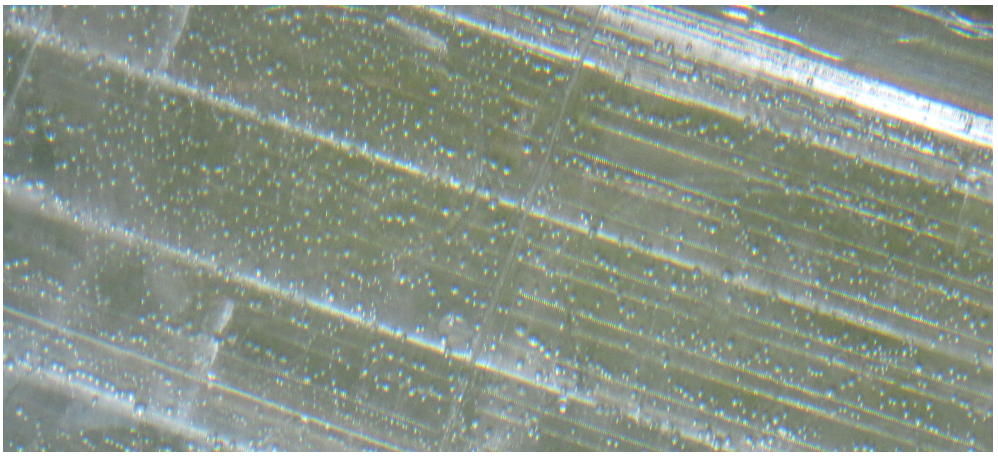

Figure 6.18: Bubbles on ridged surfaces when immersed in water

Due to the small scale and transparency of these surfaces it is hard to appreciate whether these bubbles are still within the grooves or whether they are sitting on top of the surface. The result of either is that the surface is likely to be partly wetted and the plastron quality is reduced, producing the reduction in the magnitude of $P_{\%}$ between TR1 and TR2-3 seen in Figure 6.17.

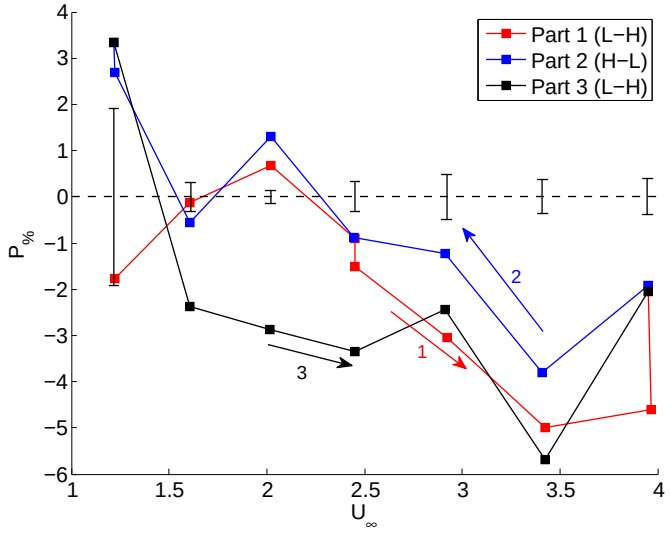

Figure 6.19: Effect of plastron on the relative drag of TR2 using Test Matrix B

Figure 6.19 shows the results of testing TR2 using Test Matrix B. This test matrix involves running from low to high speeds (L-H), back down to low speeds (H-L) and then up to high speeds again. The error bars demonstrate the magnitude of the difference between the runs in the wetted state and highlight that the difference between the three parts of Test Matrix B is significant. All three parts

show the same overall trend which is an increase in the relative drag reduction with speed, however Part 3 shows an increased effect of the plastron. This is also perhaps related to the presence of discrete bubbles on the surface as they were observed to diminish in quantity towards the end of the test matrix. The increase in effectiveness of the plastron when comparing Parts 1-2 with Part 3 could therefore be attributed to the reduction in drag caused by the reduced *roughness* of these bubbles.

The reasoning behind the appearance of bubbles on the surface for TR2 and TR3 but not TR1 is unclear, but the primary differences between the samples are that they were created at different times and tested on different dates. As the manufacturing process was the same for all samples it is unlikely that the difference is a manufacturing issue, unless there was a batch issue with the quality of the chemicals used. It is more likely that the presence of the bubbles is related to the different testing date where the water temperature was 8°C lower and perhaps more significantly the tank had recently been cleaned and the water replaced before the experiments involving TR2-3; both of which would produce an increase in the surface tension of the water. An increased surface tension would increase the possibility of the air within the cavities forming bubbles as it would be more favourable in terms of surface energy.

6.1.5 Copper mesh

Two different hydrophobic copper mesh structures were tested. The first is a coarse copper mesh on top of a fine copper mesh (CuC) and the second is two layers of a fine copper mesh (CuF) as described in Section 4.2.3. The CuF structure was tested once in a hydrophobic state and once in a wetted state. On the other hand the CuC was tested once in a hydrophobic state following Test Matrix A, and then before the plate was removed from the water the plate was run back through a range of lower speeds. This is termed a partly wetted (PW) state based on observations during the testing that the plastron was degrading. The same surface was then tested in a wetted (W) state after the complete removal of the plastron using ethanol. The CuC was then air-dried and re-tested in the next experimental session, such that the data for CuC1 and CuC2 are for the same surface tested on different dates (October 2012 & March 2013).

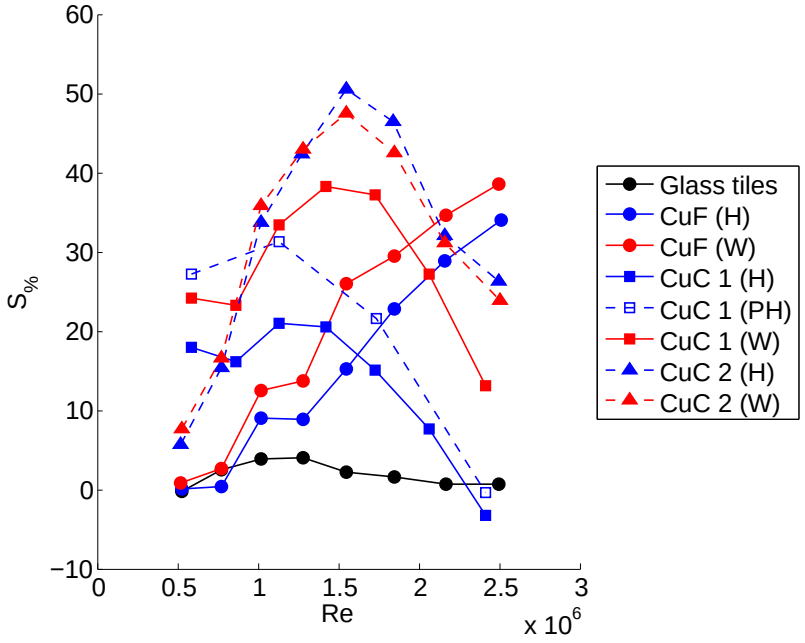

Figure 6.20: Effect of hydrophobic copper samples on drag of Plate B in comparison to smooth surface

Figure 6.20 demonstrates that the copper meshes act to increase the drag of the flat plate by up to 50%. For CuF the $S_{\%}$ increases monotonically with the Reynolds number as would typically be expected for a rough surface. For CuC1 and CuC2 in both a hydrophobic and wetted state the roughness acts to increase the drag with Reynolds number until Re $\approx 1.5 \times 10^6$ where the opposite trend occurs with $S_{\%}$ decreasing with Reynolds number. Figure 6.20 also demonstrates that - similar to the ridged surfaces - there is some systematic error apparent when considering the two different sets of results for CuC in a wetted state as both should produce the same drag result. This is an indication that the mounting of the samples into the plate is potentially influencing the drag measurements, with the CuC samples having been designed to be 0.5mm too small to ensure that there was no repeat of the overlapping from the ridged surfaces. The final point to note is that for CuF and CuC1 there is a clear effect of the plastron in reducing the drag of the surface in comparison to a wetted state.

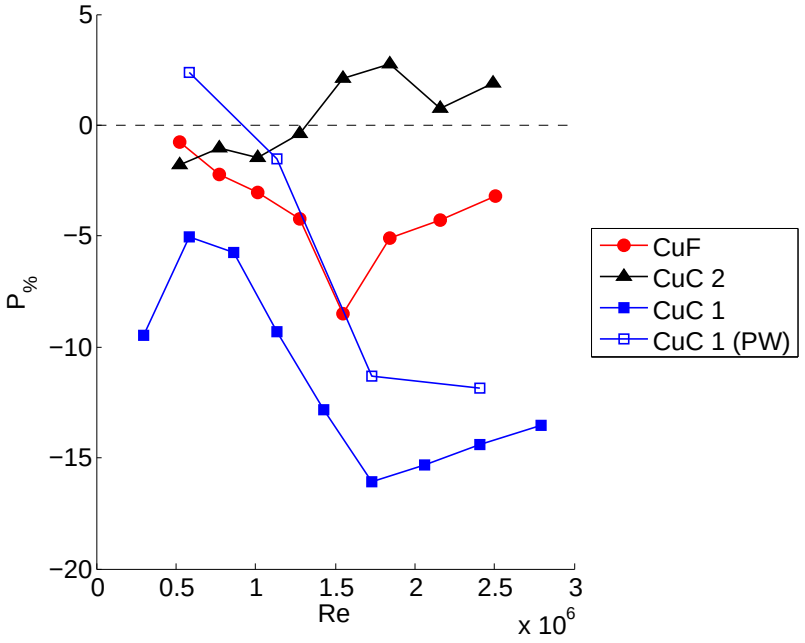

Figure 6.21: Effect of plastron on relative drag of copper samples

The effect of the plastron on the copper samples can be seen more readily in Figure 6.21, by considering the drag difference between the hydrophobic and wetted state. CuC1 shows a relative drag reduction of up to 15% whilst CuF shows a relative drag reduction of up to 8%, with both having a peak drag reduction near the middle of the Reynolds number range explored. The drag reduction is lower for CuF than CuC because of two key parameters: the height of the roughness is smaller for CuF resulting in a thinner plastron and also Table 4.1 shows that the percentage of the surface covered by air-water interface is also reduced. The peak in the drag reduction is either related to the plastron having a larger effect at a certain speed or that the quality of the plastron has degraded through the experiment. The analysis conducted on both spheres and channels in Sections 2.2 & 3.2 as well as theoretical analysis (Phillip, 1972a) suggests that increasing the value of k/L (where k is a length scale related to the roughness, plastron or slip length and L is an external flow scale) will act to increase the potential of a surface to generate slip and produce a drag reduction. Hence, as the Reynolds number increases and the boundary layer becomes thinner, the difference between the scale of the roughness/plastron and the boundary layer will decrease, producing a larger drag reduction. However, at higher speeds the experimental data for CuF and CUC1 shows the opposite trend suggesting a departure away from the idealised surface. The plastron is potentially degrading, either due to the higher shear at high Reynolds number causing the air-water interface to deform and become less

stable or due to the length of time that the surface had been immersed. The degradation of the plastron was also confirmed visually in the tests conducted on CuC1 and captured on camera for CuF. The partly wetted (PW) CuC runs were conducted immediately after the runs for CuC1(H) but starting at the highest Reynolds number rather than the lowest. It is clear in Figure 6.21 that the observed reduction in the quality of the plastron results in a reduction in the magnitude of $P_{\%}$. The re-testing of CuC1 after a few months as CuC2 produced a visibly lower quality plastron in comparison with patches of the surface appearing wetted straight from immersion and discrete bubbles also apparent. It is not clear whether this is because the samples degrade over time through exposure to light or through mechanical abrasion. However, it is likely to be the latter as the carbon carboxylate hydrophobic coating on the copper was found to be damaged when it was touched with transference of the turquoise colour to fingers during sample installation, and in some places the original copper colour could be seen. This coating degradation coincides with CuC2 not producing a significant drag reduction in Figure 6.21, and actually producing a drag increase at higher Reynolds number. This is similar to the effect seen on the hydrophobic sand and ridges where discrete bubbles on the surface resulted in an overall increase in drag and a reduced effect of the plastron respectively.

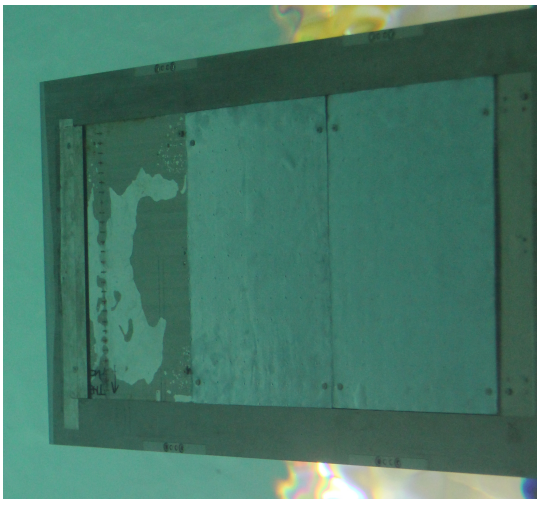

Figure 6.22: Underwater photograph of underside of Plate B with fine copper mesh in hydrophobic state (straight after immersion)

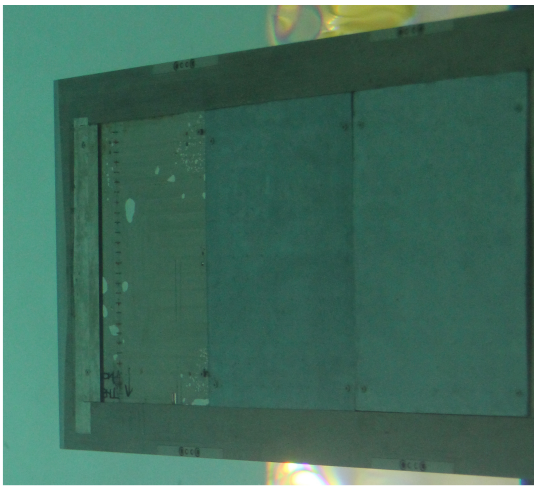

Figure 6.23: Underwater photograph of underside of Plate B with fine copper mesh in hydrophobic state (1.5 hours after immersion)

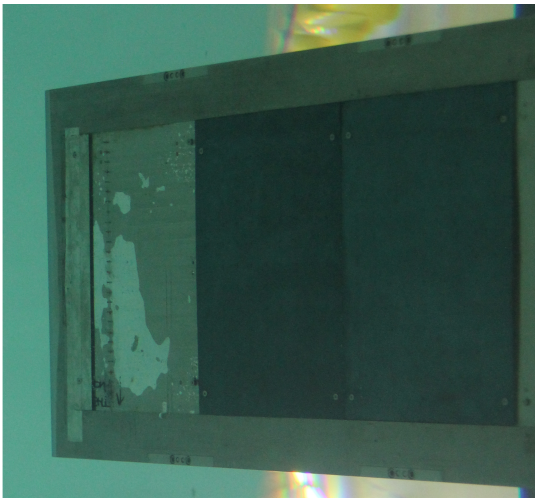

Figure 6.24: Underwater photograph of underside of Plate B with fine copper mesh in wetted state

Figures 6.22, 6.23 & 6.24 demonstrate that the reflectivity from the plastron is reducing over time. It can be inferred from this that the plastron quality is also reducing with immersion time, or at the very least that the state of the plastron is varying. However, the cause of the degradation cannot be determined as there are two possible explanations, with the plastron either degrading through diffusion of gases across the air-water interface or simply being sheared off the surface at high speeds. These two possible explanations are coupled in the experimental setup when using Test Matrix A as the length of immersion time and the maximum flow speed the sample has been subject to both increase linearly with the progression of the experiment.

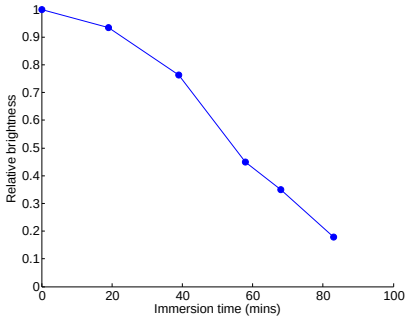

Figure 6.25: Degradation of relative reflectivity of plastron with immersion time

Analysis of photographs taken at various time intervals between Figure 6.22 & 6.23 has facilitated a quantitative assesment of the degradation of the plastron. The photographs were all cropped to include primarily the hydrophobic samples and then the relative brightness of each image is calculated. The lighting conditions within the tank are constant and therefore the brightness of the images is directly related to the relative reflectivity of the plastron and can be plotted against the time at which the photographs were taken as shown, in Figure 6.25. This shows that for CuF the plastron degrades gradually over time and is almost completely removed after 1.5 hours, as the reflectivity reduces to close to the base value. Unfortunately, due to issues with the remote control of the underwater camera no images are available where the surfaces were tested in Test Matrix B and the separate effects of immersion time and flow speed could not be distinguished at depth.

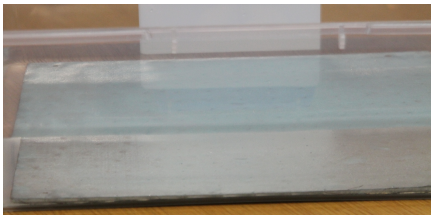

Figure 6.26: Photo of CuF straight after immersion

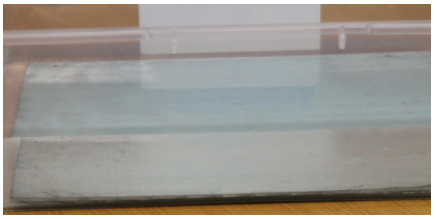

Figure 6.27: Photo of CuF 1hr after immersion

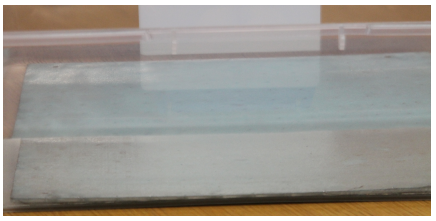

Figure 6.28: Photo of CuF 2hr after immersion

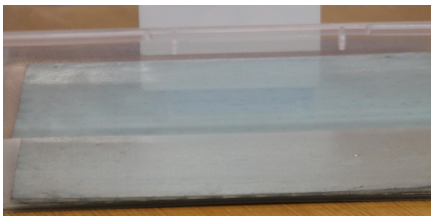

Figure 6.29: Photo of CuF 3hr after immersion

To separate the effects of immersion time and carriage speed time lapse photography was recorded of CuF when immersed in a static container of water. Figures 6.26-6.29 show that the reflectivity of the plastron remains constant over a period of 3 hours, more than double that required for the plastron to degrade in the towing tank. This suggests that the degradation of the plastron is more likely related to the effect of high shear either tearing the plastron away or causing the interface to deform and cause wetting. This is corroborated by recent experimental results which saw a similar effect of the plastron being affected by high shear (Aljallis et al., 2013) and previous immersion tests which suggest that a plastron can be maintained on a surface for at least 400 hours (Poetes et al., 2010) and even up to 160 days on the natural surface of *Notonecta Glauca* (Ditsch-Kuru et al., 2011). Furthermore, Govardhan et al. (2009) demonstrated that a plastron could last up to 5 hours, but that this reduced to 40 minutes under the application of pressure and shear.

6.2 Hot film results

6.2.1 Time mean hot film results

Hot film gauges were used throughout the experimental testing program, with experience in their application growing with each test session. The gauges were used to explore the state of the boundary layer (laminar or turbulent), mean shear stress, higher order statistics and analyse the frequency content of the shear stress fluctuations. The hot films were initially tested in the Lamont tank to determine the transition location on the plates. This was achieved by placing the hot film gauge at various streamwise locations (x_G), collecting data for a range of speeds and exploring the frequency content in the signal and the intermittency.

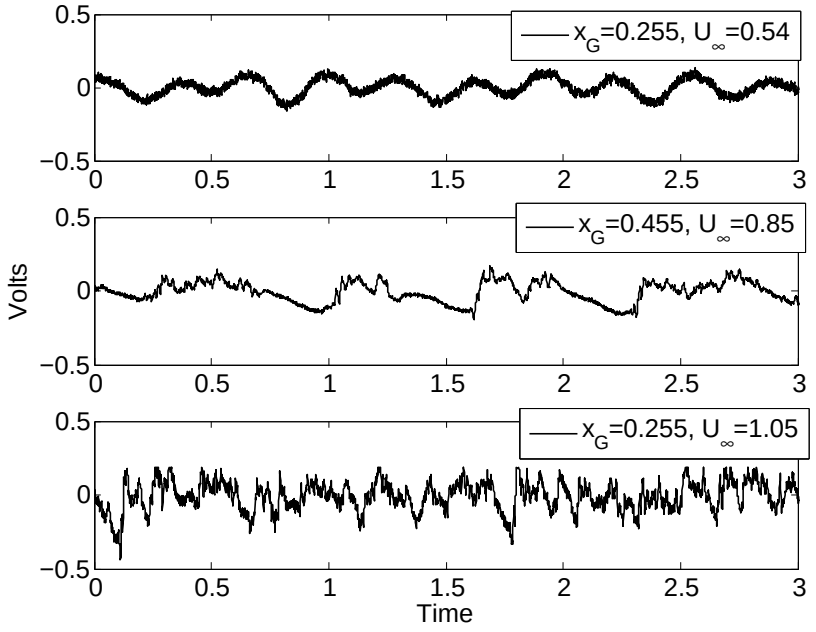

Figure 6.30: Raw hot film voltage signals for a variety of speeds and gauge locations demonstrating transition

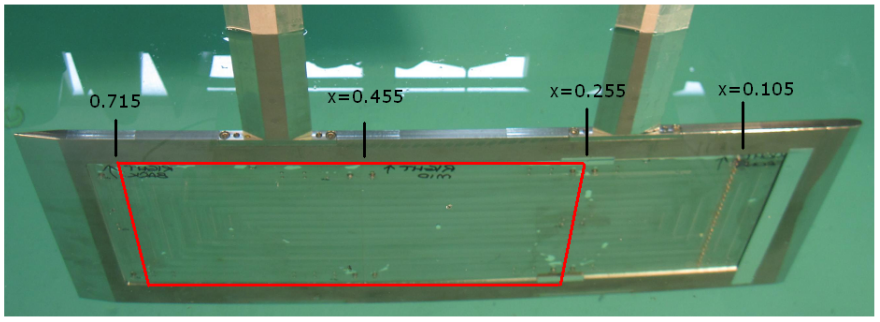

Figure 6.31: Annotation of approximate hot film locations (red=sample area)

Each hot film was placed 10mm downstream of the end of each of the sample surfaces, so that there was 10mm of smooth surface between each of the samples and the hot film measurement location. This was related to the physical size of the sensor and could not be reduced.

Figure 6.30 demonstrates a laminar[2], transitionary and fully turbulent signal. The location of the turbulators and hot film gauges are demonstrated in Figure 6.31, with the turbulators at $x = 0.105$m, the hot film gauges tested at

[2]The low frequency oscillations are a direct result of the mounting at the Lamont tank which was found to flex and oscillate at low speeds

$x_G = 0.255$ & 0.455m for determination of the transition location and then placed at $x_G = 0.715$m for the measurement of shear stress for the rough and hydrophobic samples. Figure 6.30 shows that at a speed of 0.85m/s the transition location is approximately 0.455m as the signal is intermittent suggesting the boundary layer is transitional (Binns et al., 2009). With a slight increase in speed to 1m/s the transition location is found to move in front of the hot film gauge at $x = 0.255$m such that the signal is fully turbulent. This shows that above a speed of 1m/s transition is occurring before the replaceable sample area (see area marked in red in Figure 6.31) and hence the roughness or hydrophobicity will not influence the transition location.

The results from the Lamont tank also provide a validation of the calibration procedure described in Section 5.5.3. The use of a variety of hot film locations ensures that the calibration is accurate across a range of values of shear stress and for both laminar and turbulent flow. Figure 6.32 shows that there is a linear trend between $\tau_x^{1/3}$ and E^2.

The calibration curves are slightly different between the laminar and turbulent data suggesting that a calibration for lamianr flow should not be used in turbulent flow. The difference between the two calibration curves is smaller than is perhaps expected due to the increased convection in a turbulent boundary layer. However, the data presented in the following sections is primarily focused on turbulent flow and hence the use of a turbulent calibration should be sufficient. A small amount of data is presented for laminar flow using the turbulent correlation, but this should not influence the understanding of the results as the difference between the two calibrations is small and the differences presented between laminar and turbulent flow are much more significant.

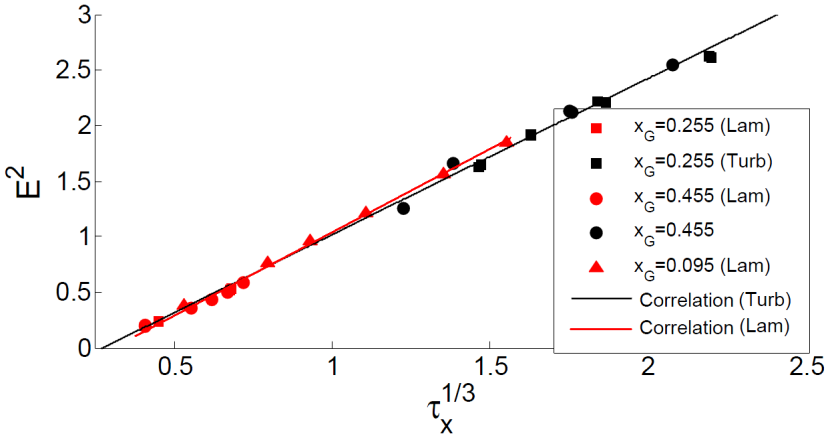

Figure 6.32: Hot film calibration for laminar and turbulent boundary layers with gauges at different streamwise locations in the Lamont tank

The hot film gauges were then applied at $x_G = 0.715$ in the SSU Tank to explore the effect of the hydrophobic samples on the shear stress. The location of the gauge ensured that the sensing element was as close as possible to the downstream end of the hydrophobic samples, however due to the size of the backing sheet to the gauge, the element itself was located 10mm (approximately $2 - 3\delta$) downstream of the end of the sample. With the hot film located at $x_G = 0.715$ the upstream samples provided a streamwise fetch of 400mm, corresponding to approximately 8-12 large eddy turn overs.

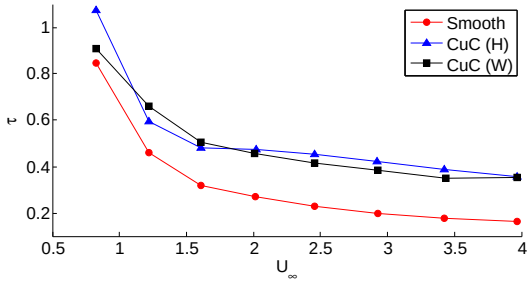

Figure 6.33: Variation of local shear stress with Reynolds number for a smooth, rough and hydrophobic surface ($x_G = 0.455$)

An example of the variation of the shear stress with Reynolds number is shown in Figure 6.33 with the curves following the expected trend with a similar shape to the variation of the drag coefficient. The data for the rough (wetted) surface shows an increase in the shear stress above that for a smooth surface as would be intuitively expected. The hydrophobic surface shows an increase in the local shear stress in comparison to the wetted surface, although the data for CuC1 showed a relative decrease in drag due to the presence of the plastron.

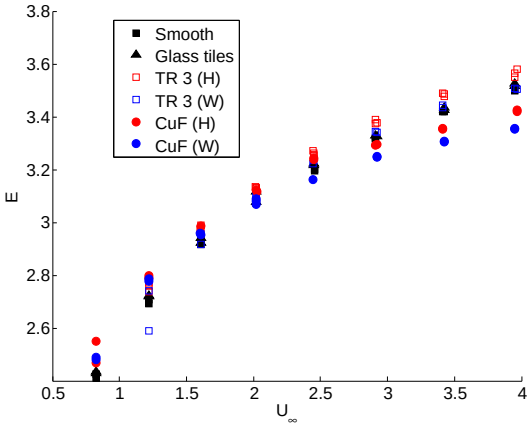

Figure 6.34: Mean hot film voltage for a range of rough and hydrophobic samples

Figure 6.34 demonstrates the increasing voltage across the heated element as the speed of the carriage is increased, showing that a higher voltage is required to maintain the hot film at a constant temperature due to the increased heat conduction rate. The raw hot film voltages are initially presented to show that the conclusions drawn are not an artifact of the calibration and data analysis conducted. The data shows that there is an increase in voltage above that for a smooth surface for TR3 in both a hydrophobic and wetted state, whilst the data for CuF shows the opposite trend with a relative decrease in the voltage. However, both show a similar trend when considering the effect of the plastron, with the hydrophobic state producing an increase in voltage in comparison to the wetted state for each case.

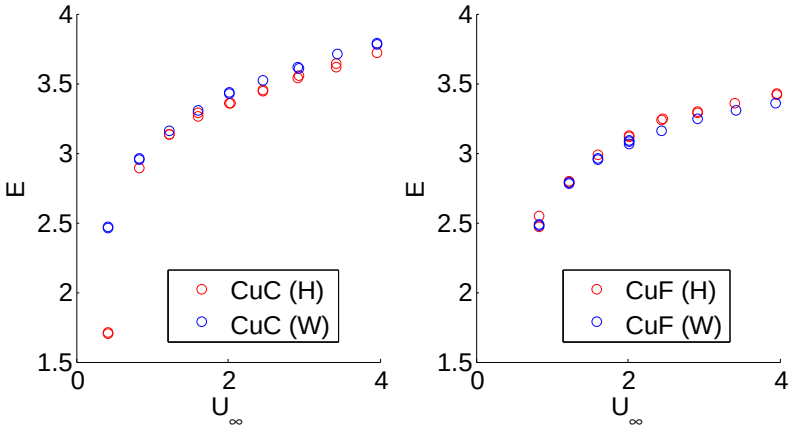

Figure 6.35: Raw hot film voltage variation with speed for CuC1 and CuF

The effect of the plastron as shown in Figure 6.34 is consistent, however the data from Figure 6.35 does not show the same trend; the plastron produces a decrease in the hot film voltage for CuC whilst it produces an increase in the hot film voltage for CuF. Both of these hydrophobic samples produced a drag reduction, but the trends between the drag measurements and hot film measurements are not consistent. To explore the effect of the plastron further, a similar parameter to $P_{\%}$ is introduced which is based on the relative difference between the shear stress in the hydrophobic and wetted state ($\tau_{\%}$).

$$\tau_{\%} = \left(\frac{\tau_H}{\tau_W} - 1 \right) \times 100\% \tag{6.4}$$

Upon investigation of the hot film data for the hydrophobic ridges and copper mesh it was determined that the plastron caused a consistent effect on the shear

stress but that this effect differed depending on whether the collected data was part of experiments run in October 2012 or in March 2013.

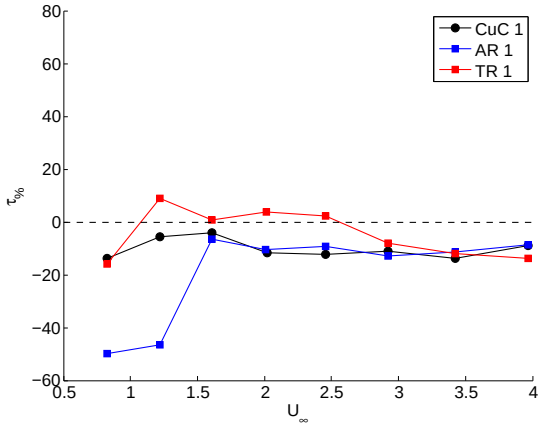

Figure 6.36: Relative effect of plastron on the shear stress in experiments conducted in October 2012

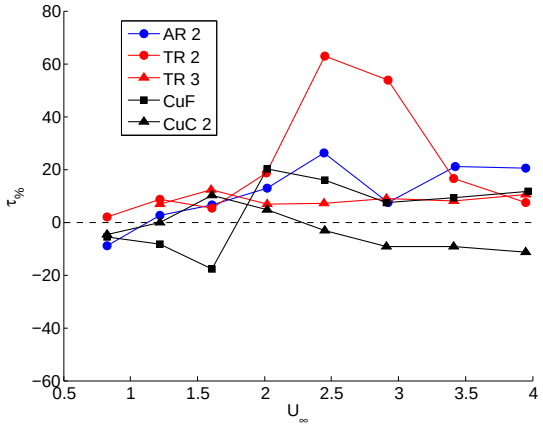

Figure 6.37: Relative effect of plastron on the shear stress in experiments conducted in March 2013

Figure 6.36 shows that the results collected in October 2012 primarily demonstrate a reduction in the shear stress due to the presence of the plastron, which correlates with the presence of a plastron producing a relative reduction in drag. However, Figure 6.37 demonstrates the opposite effect with surfaces that produced a relative drag reduction showing a relative increase in shear stress (AR2, TR2, TR3 & CuF) whilst the surface that produced a relative drag increased resulted in a reduction in the shear stress. This suggests that there is a systematic difference between the results collected on different dates even though the same physical hot film gauge was used for both experiments.

6.2.2 Frequency analysis

The time averaged values can be useful in determining the average effect of roughness and hydrophobicity on the shear stress on a flat plate. However, the turbulent fluctuations are also of interest and can help provide a deeper insight into the flow structures in the boundary layer.

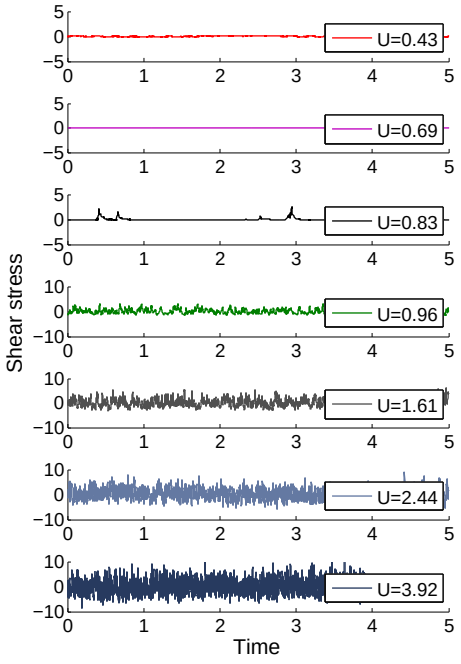

Figure 6.38: Example of hot film signals (mean adjusted) for a range of flow speeds for a smooth surface at $x_G = 0.255$m

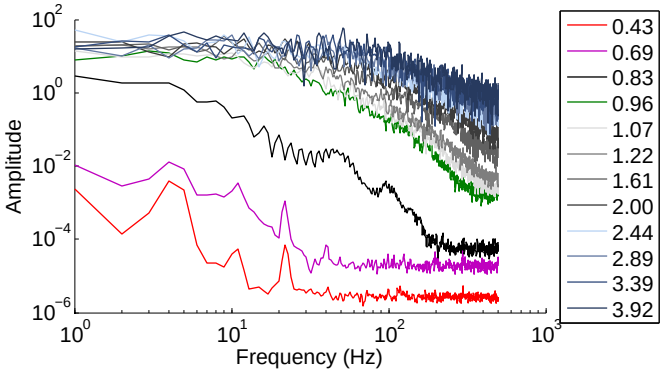

Figure 6.39: Frequency content of some of the hot film signals from Figure 6.38 with same legend for the signals shown

Figures 6.38 & 6.39 show examples of hot film signals for a smooth surface in both the time and frequency domain respectively, with the FFT conducted as detailed in

Section 5.5.3. Figure 6.38 demonstrates that the turbulent fluctuations increase in magnitude as the speed is increased. The shear stress fluctuations are found to be approximately constant when scaled by the mean value and fall in the range $0.21 < \tau_x'/\overline{\tau_x} < 0.25$ which agrees with Eckelmann (1974) who showed that the RMS turbulent fluctuations should approach 0.25 at the wall, although Alfredsson et al. (1988) demonstrated the dependence of the RMS fluctuations on the relative size of the sensor. The skewness (0.52) and flatness (3.12) of the turbulent fluctuations also match well to the range of 0.51-0.58 and 3.0-3.3 respectively, as compiled by Sreenivasan and Antonia (1977). The positive skewness of the distribution signifies that there are relatively few large negative events.

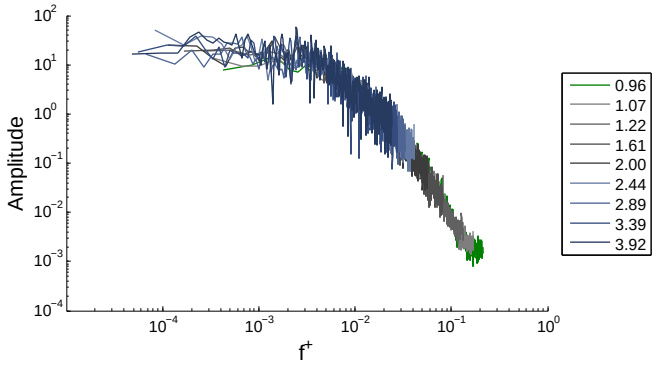

Figure 6.40: Frequency content of hot film signals from Figure 6.38 scaled in wall units

The turbulent signals from Figure 6.39 can also be scaled into wall units ($f^+ = f\mu/\tau_w$) and collapse well as shown in Figure 6.40. This shows that the turbulent fluctuations are self similar as previously shown by Hu et al. (2006) & Keith and Bennett (1991) for example. The frequency content can also be shown to follow the typical $-5/3$ power law as shown in Figure 6.41. The effect of increasing the surface roughness is to increase the frequency content especially at high frequencies, but the data still follows the same power law.

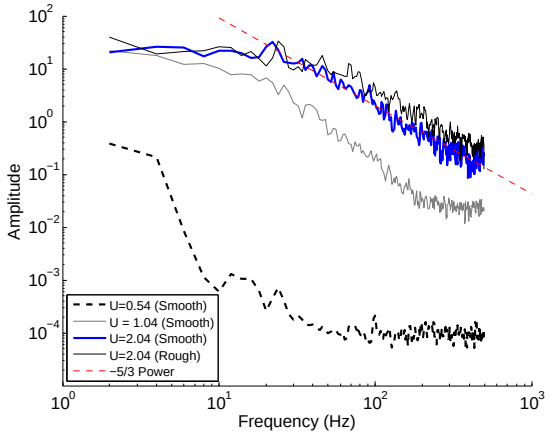

Figure 6.41: Frequency content of laminar, turbulent and rough turbulent shear stress fluctuations

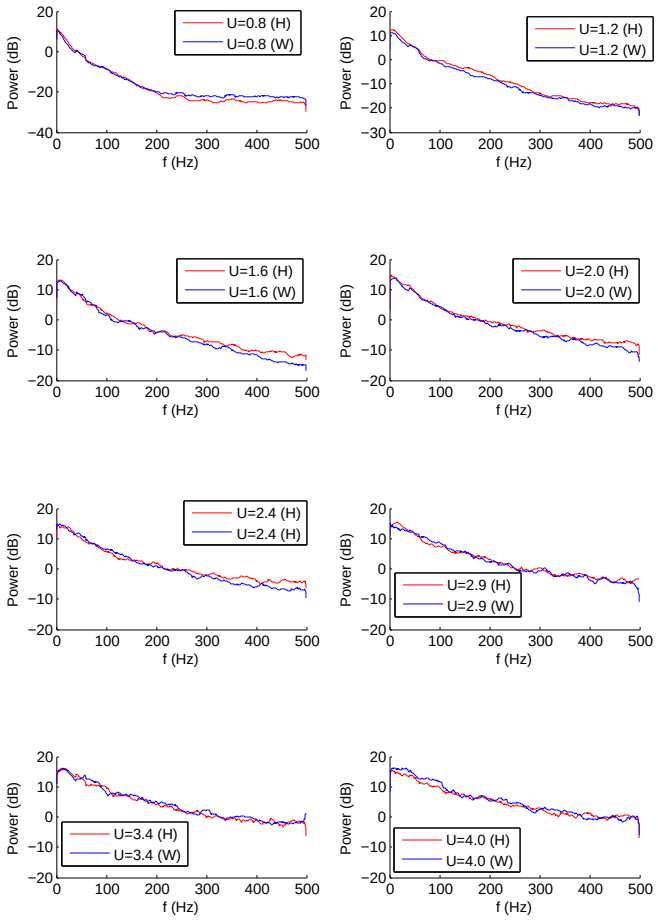

Figure 6.42: Effect of plastron on the frequency content of turbulent fluctuations for CuF

The effect of the plastron on the frequency content of the turbulent fluctuations for CuF can be seen in Figure 6.42. There is an apparent increase in the high frequency structures for the speed range ($1.2 < U_\infty < 2.6$m/s) which corresponds to the largest drag reduction, however for the other speeds there is no apparent change in the frequency content.

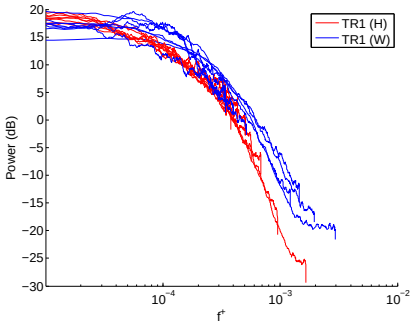

Figure 6.43: Effect of plastron on frequency content of shear stress in wall units for TR1

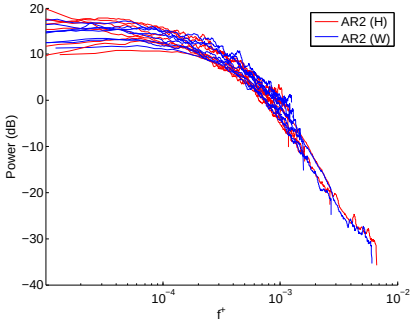

Figure 6.44: Effect of plastron on frequency content of shear stress in wall units for AR2

Conversely, Figures 6.43 & 6.44 demonstrate that the effect is not consistent across all of the samples that achieve a relative drag reduction, with TR1 producing a decrease in the energy in the high frequency content and AR2 showing no effect of the plastron when scaled in wall units. A similar degree of uncertainty is apparent in the effect of the plastron on the probability distribution of the shear stress fluctuations, with the majority of surfaces producing a narrower distribution with fewer high magnitude events (as shown in Figures 6.45 & 6.46), but CuC breaks the trend and shows a wider distribution.

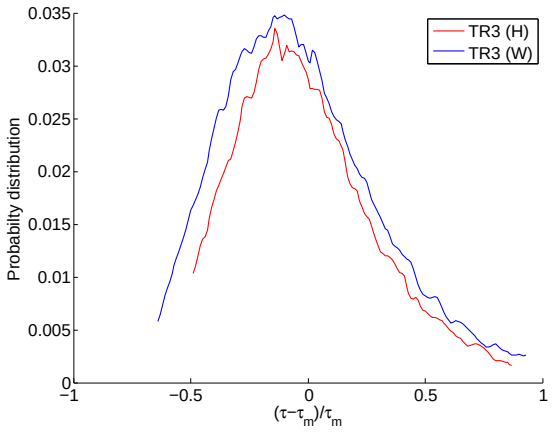

Figure 6.45: Effect of plastron on probability distribution of shear stress fluctuations for TR3

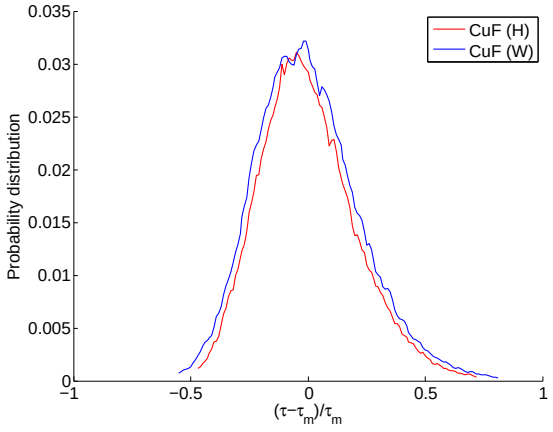

Figure 6.46: Effect of plastron on probability distribution of shear stress fluctuations for CuF

The effect of the plastron on the drag, mean shear stress, frequency content and shear stress distribution is compiled in Table 6.3 for all of the hydrophobic samples where hot film data is available. The columns for frequency content and distribution are worded to describe the relative effect of the plastron, with for example 'narrower' referring to the hydrophobic shear stress distribution being narrower than the wetted case.

For the various AR and TR it is apparent that there is a connection between the sign of $\tau_{\%}$ and the effect on the frequency content. For example for AR1 the presence of the plastron produced a reduction in the mean shear stress and a reduction in the energy at each frequency (at low speeds) whilst the opposite is true for AR2. This discrepancy was found to be dependent on the calibration as it

Surface	$P_{\%}$	$\tau_{\%}$	Effect on frequency content	Effect on distribution
TR1	-ve	-ve	Lower at all f	Reduced skew at low U_∞
TR2	-ve	+ve	None	Narrower
TR3	-ve	+ve	Higher at high f	Narrower
AR1	-ve	-ve	Lower at all f and low U_∞	None
AR2	-ve	+ve	Higher at high f and low U_∞	Narrower
CuF	-ve	+ve	Higher at high f at mid U_∞	Narrower
CuC1	-ve	-ve	Higher at high f and low U_∞	Wider
CuC2	+ve	-ve	None	None

Table 6.3: Effect of the presence of a plastron on the hot film measurements for a variety of samples

is non-linear; considering an analysis on the raw data demonstrated that the effects of hydrophobicity on the frequency spectrum are minimal. Effectively the lower mean shear stress value for AR1 resulted in a reduced scaling of the fluctuations and hence resulted in a reduction in the energy content of the spectrum. The effect of the plastron on the shear stress distribution is more consistent, with the hydrophobicity inducing a narrower distribution of the fluctuations in the majority of cases. It was found that the effect on the plastron on the shear stress distribution was not affected by the calibration (although the calibration does induce a consistent skew, as suggested by Sreenivasan and Antonia (1977)).

6.2.3 Hot film discussion

It is clear that hot film gauges can be accurately used to measure the shear stress in a smooth turbulent boundary layer. However, the conflicting results presented here suggest an inherent difficulty in the usage of such sensors in measuring the effect of hydrophobicity.

It is known that a boundary relaxes after a step change in roughness (see Section 5.2.2), with the relaxation to the new boundary layer state occurring over a few boundary layer thicknesses. The step change in roughness results in a sudden retardation or acceleration of the flow close to the surface for a smooth-to-rough and rough-to-smooth transition respectively. This means that although the roughness acts to increase the local shear stress at the location of the roughness, it causes a reduction in the local shear stress in the relaxation region of a boundary layer in a rough-to-smooth transition. A hot film gauge placed within this relaxation region will therefore show a counter-intuitive reduction in the local shear stress due to the addition of roughness, even though the roughness will act to increase the drag.

This trend was explored numerically through CFD simulations of Plate B with additional roughness at the location of the samples as discussed in Section 5.5.3. A similar, opposite trend was also observed numerically with the application of the Navier-slip condition to simulate the effect of hydrophobicity; the introduction of slip at the surface, reduced the local shear in the region where the Navier-slip condition was applied, but resulted in an increase in the shear in the downstream vicinity of the step change from Navier-slip to smooth surface. This trend was shown to be consistent regardless of whether a combination of roughness and slip was applied, with a surface producing a relative reduction in drag resulting in an increased local shear stress downstream of the sample. Therefore, a hot film gauge placed 10mm downstream of the end of the hydrophobic samples tested should demonstrate an increase in the local shear stress if a drag reduction is evident.

6.3 Discussion & evaluation

An experimental rig has been developed to measure the viscous drag of a variety of superhydrophobic surface coatings when immersed in water. Refinement of the experimental procedure, including the use of turbulators improved the repeatability of the results to achieve a best estimate of error of 0.8% in drag measurements and 4% in hot film measurements. The experimental setup was found capable of accurately measuring the drag on a smooth plate and sand grain roughness was used to further validate the setup, with the effect of the roughness collapsing well in wall units.

The effect of hydrophobicity was explored by considering the percentage drag difference to a smooth surface ($S_{\%}$) and to the same rough surface without the presence of a plastron ($P_{\%}$) by wetting it with ethanol. An overall drag reduction of up to 10% was exhibited for transverse hydrophobic ridges, with a maximum relative drag reduction due to the presence of the plastron of up to 16%. An estimated slip length can be extracted by comparing the drag reduction to the simulations conducted in Section 5.3.3 using the Navier-slip condition.

The data in Table 6.4 demonstrates the first experimental, relative drag reductions on a range of superhydrophobic surfaces using a consistent experimental setup. The use of ethanol[3] to wet out the surfaces also allows the first direct comparisons of the viscous drag of superhydrophobic surfaces with and without the effects of

[3]Initially suggested and used by McHale et al. (2009) on superhydrophobic spheres

Surface	min($S_{\%}$)	min($P_{\%}$)	Estimated slip length
MS (vert)	15	-1.5	30μm
MS (horz)	15	-3	65μm
AR	-7	-4.5	100μm
TR	-10	-9.5	235μm
CuC	-3	-16	475μm
CuF	0	-8	195μm

Table 6.4: Estimated slip lengths from measured drag reductions using numerical simulations with Navier-slip

hydrophobicity and the resultant plastron. The conclusions that can be drawn from this study are discussed shortly. However, it is pertinent to first discuss the discrepancies and anomalies in the data presented in Section 6.1.4 & 6.1.5 to ensure that the conclusions are drawn from accurate data.

There were two apparent anomalies in the measured drag data; the first is that the coarse copper mesh resulted in a change in drag that was not consistent with increasing Reynolds number (see Figure 6.20), and the second is the discrepancies between the different sets of ridged samples (see Figures 6.15 & 6.16). These anomalies appear in both the hydrophobic and wetted state and hence cannot be attributed to an effect of the plastron.

The coarse copper mesh demonstrates an increasing $S_{\%}$ with Reynolds number but only until a certain speed, where the trend is reversed and $S_{\%}$ decreases with Reynolds number. The first part of the trend is consistent with the typical effect of roughness; at higher speeds the boundary layer is thinner, with an increased turbulent friction velocity (u_τ) and hence an increase in the effective roughness in wall units (k^+). The second part of the trend suggests that the effect of the roughness is reducing with increased Reynolds number, which is contrary to the monotonic increase seen in Figure 5.4 (ignoring the special case of riblets). One possible explanation for this unexpected trend is that the increase in Reynolds number may cause a transition between a typical k-type and a d-type roughness, where the roughness elements act to shelter each other such that recirculation cells develop within the cavities. Leonardi et al. (2003) demonstrated using DNS that for transverse bars there is a peak in both the pressure and viscous drag at a width-to-height ratio of $4 < w/k < 8$, with Zhang et al. (2011) showing it is also true for mesh type roughness. Below this range the roughness elements shelter each other such that circulation cells develop within the roughness elements as seen in Figure 6.47, resulting in a drastic decrease in both the viscous and pressure drag. Furthermore, comparison of two different DNS simulations (Leonardi et al., 2003;

Ashrafian et al., 2004) suggests that a change in Reynolds number or the ratio k/δ can result in a modification of the critical value of w/k.

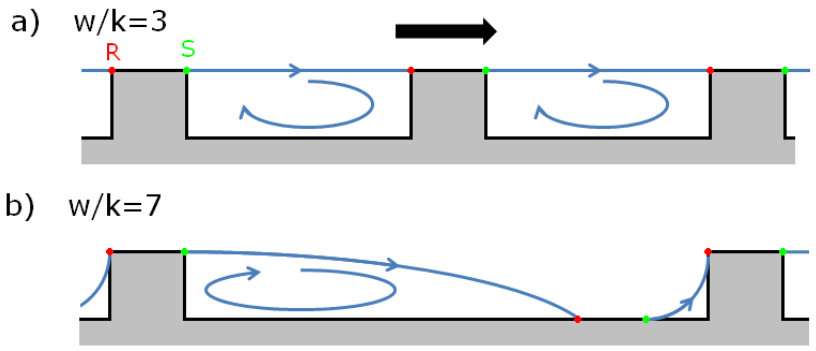

Figure 6.47: Schematic separation (S=green) and reattachment (R=red) locations for a) $w/k = 3$ and b) $w/k = 7$

The coarse copper mesh structure has a w/k close to the critical range of 3.9, with values smaller than the critical range having the largest effect on the drag. The CuC surface is a complex, three dimensional and multi scale structure, with a layer of fine copper mesh beneath the exterior coarse copper mesh and nano-flowers coating the entire surface. It is possible that this composite structure is acting as a k-type roughness at low speeds and transitioning to a d-type roughness at higher speeds resulting from a difference in the sheltering. At low speeds the flow separates from the coarse mesh elements and reattaches on the underlying fine copper mesh before the next coarse filament, and then as the Reynolds number increases the reattachment location moves downstream, producing a similar effect to a reduction in w/k, with the subsequent roughness element sheltered by the preceding and a reduction in both pressure and viscous drag components. Finally, the downward trend of $S_{\%}$ at high Reynolds numbers for CuC1 is apparent in both CuC1(W) and CuC2(W), with tests conducted on different dates and the data checked for systematic errors. Overall, this suggests that such a trend has a physical origin and that may not be anamalous.

The other anomaly that needs to be considered is that the different sets of ridged surfaces did not produce the same drag values, with discrepancies of up to 25%. This is clearly an anomaly as different sets of nominally the same surface should produce consistent results. However, as the experimental results are precise in each case - with the results being repeatable at each data point and trends being consistent for each surface - and systematic corrections to the data consistent for each case, it is clear that the change in drag between the samples is related to

difference between each sample. Each sample was sufficiently flat to be of no significance, but during testing it was observed that it was difficult to mount the ridged samples consistently. Each sheet of ridges was produced from 20-30 glass slides tiled together and there was found to be inconsistencies in the total size of each sheet. For example, in the streamwise direction each sheet had four 5cm tiles to cover a 20cm space (see Appendix F), but in some cases the slides protruded over the edge of the backing sheet. It is unclear whether the glass slides were inprecise in size, or whether the protrusion is a culmination of small gaps between successive tiles over a sheet to produce a significant increase in size. These edge protrusions meant that in some cases the tiles had to be slightly overlapped to get the samples to fit into the plate as shown in Figure 6.48, producing a slight protrusion of the tiles in the wall normal direction.

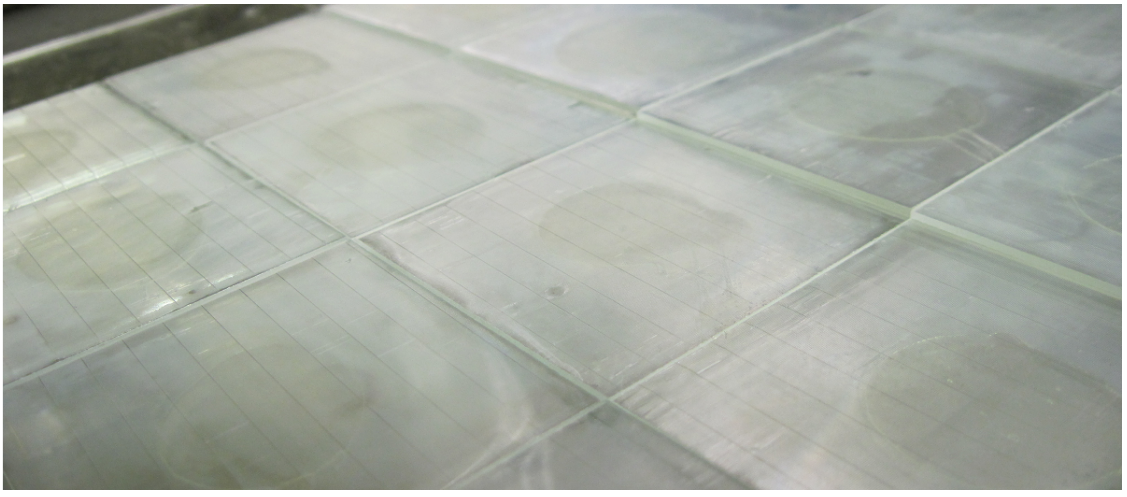

Figure 6.48: Photograph of protrusion of glass tiles demonstrating difficulty in mounting of the samples

The effect of a step on the drag of a surface can be estimated based on experimental correlations calculated for a range of step conditions. Gaudet and Winter (1973) showed that for a forward facing step the drag coefficient of the step (C_{FFS}) depends on the step height in wall units (h^+) and the undisturbed local skin friction coefficient (C_f):

$$\frac{C_{\mathrm{FFS}}}{C_f} = 60 \log h^+ - 80 \tag{6.5}$$

A similar extensive study for backward facing steps was reported by Higazy and Cockrell (1984) and allows the drag coefficient of a backward facing step (C_{BFS}) to also be estimated:

$$\frac{C_{\mathrm{BFS}}}{C_f} = 15 \log h^+ - 8 \tag{6.6}$$

These equations can then be used to calculate the effect of a step on the drag of a smooth surface and determine whether such a misalignment of the surfaces could account for the magnitude of differences evident between the samples. A similar scale effect was also demonstrated by Young and Paterson (1981) for small transverse cavities, much the same as would be evident between two sample plates in the current experimental setup. Estimating a step height of 1mm for both a forward and backward facing step - suggesting that one of the samples is slightly proud of the surrounding areas - produces a change in the drag by up to 6%.

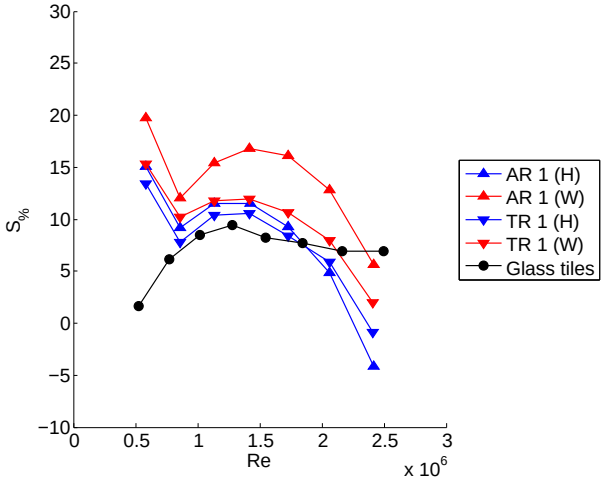

Figure 6.49: Effect of AR and TR on drag in comparison to a smooth surface after the data has been corrected to allow for a step

Figure 6.49 demonstrates the effect of including the effect of a 1mm step at the start and finish of the sample plates for the smooth surface and can be compared to Figures 6.15 & 6.16. Although the smooth surface was repeatable between different test sessions, the same physical sample perspex sheets were used for each test, suggesting that a step or gap between the plates could have been consistently appearing in each of the smooth data sets. The data in Figure 6.49 shows that the overall drag reduction of up to 9.5% is much reduced by the inclusion of the effect of a step. It is apparent therefore that small steps, or gaps between the samples can have a large influence on the values of $S_{\%}$. This is especially true for the hydrophobic ridge samples where it was notably difficult to achieve a smooth transition between the sample sheets and the plate.

These protrusions will clearly result in a systematic error in the drag that will be consistent for each sample in both the hydrophobic and wetted state (as the sample was tested back to back without removing the sheets), but will introduce a random error when comparing the different samples. This therefore does not influence the precision of the results or the ability to determine the effect of the plastron through $P_{\%}$, but does influence the accuracy of the results in terms of $S_{\%}$. This is corroborated by the consistency in the effect of each sample in terms of $P_{\%}$, when taking into consideration the effect of discrete bubbles on the surface.

What remains of interest is that the samples TR1(W), AR1(H) and AR1(W) produced an overall drag reduction, but with difficulties in determining an accurate value of $S_{\%}$ the reliability of these drag reductions is unclear. However, any systematic error in the mounting of the plates can only act to increase the drag of the surface in comparison to a smooth surface; any protrusion, recession, gap or misalignment will result in an increased disturbance of the flow and hence increase the drag. Figure 6.49 demonstrates that even if a correction for a 1mm step is applied to a smooth surface, a negative value of $S_{\%}$ is still evident for both AR1 and TR1. Furthermore, although difficulties were faced in terms of achieving a flat surface, it is considered that a 1mm step is quite large. This suggests that any reduction in drag in comparison to a smooth surface will likely be related to the drag reducing properties of the surface rather than an inaccuracy in the drag measurement as a result of difficulties mounting the sample, although this inaccuracy makes the magnitude of the overall drag reduction difficult to determine.

In conclusion, it is clear that the superhydrophobic surfaces have demonstrated an ability to reduce the viscous drag in turbulent boundary layer flow, with each of the surfaces tested on Plate B showing a relative drag reduction due to the presence of the plastron of up to 16%. TR1 and AR1 also each potentially showed evidence of an overall drag reduction, with TR1 showing the largest effect with $S_{\%} = 9.5\%$ and AR1 demonstrating an augmented riblet effect of up to 4.5%. This study therefore acts as a proof of concept, in demonstrating that superhydrophobic surfaces are capable of producing a reduction in the viscous drag in high Reynolds number flows. The testing of a wide range of superhydrophobic surfaces allows comparisons to be made about their relative efficiency and practicality in producing a drag reduction and determining the key features of the surfaces that contribute to the drag reduction mechanism. Further surfaces can be developed in the future based on the increased understanding of the effects of the plastron.

The main conclusion that can be drawn from consideration of all of the drag measurements is that it is the presence of a plastron on the surface which is causing a drag reduction, as all surfaces showed an increased drag once the plastron has been removed. This suggests that the plastron or air layer is creating the expected effect and acting to lubricate the surface with a less viscous fluid, allowing non-zero velocity at the air-water interface and resulting in a reduction in shear stress.

Another conclusion that can be drawn is that the quality of the plastron is also a key consideration and can impact on whether a drag reduction is achievable. In a horizontal configuration it was demonstrated that MS produced an increased effect of the plastron in producing a drag reduction. In this configuration the effect of buoyancy is constant, unlike in a vertical configuration where it acts to redistribute the majority of the plastron to the upper edge. Confocal images of the MS surface showed that the larger sand grains were protruding above the air-water interface and with a reduced thickness of the plastron across the majority of the surface area, the number of protrusions and hence the effective roughness would increase. A similar effect was seen with the G1, TR2, AR2 and TR3 surfaces where discrete bubbles appeared on the surface. The main consequence of such bubbles is that as they protrude above the surface they act to increase the pressure drag on the surface, negating some of the potential drag reducing effect of the plastron. This suggests that to improve the drag reduction a superhydrophobic surface should support a plastron which produces a flat composite interface, where neither the roughness elements or the air-water interface cause protrusions into the flow field. This is confirmed by the confocal images of the ridged hydrophobic samples, which demonstrate a flat composite interface within $\approx 20\mu m$ and facilitated TR1 and AR1 in achieving an overall drag reduction.

The quality of the plastron was also found to vary with the effect of high speeds and high shear, with both confocal microscopy and time lapse photography demonstrating that the degradation of the plastron was not due to immersion time. CuC1 and CuF both showed a peak in the relative drag reduction potential which was deemed to be related to the effect of high speed runs on the plastron. The reduction in plastron reflectivity shown in underwater photographs and the reduced effect of the plastron of CuC1 in a partly wetted state confirm that high speed runs cause a degradation of the plastron. This apparent critical speed does not appear in the results for the ridges, with each sample showing an approximately consistent increase in the effect of the plastron with Reynolds number. This is likely to be due to the smaller scale of the ridged sample giving an increased stability of the interface; with a smaller length scale the air-water interface will experience a

reduction in the Weber number ($\mathrm{We} = \rho u^2 l/\gamma$), which suggests a reduction in the effects of inertia in comparison to the surface tension effects.

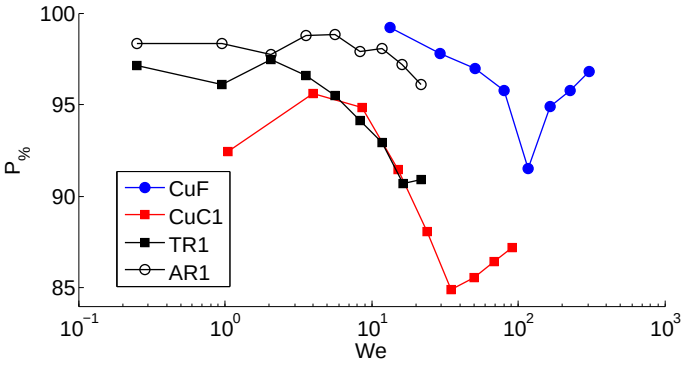

Figure 6.50: Effect of Weber number on relative drag reduction produced by a plastron

Figure 6.50 shows that there is a critical Weber number range (We $\approx$ 30 for CuC1 and We100 for CuF) above which the effect of the plastron is reduced. The Weber number limit suggests that the plastron is deforming under high shear and results in wetting of the surface. This is consistent with Busse and Sandham (2012c) where an increase in the Capillary number ($\mathrm{Ca} = \mathrm{We}/\mathrm{Re}$)[4] resulted in an increase in the deformation of bubbles trapped on a wall in Couette and Poiseuille flow and a related increase in the drag. This demonstrates the original concern with this project as a whole, which was whether or not it would be possible to scale up a superhydrophobic surface, due to the potential limitations of scale on the ability to retain a plastron. Clearly, the roughest surfaces tested have shown that such a limit does exist and the exact limit will depend on the surface geometry. However, it is apparent that surfaces above a scale of 1mm will struggle to retain a plastron when subjected to high flow speeds.

A range of comparisons can be made between the effect of the surfaces explored in this study to facilitate the future design of superhydrophobic surfaces. CuC was shown to produce a larger drag reduction than CuF, and this was linked to the larger scale of the roughness producing a thicker plastron. The thicker plastron results in a closer matching of the scale of the boundary layer to the thickness of the plastron and results in increased slip as demonstrated numerically in Chapter 3. However, the Weber number limit suggests that the roughness of superhydrophobic surfaces cannot be made much larger than the scales of CuC and still be able to

[4]The Weber number varies with u^2 whilst the Reynold number varies with u, so in this experimental setup, an increased speed results in an increase in Ca, We and Re

support a plastron; hence it is unlikely that further gains could be achieved using a larger scale of surface roughness. Furthermore, comparing the results of CuC with MS, suggests that it is necessary but not sufficient for a superhydrophobic surface to have a large scale of roughness if it is to generate a large drag reduction. It is apparent that a random rough surface does not perform as well at producing a drag reduction as a structured surface, but it is not clear whether the random arrangement reduces the potential for generation of slip at the surface, or whether the increase in drag due to the random protrusions through the interface is the primary effect.

The variation of the contact angle on the surfaces also demonstrates that a high contact angle is necessary to maintain a high quality plastron. The contact angle of G1 and G2 when coated with Granger's solution is relatively high but covers a wide range (102-133° and 108-140° respectively), furtheromore observations during testing showed that the longevity of a plastron on these samples was poorer than the other samples. The same Granger's solution was used to coat the hydrophobic ridges and both the sand and these ridged samples performed poorly in some cases due to bubbles appearing on the surface. This suggests that the relative performance of these surfaces could be enhanced if the hydrophobic coating were improved to produce a stable, higher contact angle. Improving the contact angle of the surface and using a second scale of roughness would result in a higher quality plastron and make the surface less susceptible to wetting. Although these concepts were incorporated into the design of the copper surfaces relative improvements could be made, with many sources quoting contact angles close to 180°(Gao and McCarthy, 2006; Park et al., 2010; Hsu and Sigmund, 2010). Furthermore, the multi-scale roughness surfaces tested in this study (CuC and CuF) successfully fulfilled the design criteria of using a second layer of mesh to act as a reservoir of air and retained the best quality plastron of the surfaces studied.

A comparison between the relative effects on both $S_{\%}$ and $P_{\%}$ by the two copper surfaces suggests that the increase in scale of the roughness acts to increase both the relative drag increase due to the increased roughness and the increase in the drag reduction due to the thicker plastron. Therefore, to improve the overall effect of the surface on the total drag reduction it may be more important to optimise the surface structure rather than modifying the scale. The transverse and aligned ridges showed an overall drag reduction, so it is logical to attempt to optimise the design of these surfaces further. The simulations conducted in Chapter 2 suggest that to improve the slip length of the surface the percentage of surface area covered by air-water interface can be increased.

Overall, it appears that a surface could be designed to produce an improved effect of the plastron and hence a larger drag reduction. The surfaces designed in this study were chosen initially with ease of manufacture in mind, so that a wide range of surfaces could be developed. Future testing can now focus on a narrower range of surfaces, with more time and funds spent on creating more complex samples as this Thesis has demonstrated that the presence of a plastron can produce a reduction in drag. Based on the conclusions drawn above it is apparent that an optimised version of the aligned and transverse ridges would potentially produce an increased drag reduction with the following improvements:

1. Increased structure size, in the range $200 - 500\mu$m to produce the thickest plastron possible within the Weber number limits
2. Increased contact angle to improve hydrophobicity and plastron retention.
3. Increased percentage of surface area covered by air-water interface to improve the effective slip length.
4. Additional dual scale roughness to improve contact angle and aid in supporting the plastron.
5. Increased depth of surface roughness to provide a reservoir of air.

It is also necessary to improve the manufacturing error margins to ensure that the samples can be mounted into Plate B to produce a continuous and flat surface. These improvements could possibly be achieved by machining a copper substrate with regular grooves and then using an approach similar to that to coat the CuC and CuF with a superhydrophobic coating of nano-structures.

Chapter 7

Conclusions

This thesis has explored the potential drag reducing benefits of superhydrophobic surfaces. The current state of research on hydrophobic surfaces has been surveyed and it has been demonstrated that such surfaces are capable of producing a drag reduction in small geometries such as patterned micro-channels, where an air layer or plastron, acts to lubricate the flow. Numerous attempts have been made to apply this technology to larger scale flow problems and although drag reductions are evident in some of the experimental work there are questions regarding the consistency of the experimental setup. It is unclear whether the drag reductions are a result of a reduction in the viscous drag, or as a consequence of a change in the location of separation or transition to turbulence, with the latter having a more localized and less easily applicable effect. This work has been aimed at exploring whether a viscous drag reduction is possible in high Reynolds number flows, where the limits of interfacial forces are stretched.

Numerical simulations were initially conducted on a superhydrophobic sphere and demonstrated that a reduction in drag is possible and that it is primarily related to the delay in separation location, caused by the change in the effective boundary condition. The potential drag reduction was found to deteriorate as the surface features moved away from an idealised state towards a surface capable of retaining a plastron, as the surface features reduced the fetch of the flow over the interface and reduced the circulation within the plastron. A numerical study was also conducted on the effect of the Navier-slip condition in both Stokes channel flow and turbulent channel flow with the results validated against an analytical solution and DNS results respectively. The Navier-slip condition was implemented to show that a feasible slip length (based on current research) could produce a measurable drag reduction in flows of a scale that would be applicable to small water craft. The

design of superhydrophobic surfaces was investigated by conducting a numerical, parametric study of the key design parameters, with the main requirements for a large drag reduction being a high cavity fraction, a sufficiently deep cavity and a small length scale ratio between the roughness and external flow scales. Comparisons between the Navier-slip model and coupled-interface model in channel flow demonstrated that as the Reynolds number increases each model showed a different effect. The Navier-slip model showed an increase in the drag reduction whilst the coupled interface model established that it is actually harder to achieve a given slip length at higher Reynolds numbers. This suggests that care must be taken when considering the results of implementations of the Navier-slip model as it inherently assumes that the slip length is a property of the surface.

An experimental setup has been developed to directly measure the viscous drag on a flat plate (aligned with the flow) at high Reynolds numbers in a towing tank. The plate was designed to ensure that changing part of the wetted surface would not influence the experimental conditions and allow a valid comparison between a standard and a superhydrophobic surface. Successive experimental design improvements allowed the error in the drag measurements to be reduced to 0.8%, with the key features for repeatability being the use of turbulators to ensure transition to turbulence upstream of the sample and the accurate alignment of the plate with the towing direction. A broad spectrum of superhydrophobic surfaces, with a variety of construction methods and complexities, were developed as part of the project and were tested in this experimental setup. Systematic variations between the design of samples ensured that the effect of key design parameters on the drag reduction could be investigated, facilitating the optimisation of designs in the future. Based on experiences with superhydrophobic sand and ridges a dual-scale, composite, superhydrophobic copper mesh was developed, to improve the ability of the surface to retain a plastron through increasing the cavity depth and providing a reservoir of air.

The experimental results demonstrated that a relative drag reduction was evident on the majority of the superhydrophobic surfaces tested. The cause of the relative drag reduction was confirmed to be the presence of a plastron on the surface by the removal of the plastron using ethanol; this allowed a comparison of the same rough surface both with, and without a plastron. However, the roughness required to support the plastron was found to produce an increase in drag which the drag reducing effect of the plastron could not overcome. Overall it was demonstrated that the ability of a superhydrophobic surface to produce a relative drag reduction is linked not only to the presence, but to the quality of the plastron. Although it

is necessary for the hydrophobic surfaces to retain a plastron in order to achieve a drag reduction it is not sufficient that the surface is hydrophobic or capable of retaining a plastron; indeed many of the samples tested had either a negligible or negative impact on the relative drag even though they held a plastron on the suface.

The quality of the plastron was explored through underwater photographs and the use of confocal microscopy. The microscopy provided the first high resolution images of the position of the air-water interface on a range of superhydrophobic surface. The images confirmed the presence of the plastron and demonstrated the relative curvature, height and uniformity of the plastron on each surface. The surfaces with the thickest and most uniform plastron were found to produce the largest drag reduction as this provides a closer matching between the scales of the plastron and the external flow. The protrusion of large bubbles or large, random roughness elements were found to be detrimental as they produced an additional drag component and reduced the interfacial velocity in the vicinity of such elements. Buoyancy was also a key effect and found to redistribute the plastron unevenly over the surface in a vertical configuration, reducing the overall efficacy of the surface.

The plastron was found to degrade through the experiment on the majority of the surfaces and this was linked to the increased inertial effect (or reduced effect of interfacial forces) at high Reynolds/Weber number acting to reduce the stability of the air-water interface. The best performing surfaces in this regard were the copper mesh surfaces, which were successfully designed to hold a reservoir of air beneath the external mesh layer. However, even these surfaces suffered from plastron degradation, suggesting that increasing the scale of the surfaces further would likely result in the surfaces having highly unstable plastrons, if they were able able to support a plastron at all. This clearly limits the applicabilty and size of the potential drag reduction.

Overall, the work presented in this thesis has provided a proof of concept, in that a relative drag reduction has been achieved in high Reynolds number boundary layer flow through the use of superhydrophobic surfaces, with weak evidence of an overall drag reduction with ridged hydrophobic samples. Extrapolation of the results of Navier-slip calculations suggest that slip lengths of up to 475μm have been achieved, which are comparable to the results achieved in micro-devices. It is suggested that there is sufficient evidence to support further development of

superhydrophobic surfaces to achieve improvements in the relative drag reduction and minimise the drag increase through careful structuring of the supporting roughness. It has been argued that this would be best accomplished through the development of complex, multiscale superhydrophobic surfaces with higher contact angles than those achieved in this thesis, although experience thoughout this project suggests that this will be difficult, time-consuming and expensive. Further experiments should also be conducted in a static environment such as a flume, to allow more indepth analysis of the flow structure through the use of PIV or LDA. The current setup could also be used to explore the effect of a range of superhydrophobic surfaces on the effect of the location of transition to turbulence.

Appendix A

Navier-slip condition implementation

```
/*
   ************************************************************************


   File name: navier_slip_bc.c
   Author: Brian Gruncell
   Environment: FLUENT 6.33
   Date: 02/11/09

   Description: UDF for specifying a slip velocity based on the
   navier
   slip boundary condition u_s = b * du/dn

   b = slip length (metres)

   This UDF is used as part of a simulation within FLUENT. This file
   needs to be interpreted and then applied as a boundary condition
   to a boundary ALIGNED IN THE X-DIRECTION ONLY (modify gradient
   direction
   for other applications).


   ************************************************************************
   */
#include "udf.h"

double dudy,shear,shear_ave,grad_ave,vel_ave,vel;
double b = 0.01; //define the slip length
```

```
double nf = 300; //number of faces on wall, required for calculating
    averages
FILE *fout;

//The following parameters are only needed for the analytic solution
double dp = 1e-6;
double h = 2;
double mu = 1e-3;
double l = 4;

double current_vel;

double opt = 0; // 0 = Navier slip, 1 = analytic
DEFINE_PROFILE(NAVIER_SLIP_BC, thread, position)
{
  face_t f; // face f at the boundary where the condition will be
  applied
  cell_t c; // cell c adjacent to face f where the gradient will be
  accessed from
  Thread *tc; // thread of cell c

  double grad_sum = 0.0;
  double vel_sum = 0.0;
  double current_vel_sum = 0.0;


  begin_f_loop(f, thread) // loop over all faces in thread 'thread'
  {

  c = F_C0(f,thread);      //access the cell next to face f
  tc = THREAD_T0(thread);          //access the thread of cell c
  if (opt > 0 )
    {
      dudy = dp*h*h/(2*mu*l*(h-b)); //apply analytic Navier-slip
  }
  else
  {
        dudy = C_U_G(c,tc)[1];
  }
  current_vel = F_U(f,thread);
  current_vel_sum = current_vel_sum +current_vel;
  vel = (b*dudy+200*current_vel)/201;
  F_PROFILE(f, thread, position) = vel;

  vel_sum = vel_sum + vel;
  grad_sum = grad_sum + dudy;
```

```
    }
  end_f_loop(f, thread)
  vel_ave = vel_sum/nf;
  grad_ave = grad_sum/nf;
  current_vel = current_vel_sum/nf;
  fout = fopen("output2.txt","a");
  fprintf(fout, "%e %e %e\n",grad_ave,vel_ave,current_vel);
  fclose(fout);
}
```

Appendix B

Application of the coupled interface boundary condition

A coupled boundary condition is used to represent the air-water interface. The main issues with this approach are the transfer of data across the interface and ensuring that the data from one side of the interface is transferred to the correct location on the opposite side. The matching of the tangential velocity across the interface is relatively simple as it only involves the transfer of the two components of velocity across the interface. However, the matching of the tangential shear stress is more convoluted, as it requires a conversion from Cartesian coordinates to surface normal coordinates and then back to Cartesian. In tensor notation the shear stress can be expressed as

$$\tau_{ij} = \mu \left(\frac{\partial u_i}{\partial x_j} + \frac{\partial u_j}{\partial x_i} \right). \tag{B.1}$$

For a curved surface the Cartesian coordinate system is replaced with a coordinate system aligned with the surface. At each point the Cartesian system can be rotated by an angle (θ) so that the x-axis becomes aligned with the surface (s-axis) and the y-axis becomes the surface normal direction (n-axis). To calculate τ_{sn} requires velocity gradients in the surface normal coordinate system and these can be calculated based on the gradients in the Cartesian system using a tensor rotation matrix

$$\nabla \mathbf{u}' = \mathbf{A} \nabla \mathbf{u} \mathbf{A}^T, \tag{B.2}$$

where

$$\nabla \mathbf{u} = \begin{pmatrix} \frac{\partial u}{\partial x} & \frac{\partial v}{\partial x} \\ \frac{\partial u}{\partial y} & \frac{\partial v}{\partial y} \end{pmatrix} \qquad \text{and} \qquad \mathbf{A} = \begin{pmatrix} \cos\theta & -\sin\theta \\ \sin\theta & \cos\theta \end{pmatrix}. \tag{B.3}$$

The values of $\cos\theta$ and $\sin\theta$ can be calculated easily if the sphere has its centre located at the origin by using the position of the centre of each face on the boundary ($\mathbf{P}$)

$$\cos\theta = \frac{P_x}{|\mathbf{P}|} \qquad \sin\theta = \frac{P_y}{|\mathbf{P}|} \tag{B.4}$$

The boundary conditions are applied in a Cartesian coordinate system and hence the final value of wall shear stress needs to be projected in the x- and y- directions

$$\tau_x = \tau_{sn}\cos\theta \qquad \tau_y = \tau_{sn}\sin\theta \tag{B.5}$$

The values for tangential shear stress and tangential velocity are calculated at the start of each iteration based on the values from the previous iteration and then applied as a boundary condition.

Appendix C

UDF - coupled interface model

```
#include "udf.h"//FILE *fout;

double vel,shear_air,shear_water;
double mu_air = 1.845e-5;
double mu_water = 1e-3;

DEFINE_PROFILE(interface_velocity2, thread, position)
{
  face_t f; // face f at the boundary where the condition will be
   applied
  cell_t c_opp; // cell c adjacent to face f where the gradient will
    be accessed from
  Thread *tc_opp; //thread of cell c

  begin_f_loop(f, thread) // loop over all faces in thread 'thread'
  {
  tc_opp = THREAD_T1(thread);      //extract the thread of cell in
   cell in domain behind wall
  c_opp = F_C1(f,thread);      //extract the cell reference of this
   cell

  vel = (C_U(c_opp,tc_opp));     //extract the velocity in this cell
   at previous iteration
  F_PROFILE(f, thread, position) = vel;  //apply this as a boundary
   condition
  }
  end_f_loop(f, thread)
}

DEFINE_PROFILE(interface_shear_water, thread, position)
{
```

```
  face_t f; // face f at the boundary where the condition will be
  applied
  cell_t c_air, c_water;  // cell c adjacent to face f where the
  gradient will be accessed from
  Thread *tc_air, *tc_water,*t_air,*t_water;

  begin_f_loop(f, thread) // loop over all faces in thread 'thread'
  {
  tc_air = THREAD_T1(thread);
  c_air = F_C1(f,thread);

  shear_water = (mu_water*C_U_G(c_air,tc_air)[1]);
  F_PROFILE(f, thread, position) = shear_water;

  }
  end_f_loop(f, thread)
}

DEFINE_PROFILE(interface_shear_air, thread, position)
{
  face_t f; // face f at the boundary where the condition will be
  applied
  cell_t c_air, c_water;  // cell c adjacent to face f where the
  gradient will be accessed from
  Thread *tc_air, *tc_water,*t_air,*t_water;

  begin_f_loop(f, thread) // loop over all faces in thread 'thread'
  {
  tc_air = THREAD_T1(thread);
  c_air = F_C1(f,thread);

  shear_air = (mu_air*C_U_G(c_air,tc_air)[1]);
  F_PROFILE(f, thread, position) = shear_air;

  }
  end_f_loop(f, thread)
}
```

Appendix D

Influence of slip length in channel flow

In fully developed channel flow the axial mean momentum equation can be reduced to a balance between the shear stress gradient and the pressure gradient (Pope, 2009)

$$\frac{\partial \tau}{\partial y} = \frac{\partial P}{\partial x}, \tag{D.1}$$

where the total shear stress can be written as

$$\tau = \rho\nu\frac{dU}{dy} - \rho u'v' \tag{D.2}$$

.

Assuming that the same shear stress is applied at each wall (τ_w), which are spaced a distance of $2h$ apart, then the shear stress is zero at the channel centre ($y = h$):

$$\tau_w = \tau\left(0\right) = -\tau\left(2h\right) \qquad and \qquad \tau\left(h\right) = 0, \tag{D.3}$$

then the shear stress profile can be calculated as:

$$\tau\left(y\right) = \tau_w\left(1 - \frac{y}{h}\right). \tag{D.4}$$

Rearranging Equation D.2 and substituting in Equation D.4:

$$\frac{dU}{dy} = \frac{\tau - \rho u'v'}{\rho\nu} = \frac{\tau_w\left(1 - \frac{y}{h}\right) - \rho u'v'}{\rho\nu}. \tag{D.5}$$

Integrating with respect to y produces:

$$U(y) = \int \frac{\tau_w}{\rho\nu}\left(1 - \frac{y}{h}\right) - \frac{\rho u'v'}{\rho\nu}.dy \tag{D.6}$$

$$U(y) = \frac{\tau_w y}{\rho\nu} - \frac{\tau_w}{\rho\nu}\frac{y^2}{2h} - \frac{\rho u'v'y}{\rho\nu} + C \qquad \text{where} \qquad C = \text{const.} \tag{D.7}$$

Applying the Navier-slip condition,results in a finite velocity (u_s) at the wall

$$U(0) = u_s = b\left(\frac{dU}{dy}\right)_{y=0} = \frac{b\tau_w}{\rho\nu} \tag{D.8}$$

At $y = 0$ Equation D.7 becomes $U(0) = C$ and hence $C = u_s$. This results in a final velocity profile of

$$U(y) = \frac{\tau_w y}{\rho\nu} - \frac{\tau_w}{\rho\nu}\frac{y^2}{2h} - \frac{\rho u'v'y}{\rho\nu} + \frac{b\tau_w}{\rho\nu} \tag{D.9}$$

The final term accounts for the effect on the velocity profile and results in a bulk flow addition to the velocity profile for the no-slip boundary condition ($U_n(y)$.

$$U(y) = U_n(y) + \frac{b\tau_w}{\rho\nu} \tag{D.10}$$

Appendix E

Hot film shear stress relationship

This section aims to demonstrate that that wall-shear stress is related to the heat transfer rate at the wall, following Reference Keith (1990). The thermal energy integral equation can be written as the following Bellhouse and Schultz (1966).

$$\frac{d}{dx}\int_{x}^{\delta_t(x)} u(y)T_0(y)dy = \frac{q_f(x)}{\rho c_P} = -K\frac{\partial T_0}{\partial y}\bigg|_{y=0} \tag{E.1}$$

Assume a thermal boundary layer profile with the following form:

$$T_0 = b\left(1-\eta\right)^3\left(1+\eta\right) = b\left(1-\eta\right)^2\left(1-\eta^2\right) \qquad \text{where :} \qquad \eta = \frac{y}{\delta_t(x)} \tag{E.2}$$

The derivative of this equation can be calculated as:

$$\frac{\partial T_0}{\partial y} = \frac{\partial T_0}{\partial \eta}\frac{\partial \eta}{\partial y} = \frac{\partial}{\partial \eta}\left[b\left(1-\eta\right)^2\left(1-\eta^2\right)\right]\frac{1}{\delta_t(x)} \tag{E.3}$$

$$\frac{\partial T_0}{\partial y} = \frac{b}{\delta_t(x)}\left[-2\left(1-\eta\right)\left(1-\eta^2\right)+\left(1-\eta\right)^2\left(-2\eta\right)\right] \tag{E.4}$$

Hence, at the wall

$$\frac{\partial T_0}{\partial y}\bigg|_{y=0} = \frac{-2b}{\delta_t(x)} \tag{E.5}$$

Assume the thermal boundary layer is entirely within the viscous sublayer, where there is a linear distribution of velocity and the wall normal velocity gradient is constant, such that:

$$u(y) = \frac{y\tau_w}{\mu} \tag{E.6}$$

Combining Equations (E.5) and (E.6) with Equation (E.1) gives:

$$\frac{2bK}{\delta_t(x)} = \frac{d}{dx}\int_0^{\delta_t(x)} \tau_0 y b \left(1-\eta\right)^2 \left(1-\eta^2\right) dy \tag{E.7}$$

$$\frac{2K}{\delta_t(x)} = \frac{d}{dx}\int_0^1 \frac{\tau_0}{\mu}\left[\delta_t^2(x)\left(1-\eta\right)^2\left(1-\eta^2\right)\eta\right]\partial\eta \tag{E.8}$$

Assume τ_0 does not vary over the thermal boundary layer

$$\frac{2K}{\delta_t(x)} = \frac{\tau_0}{\mu}\frac{d}{dx}\delta_t^2(x)\int_0^1 \left[\left(1-\eta\right)^2\left(1-\eta^2\right)\eta\right]\partial\eta \tag{E.9}$$

$$\frac{2K}{\delta_t(x)} = \frac{\tau_0}{15\mu}\frac{d}{dx}\delta_t^2(x) \tag{E.10}$$

Integrate Equation (E.10) over the streamwise extent of the sensor:

$$\int_{x_0}^{x_0+L} K.dx = \frac{\tau_0}{15\mu}\int_0^{\delta_{tL}} \delta_t^2(x).d\delta_t(x) \qquad \text{where} \qquad \delta_{tL} = \delta_t|_{x=x_0+L} \tag{E.11}$$

$$KL = \frac{\tau_0}{45\mu}\delta_{tL}^3 \tag{E.12}$$

Define L^+ in terms of wall units:

$$L^+ = \frac{Lu_\tau}{\nu} \tag{E.13}$$

Rearrange to produce:

$$\frac{\delta_{tL}}{L} = \left(\frac{45}{\mathrm{Pr}}\right)^{1/3} L^{+(-2/3)} \tag{E.14}$$

Equation (E.14) provides a check to see whether the thermal boundary layer is within the viscous sublayer to confirm the assumption above. The average mean heat transfer over the gauge can now be calculated by averaging over the streamwise extent of the gauge:

$$\overline{q_f} = \frac{1}{L}\int_{x_0}^{x_0+L} q_f(x).dx \tag{E.15}$$

From Equations (E.1), (E.5) and (E.10)

$$\frac{q_f(x)}{\rho c_P} = -K\frac{\partial T_0}{\partial y}\bigg|_{y=0} = \frac{2Kb}{\delta_t(x)} = \frac{2b\tau_0}{15\mu}\delta_t(x)\frac{d\delta_t(x)}{dx} \tag{E.16}$$

Hence Equation (E.15) becomes:

$$\overline{q_f} = \frac{2\rho c_P \tau_0 b}{15\mu L} \int_0^{\delta_{tL}} \delta_t(x).d\delta_t(x) = \frac{\rho c_P \tau_0 b \delta_{tL}^2}{15\mu L} \tag{E.17}$$

But from Equation (E.12):

$$\delta_{tL}^2 = \left(\frac{45\mu K}{\tau_0 L^2}\right)^{(2/3)} L \tag{E.18}$$

Hence

$$\overline{q_f} = \frac{\rho c_P \tau_0 b}{15\mu L} \left(\frac{45\mu K}{\tau_0}\right)^{(2/3)} = kb \left(\frac{3}{5\mu L K}\right)^{(1/3)} \tau_0^{1/3} \tag{E.19}$$

Finally, it is clear that the average mean heat transfer is proportional to the shear stress at the wall

$$\overline{q_f} \propto \tau_0^{1/3} \tag{E.20}$$

Appendix F

Tile arrangement for ridged samples

The design of Plate B included modularity to allow different mounting of the samples. This was used primarily for the ridged samples, where the manufacturing processing dictated the mounting locations.

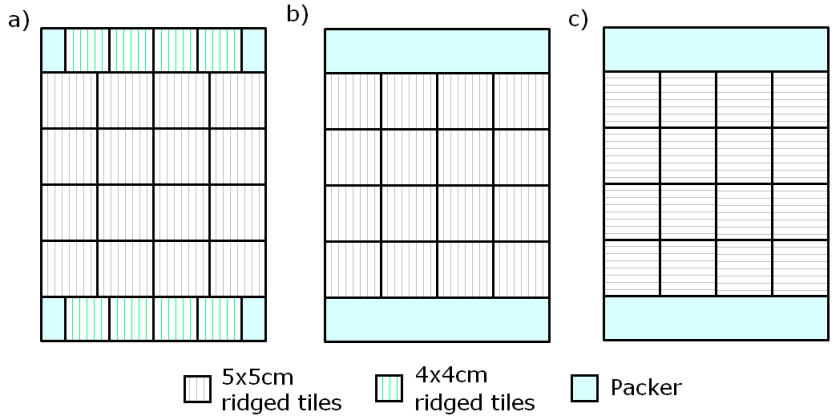

Figure F.1: Schematic of surface tiling for individual sample sheets for a) transverse ridges with full surface covering, b) transverse ridges with 71% surface covering and c) aligned ridges with 71% surface covering

For AR1 two sample sheets were used on each side of the plate (Figure F.2a) with the tiles arranged as in Figure F.1a)). For TR1 one of these sheets was rotated on each side to produce the arrangement shown in Figure F.2b). The remaining samples were constructed with an increased packer area (as shown in Figure F.1b) and c)), as this removed the requirement to cut glass tiles to fit around the edge and reduced the manufacture time from 1 month to 1 week for a set of 4 sheets.

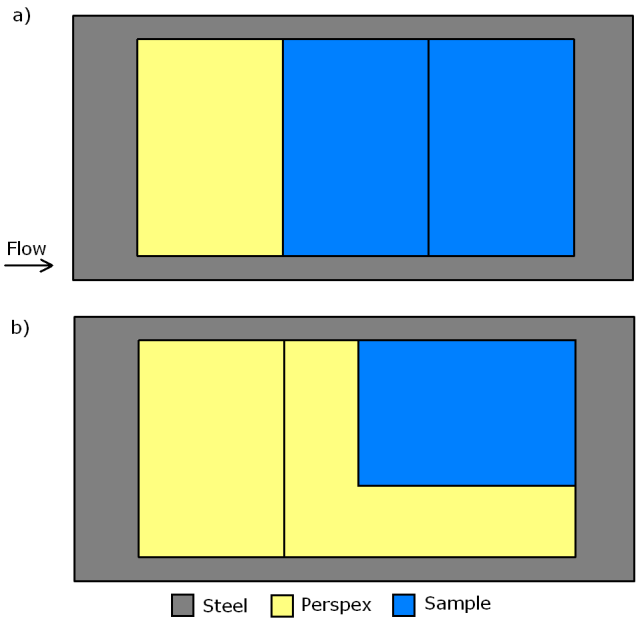

Figure F.2: Effect of AR on drag of Plate B in comparison to a smooth surface. Further details in text

Bibliography

E. Achenbach. The effects of surface roughness and tunnel blockage on the flow past spheres. *J. Fluid Mech.*, 65(1):113–125, 1974.

L. Afferrante and G. Carbone. Microstructured superhydrorepellent surfaces: Effect of drop pressure on fakir-state stability and apparent contact angles. *arXiv:0911.2690v2*, 2009.

N. Ahmad and R. N. Parthasarathy. Turbulence measurements in channel flows with rough and hydrophobic walls. *Proc. FEDSM2007*, 2007.

P. H. Alfredsson, A. V. Johansson, J. H. Haritonidis, and H. Eckelmann. The fluctuating wall shear stress and the velocity field in the viscous sublayer. *Phys. Fluids*, 31(5):1026–1033, 1988.

E. Aljallis, M. A. Sarshar, R. Datla, V. Sikka, and A. Jones. Experimental study of skin friction drag reduction on superhydrophobic flat plates in high Reynolds number boundary layer flow. *Phys. Fluids*, 25(025103):1–14, 2013.

J. D. Anderson. *Computational Fluid Dynamics*. McGraw Hill International, 1995.

J. D. Anderson. *Fundamentals of Aerodynamics*. McGraw Hill International, 2005.

R. A. Antonia and R. E. Luxton. The response of a turbulent boundary layer to a step change in surface roughness. part 2. rough-to smooth. *J. Fluid Mech*, 53: 737–57, 2004.

R. A. Antonia and D. H. Wood. Calculation of a turbulent boundary layer downstream of a small step change in surface roughness. *Aeronautical Quarterly*, 26: 202–10, 1975.

A. Ashrafian, H. I. Andersson, and M. Manhart. DNS of turbulent flow in a rod-roughened channel. *Int. J. Heat and Fluid Flow*, 25:373–383, 2004.

G.H. Atefi, H. Niazmand, and M. R. Meigounpoory. Numerical analysis of 3-d flow past a stationary sphere with slip condition at low and moderate Reynolds numbers. *Journal of Dispersion Science and Technology*, 28(4):591–602, 2007.

A. K. Balasubramanian, A. C. Miller, and O. K. Rediniotis. Microstructured hydrophobic skin for hydrodynamic drag reduction. *AIAA Journal*, 42(2):411–414, 2004.

N. C. Barford. *Experimental measurements: precision, error and truth.* John Wiley & Sons, Chichester, 1985.

W. Barthlott and C. Neinhuis. Purity of the sacred lotus, or escape from contamination in biological surfaces. *Planta*, 202:1–8, 1997.

W. Barthlott, T. Schimmel, S. Wiersch, K. Koch, M. Brede, M. Barczewski, S. Walheim, A. Weis, A. Kaltenmaier, A. Leder, and H. Bohn. The salvinia paradox: superhydrophobic surfaces with hydrophilic pins for air retention under water. *Advanced Materials*, 22(21):2325–2328, 2010.

G. K. Batchelor. *An Introduction to Fluid Mechanics.* Cambridge University Press, 1967.

J. Baudry, E. Charlaix, A. Tonck, and D. Mazuyer. Experimental evidence for a large slip effect at a non-wetting fluid-solid interface. *Langmuir*, 17:5232–5236, 2001.

D.W. Bechert, M. Bruse, W. Hage, J. G. T. Van der Hoeven, and G. Hoppe. Experiments on drag-reducing surfaces and their optimization with an adjustable geometry. *J. Fluid Mech.*, 338:59–87, 1997.

B. J. Bellhouse and D. L. Schultz. Determination of mean and dynamic skin friction separation and transition in low-speed flow with a thin-film heated element. *J. Fluid Mech.*, 24(2):379–400, 1966.

R. Benzi, L. Biferale, M. Sbragaglia, S. Succi, and F. Toschi. Mesoscopic modelling of heterogenous boundary conditions for microchannel flows. *J. Fluid Mech.*, 548:257–280, 2006.

P. R. Bevington and D. K. Robinson. *Data reduction and error analysis for the physical sciences.* McGraw Hill, New York, 2003.

B. Bhushan, Y. Wang, and A. Maali. Boundary slip study on hydrophilic, hydrophobic and superhdyrophobic surfaces with dynamic atomic force microscopy. *Langmuir*, 25(14):8117–8121, 2009.

T. Biben and L. Joly. Wetting on nanorough surfaces. *Physics Review Letters*, 100(18):1–4, 2008.

J. R. Binns, F. O. Albina, and I. A. Burns. Looking for laminars: Measuring intermittency on the america's cup race course. *Experimental Thermal and Fluid Science*, 33:865–874, 2009.

M. S. Bobji, S. V. Kumar, A. Asthana, and R. N. Govardhan. Underwater sustainability of the cassie state of wetting. *Langmuir*, 25(20):12120–12126, 2009.

P. Bradshaw. A note on critical roughness height and transitional roughness. *Phys. Fluids*, 12(6):1–4, 2000.

G. L. Brown. *Theory and application of heated films for skin friction measurements*. Stanford University Press, 1967.

A. Busse and N. D. Sandham. Influence of an anisotropic slip-length boundary condition on turbulent channel flow. *Phys. Fluids*, 24:055111, 2012a.

A. Busse and N. D. Sandham. Parametric forcing approach to rough-wall turbulent channel flow. *J. Fluid Mech*, 712:169–202, 2012b.

A. Busse and N.D. Sandham. Drag of laminar flow over trapped bubbles. In *Proceedings of the XXIII ICTAM, 1924 August 2012, Beijing, China*, 2012c.

M. Campbell, I. Campbell, and J. Robinson. The accuracy and repeatability of tank testing from experience of ACC yacht developments. *High Performance Yacht Design Conference*, 2002:81–88, 2002.

B.-Y. Cao and Z.-Y. Guo. Liquid flow in surface-nanostructured channels studied by molecular dynamics simulation. *Physical Review E*, 74(6):1–7, 2006.

G. Carbone and L. Mangialardi. Hydrophobic properties of a wavy rough substrate. *Eur. Phys. J. E.*, 16:67–76, 2005.

A. B. D. Cassie and S. Baxter. Wettability of porous surfaces. *Trans. Faraday Soc.*, 40:546–551, 1944.

L. P. Chamorro and F. Porte-Agel. Velocity and surface shear stress distributions behind a rough-to-smooth surface transition: a simple new model. *Boundary-Layer Meteorol.*, 130:29–41, 2009.

Y.P. Cheng, C. J. Teo, and B. C. Khoo. Microchannel flows with superhydrophobic surfaces, effects of Reynolds number and pattern width to channel height ratio. *Physics of Fluids*, 21(12):1–12, 2009.

C. H. Choi and C. J. Kim. Large slip of aqueous liquid flow over a nanoengineered superhydrophobic surface. *Physical Review Letters*, 96(6):1–6, 2006.

C. H. Choi, U. Ulmanella, J. Kim, C. M. Ho, and C. J. Kim. Effective slip and friction reduction in nanograted superhydrophobic microchannels. *Physics of Fluids*, 18:1–8, 2006.

H. Choi, P. Moin, and J. Kim. Direct numerical simulation of turbulent flow over riblets. *J. Fluid Mech*, 255:503–539, 1993.

K.-S. Choi and N. Fujisawa. Possibility of drag reduction using d-type roughness. *Applied Scientific Research*, 50(315):315–324, 1993.

K. B. Chuah, S. T. Olszowski, and T. R. Thomas. Plate roughness and hydrodynamic drag. *Wear*, 83:369–383, 1982. 0043-1648/82.

C. F. Colebrook. Turbulent flow in pipes with particular reference to the transition region between the smooth and rough pipe laws. *Journal of the ICE*, 11(4):133–56, 1939.

C. F. Colebrook and C. M. White. Experiments with fluid friction in roughened pipes. *Proceedings of the Royal Society of London. Series A, Mathematical and Physical Sciences*, 161(906):367–381, Aug 1937.

C. Cottin-Bizonne, A. Steinberger, and E. Charlaix. Boundary slip on smooth hydrophobic surfaces: Intrinsic effects and possible artifacts. *Physical Review Letters*, 94(5):1–4, 2005.

D. J. Crisp and W. H. Thorpe. The water-protecting properties of insect hairs. *Discussions of the Faraday Society*, 3:210–20, 1948.

J. Cui, V. C. Patel, and C.-L. Lin. Large-eddy simulation of turbulent flow in a channel with rib roughness. *Int. J. Hear and Fluid Flow*, 24:372–388, 2003.

Z. Cui, Y. Long, W. Qingjun, D Jianfu, and C. Qingmin. A facile dip-coating process for preparing highly durable superhydrophobic surface with multi-scale structures on paint films. *Journal of Colloid and Interface Science*, 337:531–537, 2009.

R. J. Daniello, N. E. Waterhouse, and J. P. Rothstein. Drag reduction in turbulent flows over superhydrophobic surfaces. *Physics of Fluids*, 21(8):1–9, 2009.

J. Davies, D. Maynes, B. W. Webb, and B. Woolford. Laminar flow in a microchannel with superhydrophobic walls exhibiting transverse ribs. *Physics of Fluids*, 18(8):1–11, 2006.

D. M. Deaves. Computations of wind flow over changes in surface roughness. *Journal of Wind Engineering and Industrial Aerodynamics*, 7:65–94, 1981.

P. Ditsch-Kuru, E. S. Schneider, J. E. Melskotte, M. Brede, A. Leder, and W. Barthlott. Superhydrophobic surfaces of the water bug notonecta glauca, a model for friction reduction and air retention. *Belstein Journal of Nanotechnology*, 2:137–144, 2011.

J. F. Douglas, J. M. Gasiorek, J. A. Swaffield, and L. B. Jack. *Fluid Mechanics*. Pearson, Prentice Hill, 2005.

H. Eckelmann. The structure of the viscous sub-layer and the adjacent wall region in a turbulent channel flow. *J. Fluid Mech.*, 65:439, 1974.

V. Efros and P.-A. Krogstad. Development of a turbulent boundary layer after a step from smooth to rough. *Exp. Fluids*, 51:1563–75, 2011.

B. R. Elbing, E. S. Winkel, K.A. Lay, S. L. Ceccio, D.R. Dwoling, and M. Perlin. Bubble-induced skin-friction drag reduction and the abrupt transition to air-layer drag reduction. *J. Fluid Mech.*, 612:201–236, 2008.

R. Enright, T. Dalton, P. Kolodner, M. Hodes, C. Eason, T. Salamon, and T Krupenkin. Friction factors and nusselt numbers in microchannels with superhydrophobic walls. *Proceedings of ICNMM*, pages 1–11, June 2006. ICNMM2006-96134.

H. J. Ensikat, A. J. Schulte, K. Koch, and W. Barthlott. Droplets on superhydrophobic surfaces: Visualization of the contact area by cryo-scanning electron microscopy. *Langmuir*, 25(22):13077–13083, 2009.

L. P. Erm and P. N. Joubert. Low Reynolds number turbulent boundary layers. *J. Fluid Mech*, 230:1–44, 1991.

Z.-G. Feng. A correlation of the drag force coefficient on a sphere with interface slip at low and intermediate Reynolds numbers. *Journal of Dispersion Science and Technology*, 31(7):968–74, 2010.

A. Field. *Discovering Statistics Using SPSS*. Sage, 2005.

Fluent Inc. *Fluent 6.3 User Guide*. Fluent Inc., 2005.

M. R. Flynn and J. W. Bush. Underwater breathing, the mechanics of plastron respiration. *Journal of Fluid Mechanics*, 608:275–296, 2008.

J. H. M Fransson and L. Brandt. Experimental study of the stabilization of Tollmien Schlichting waves by finite amplitude streaks. *Phys. Fluids*, 17:054110, 2005.

P. Freymuth. Calculation of square wave test for frequency optimised hot-film anemometers. *J. Phys. E: Sci. Instrum.*, 14:238–240, 1981.

K. Fukagata and N. Kasagi. A theoretical prediction of friction drag reduction in turbulent flow by superhydrophobic surfaces. *Phys. Fluids*, 18:1–8, 2006. 051703.

K. Fukuda, J. Tokunaga, T. Nobunaga, T Nakatani, T. Iwasaki, and Y. Kunitake. Frictional drag reduction with air lubricant over a super-water-repellent surface. *J. Mar. Sci. Technol.*, 5:123–130, 2000.

E.S. Gadelmawla, M.M. Koura, T.M.A. Maksoud, I.M. Elewa, and H. H. Solimann. Roughness parameters. *Journal of Materials Processing Technology*, 123(1):133–45, 2002.

L. Gao and T. J. McCarthy. A perfectly hydrophobic surface. *J. A. Chem. Soc.*, 128(28):9052–9053, 2006.

L. Gaudet and K. G. Winter. Measurements of the drag of some characteristic aircraft excrescences immersed in turbulent boundary layers. *DTIC Document*, (No. RAE-TM-AERO-1538):1–25, 1973. Royal Aircraft Establishment Farnborough.

S. Gogte, P. Vorobieff, R. Truesdell, A. Mammoli, F Swoi, P. Shah, and C. J. Brinker. Effective slip on textured superhydrophobic surfaces. *Phys. Fluids*, 17 (5):1–4, 2005. 051701.

R. N. Govardhan, G. S. Srinivas, Asthana A., and M. S. Bobji. Time dependence of effective slip on textured hydrophobic surfaces. *Physics of Fluids*, 21(5):1–8, 2009.

B. R. K. Gruncell, N. D. Sandham, and G. McHale. Simulations of laminar flow past a superhydrophobic sphere with drag reduction and separation delay. *Physics of Fluids*, 25(4):046301, 2013a.

B.R.K. Gruncell, N.D. Sandham, M.P. Prince, I.M. Campbell, A. Busse, G. McHale, M.I. Newton, S. Stanley, N.J. Shirtclie, and J. Brennan. Experiments on the drag reducing properties of superhydrophobic surfaces. In *Sports Physics*, pages 428–39. Les Editions de l'Ecole Polytechniques, 2013b.

J. Happel and H. Brenner. *Mechanics of fluids and transport processes.* Martinus Nijhoff Publishers, 1986.

J. H. Haritonidis. The measurement of wall shear stress. *Advances in Fluid Mechanics Measurements*, 45(7):229–261, 1989.

M. Hasegawa, Nitta S., and H. Ueno. Drag reduction effect and wettability of surface with dual-length micro-pillars. *Journal of Fluid Science and Technology*, 4(3):614–622, 2009.

B. He, N. A. Patankar, and J. Lee. Multiple equilibrium droplet shapes and design criterion for rough hydrophobic surfaces. *Langmuir*, 19:4999–5003, 2005.

E. Hecht. *Optics 2nd Ed.* Addison-Wesley, 1987.

C. Henoch, T. N. Krupenkin, P. Kolodner, J. A. Taylor, M. S. Hodes, A. M. Lyons, C. Peguero, and K. Breuer. Turbulent drag reduction using superhydrophobic surfaces. *Proc. 3rd AIAA Flow Control Conference*, pages 1–5, June 2006. AIAA 2006-3192.

M. G. Higazy and D. J. Cockrell. The measurements of drag resulting from small surface irregularities immersed in turbulent boundary layers. *Experiments in Fluids*, 2:197–202, 1984.

E. L. Houghton and P. W. Carpenter. *Aerodynamics for Engineering Students.* Heinemann, 2006.

S.-H. Hsu and W. M. Sigmund. Artificial hairy surfaces with a nearly perfect hydrophobic response. *Langmuir*, 26(3):1504–1506, 2010.

Z. W. Hu, C. L. Morfey, and N. D. Sandham. Wall pressure and shear stress spectra from direct numerical simulations of channel flow. *AIAA Journal*, 44 (7):1541–49, 2006.

ITTC. *Recommended procedures - Testing and Extrapolation Methods Propulsion, Performance Propulsion Test.* International Towing Tank Conference, 2002. 7.5-02-03-01.1.

P. S. Jackson. On the displacement height in the logarithmic velocity profile. *J. Fluid Mech.*, 111:15–25, 1981.

K. Jeffs, D. Maynes, and B. W. Webb. Prediction of turbulent channel flow with superhydrophobic walls consisting of micro-ribs and cavities oriented parallel to the flow direction. *International Journal of Heat and Mass Transfer*, 53(4): 786–796, 2009.

J. Jimenez. Turbulent flows over rough walls. *Annu. Rev. Fluid Mech.*, 36:173–196, 2004.

Y.C. Jung and B. Bhushan. Biomimetric structures for fluid drag reduction in laminar and turbulent flows. *Journal of Microscopy*, 229(1):127–140, 2008.

Y.C. Jung and B. Bhushan. Biomimetric structures for fluid drag reduction in laminar and turbulent flows. *Journal of Physics, Condensed Matter*, 22:1–9, 2010.

W. L. Keith. Spectral measurements of the wall shear stress and wall pressure in a turbulent boundary layer. *NUSC Technical Report*, 8295:1–13, 1990.

W. L. Keith and J. C. Bennett. Low-frequency spectra of wall shear stress and wall pressure in a turbulent boundary layer. *AIAA Journal*, 29(4):526–30, 1991.

B. C. Khoo, Y. T. Chew, C. J. Teo, and C. P. Lim. The dynamic response of a hot-wire anemometer: Iii. voltage pertubation versus velocity-pertubation testing for near-wall hot-wire/film probes. *Meas. Sci. Technol.*, 10:152–169, 1999.

L. Kirkup. *Experimental Methods. An Introduction to the Analysis and Presentation of Data.* John Wiley and Sons, 1994.

K. Koch, B. Bohn, and W. Barthlott. Hierarchically sculptured plant surfaces and superhydrophobicity. *Langmuir*, 25(24):14116–14120, 2009.

T. Krupenkin, J. A. Taylor, P. Kolodner, and M. Hodes. Electrically tunable superhydrophobic nanostructured surfaces. *Bell Labs Technical Journal*, 10(3): 161–170, 2005.

E. Lauga, M. P. Brenner, and H.A. Stone. *The No-Slip Boundary Condition*, chapter 15. Springer, New York, 2005.

C. Lee and C.-J. Kim. Maximizing the giant liquid slip on superhydrophobic microstructures by nanostructuring their side walls. *Langmuir*, 25(21):12812–12818, 2009.

J. G. Leidenfrost. De aquae communis nonnullis qualitatibus tractatus. 1756. transl. C. Wares, On the fixation of water in diverse fire. Int. J. Heat Mass Transfer **9**, 11531166 (1966).

E. W. Lemmon, M. O. McLinden, and D. G. Friend. Thermophysical properties of fluid systems. In Linstrom P. J. and Mallard W. G., editors, *NIST Chemistry WebBook, NIST Standard Reference Database Number 69*. National Institute of Standards and Technology, Gaithersburg MD, 20899, 2011. http://webbook.nist.gov (retrieved April 27, 2011).

S. Leonardi, P. Orlandi, R. J. Smalley, L. Djenidi, and R. A. Antonia. Direct numerical simulations of turbulent channel flow with transverse square bars on one wall. *J. Fluid Mech*, 491:229–238, 2003.

M. Li, J. Zhai, H. Liu, Y. Song, L. Jiang, and D. Zhu. Electrochemical deposition of conductive superhydrophobic zinc oxide thin films. *J. Phys. Chem. B.*, 107: 9954–9957, 2003.

E J. Lobaton and T.R. Salamon. Computation of constant mean curvature surfaces, application to the gasliquid interface of a pressurized fluid on a superhydrophobic surface. *Journal of Colloid and Interface Science*, 314:184–198, 2007.

J. B. R. Loureiro, F. B. C. C. Sousa, J. L. Z. Zotin, and A. P. Silva Freire. The distribution of wall shear stress downstream of a change in roughness. *International Journal of Heat and Fluid Flow*, 31:785–93, 2010.

S. Lu, Z. Yao, P. Hao, and C. Fu. Drag reduction in ultrahydrophobic channels with micro-nano structured surfaces. *Science China, Physics, Mechanics and Astronomy*, 53(7):1298–1305, 2010.

N. K. Madavan, S. Deutsch, and C. L. Merkle. Measurements of local skin friction in a micro-bubble modified turbulent boundary layer. *J. Fluid Mech.*, 156:237–256, 1985.

M. B. Martell, J. B. Perot, and J. P. Rothstein. Direct numerical simulations of turbulent flows over superhydrophobic surfaces. *Physics of Fluids*, 620:31–41, 2009.

M. B. Martell, J. P. Rothstein, and J. B. Perot. An analysis of superhydrophobic turbulent drag reduction mechanisms using direct numerical simulation. *Physics of Fluids*, 22:1–13, 2010.

D. Maynes, K. Jeffs, B. Woolford, and B. W. Webb. Laminar flow in a microchannel with hydrophobic surface patterned microribs oriented parallel to the flow direction. *Physics of Fluids*, 19(9):1–12, 2007.

S. T. McClain, S. P. Collins, and B. K. Hodge. The importance of the mean elevation in predicting skin friction for flow over closely packed surface roughness. *J. Fluids Eng.*, 128(3):579–586, 2006.

G McHale, N. J. Shirtcliffe, C. R. Evans, and M. I. Newton. Terminal velocity and drag reduction measurements on superhydrophobic spheres. *Applied Physics Letters*, 94:1–4, 2009. 064104.

G McHale, M. R. Flynn, and M. I. Newton. Plastron induced drag reduction and increased slip on a superhydrophobic sphere. *Soft Matter*, 7(21):10100–10107, 2011.

C. L. Merkle. An analytical study of the effects of surface roughness on boundary layer transition. *National Technical Information Service, AD/A-004 786*, 40: 1–26, 1974.

T. Min and J. Kim. Effects of hydrophobic surface on skin friction drag. *Physics of Fluids*, 16(7):1–4, 2004. 108106.

S. Moulinet and D. Bartolo. Life and death of a fakir droplet: impalement transitions on superhydrophobic surfaces. *Eur. Phys. J. E*, 24:251–60, 2007.

P. Muralidhar, N. Ferrer, R. Daniello, and J. P. Rothstein. Influence of slip on the flow past superhydrophobic circular cylinders. *J. Fluid Mech.*, 680:459–76, 2011.

R. Narasimha and S. N. Prasad. Leading edge shape for flat plate boundary layer studies. *Experiments in Fluids*, 17(5):358–360, 1995.

C. L. M. Navier. Memooire sur les lois du mouvement des fluids. *Memoires de l'Academie Royale des Sciences de l'Institut de France*, 6:389–440, 1823.

A. Niavarani and N. V. Priezjev. The effective slip length and vortex formation in laminar flow over a rough surface. *Physics of Fluids*, 21(5):1–10, 2009.

M. A. Nilsson, R.J. Daniello, and Rothstein J. P. A novel and inexpensive technique fo creating superhydrophobic surfaces using teflon and sandpaper. *Journal of Physics D, Applied Physics*, 43:1–5, 2010.

M. Nosonovsky and B. Bhushan. *Multiscale dissipative mechanisms and hierarchical surfaces: Friction, superhydrophobicity and biomimetrics*. Springer, Berlin, 2008.

S. Ogata and K. Shimizu. Drag reduction by hydrophobic microstructures. *Journal of Environment and Engineering*, 6(2):291–301, 2011.

D. Oner and T. J. McCarthy. Ultrahydrophobic surfaces. effects of topography length scales on wettability. *Langmuir*, 16:7777–7782, 2000.

J. Ou and J. P. Rothstein. Direct velocity measurements of the flow past drag-reducing ultrahydrophobic surfaces. *Physics of Fluids*, 17(10):1–10, 2005.

J. Ou, B. Perot, and J. P. Rothstein. Laminar drag reduction in microchannels using ultrahydrophobic surfaces. *Physics of Fluids*, 16(12):4635–4643, 2004.

S.-G. Park, S. Y. Lee, S. G. Jang, and S. M. Yang. Perfectly hydrophobic surfaces with patterned nanoneedles of controllable features. *Langmuir*, 26(8):5295–5299, 2010.

J. R. Phillip. Flows satisfying mixed no-slip and no-shear conditions. *Z. Angew. Math. Phys.*, 23:353–370, 1972a.

J. R. Phillip. Integral properties of flows satisfying no-slip and no-shear conditions. *Z. Angew. Math. Phys.*, 23:960–968, 1972b.

R. Poetes, K. Holtzmann, K. Franze, and U. Steiner. Metastable underwater superhydrophobicity. *Physical Review Letters*, 105:1–4, 2010.

S. B. Pope. *Turbulent Flows*. Cambridge University Press, 2009.

M. Reyssat, J. M. Yeomans, and D. Quere. Impalement of fakir drops. *EPL*, 81: 1–5, 2008.

J. P. Rothstein. Slip on superhydrophobic surfaces. *Ann. Rev. Fluid Mech.*, 42: 89–109, 2010.

C. W. Rowley and D. R. Williams. Dynamics and control of high-Reynolds number flows over open cavities. *Annu. Rev. Fluid Mech.*, 38:251–76, 2006.

T. Salamon, W. Lee, Hodes M., and P. Kolodner. *Proceedings of IMECE*, pages 1–11, Nov 2005.

M. A. Samaha, V. H. Tafreshi, and M. Gad-el Hak. Modeling drag reduction and meniscus stability of superhydrophobic surfaces comprised of random roughness. *Phys. Fluids*, 23:1–8, 2011.

V. A. Sandborn. *Resistance Temperature Transducers*. Meteorology Press, Colorado, 1972.

V. A. Sandborn. Evaluation of time-dependent surface shear stress in turbulent flows. *ASME paper*, pages 79–WA/FE–17, 1979.

H. Schlichting. *Boundary Layer Theory*. McGraw Hill International, 1960.

P. N. Shankar and M. D. Deshpande. Fluid mechanics in the driven cavity. *Annu. Rev. Fluid Mech.*, 32:93–136, 2000.

K. Shin and J. K. Hammond. *Fundamentals of Signal Processing for Sound and Vibration Engineers*. John Wiley and Sons, 2008.

N. J. Shirtcliffe, McHale G., M. I. Newton, C. C. Perry, and P. Roach. Porous materials show superhydrophobic to superhydrophilic switching. *Chem. Commun.*, 0:3135–3137, 2005.

N. J. Shirtcliffe, McHale G., M. I. Newton, C. C. Perry, and F. B. Pyatt. Plastron properties of a superhydrophobic surface. *Appl. Phys. Lett.*, 89(10):104106 – 104106–2, 2006.

N. J. Shirtcliffe, McHale G., M. I. Newton, and Y. Zhang. Superhydrophobic copper tubes with possible flow enhancement and drag reduction. *Applied Materials and Interfaces*, 1(6):1316–1323, 2009.

A. Sigal and J. E. Danberg. New correlation of roughness density effect on the turbulent boundary layer. *AIAA Journal*, 28(6):554–556, March 1990.

S. W. Smith. *The Scientist and Engineer's Guide to Digital Signal Processing*. California Technical Publishing, 1997.

Y. Song, R. P. Nair, and M. Zou. Superhydrophobic surfaces produced by applying a self assembled monolayer to silicon micro/nano-textured surfaces. *Nano. Res.*, 2:143–150, 2009.

P. D. M. Spelt. Shear flow past two dimensional droplets pinned or moving on an adhering channel wall at moderate Reynolds numbers: a numerical study. *J. Fluid Mech.*, 561:439–463, 2006.

D. M. Spori, T. Drobek, S. Zurcher, M. Ochsner, C. Sprecher, A. Muhlebach, and N. D. Spencer. Beyond the lotus effect: Roughness influences on wetting over a wide surface-energy range. *Langmuir*, 24:5411–17, 2008.

K. R. Sreenivasan and R. A. Antonia. Properties of wall shear fluctuations in a turbulent duct flow. *J. Applied Mechanics*, pages 389–95, 1977.

S. Taneda. Experimental investigation of the wake begind a sphere at low Reynolds numbers. *Journal of the Physical Society of Japan*, 11(10):1104–1108, 1956.

I. Tani, H. Munakata, A. Matsumoto, and K. Abe. Turbulence management by groove roughness. In H. W. Leipman and R. Narasimha, editors, *Turbulence management and relaminarisation*. Berlin:Spinger-Verlag, 1987.

J. B. Taylor, A. L. Carrano, and S. G. Kandlikar. Characterization of the effect of surface roughness and texture on fluid flow - past, present and future. *International Journal of Thermal Sciences*, 45:962–968, 2006.

R. P. Taylor, J. K. Taylor, M. N. Hosni, and H. W. Coleman. Relaxation of the turbulent boundary layer after an abrupt change from rough to smooth wall. *J. Fluids Eng.*, 115:379–82, 1993a.

R. P. Taylor, J. K. Taylor, M. N. Hosni, and H. W. Coleman. The turbulent thermal boundary layer with an abrupt change from a rough to a smooth wall. *Int. J. Heat and Mass Transfer*, 36(1):141–46, 1993b.

C. J. Teo and B. C. Khoo. Flow past superhydrophobic surfaces containing longitudinal grooves, effects of interface curvature. *Journal of Colloid and Interface Science*, 344(2):575–83, 2010.

J. Tian and Q. Xue. Plate drag reduction with low surface energy coating in a water tunnel. *Chinese Science Bulletin*, 42(4):307–310, 1997.

A. A. Townsend. The response of a turbulent boundary layer to abrupt changes in surface conditions. *J. Fluid Mech*, 22:799–822, 1965.

I.U. Vakarelski, J.O. Martson, D.Y.C. Chan, and S.T. Thoroddsen. Drag reduction by Leidenfrost vapour layers. *Physical Review Letters*, 106:214501, 2011.

I.U. Vakarelski, N.A. Patankar, J.O. Martson, D.Y.C. Chan, and S.T. Thoroddsen. Stabilization of leidenfrost vapour layer by textured superhydrophobic surfaces. *Nature*, 489:274–77, 2012.

O.I. Vinogradova. Drainage of a thin liquid film confined between hydrophobic surfaces. *Langmuir*, 11:2213–2220, 1995.

M. J. Walsh. Riblets as a viscous drag reduction technique. *AIAA Journal*, 21(4): 485–86, 1983.

S. Wang, L. Feng, and L. Jiang. One-step solution-immersion process for the fabrication of stable bionic superhydrophobic surfaces. *Advanced Materials*, 18: 767–770, 2006.

Y. X. Wang and M. Gaster. Effect of surface steps on boundary layer transition. *Experiments in Fluids*, 39:679–686, 2005.

K. Watanabe, S. Ogata, A. Hirose, and A. Kimura. Flow characteristics of the drag reducing solid wall. *Journal of Environment and Engineering*, 2(1):108–114, 2007.

R. N. Wenzel. Resistance of solid surfaces to wetting by water. *Ind. Eng. Chem.*, 28(8):988–994, 1936.

F. M. White. *Viscous Fluid Flow*. McGraw Hill International Edition, 2006.

A. Wietrzak and R. M. Lueptow. Wall shear stress and velocity in a turbulent axisymmetric boundary layer. *J. Fluid Mech.*, 259:191–218, 1994.

G. Woan. *The Cambridge book of physics formulas*. Cambridge University Press, 2009.

T.-S. Wong and C.-M. Ho. Dependence of macroscopic wetting on nanoscopic surface textures. *Langmuir*, 25(22):12851–12854, 2009.

B. Woolford, J. Prince, D. Maynes, and Webb W. Particle image velocimetry characterization of turbulent channel flow with rib patterned superhydrophobic walls. *Physics of Fluids*, 21(8):1–12, 2009.

C. Ybert, C. Barentin, C. Cottin-Bizonne, P. Joseph, and L. Bocquet. Achieving large slip with superhydrophobic surfaces, scaling laws for generic geometries. *Physics of Fluids*, 19(12):1–10, 2007.

A. D. Young and J. H. Paterson. Aircraft excrescence drag. *Advisory Group for Aerospace Research & Development*, 264:1–159, 1981. ISBN: 92-835-1392-4.

Y. S. Yu and Qing. D. Wei. Experimental study on physical mechanism of drag reduction of hydrophobic materials in laminar flow. *Chin. Phys. Lett.*, 23(6): 1634–1637, 2006.

T. A. Zawodzinski, M. Neeman, L. O. Sillerud, and S. Gottesfeld. Determination of water diffusion-coefficients in perflurosulfonate ionomeric membranes. *J. Phys. Chem.*, 95(15):6040–44, 1991.

A. C. Zettlemoyer. *Hydrophobic surfaces*. Academic Press, 1969.

H.-Q. Zhang, H. Lu, B. Wang, and X.-L. Wang. Experimental investigation of flow drag and turbulence intensity of a channel flow with rough walls. *Chin. Phys. Lett.*, 28(8):1–3, 2011.

J.-P. Zhao, X.-D. Du, and X.-H. Shi. Experimental research on friction reduction with superhydrophobic surfaces. *Journal of marine Science and Application*, 6 (3):56–81, 2010.